SINGLE-CHAMBER SOLID OXIDE FUEL CELLS: MODELLING AND EXPERIMENTS

by

NAVEED AKHTAR

A thesis submitted to
The University of Birmingham
for the degree of
DOCTOR OF PHILOSOPHY

School of Chemical Engineering
The University of Birmingham
March 2010

ABSTRACT

The objective of this work is to compare the performance of different geometries (i.e. planar, co-planar and micro-tubular) under single-chamber (mixed-reactant) solid oxide fuel cell (SC-SOFC) conditions. In this respect, these designs have been computer analyzed and it is found that the micro-tubular design eliminates the possibility of cross diffusion/convection from the counter electrode, which is an inherent disadvantage in planar and co-planar designs. This is the first experimental report describing that the micro-tubular design offers the highest fuel utilization, cell efficiency and an acceptable level of performance (under single-chamber conditions) as compared to other designs. With the help of developed numerical model (also the first one, on mixed-reactant, micro-tubular design), it is demonstrated that there is a possibility of further improvement in performance, e.g. cell positioning, micro-tube diameter and cathode morphology (its micro-structure and material) are important factors to consider. Other parameters such as, flow rate, temperature and mixing ratio are also very effective in improving the cell performance but these parameters should be carefully controlled in order to avoid their counter-effects, like, lower fuel utilization, material degradation, anode coking and oxidation-reduction. There are some other parameters such as, electrode porosity, permeability and cathode radiative emissivity, which have minimal effect in performance enhancement and it is suggested before investing time on these parameters, a net energy and cost analysis would be very helpful.

There are still some issues with choosing appropriate materials for building an SC-SOFC with both an acceptable lifetime and production of electrical energy. While it has been observed that most of the problems related to material degradation are thermally driven, it would be very helpful to lower the operating temperature by using intermediate-temperature SOFC materials. Further to this, long term degradation studies and performance cycling will benefit in order to determine their suitability under mixed-reactant environment.

ACKNOWLEDGEMENTS

I would like to thank my supervisors, Professor S.P. Decent, Dr. D. Loghin and Professor K. Kendall (FRS) for their continued support throughout my PhD. Thank you, Waldek, for your support in providing the latest version of COMSOL-Multiphysics available in the fuel cell lab.

The financial support form E.ON-UK and EPSRC is also gratefully acknowledged.

Last but not least, special thanks go to my wife, Maida, and my son, Shaheer, for their understanding and unconditional help throughout the study. No doubt, without their sacrifice, I would not be able to write a number of scientific publications.

CONTENTS

LIST OF FIGURES

List of Tables

NOMENCLATURE

$\mathbf{n}$	normal vector
$\mathbf{u}$	velocity vector
p	pressure
Y_i	mass fraction of the ith species
X_i	mole fraction of the ith species
h_i	specific enthalpy of the ith species
N	total number of species in the mixture
D_{ij}	binary diffusion coefficient for pair $i-j$
$\mathbf{j}_i$	mass diffusion flux of the ith species
r, z	axisymmetric coordinates
u	velocity in r direction
v	velocity in z direction
R	reaction rate
R_i	reaction rate for an individual reaction
$\mathbf{F}$	momentum source term in the Brinkman equation
M	average (mixture) molecular weight
M_i	molecular weight of the ith species
R_g	universal gas constant
T	temperature
c_i	concentration of the ith species
B^{-1}	matrix function of inverted binary diffusion coefficients
B_{ii}	diagonal elements of inverted binary diffusion coefficient matrix
B_{ij}	non-diagonal elements of inverted binary diffusion coefficient matrix
D	matrix of Fick diffusion coefficients
$\mathcal{D}_{ij}$	Maxwell-Stefan diffusivity for pair $i-j$
V_i	molecular diffusion volume
CH_4	methane
CO_2	carbon dioxide
CO	carbon monoxide
H_2	hydrogen
O_2	oxygen
H_2O	water
N_2	nitrogen
e^{-1}	electron
O^{2-}	oxygen ion
D_{DG}^{eff}	Fick effective dusty gas diffusivity matrix
$D_{DG_{i,j}}^{eff}$	Fick effective dusty gas diffusivity for pair $i-j$
$\mathcal{D}_{DG_{i,j}}$	Maxwell-Stefan dusty gas diffusivity for pair $i-j$
$\mathcal{D}_{DG_{i,j}}^{eff}$	Maxwell-Stefan effective dusty gas diffusivity for pair $i-j$

$\mathcal{D}_{k,i}$	Knudsen diffusivity
$B^{eff}_{DG_{ii}}$	diagonal elements of inverted binary effective dusty diffusion coefficient matrix
$B^{eff}_{DG_{ij}}$	non-diagonal elements of inverted binary effective dusty diffusion coefficient matrix
d_p	average pore diameter
A_s	electrochemically active surface area of the medium per unit volume
S_m	mass source term
S_i	species source term
S_ϕ	current source term
E	energy source term
ΔH	enthalpy of formation
i_a	anodic current density
i_c	cathodic current density
$i_{0,a}$	anodic exchange current density
$i_{0,c}$	cathodic exchange current density
V_c	cell voltage
V_{oc}	open circuit (Nernst) voltage
V^o	ideal (standard) voltage
z	number of electrons participating per electrochemical reaction
F	Faraday's constant
exp	exponent
k_s	thermal conductivity of solid (i.e. cell components)
$C_{p,s}$	specific heat of solid (i.e. cell components)
k_{eff}	effective thermal conductivity of solid and gas phase
ρ_{eff}	effective density of solid and gas phase
$C_{p,eff}$	effective specific heat of solid and gas phase
k	thermal conductivity of gas
C_p	specific heat of gas
ds	change in entropy generation
E_{act}	activation energy
R_{mix}	methane-to-oxygen ratio
D_t	micro-tube diameter
D_c	gas-chamber diameter
L_c	gas-chamber length

Greek letters

∇	differential operator
∇^2	Laplace operator
ϕ_s	solid phase (electronic) potential
ϕ_e	electrolyte phase (ionic) potential
μ	dynamic viscosity
ρ	average (mixture) gas density
ρ_i	density of the ith species
ρ_s	density of solid (i.e. cell components)
Γ	thermodynamics matrix
κ	permeability
ϵ	porosity
ϵ_{rad}	radiative emissivity
τ	tortuosity
π	constant (3.14159)
σ	conductivity

σ_o	Stefan-Boltzmann constant
α	charge transfer coefficient
γ	pre-exponential coefficient
η	overpotential

Subscripts

GC	gas-chamber
a	anode
e	electrolyte
c	cathode
rev	reversible
irr	irreversible
ohm	ohmic
act	activation
eff	effective
s	solid phase (electronic)
FOX	full combustion (oxidation)
SR	steam reforming
DR	dry reforming
SH	water-gas shift reaction
PAR	methane parasitic combustion

Superscripts

ref	reference
a	anodic
c	cathodic
d	methane parasitic index
f	oxygen parasitic index

CHAPTER 1

INTRODUCTION

A fuel cell is a device that converts the chemical energy of a fuel (hydrogen, hydrocarbons, ammonia, etc.) and an oxidant (air or oxygen) into electricity. In principle, fuel cells and batteries are very similar in function. Both, the fuel cells and batteries consist of an electrolyte sandwiched in between the two electrodes (i.e. anode and cathode). Both devices generate electrical energy via consumption of chemical energy of the fuel. In a fuel cell, the specific electrochemical reactions occur at the triple phase boundaries (TPBs), where the electrode, electrolyte and the gas phase are in contact with each other. The ionic current transfer takes place through the electrolyte, and the electrons move through an external path to complete the circuit. Individual cells of both the batteries and the fuel cell generate small amount of currents/voltages, and several cells need to be combined to obtain a useful current/voltage. The method of combining the cells, either in parallel or in series, is called stacking.

The major difference in between the fuel cells and batteries lies in the nature of their anode and cathode. In a battery, the anode and cathode are metals and form an integral part of the battery structure. They are consumed during the reaction to generate electrical current. However, in case of fuel cells, the anode and cathode are never consumed and the electrical power is generated so long as the reactants are supplied to the anode and cathode.

1.1 Fuel Cells - An Overview

A conventional fuel cell consists of two electrodes (i.e. anode and cathode, which are porous), an electrolyte (which is non-porous, and sandwiched between the two electrodes), an interconnect (for current collection/stacking) and channels (also called bipolar plates) for fuel and air supply. Air or oxygen passes over one electrode, and fuel over the other, generating electricity, water (as a reaction product) and heat. Fuel cells electrochemically combine the molecules of a fuel and oxidizer leading

to higher overall efficiencies, in contrast to direct chemical combustion causing pollution and system losses.

The different types of fuel cells are mainly distinguished by the use of their electrolyte. The electrolytes are further differentiated via their phase (solid or liquid), operating temperature (low or high) and mobile ion transport (hydrogen, oxygen, hydroxyl or carbonate) mechanism. Low-temperature fuel cells require a noble metal catalyst such as Platinum to improve activation, whereas, high-temperature fuel cells do not require a costly catalyst and are very flexible in the type of fuel to be used. A detailed classification of different types of fuel cells and their respective operating temperature range is given in Table 1.1 [1]:

Fuel cell type	Abbreviation	Mobile ion	Temperature range
Alkaline Fuel Cell	AFC	OH^-	50-200°C
Proton Exchange Membrane Fuel Cell	PEMFC	H^+	50-100°C
Phosphoric Acid Fuel Cell	PAFC	H^+	ca.220°C
Molten Carbonate Fuel Cell	MCFC	${CO_3}^{-2}$	ca.650°C
Solid Oxide Fuel Cell	SOFC	O^{-2}	600-1000°C

Table 1.1: Fuel cell types

In general, a fuel cell can operate on a variety of fuel and oxidant compositions. The most simplified and common approach is to use hydrogen as the fuel and air as the oxidant. The use of hydrogen directly fed to the anode of a fuel cell, eliminates the need of complex reforming reactions as normally exist in the case of hydrocarbon based fuels. Oxygen is the most commonly used oxidant due to its abundance in the ambient air. The selection of a suitable type of fuel depends on the fuel cell type, which in turn is sensitively dependent on the electro-catalyst employed for the anode. Most low-temperature fuel cells show rapid degradation in their performance due to the presence of very low level of impurities, such as carbon-monoxide. On the other hand, carbon-monoxide is itself a fuel for high-temperature fuel cells (e.g. solid oxide fuel cell) and generate electricity by electrochemical oxidation.

The main advantage of low-temperature fuel cells is their quick start-up capability and less thermo-mechanical stresses due to their low operating temperature range. The benefits associated with high-temperature fuel cells allow fuel flexibility and high-grade waste heat available for co-generation purpose. Last but not least, high-temperature fuel cells (such as SOFC) do not require expensive noble metal catalyst (e.g. Platinum), allowing less expensive materials (e.g. Nickel) to be used as the catalyst.

1.2 Solid Oxide Fuel Cells

The SOFC uses a solid electrolyte that conducts (O^{-2}) ions from the cathode to the anode. This is in opposite to most of the low-temperature fuel cells, which uses hydrogen as a mobile ion carrier from anode to cathode. An SOFC consists of the following components:

• Fuel electrode (anode), usually Nickel-Yttria stabilized Zirconia (Ni-YSZ).

• An electrolyte, usually Yttria stabilized Zirconia (YSZ).

• An air electrode (cathode), usually Lanthanum Strontium Maganite (LSM).

The two most advanced designs of SOFCs are the tubular and planar type configurations. Each of these two have merits and limitations, which will be described later, in detail.

1.2.1 Operating Principle

Solid oxide fuel cells can operate using pure hydrogen or hydrocarbon fuels. Since hydrogen is an energy carrier and not a primary energy source, current research focuses on using hydrocarbons as the main fuel for SOFC. Among various hydrocarbons, methane is the most commonly accepted choice because of its widespread availability, at present. In the anode of an SOFC, methane can be catalyzed into hydrogen and carbon-monoxide via different reaction schemes, as shown in Table 1.2, and oxygen undergoes a reduction reaction at the cathode (Table 1.3).

1) Reaction at the anode [2, 3]:

Reaction	Equation	Δ Q $kJmol^{-1}$
Methane steam reforming	$CH_4 + H_2O \rightarrow 3H_2 + CO$	226
Methane dry reforming	$CH_4 + CO_2 \rightarrow 2H_2 + 2CO$	259
Shift reaction	$CO + H_2O \rightarrow H_2 + CO_2$	-33
Methane full combustion	$CH_4 + 2O_2 \rightarrow 2H_2O + CO_2$	-803
Methane partial oxidation	$CH_4 + \frac{1}{2}O_2 \rightarrow 2H_2 + CO$	-36
Hydrogen full combustion	$H_2 + \frac{1}{2}O_2 \rightarrow H_2O$	-249
Carbon monoxide full combustion	$CO + \frac{1}{2}O_2 \rightarrow CO_2$	-282
Methane electrochemical oxidation	$CH_4 + 4O^{-2} \rightarrow 2H_2O + CO_2 + 8e^-$	$n.k.^a$
Carbon monoxide electrochemical oxidation	$CO + O^{-2} \rightarrow CO_2 + 2e^-$	$n.k.$
Hydrogen electrochemical oxidation	$H_2 + O^{-2} \rightarrow H_2O + 2e^-$	$n.k.$
Methane cracking	$CH_4 \rightarrow 2H_2 + C$	75
Boudouard reaction	$2CO \rightarrow CO_2 + C$	86

[a] = not known

Table 1.2: Possible reactions in an SOFC anode

2) Reaction at the cathode:

Reaction	Equation	Δ Q $kJmol^{-1}$
Oxygen electrochemical reduction	$\frac{1}{2}O_2 + 2e^- \rightarrow O^{2-}$	$n.k.$

Table 1.3: Reactions in an SOFC cathode

The O^{-2} ion is drawn through the electrolyte from the cathode to the anode and electrochemically combines with hydrogen or carbon monoxide in the anode, while electrons are forced through an external circuit from the anode to the cathode (Figure 1.1).

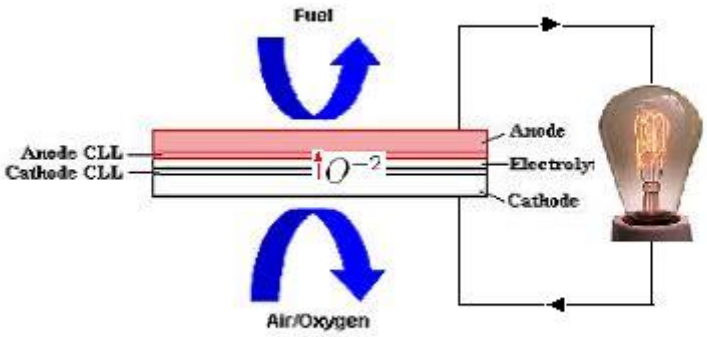

Figure 1.1: Schematic diagram of SOFC principle

1.2.2 Electrochemical Basics for SOFCs

Heating Voltage

The heating voltage related to the reaction enthalpy (heating value) of the fuel gas can be determined by using [1]:

$$U_{\Delta H} = \frac{-\Delta H}{zF} \tag{1.1}$$

where $U_{\Delta H}$ is the heating voltage, ΔH is the heating value (total thermal energy available) based on either higher heating value (HHV) or lower heating value (LHV), F is the Faraday's constant ($96485\ As\ mol^{-1}$) and z is the number of electrons participating per electrochemical reaction. Table 1.4 presents heating voltages for hydrogen and methane based on higher and lower heating values [1].

The heating values expressed above as HHV and LHV, both refer to total heat released during the

Fuel	$U_{\Delta H}$ (V)
Hydrogen(LHV)	1.25
Hydrogen(HHV)	1.48
Methane(LHV)	1.04
Methane(HHV)	1.14

Table 1.4: Heating voltage for hydrogen and methane

complete combustion of fuel. The only difference among them is the byproduct water in liquid form in the former case and in gaseous form in the later case.

Gibbs Free Energy

In the case of a chemical reaction at constant pressure, there is only a certain amount of energy that can be transferred into electrical energy, the remaining appears as heat. This useful energy in the form of electrical work is known as the Gibbs free energy [4].

$$\Delta G = \Delta H - T\Delta S \tag{1.2}$$

where, ΔG is the Gibbs free energy and $T\Delta S$ is the heat loss to the environment. The change in the free energy of a system that occurs during a reaction can be measured under any set of conditions. If the data are collected under standard-state conditions, the result is the standard-state free energy of reaction, ΔG^o, and equation (1.2) can be written for standard conditions [4]:

$$\Delta G^o = \Delta H^o - T\Delta S^o \tag{1.3}$$

Ideal Voltage

This describes the maximum energy that can be transferred into electrical energy measured at the relevant conditions. It is related to ΔG voltage [1]:

$$U^o = \frac{-\Delta G(T)}{zF} \tag{1.4}$$

The values of ideal voltages for hydrogen and methane are listed in Table 1.5 at standard conditions (25°C, 1 bar) [1].

Fuel	U^o (V)
Hydrogen(LHV)	1.18
Hydrogen(HHV)	1.23
Methane(LHV)	1.04
Methane(HHV)	1.06

Table 1.5: Ideal voltage for hydrogen and methane at standard conditions (25°C, 1 bar)

Nernst (Open Circuit) Voltage

As can be seen from the above, the ideal voltage is defined at the standard conditions. However, the operating temperature of any fuel cell is always above the standard conditions. In the case of SOFCs, the nominal operating temperature range is in between 600-1000°C. Also, the reactant concentration and the operating pressure may deviate from that considered at standard conditions. In order to take into account the deviation in the reactant concentration, operating temperature and pressure, an additional term is incorporated in equation (1.4) [1]:

$$U_N(T,p) = \frac{-\Delta G(T)}{zF} - \frac{RT}{zF}\Sigma ln\frac{p_i^{v_i,products}}{p_i^{v_i,reactants}} \tag{1.5}$$

where, U_N is the Nernst (open circuit) voltage (OCV), R is the molar gas constant ($8.313J\ mol^{-1}\ K^{-1}$), v_i number of moles participating in the reaction and p_i is the partial pressure of the reactants/products.

Losses in Solid Oxide Fuel Cells

The operating cell voltage (U_c) is always lower than the Nernst (open-circuit) voltage (U_N) due to various polarizations (ohmic, activation, and concentration). The operating cell voltage can be expressed as [4]:

$$U_c = U_N - \eta_{act}(i) - \eta_{ohm}(i) - \eta_{conc}(i) \tag{1.6}$$

where, η_{act} is the activation polarization in the two electrodes, η_{ohm} is the ohmic polarization (ionic and electronic) and η_{conc} is the concentration polarization in the two electrodes.

Activation Polarization

Activation polarization (η_{act}) is caused by slow charge-transfer reactions at the electrode-electrolyte interfaces, and for small currents and/or rapid mass transfer, it is related to the current density, i, through the Butler-Volmer equation. For anode and cathode, the Butler-Volmer equation can be writ-

ten as [5]:

$$i_a = i_{0,a}[exp(\frac{\alpha_a^a F \eta_{act,a}}{RT}) - exp(-\frac{\alpha_c^a F \eta_{act,a}}{RT})] \tag{1.7}$$

and

$$i_c = i_{0,c}[exp(\frac{\alpha_a^c F \eta_{atc,c}}{RT}) - exp(-\frac{\alpha_c^c F \eta_{atc,c}}{RT})] \tag{1.8}$$

where $i_{0,a}$, $i_{0,c}$ are the exchange current densities for anode and cathode, respectively. Here α_a^a, α_c^a, α_a^c and α_c^c are the anodic-anodic, anodic-cathodic, cathodic-anodic and cathodic-cathodic charge transfer coefficients, respectively.

Ohmic Polarization

The ohmic overpotential has two contributions, linked to the electronic and ionic resistance:

$$\eta_{ohm}(i) = iR_i \tag{1.9}$$

where i is the current density ($A\ cm^{-2}$), R_i is the area specific ohmic resistance of the cell (Ωcm^2). Here R_i includes the resistance of the electrolyte, the electrodes, and the contact resistances associated with current collection and all of the cell-layer interfaces. It can be expressed as a function of the conductivity (σ) and the thickness (t) under consideration, namely:

$$R_i = \frac{t}{\sigma} \tag{1.10}$$

Concentration Polarization

Concentration polarization of the cell (η_{conc}) occurs due to the slow mass transport of gas-phase reactant and/or product species through the porous anode and cathode. The electrode process can be dominated by the concentration polarization at high current densities and/or when the porosity is low or insufficient. If the electrode process is completely controlled by concentration polarization, the limiting current is reached and the cell voltage drops rapidly.

Since the main cause of concentration polarization is the limited mass transport into the porous electrodes, a detailed model incorporating multi-component mass transport in a porous media will be required to consider this polarization effect. This will be presented in the following chapters, in detail.

1.2.3 Effective Fuel Utilization

Fuel utilization during fuel cell operation will be a useful tool to estimate the effective performance of the cell. There are two approaches (as shown in Equation (1.11) and (1.12)) to calculate the fuel utilization reported in the literature [6, 87, 8, 9, 10]:

$$\eta_U = \frac{\dot{m}_{f,reacted}}{\dot{m}_{f,in}} = \frac{MI_{tot}}{zF\dot{m}_{f,in}} \tag{1.11}$$

and

$$\eta_U = 1 - \frac{\dot{m}_{f,out}\Delta h_{f,out}}{\dot{m}_{f,in}\Delta h_{f,in}} \tag{1.12}$$

where η_U is the fuel utilization, $\dot{m}_{f,reacted}$ is the mass flow rate of fuel reacted in the cell $(kg\ s^{-1})$, $\dot{m}_{f,in}$ is the mass flow rate of fuel entering the cell $(kg\ s^{-1})$, M is the molar mass of reacting fuel $(kg\ mol^{-1})$, I_{tot} is the total current at the peak power density (A), $\dot{m}_{f,out}$ is the mass flow rate of fuel at the outlet $(kg\ s^{-1})$, $\Delta h_{f,in}$ is the specific enthalpy associated with completely oxidizing the inlet fuel $(kJ\ kg^{-1})$ and $\Delta h_{f,out}$ is the specific enthalpy associated with completely oxidizing the exhaust fuel $(kJ\ kg^{-1})$.

Each of these two approaches has merits and limitations. For example, fuel utilization calculated by Equation (1.11) only considers the amount of fuel converted into electrical power directly available at the cell or stack (i.e. DC power in front of inverter). This does not take into account any heating effects, i.e. reversible loss, irreversible losses (such as activation, ohmic and concentration polarization), loss of energy (J) equivalent to $2FU^o$(only 6 electrons participating per electrochemical reaction, in the case of single-chamber SOFC utilizing methane/air mixture), or the part of the heat that will be carried away by exhaust gases (fuel, inert and product gases), or some of the heat can be lost into the environment, or some can be stored in the cell components. Not only this, the usual tradition of laboratory based experiments requires electrical heating to maintain the cell operating temperature, which further complicates the overall energy balance due to furnace heating. Moreover, not only are the various heating losses (as discussed above) neglected in Equation (1.11), but also the current collection efficiency, which plays a major role in this calculation, is not being taken into account.

The term "Fuel Utilization" as described in Equation (1.12) considers the differences in heating values of the inlet and exhaust fuels divided by the heating value of inlet fuel (all based upon com-

pletely oxidizing the available fuels). Although, this approach accounts for both the thermal heating and the electrical power produced by the cell, calculating the fuel utilization in terms of thermal heat that has not been effectively utilized makes little sense. For example, in the case of a single-cell (where the heat produced is not effectively utilized) it is not worth considering fuel utilization towards non-effective heat produced. Though, some portion of this heat may be participating in improving the overall system performance via enhancing the local ionic conductivity of the electrolyte, resulting in improved electrical performance, it is very difficult to calculate the effective contribution of this heat. Moreover, calculating the amount of exhaust fuel requires additional equipment such as a gas chromatograph (or gas analyzer). Furthermore, the outlet fuel is diluted with various product gases, and, one cannot simply use the heating values of various exhausted fuels in concentrated form. Instead, heating values of exhausted fuels must be calculated by considering the dilution factor.

Due to the above complications, we propose the use of Equation (1.11) for fuel utilization and term this as "Effective Fuel Utilization" in our future experiments, as at present we do not plan to utilize thermal heat produced and are only interested in electrical output from the cell.

1.2.4 Effective Efficiency

The effective efficiency informs the electrical efficiency calculated at the specific operating cell voltage. It can be calculated by using the following formula:

$$\eta_{eff} = \eta_{ideal}\eta_V\eta_U \tag{1.13}$$

where,

$$\eta_{ideal} = \frac{U^o}{U_{\Delta H}} \tag{1.14}$$

and

$$\eta_V = \frac{U_c}{U^o} \tag{1.15}$$

where η_{eff} is the effective efficiency, η_{ideal} is the ideal efficiency, η_V is the voltage efficiency and U^o, $U_{\Delta H}$, U_c are the ideal (standard), heating and cell voltage respectively.

1.2.5 Solid Oxide Fuel Cells: Materials and Components

The operating principle of a SOFC is not as complicated as the selection of materials for the individual components. This gives major challenges to overcome in order to find appropriate materials for all components of an SOFC. In general, mechanical and chemical compatibility among various components, reliability, durability and cost-effectiveness should be encountered. The four main components of an SOFC are: anode, electrolyte, cathode and an interconnect. These components and their respective materials are discussed below in detail.

Cathode

The cathode should possess an adequate porosity to offer enhanced mass transport and should be an electrical conductor to facilitate electron flow. The cathode should also have better oxygen surface exchange kinetics and oxygen ion transport capability. In this respect, a mixed ionic-electronic conductor (MIEC) would be an ideal candidate. Cathode material should also be mechanically compatible with the electrolyte (matching coefficient of thermal expansion in between the cathode and electrolyte) in order to reduce the risk of mechanical failure by thermal stresses. The cathode should also be chemically compatible with the electrolyte in order to ensure that the inter-diffusion of cathode material during sintering should not happen.

The conventional SOFC cathode is the Lanthanum Strontium Manganate (LSM) which is a high-temperature electronic conductor. The main problem with this cathode is that it does not provide an ionic current transport path, therefore the active regions are limited to the cathode-electrolyte interface. Another problem with this cathode material is the high polarization with decreasing temperature.

Now-a-days, there is a common trend to lower the operating temperature of SOFCs, therefore, intermediate-temperature SOFCs (IT-SOFC) are gaining considerable interest. However, lowering the operating temperature puts strict limitations on the selection of the electrode and electrolyte materials. It is widely reported that among all the components, the cathode is the most sensitive one, as reducing the operating temperature increases the cathode polarization. In order to tackle this problem, MIEC such as Lanthanum Strontium Cobaltite Ferrite (LSCF), Strontium doped Samarium Cobaltite (SSC) and Barium Strontium Cobaltite Ferrite (BSCF) are the ideal candidates for IT-SOFC.

Electrolyte

Electrolytes in SOFC should only possess high ionic conductivity with no or negligible electrical conductivity. The electrolyte should also be dense (pore free) in order to prevent current leakage and short-circuit. It should also be as thin as possible to minimize the resistive losses. Also, similar to the cathode, it must be chemically and mechanically stable. One of the very important requirements to be met is that the electrolyte should stably operate in both the reducing (anode side) and oxidizing (cathode side) environment.

The most common candidate for high-temperature SOFC is the Yttria-stabilized-Zirconia (YSZ). It is a high-temperature ionic conductor (operating at or above 800°C) and with reduction in operating temperature, its ionic conduction decreases significantly. For this reason, other intermediate-temperature ionic conductors, such as Gadolinium doped Ceria (GDC), Samarium doped Ceria (SDC), Scandium stabilized Zirconia (ScSz) and Magnesium doped Lanthanum Gallate (LSGM) are best suited for IT-SOFC.

Anode

The anode must meet most of the same requirements as the cathode, such as porosity, electrical conductivity, chemical and mechanical compatibility. Similarly to the cathode, in order to extend the triple phase boundaries, the anode should also possess some ionic conductivity. As stated before for the cathode, MIEC will be an ideal candidate for the anode, as well. The most commonly used anode material is the Nickel-Yttria-stabilized-Zirconia (Ni-YSZ). However, this material faces problems of carbon formation (coking) when operated with hydrocarbon fuels. It has been well documented that the Nickel is the most sensitive part of the anode material towards coking. The other problem with the Nickel is the large variations in volume upon reduction and re-oxidation (RedOx) cycles. Faes et al. [11] have reported -41.6% volume decrease upon reduction and +71.2% volume increase upon re-oxidation of Nickel. The most common outcome of this volume change is the Nickel sintering due to change of morphological structure.

Due to the above problems, there is a strong research trend to look for alternative anode materials. Ceria based anodes are reported as the best candidates for solving the coking problem. Ceria is a good MIEC and does not allow carbon formation. Although, the coking problem has been solved to a certain extent, RedOx behavior is still under active research for Ceria based anodes. The most widely accepted alternative anode materials are Nickel-Gadolinium doped Ceria (Ni-GDC), Nickel-

Samarium doped Ceria (Ni-SDC), Copper-Cerium Oxide, Yttria-stabilized Zirconia (Cu-CeO-YSZ) and Lanthanum Strontium Manganese Chromite (LSCM).

Interconnect

The power density (in the $mWcm^{-2}$ range) obtained from a single cell is not enough to be practical for a real application. Although, this power could be sufficient for milli or micro power range applications, it is still too low for a little larger load applications. In order to meet this requirement, several cells must be stacked together either in series or in parallel, and this task can be achieved by interconnecting several cells.

Interconnects have to meet most of the above requirements listed for electrodes, such as being mechanically and chemically compatible, having high electrical conductivity, corrosion resistive and stable operation under RedOx environment. Since metallic interconnects such as stainless steel are much cheaper than the ceramics, the current research trend is to employ metals as interconnects. This could significantly reduce the manufacturing cost and offer high electrical conductivities solely required for this purpose. Besides, various advantages of using metallic interconnects such as stainless steels, suffer from corrosion and volatility problems. Since Chromium (Cr) is one of the component present in stainless steel, it is highly volatile and causes inter-diffusion problems in most of the cathodes used for SOFC applications. Crofer 22, Haynes 230 and Inconel 718 are possible alternatives and are under active research [12].

1.2.6 Solid Oxide Fuel Cell Designs

In general, the following designs are adopted for SOFCs:

Planar Design

Planar design consists of flat plates for cell components, which sometimes have channels embedded for air and fuel supply in the current collector plates (Figure 1.2). This design gives high power densities because of low ohmic resistance for current collection as compared to tubular design (Figure 1.3). Another advantage of the planar design is their lower manufacturing costs because of simplicity in design and low cost fabrication methods such as screen printing and tape casting can be used. One of the major disadvantages of planar design is the reactants leakage through the cell edges, requiring gas-tight sealing. The sealing material further puts stringent requirement in their selection; for example, it has to be mechanically compatible (matching coefficient of thermal expansions with adjacent

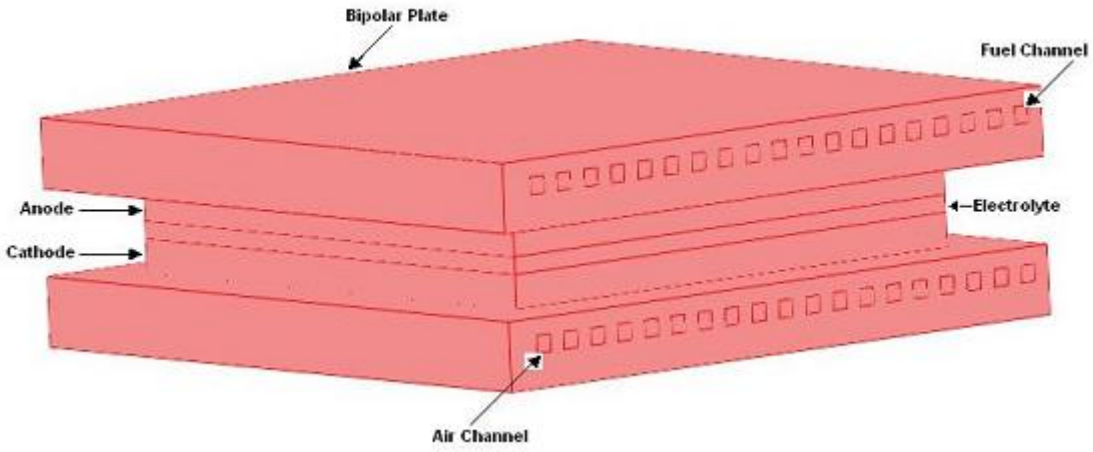

Figure 1.2: Planar type SOFC

components) and chemically stable (long term stability under RedOx environment).

Tubular Design

The tubular SOFC was pioneered by the US Westinghouse Electric Corporation (now Siemens Westinghouse Power Corporation or SWPC) in the late 1970s. It is the most advanced SOFC and SWPC already demonstrated a 200 kW system. This technology is based on ceramic tubes, which are manu-

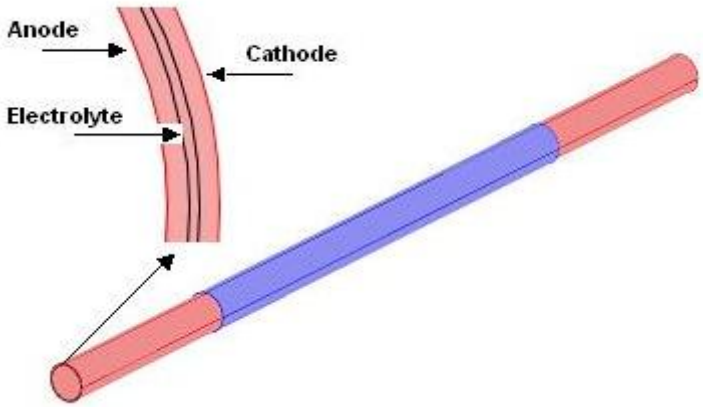

Figure 1.3: Tubular type SOFC

factured by extrusion, sintering and coating. The tubular design has the advantage of good mechanical stability and the disadvantage of high internal resistance. A typical view of the tubular-SOFC is shown in Figure 1.3.

Integrated Planar Design

In order to take advantage of both the planar and tubular geometry, the integrated planar SOFC configuration has been proposed and practically adopted by Rolls Royce. It has many similar features to the original Westinghouse tubular design and consists of an assembly of small planar SOFCs fabricated on a ceramic housing (Figure 1.4). The housing serves as a manifold for the fuel gas, with a novel

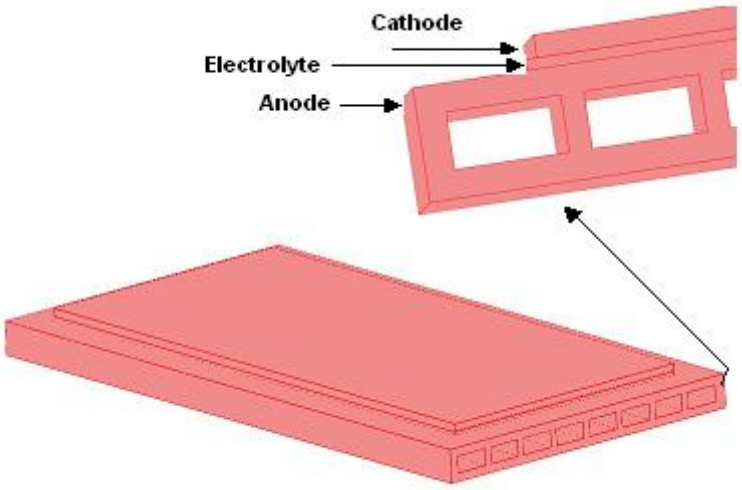

Figure 1.4: Integrated-planar type SOFC

sealing arrangement. Rather than using a bipolar plate, the cells are connected by an inter-connector fabricated onto the cell housing. This design offers high volumetric power densities with ease in cell manufacturing via screen printing technology.

Honeycomb Design

Both the planar and the tubular designs have evolved from a single cell and the concept of producing a stack has been problematic. The tubular design offers the possibility of creating gas seals outside of the functional high temperature zone, but power densities are relatively low. Planar stacks have the advantage of high power densities, but difficulties associated with sealing and manifolding issues are yet to be overcome. Honeycomb stack design (Figure 1.5) offers the energy density of planar stacks with the possibility of cold gas seals from tubular design.

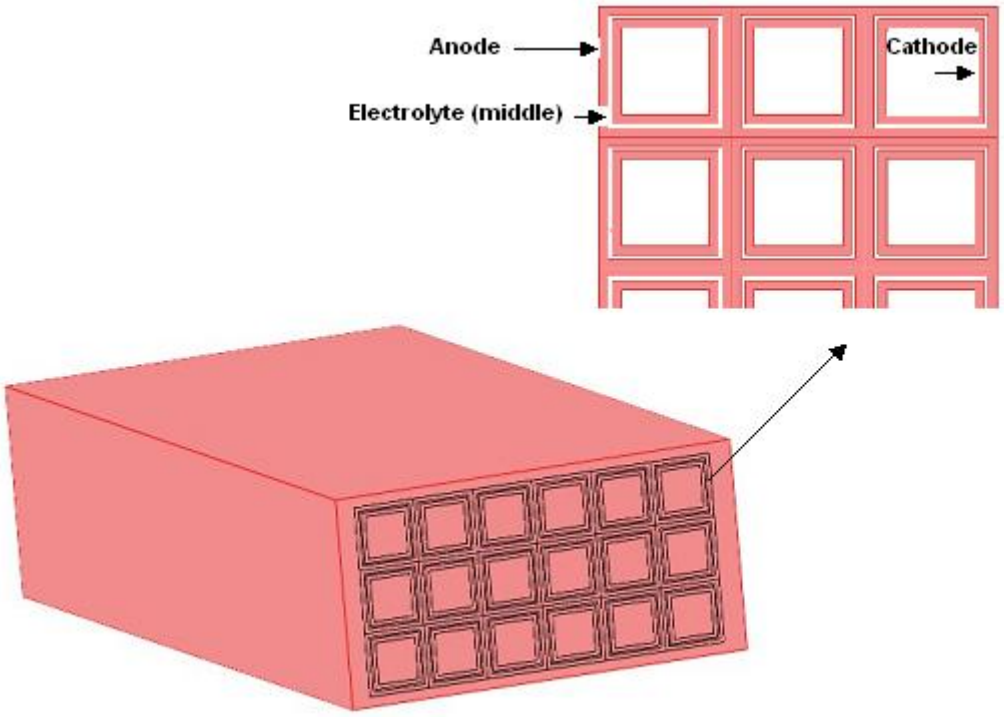

Figure 1.5: Honeycomb type SOFC

1.3 Challenges in Solid Oxide Fuel Cells

Solid oxide fuel cells (SOFCs) have received much recent attention as next-generation alternative energy conversion devices because of their high overall efficiencies and good fuel flexibility. However, the high-temperature operation results in a number of challenges that need to be overcome, including interfacial diffusion between cell components, mechanical stress due to their different thermal expansion coefficients, and electrode deactivation by poisoning and sintering. In particular, failure to obtain a gas-tight seal between chambers is a very serious problem, causing gas leakage and eventual destruction of the stacked cells. Moreover, the addition of a large amount of steam to hydrocarbon fuels is needed to avoid carbon formation on the anode surface, requiring complicated water management in SOFC systems. One approach toward addressing the above challenges is to design an SOFC with only one gas chamber. This type of SOFC is known as ”single-chamber SOFC” (SC-SOFC) and will be addressed in detail.

1.4 Single-Chamber Solid Oxide Fuel Cell (SC-SOFC)

Single-Chamber Solid Oxide Fuel Cells (SC-SOFCs) operate on a mixed reactant supply (air-fuel mixture) using selective electrodes by using catalysts coated onto the surface of electrodes. Ideally,

the anode is active only for the electro-catalytic oxidation of fuel, while the cathode has high electro-catalytic activity for oxygen reduction. In cases where hydrocarbons are used as a fuel, the catalytic activity (of the anode) towards partial oxidation is also necessary in order to produce electrochemically active species.

In Figure 1.6, planar-type SC-SOFC is placed in the middle of a rectangular duct. The cell often known as PEN (positive electrode, electrolyte and negative electrode) can be placed either in a horizontal position (Figure 1.6a) or in an anode first vertical position (Figure 1.6b) or a cathode first vertical position (Figure 1.6c).

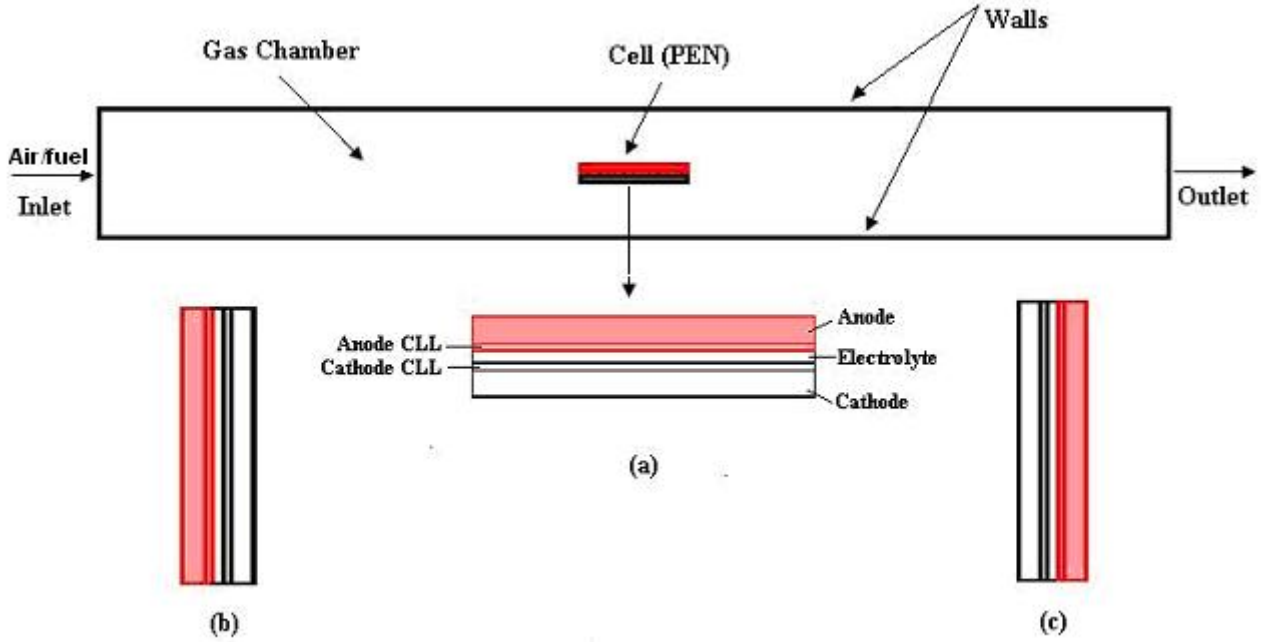

Figure 1.6: Single-chamber solid oxide fuel cell design

Advantages of SC-SOFCs

The SC-SOFC design offers some advantages over conventional SOFC design: In case of conventional planar-type SOFC, channels are usually embedded into the bipolar plates for air and fuel flow management. In contrast to this, SC-SOFC design does not require complicated channel design, thus offering a lightweight and compact design. For conventional SOFCs, separation between air and fuel is mandatory, normally achieved via a solid (non-porous) electrolyte layer in between the anode and cathode. The pore-free electrolyte manufacturing process requires high sintering temperatures and costly fabrication techniques. Quite opposite to this, in SC-SOFCs, the electrolyte can be porous, therefore cheap processing is possible. Moreover, the SC-SOFC works on the principle of partial

oxidation of fuel, exothermic heat from the reaction can be used to self-sustain the system. By doing so, the operational temperature can be lowered which is not possible in conventional SOFCs, because they normally work on fuel reforming principle which is an endothermic reaction. The conventional SOFCs require sealing between the anode and cathode in order to ensure leak-proof system. On the contrary, the SC-SOFC design completely eliminates the requirement of sealing because of no separation is required between the air and fuel. In SC-SOFCs, life-time can be longer than conventional SOFCs because the cell in SC-SOFC configuration can work even with some cracks. However, it is not possible to use a cracked cell for conventional SOFC operation because of risk of air and fuel mixing.

Challenges of SC-SOFCs

Besides may advantages, the SC-SOFCs have to face some challenges, yet. The first very important issue is to look for ideally selective electrode materials. Since both the electrodes are exposed to the same air/fuel mixture, these electrodes should be smart enough to catch their own feed from a gaseous mixture; for example, the anode should only select fuel and ignore the air and the cathode does the vice versa. Because of the lack of this selectiveness, most of the fuel is not completely utilized by the anode, therefore the fuel utilization and the electrical efficiencies for SC-SOFCs are very low. The second major challenge is to improve the fuel utilization and electrical efficiencies of SC-SOFCs which could be done by optimizing the flow management, microstructure and by improving the catalytic activity of the electrodes. Furthermore, the SC-SOFC's electrodes have to work in both the reducing (fuel-side) and oxidizing (air-side) environment, thus it is very essential to demonstrate their long-term stability in dual-atmosphere. Another major challenge against their practical implementation is to ensure their safe operation.

1.5 Summary

In this chapter, the fuel cell basics with some commonly used terms in fuel cell research, such as effective fuel utilization and effective electrical efficiency have been discussed. The different types of fuel cells with special focus on solid oxide fuel cells have also been presented with some details on electrode and electrolyte materials commonly used in SOFCs. An effort has also been made to give a brief on different fuel cell designs with main emphasis on single-chamber SOFCs. Finally, current research challenges with some advantages of SC-SOFCs have been discussed.

CHAPTER 2

RESEARCH OBJECTIVES

2.1 Background

Solid oxide fuel cells are gaining increasing interest as a next-generation energy conversion device with environmental friendly power generation. Though most of the problems associated with performance and material issues have been resolved to a certain extent, commercial applications of SOFCs still suffer from high costs and high temperature requirements. Although there is plenty of research going on to reduce their operating temperature, the so-called intermediate-temperature solid oxide fuel cells (IT-SOFCs) are gaining more and more interest. Besides all these efforts, they are still not applicable for small portable applications, where quick start-up/shut-down is mandatory. While it has been well agreed that micro-tubular geometry meets most of the common requirements of portable applications, the high-temperature operation of commonly employed conventional materials (i.e. Ni-YSZ/YSZ/LSM) is at a high risk of developing thermo-mechanical stresses, thereby reducing the lifetime.

One of the problems related to high cost is due to the complex system design requirement for high-temperature SOFCs. Since fuel flexibility is one of the major advantage of SOFCs, the most efficient strategy would be to use Natural gas such as methane for fueling the SOFCs. Before, methane is fed to the SOFC, it must be reformed either externally or internally. External reforming requires an additional reformer, increasing overall systems cost. On the other hand, internal reforming demands presence of steam, thereby diluting the inlet fuel and reducing the overall performance. The other problem with internal reforming is that it is highly endothermic and the local cell performance at the inlet is badly hit by the lower inlet cell temperature. The other factor contributing to high systems cost is their bulky design, especially in case of planar cells, where heavy weight, large volume and com-

plicated channel design could contribute significantly in terms of manufacturing cost. Furthermore, sealing of planar cells is still a major challenge to be met.

Due to the above mentioned problems of high cost and high operating temperature requirement, it is very necessary to look for alternatives. Among various alternatives such as the use of micro-tubular or monolithic geometry for weight and volume reduction and intermediate-temperature SOFCs for low temperature operation, the SC-SOFCs are the most efficient and appropriate for handling both of the issues related to cost and temperature. The cost problem can be handled via eliminating the heavy weight (and complex flow channel design) of bipolar plates by looking at alternative designs such as micro-tubes under single-chamber conditions. Due to intrinsically sealless design of micro-tubular configuration it provides easy gas manifolding. Furthermore, its high volumetric power density and quick on-off characteristics provides very compact design suitable for portable applications. The operational temperature of SC-SOFC has to be lower because the selectivity of conventional cathode materials degrades with increase in temperature. Therefore, low or intermediate-temperature SOFC materials are best suitable for SC-SOFC applications.

2.2 Objectives

The objectives of this study are:

• To perform a detailed literature review on SC-SOFC activities and to suggest new topics of research not addressed so far.

• To perform a theoretical study in order to suggest a window of operation with respect to safety, stability and optimum output performance.

• To study different SC-SOFC designs such as planar, co-planar and micro-tubular, via detailed modelling and to propose a best geometrical design.

• To demonstrate the practical feasibility of the opted geometry and discuss its operation under different operating conditions.

• To measure the anode surface temperature in order to investigate the temperature gradients over the cell length and its effects on performance degradation.

• To investigate the structural stability of the cell components under mixed-reactant conditions.

• With the help of developed numerical model, a parametric study should be carried out in order to suggest improvement in the experimental setup.

2.3 Description of the Work

The entire project is divided into two main streams, i.e. Modelling and Experiments. Chapter-3 describes the literature review and suggests new topics of research for this thesis. In Chapters 4-6, detailed modelling has been carried out for a novel planar, conventional-planar and co-planar geometries. These chapter give the direction for choosing the right configuration for SC-SOFC experimental work. In Chapter-7, the feasibility study of micro-tubular, SC-SOFCs has been performed. Chapter-8 is an extension of the experimental work, exploring more about local temperature gradients during SC-SOFC operation and micro-structural analysis of the cell. In Chapter-9, a numerical model is developed for micro-tubular SC-SOFC, which is calibrated and validated with the help of experimental data. Furthermore, a detailed parametric study has also been carried out in Chapter-9. In Chapter-10, conclusions and further future work have been discussed.

2.4 Summary

This chapter summarizes the background issues responsible for considering SC-SOFCs and to realize the need and importance of this current research project. This chapter also gives a list of main objectives needed to be accomplished for this project.

CHAPTER 3

LITERATURE REVIEW

3.1 Introduction

As stated earlier in Chapter-1, SC-SOFC is an electrochemical device that can operate with uniform mixtures of air and fuel, generating electricity and heat. This type of fuel cell has received different nomenclature by different researchers. The most commonly used nomenclature is the ”Single-Chamber, Solid Oxide Fuel Cells (SC-SOFCs)”. The other less frequently used terms are, ”Mixed-Reactant Fuel Cells (MRFCs)”, ”Compact Mixed Reactant (CMR) Fuel Cell”, ”Fuel Cell with One Chamber” and ”Fuel Cells with Reaction Selective Electrodes”. I would also like to mention here that the solid-oxide fuel cells can broadly be classified into the following three types according to the chamber set-up:

• Dual-chamber (conventional) SOFC.

• Single-chamber (mixed-reactant) SOFC.

• No-chamber (direct flame) SOFC.

While dual and single-chamber SOFCs have been briefly discussed in Chapter-1, ”No-chamber SOFC” is a recent research focusing on using the fuel cell under direct flame exposure. This type of fuel cell is also named as Direct Flame Fuel Cell (DFFC). There are some benefits associated with this concept: such as 1) no-chamber requirement; 2) high selectivity of electrodes is not necessary; and 3) explosion risks are avoided due to unconfined chamber configuration. However, this design is much more susceptible to mechanical damage due to direct exposure under flame. The most favorable combination of different SOFC concepts is, to look for simplicity (not present in the dual-chamber SOFC) and structural stability (not available in the DFFC), both available in the SC-SOFC design.

3.2 SC-SOFC's Operational Issues

The design concept of SC-SOFC relies on operating the fuel cell in uniform mixtures of air and fuel, and gives several open questions related to safety and stability. In principle, any fuel and air mixture can be employed for SC-SOFC, so long as both of the above criteria are fulfilled. There is another linked issue between safety and stability, called the optimum performance point. The best engineering way to integrate them is to first check the safety, then look for optimum performance and finally confirm stable operation. We will address these in turn in subsequent sections:

3.2.1 Safety Issues

The safe operation is the prime issue for any device, not only limited to SC-SOFCs. However, in case of SC-SOFCs the level of safety is of much more concern because of the explosive nature of air/fuel mixtures. At this stage, it would be appropriate to consider most commonly used fuels such as hydrogen or hydrocarbons because of their well known application history in SOFCs. For instance, hydrogen/air mixtures could be the right candidates in terms of being less problematic for commonly used Nickel anodes (no coking problem), however their safety concerns are exceptionally very high. Hydrogen is considered as explosive in the flammability range of 4-75% by volume in air at standard conditions (ambient pressure and temperature) and this limit widens as the operating temperature increases. Moreover, the auto-ignition temperature of a combustible hydrogen/air mixture is 585°C, far too low than a typical operating condition for an SOFC. For hydrogen/air mixtures to be practical for SC-SOFCs, their safety window of operation is quite narrow, for example either below 2% or above 93% hydrogen (by volume in air) may be considered as safe at temperatures up to 200-300°C. Unfortunately, there is no practical study available for hydrogen/air mixture at the higher temperatures necessary for SC-SOFC operation. Even though, if we assume that the mixture is safe at higher temperatures, it is still impractical due to: 1) The use of rich fuels ($>$93% hydrogen) may result in extremely low fuel utilization, because all the fuel passed through the cathode will be nearly unutilized, 2) The use of lean fuels ($<$ 2% hydrogen) will result in fuel deficiency at the anode. Another problem in working with rich fuels could be the fuel concentration may fall into the explosive range because of utilization. Open tube exhaust flow could lead into back diffusion problems of ambient air, thus disturbing the operating conditions. Another commonly used term "Quenching distance", defined by the diameter of the gas-chamber tube, should be kept as low as possible in order to extinguish the

flame in case of fire. Flashback arrestors and back flow preventing valves will increase the systems' safety level.

In contrast to hydrogen/air mixtures, hydrocarbon/air mixtures are much safer because of their quite narrow explosive regime. In Table 3.1, upper explosive limits (UEL) and lower explosive limits (LEL) are given (at standard conditions) for some common hydrocarbons used in SOFCs [13]:

Hydrocarbon	Formula	H/C ratio	LEL in air %	UEL in air %	Boiling Temperature °C
Methane	CH_4	4.0	5.0	15.0	-164
Ethane	C_2H_6	3.0	3.0	12.4	-89
Propane	C_3H_8	2.7	2.1	9.5	-42
n-Butane	C_4H_{10}	2.5	1.8	8.4	-0.5

Table 3.1: Physical properties of some common hydrocarbons

As can be seen in Table 3.1, the UEL and LEL decrease with increasing carbon number in hydrocarbons. It seems that Propane and n-Butane are much safer than methane or ethane, they are easy to store and transport because of liquefaction at moderate pressures. The other benefit is, the higher the carbon number in the hydrocarbon, the more are the electrochemically active species (hydrogen and carbon monoxide) and higher exothermic reaction heat as a result of partial oxidation. The reaction heats (in case of partial oxidation at 423°C) for some hydrocarbons are given below in Table 3.2 [14]. This reaction heat would serve as lowering the electrode resistance and possibly to thermally self-sustain the system. From the above discussion, it comes out that higher hydrocarbons are much more suitable for SC-SOFCs; however there are some limitations: 1) The higher the carbon number, the more chances for carbon formation over the commonly used Nickel anode because of lower H/C ratio; 2) The higher the carbon number, the more will be the reaction heat causing local thermal shock problems.

Reaction	Equation	Δ Q $kJmol^{-1}$
Methane partial oxidation	$CH_4 + \frac{1}{2}O_2 \rightarrow 2H_2 + CO$	-25.03
Ethane partial oxidation	$C_2H_6 + O_2 \rightarrow 3H_2 + 2CO$	-120.66
Propane oxidation	$C_3H_8 + \frac{3}{2}O_2 \rightarrow 4H_2 + 3CO$	-208.29
n-Butane partial oxidation	$C_4H_{10} + 2O_2 \rightarrow 5H_2 + 4CO$	-292.54

Table 3.2: Possible reactions in an SOFC anode

Due to the above limitations, we will restrict our study to lower number of carbon containing hydrocarbons such as ethane or methane. Among these two, methane is the most widely used and abundant resource till date.

Therefore, we look at the pros and cons of methane/air mixtures. As can be seen in Table 3.1, methane is explosive in the range of 5-15% by volume in air. Therefore, they are two possibilities: either use methane concentration of greater than 15% or less than 5% in air. To be on safe side, these operation regimes should be more restricted because the 5-15% range widens with increasing temperature. Likewise, hydrogen/air mixtures, there will be fuel deficiency problems when working with less than 5% concentrated methane. Both the Nernst potential and power density drops with fuel dilution. It is evident that working with more than 15% concentrated methane could eliminate the fuel deficiency problem, but the upper limit should not be too high to cause fuel utilization problems. The reaction heat values given in Table 3.2 are strongly dependent on temperature and fuel concentration (i.e. fuel/air ratio). A suitable compromise between operating temperature and mixing ratio is extremely important for safety purposes during operation.

3.2.2 Performance Issues

Once the safety window is established, the next effort would be to find an optimum performance window within the safety window. This entirely depends upon the operating temperature and mixing ratio. For example, working at high temperatures with rich fuels will boost-up the performance, but the fuel utilization will be very poor in case of rich fuels. Moreover, the use of too rich fuels can also cause stability problems which will be discussed in the next section. One way to address this issue is to fix the air/fuel ratio to an optimum value and increase the flow rate via diluting with inert gas such as Argon or Helium. This will help in improving the fuel utilization on some sacrifice of output performance. It is also clear that the use of lean fuels will shift the partial oxidation reaction towards full oxidation, thereby, providing excess heat which helps in improving the output performance. Again, there is a trade-off in between stability and performance.

3.2.3 Stability Issues

After both of the windows (the safety window and the performance window) have been selected for operation, the next very important step will be to comment on stability in performance. The SC-SOFC operation which is safe and giving the best performance may lack stability. The reduction/oxidation (RedOx) and coking are two of the major problems in commonly used Nickel anodes. On one side, too lean fuels can result in oxidation of the Nickel anode, on the other hand, too rich fuels can cause coking problems in case of hydrocarbon/air mixtures. Therefore, stable operation should be confirmed

by measuring the current or voltage stability over a long period of time.

As far as the present author knows, these issues have never been reported in detail. Most of the authors of previous papers completely ignore the safety aspects, most of them did not confirm stability, besides there have been huge efforts towards finding optimum performance. We, for the first time, have reported their importance and inter-connectivity. Below, we will report some brief review on SC-SOFC work done by earlier researchers. For a detailed history, the reader should refer to the work of Buergler [15].

3.3 SC-SOFC: Experimental Review

Hibino et al. [14] is the first scientist who introduced the term "Single-Chamber" and made significant contribution to the development of this technology. In one of his recent studies [16], he summarized three main types of SC-SOFCs as shown in Figure 3.1.

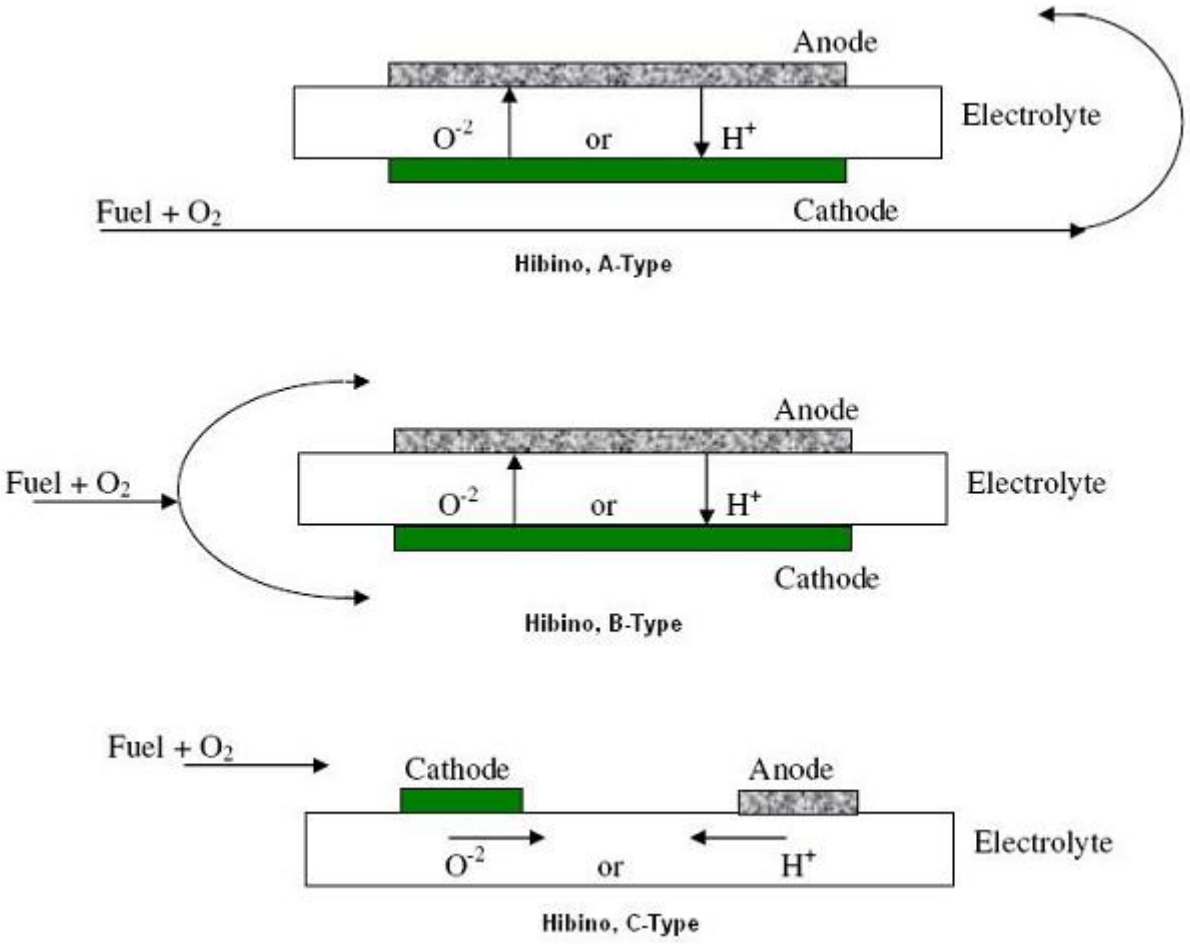

Figure 3.1: Hibino, SC-SOFC type: A, B and C

In Hibino type-A, the fuel/oxygen mixture is first delivered to the cathode and then afterwards to the

anode. The reason for this arrangement is to ensure that the cathode gets maximum oxygen supply to be able to provide large number of oxygen ions for electrochemical conversion of fuel species. On the contrary, if the fuel/oxygen mixture is first passed over the anode and then to the cathode, it is quite possible that the anode will consume most of the oxygen via partial or full oxidation, leaving behind oxygen deficient mixture for the cathode. This type of design requires an injector for directing the fuel/oxygen mixture first to the cathode, also a closed end gas-chamber tube, to divert the flow back to the anode. In this design, thin electrolytes are favored because of minimum ohmic resistance.

Hibino type-B, is a similar arrangement to conventional SOFCs, where both of the electrodes get their feed simultaneously. Although, this design provides simplicity in gas flow management, the cell performance is limited by the electrolyte thickness, therefore, anode supported cells are favored in this configuration. Due to the open end of the gas-chamber tube, back flow problems may arise, which can be overcome via reducing the outlet diameter or by providing a back-flow preventing valve.

Hibino type-C (co-planar) configuration offers very compact design, suitable for printing cells over small chip like electronic circuits. In this design, contrary to conventional SOFCs, both of the electrodes can be placed on same side of the electrolyte. Therefore, (in opposite to conventional SOFCs) this design favors thick electrolytes because ionic current transfer is in the longitudinal direction and not through the thickness. Besides, advantages like compactness and easy electrode printing techniques can be employed, this design requires a short inter-distance (gap) between the cells in order to reduce the ionic transport losses. This short inter-distance is further limited by the cross-diffusion and intermixing of species in the adjacent electrodes.

The work on SC-SOFCs is mainly experimentally driven by many researchers [16-71], with a few studies on Modelling of SC-SOFCs. A brief review of experimental activities is given in Table 3.3. The most important observations from this table are summarized as follows:

Most of the studies focused on Hibino, type-B (conventional SOFC design) with methane/air mixture as the most commonly used gaseous mixture. The influence of the flow rate, operating temperature and mixing ratio of hydrocarbon/air mixtures on the performance of SC-SOFCs has been observed by many researchers. It became clear that increasing the flow rate had positive effect on the cell performance. The increase in flow rate improves the catalytic/electrochemical reactions at the anode because of the heat evolved by hydrocarbon oxidation, causing increase in the cell temperature.

Fuel	Type[a]	Anode	Electrolyte	Cathode	Electrolyte thickness / mm	Furnace Temperature / °C	OCV/ mV	p_{max}/ mWcm^{-2}	R_{mix}	Total flow rate / mLmin^{-1}	η_U/ %	Ref.
C_4H_{10}	B	Ni-SDC	SDC	SSC	0.15	300	800	38	0.5	300	-	[14]
C_3H_8	B	Ni-SDC	SDC	BSCF-SDC	0.02	500	ca. 700	440	0.44	490	-	[17]
CH_4	C	Pd	BaCeGd	Au	1.0	950	700	-	2.0	300	-	[18]
C_3H_8	B	Ni-SDC	SDC	BSCF-SDC	0.02	500	700	247	0.44	490	-	[19]
CH_4	B	Ni-YSZ	YSZ	LSM(SDC)[g]	0.015	700	1820[k]	371[k]	1.0	400	~1.0	[20]
CH_4	B	Ni-YSZ	YSZ	LSCF	0.001-0.002	750	830	120	ca. 1.0	300	2.4	[21]
C_3H_8	B	Ni-SDC	SDC	SSC-SDC	0.01	525	650	210	0.4	540	-	[22]
C_3H_8	B	Ni-SDC	SDC	SSC-SDC	0.01	525	750	185	0.33	160	-	[22]
CH_4	B	Ni-YSZ	YSZ	LSM	0.008	600	940	220	1.0	450	-	[23]
C_2H_6	B	Ni-SDC	SDC	SSC	0.15	500	920	403	1.0	300	-	[24]
CH_4	B	Ni-SDC	GDC-BCY-GDC	SSC	0.003	500	ca. 880	302	2.0	300	-	[25]
CH_4	C	Ni-YSZ	YSZ	LSM	-	770	500	1	-	-	-	[26]
CH_4	C	Ni-YSZ	YSZ	LSM	0.2	800	850	40	2.0	350	-	[27]
CH_4	C	Ni-YSZ	YSZ	LSM	1.0	800	615	1.2	ca. 1.48	245	-	[28]
CH_4	C	Ni-GDC	YSZ	LSM[h]	0.5	950	ca. 800	102	1.0	300	-	[32]
CH_4	B	Ni-GDC	YSZ	LSM[h]	0.3	950	ca. 810	204	1.0	300	-	[32]
CH_4	B	Ni-YSZ	YSZ	LSM	0.008	750	915	100	ca. 2.0	400	-	[33]
CH_4	B	Ni-YSZ	YSZ	LSM(SDC)[g]	0.008	750	968	404	ca. 2.0	400	-	[33]
CH_4	B	Ni-YSZ	YSZ	LSM	0.2	800	1020	85	-	-	-	[34]
CH_4	C	Ni-GDC	GDC	SSC	-	650	770	17	2.0	100	-	[35]
CH_4	B	Ni-SDC-Pd	SDC	SSC	0.15	550	ca. 800	644	2.0	300	-	[36]

CH_4	B	Ni-SDC	SDC	BSCF-SDC	0.02	650	710	760	ca. 1.08	487	-	[37]
C_3H_8	B	Ni-YSZ	YSZ	LSCF	0.1	600	800	-	ca. 0.53	300	-	[38]
C_3H_8	B	Ni-GDC	YSZ	LSCF	0.1	600	800	-	ca. 0.53	300	-	[38]
C_3H_8	B	Ni-SDC	YSZ	LSCF	0.1	600	800	-	ca. 0.53	300	-	[38]
CH_4	B	Ni-GDC	YSZ[c]	LSM[h]	0.3	950	845	256	1.0	300	-	[39]
CH_4	C	Ni-GDC	YSZ[c]	LSM[h]	0.3	950	800	143	1.0	300	-	[39]
CH_4	C	Ni-GDC-Pd	YSZ	LSM-GDC	-	900	804	101.2	ca. 3.57	240	-	[40]
CH_4	B	Pt	BCY	Au	0.5	950	ca. 800	170	2.0	210	-	[41]
C_4H_{10}	C	Ni-SDC-Pd	SDC	SSC	2.0	600	ca. 800	ca. 245	ca. 0.53	300	-	[42]
C_2H_6	C	Ni-SDC	SDC	SSC	2.0	600	ca. 800	ca. 75	ca. 1.13	300	-	[42]
CH_4	B	Pt - (MnO_2)	YSZ[d]	Au[i]	0.5	950	ca. 600	50.4	1.0	300	-	[43]
CH_4	C	Pd	BaCeGd	Au	-	950	700	-	2.0	300	-	[45]
CH_4	B	Ni-YSZ	YSZ	LSM	0.2	800	860	360	0.88	350	-	[46]
CH_4	B	Ni-YSZ	YSZ	LSM	0.01	800	1050	260	2.0	350	-	[47]
CH_4	B	Ni-YSZ	YSZ[e]	LSCF	0.018	606	780	660	1.0	900	~5.0	[48]
CH_4	B	Pt	YSZ[f]	Au	-	950	-	3	2.0	120	-	[49]
CH_4	B	Pt	YSZ[f]	Au	0.5	950	700	34	2.0	210	-	[50]
C_3H_8	B	Ni-SDC	SDC	LSCF-SDC	0.5	650	780	210	ca. 0.53	300	-	[51]
C_3H_8	B	Ni-SDC	SDC	LSCF-SDC	0.5	575	800	111.12	ca. 0.53	300	-	[53]
C_3H_8	B	Ni-SDC	SDC	SSC-SDC	0.8	600	720	18.5	ca. 0.53	300	0.37	[54]
C_4H_{10}	B	Ni-SDC	GDC	SSC	0.015	300	921	176	0.5	300	-	[55]
C_4H_{10}	B	Ni-SDC-Ru	GDC	SSC	0.015	200	ca. 900	44	0.5	300	-	[55]
CH_4	B	Ni	YSZ	LSM	1.0	950	ca. 795	121	1.0	300	-	[56]

CH_4	B	Ni-LSCM	BLI	SSC	0.5	800	657	64.7	ca. 4.76	200	-	[57]
CH_4	C	Ni-SDC	YSZ	LSM	1.0	900	355	73.5	ca. 3.57	280	-	[58]
C_2H_6	B	Ni-SDC	LSGM	SSC	0.18	600	ca. 1000	ca. 350	1.0	300	-	[59]
CH_4	B	Ni-GDC	GDC	SSC	0.29	600	ca. 680	468	1.6	1500	-	[60]
C_4H_{10}	B	Ni-SDC	GDC	SSC	0.015	300	ca. 900	59	0.5	350	-	[61]
DME[b]	B	Ni-SDC-Ru	GDC	SSC	0.015	300	ca. 771	64	1.8	350	<2.0	[61]
Ethanol	B	Ni-SDC-Cu/Zn/Al	GDC	SSC	0.015	300	811	117	0.4	350	<2.0	[61]
CH_4	C	Ni-YSZ	YSZ	LSM[j]	0.2	700	ca. 900	2.3	2.0	150	-	[66]
CH_4	B	Ni-YSZ	YSZ	LSM	0.5	700	925	ca. 200	1.0	450	-	[66]
CH_4	C	Ni-YSZ	YSZ	LSM[j]	0.2	700	ca. 800	1.3	2.0	150	-	[67]
CH_4	B	Ni-SDC	SDC	BSCF-SDC	0.02-0.03	600	ca. 740	570	ca. 1.13	470	-	[68]
CH_4	B	Ni-SDC	SDC	BSCF-SDC	0.02-0.03	600	ca. 740	570	ca. 1.13	470	-	[68]
CH_4	C	Ni-YSZ	YSZ	LSM[j]	0.2	700	961	9.37	2.0	150	-	[69]
CH_4	B	Ni-SDC	GDC	BSCF-SDC	0.015	650	710	760	ca. 1.16	462	-	[73]

[a]Type = A,B and C as defined in Ref. [16], [b]DME = Dimethyl Ether, [c]YSZ dipped into $(MnNO_3)_2$, [d]YSZ modified with 1wt%MnO_2, [e]Porous YSZ, [f]Pr doped YSZ, [g] SDC impregnated LSM, [h]LSM modified with 15wt%MnO_2, [i]Au modified with 20wt%MnO_2, [j]active layer of LSM-YSZ prior to LSM cathode, [k]Two cell stack., p_{max} = peak power density, R_{mix} = methane-to-oxygen ratio, η_U = fuel utilization.

Table 3.3: Experimental work on SC-SOFC conducted by various research groups

The increase in cell temperature enhances the ion conductivity of the electrolyte and the catalytic activity of the electrodes. However, it should be noted that the fuel utilization and the electrical efficiency is significantly reduced by increasing the flow rate of the gas mixture because a large amount of the fuel passes through the fuel cell without reacting at the electrodes.

The effect of varying the fuel/oxidant ratio was also studied by many researchers. It appears that oxygen-rich mixtures are suitable for cell performance, compared to the stoichiometric mixture for the partial oxidation of methane by oxygen (methane/oxygen ratio=2.0). We, for the first time reported [72] that although oxygen-rich mixtures give best performance, the long term stability is not guaranteed under such mixing ratios.

Though the highest OCV reported is $1.05V$ [47] using conventional Ni-YSZ/YSZ/LSM materials which is comparable to conventional (double-chamber) SOFCs, the electrochemical performance is still quite low. The main reason for low cell performance in case of SC-SOFCs is the poor selectivity of conventional electrode materials. Continuing improvements in the SC-SOFCs, a number of research groups proposed more selective electrode materials and more effective cell designs. As a consequence, SC-SOFCs could provide fuel cell performance comparable to that of conventional SOFCs. Moreover, some new avenues of SC-SOFCs for various applications were proposed on the basis of cell designs, thermal properties, and fabrication processes. However, challenges still remain for further improvements in SC-SOFCs, especially in terms of the energy conversion efficiency. As described by several researchers, the efficiencies estimated in single-cell tests were only a few percent ($< 3\%$) since a large amount of unreacted fuel and oxygen were exhausted from the fuel cells. At present, ideally selective anode and cathode materials for fuel oxidation and oxygen reduction, respectively, are not yet available for SC-SOFCs and further efforts are needed to realize these.

3.4 SC-SOFC: Modelling Review

The modelling work on SC-SOFCs is quite limited [73-78]. In below, we will briefly discuss the modelling work on SC-SOFCs.

Hao et al. [73] developed a two-dimensional numerical model of Hibino, B-type SC-SOFC. They used Ni-YSZ/YSZ/BSCF-SDC cells as the base-case for their model and compared the results of YSZ based pure ionic conducting electrolyte with that of SDC based MIEC. Their model shows that the SDC electrolyte delivers much better performance than YSZ in the temperature range of 650-750°C. The higher ionic conductivity of SDC electrolyte as compared to YSZ electrolyte in the operating

temperature range was given as the reason for this behavior.

Haile and co-workers [74] developed an experimentally validated numerical model for SC-SOFC. They considered Ni-SDC/SDC/BSCF-SDC cells operated with helium diluted CH_4/O_2 mixtures. They achieved a relatively high power density of $760 mW cm^{-2}$ at a furnace temperature of 650°C. They claimed the reason to be the excellent oxygen electro-reduction activity of the BSCF cathode combined with its inactivity towards methane chemical oxidation.

Chung et al. [75] developed a two-dimensional model for co-planar type SC-SOFC running on hydrogen/air mixtures. Surprisingly, they used 50:50% mixture of hydrogen and air without any comments on safety aspects. They reported two important consequences of their simulations; i.e. short inter-distance between the electrodes and thick electrolytes giving the best performance. However, there were no comments on the boundary-line of these parameters. In the forthcoming chapters we will show that both these parameters need an optimum. A quite similar outcome was reported by them in another study [76].

One of the most interesting studies carried out by Hao et al. [77] discusses the importance of efficiency and fuel utilization in case of SC-SOFCs. The outcome of their work was that the fuel utilization should include both the electrical and thermal heat produced by an SC-SOFC. Their model predicts over 10% maximum efficiency in case of a single-cell with above 5% at typical SC-SOFC operating conditions. They claimed that SC-SOFCs can have significantly higher efficiencies than the commonly reported 1% in literature [77]. In one of our recent publications [72], we tried to differentiate the contribution of fuel utilization towards effective and non-effective utilization. Our experimental study suggests that the contribution of heat produced towards fuel utilization will only be useful when this heat is effectively utilized.

Hao et al. [78] studied the effect of the presence of large amounts of oxygen in SC-SOFCs and identified three distinct reaction layers of different thicknesses in the anode. According to them, these three distinct regions are combustion, reforming and water-gas shift reaction region. They showed that the fuel chemistry on anode side of an SC-SOFC is not as simple as assumed previously. Instead, it is a very complex phenomena consisting of partial and full combustion of fuel along with internal reforming reaction.

As can be seen from above, the modelling literature on SC-SOFC is quite limited. Therefore, it will worth to study the modelling literature on conventional SOFCs and make their possible relevance

to SC-SOFC modelling work. In below, we report modelling work on conventional SOFCs and highlight their usefulness in SC-SOFC modelling.

Chan and Xia [79] presented one-dimensional, one electrode (anode) model in order to study anode polarization with respect to particle size. Their results show that the polarization reaches a minimum at a certain particle size. They highlighted the link between the particle size and anode thickness, according to them the larger the particle size, the thicker should be the anode for providing sufficient active sites. From these results we can benefit and plan our experimental work, as whether to opt anode-supported, cathode or electrolyte supported design? What porosity we should select in order to have minimal diffusion transport problems etc.

In another study, Chan et al. [80] developed a cathode electrode model for studying cathode overpotential based on complex transport phenomena, electrode microstructure and under different operating conditions. They investigated YSZ to LSM particle size ratio in a composite cathode and reported that the higher particle size ratio (YSZ to LSM) is better in order to achieve a reduced cathode polarization. They obtained similar results for cathode thickness and particle size effect as above in anode electrode model. This study is helpful for our work in a sense that we can prepare our cathode inks and ensure sufficient ionic and electronic percolating network.

Ahmed et al. [81] studied monolithic design by developing a cross-flow model. Their model consists of flow, electrochemistry and thermal equations applied to a honeycomb design. They simulated hydrogen and coal as possible fuels, and air as an oxidant. Their results show that the coal and hydrogen based fuel cells gave same cell voltage but the net power output and average current density of coal based fuel cell was lower than that of hydrogen fed fuel. They explained the reason for this effect is due to lower hydrogen yield in case of coal based fuel. This explains that in order to have higher power output, we should select those catalysts that can ensure higher hydrogen yield.

Hirano et al. [82] developed a non-isothermal model for a tubular SOFC based on internal reforming. They opted natural gas fed fuel and pure oxygen as an oxidant. They simulated the model for different operating current densities with fuel recycling and validated their model with their experimental work. Their work is indeed helpful in developing SC-SOFC model, as the reforming chemistry is required to be implemented.

The model developed by Karoliussen and Nisancioglu [83] studied various flow cases; co-flow, counter-flow and cross flow with internal reforming of methane. They considered only convection

heat and mass transfer in the gas-phase and conduction heat/mass transfer in the porous electrodes and neglected the radiation effects. They observed a cooling zone near the cell inlet due to endothermic reforming of methane and suggested fuel recycling in order to diminish the steep temperature gradients along the cell length. In a single-chamber setup, one would expect similar temperature gradients but due to methane exothermic reforming (full combustion) instead of endothermic reforming. The proposed solution of homogenizing the temperature gradients by Karoliussen and Nisancioglu [83] can be useful in our study as well. The heat produced can be taken away if we provide a heat-exchanger at the cell inlet portion.

Achenbach, in one of his study [84] considered transient effects by using internally reformed methane fuel and studied gas-recycling by implementing complete heat transfer equations, i.e. conduction, convection and radiation. However, he assumed electrodes as electron conducting media, therefore neglecting the interconnects. The results shows that the highest cell efficiency is reached for counter flow and the most uniform current density is observed for co-flow design. He also pointed out the importance of thermal insulation in order to prevent cell cooling. The results presented by him can be quite useful in developing a numerical model for SC-SOFC, as neglecting the effect of interconnects can reduce computational effort and incorporating complete heat transfer mechanism can give realistic results.

Bove et al. [85] developed a three dimensional numerical model for a planar, radial-flow, solid oxide fuel cell. They argued that there are several tri-dimensional phenomena that cannot be fully analyzed in a two or quasi-three dimensional models. For example, the flow distribution within the gas channels, in-plane gas diffusion and resistances can be fully resolved in three-dimensional domains. They validated their model against different experimental polarization curves with a fair agreement between model and experimentally predicted results. The model developed by them was based on computational fluid dynamics (CFD) and can be quite useful as a basis for developing numerical model for our work.

Serincan et al. [86] studied micro-tubular design for conventional SOFCs. They adopted an axisymmetric model in order to take benefit from symmetrical structure of the micro-tubular cell. They solved coupled mass, momentum, species and heat balances along with ionic and electronic charge transfers. Due to the use of ceria-based electrolyte which becomes an electronic conductor in reducing environment, they implemented a leakage term to account for performance loss. By validating

their model against experimental work reported by Suzuki et al. [87], they found a very good agreement between model and experimental results. Their model can provide base-guidelines when a micro-tubular geometry is examined, and to see whether there are any benefits in adopting such design under single-chamber conditions? To our knowledge, micro-tubular design is not analyzed in a mixed-reactant environment.

Suwanwarangkul et al. [88] modelled transport phenomena inside an SOFC anode using three different models, namely; Fick, Stefan Maxwell and Dusty Gas model. Experimental data from literature were used to compare the calculated concentration overpotentials for different species. They highlighted the importance of molecular and Knudsen diffusion mechanism and compared the results of three different models. It was observed that the Dusty Gas Model (DGM) takes into account both modes of diffusion and suggested for transport modelling in a porous media. In our modelling work, we plan to model species transport by Stefan-Maxwell inside the gas channels and by using DGM in porous electrodes.

Yakabe et al. [89] presented three-dimensional calculation for a planar SOFC limited to a single-unit model with double channels of co-flow or counter-flow pattern. They used CFD tool (STAR-CD) to study thermo-fluid interaction and a finite element software package (ABAQUS) for thermal stress analysis. The temperature field obtained from CFD model was exported to ABAQUS and principal stresses were analyzed in the solid part. Their study is indeed very helpful if one plans to study thermal stresses in an SC-SOFC. Due to severe combustion reaction occuring in the cell inlet, thermal stresses are likely to develop and deteriorate the cell performance. Therefore, modelling thermal stresses in SC-SOFCs will provide guidelines for operating conditions and safety measures against cell failure.

Haynes and Wepfer [90] developed a heat transfer model for analyzing steady-state heat transfer and improving thermal management within Siemens Westinghouse tubular SOFCs. They compared their temperature profiles with those of Bessette et al. [91]. Their results show good agreement between calculated and measured temperature profiles. With the help of their detailed heat transfer model we can certainly extend our numerical model capability which will help in validating our model against experimental results.

King et al. [92] presented a mathematical model for a tubular SOFC by implementing advection, convection and electrochemistry. The chemical reaction scheme includes both the effects of steam reforming and partial oxidation of methane. They also implemented additional equations to take into

account for carbon deposition on anode electrode. Indeed, in an SC-SOFC, both steam reforming and partial oxidation reactions are occuring, therefore modelling of such complex chemical reactions is necessary. In order to model detailed chemical reactions, the reaction rates and constants can be adopted from their study.

The study by Aguiar et al. [93] examined the effect of indirect internal reforming for both counter-flow and co-flow configurations to study the mismatch between the thermal load associated with the steam reforming rate and the available heat via electrochemical reactions. In order to eliminate this mismatch, they studied the effect of different catalyst activities, fuel inlet temperature, operating current density, operating pressure and flow manifolding. A similar thermal mismatch is expected to occur in SC-SOFCs, and different strategies are required to reduce this. For example, studies related to the effect of cathode size, location, material and microstructure could help.

Chan et al. [94] studied two simple SOFC power systems, one fed by hydrogen, the other by methane. They developed a detailed thermodynamic model, with all performance related parameters expressed as a function of temperature. Their results show that the hydrogen fed fuel cell gave better performance than that of methane powered fuel cell. Indeed, hydrogen is an ideal fuel for fueling the SOFC, giving best performance as compared to other fuels. However, the production and availability of hydrogen is still a major challenge to be met. In this respect, single-chamber SOFCs are well applicable, as hydrogen can be produced in-situ. Nevertheless, high hydrogen selectivity and production yield is required and therefore different electrode materials must be analyzed.

The modelling work presented by Recknagle et al. [95] was based on a commercial CFD package (STAR-CD). They calculated temperature, current density, species distribution along with the anodic/cathodic flow distribution and fuel utilization. They validated their modelling results against experimental work with a good agreement. They studied different designs such as co-flow, counter-flow and cross-flow with the assumption of adiabatic walls. According to them, the most uniform temperature distribution and the smallest temperature gradients were observed in the co-flow design. Since, we also aim to model the above distribution profiles and to study temperature gradients in an SC-SOFC, their study is a good basis for our work.

Van Herle et al. [96] developed a model for small cogeneration SOFC system fed with biogas. In their model, they varied system operating parameters such as inlet fuel composition, reforming technology, stack temperature, stack current density and implemented a process flow diagram. They

also discussed some limitations of their model such as an absence of reforming chemistry, absence of electrode diffusion overpotential with the assumption of isothermal conditions for SOFC stack and reformer. Their results well agreed with the experimental results, showing comparable magnitude of electrical output and stack efficiency. The model developed by them can be useful for the study of SC-SOFC micro-cogeneration system. Most of the parameters related to stack configuration and heat recovery for cogeneration can be adopted with a little modification for SC-SOFC micro-cogeneration study. Although, this is not the objective of the current research but still the study reported by Van Herle et al. [96] will worth for future studies in SC-SOFC combined heat and power applications.

Direct electrochemical oxidation is highly preferred in SOFCs because it does not require upstream fuel processing. Walters et al. [97] developed a one dimensional plug flow model incorporating direct electrochemical oxidation of hydrocarbon fuel. The model included gas-phase chemistry along the anode channel as a function of cell design and operating conditions. The model presented interesting predictions of coking along the cell length. Near the channel entrance due to little oxygen content, the equilibrium predictions showed high coking levels. In contrast, the kinetic predictions showed small concentrations of carbon formation. In downstream regions of the channels their model predicted quite opposite behavior. Due to increasing concentration of oxygen downstream, chemical equilibrium favored volatile carbon compounds and deposits. However, the kinetic predictions show high levels of coking downstream. This crossover trend depends on operating temperature, fuel flow rate, operating current density etc. They pointed out that the temperature had significant influence on coking as compared to other operating parameters. The numerical results reported by them are helpful for our study. We plan to operate SC-SOFCs with various methane/air mixtures and knowing the boundaries of coking/re-oxidation is of paramount importance in SC-SOFC operation.

Pasaogullari and Wang [98] developed a multi-physics, multi-dimensional model using internal reforming of methane. Unlike traditional three layer approach for modelling membrane electrode assembly, they used two additional interlayers for anode and cathode sides. They used commercial CFD package (Fluent) to predict polarization curve, species distribution and current density. Since electrochemistry model is not available in Fluent, they incorporated their own subroutines and coupled them as user-defined functions (UDFs). One limitation of their model was that they did not implement separate equations for interconnects, instead treated them as an integral part of the electrodes. Their model can be useful for our work as it can serve as a building block to develop a comprehensive CFD

model for SC-SOFCs. The fundamental equations for mass, momentum, species and charge transfer will remain same, however, the reactant properties will be modelled as mixture properties instead of individual fuel and oxidant.

Li and Chyu [99] developed a numerical model based on finite element method. Instead of using a commercial package, they wrote their own codes to predict flow, heat/mass transfer, chemical and electrochemical performance for a tubular SOFC. They compared their model predicted results with experimental ones published by different researchers. Their model results showed that the calculated terminal voltage agreed with the experimental data with a deviation of less than 8%. The temperature distribution is also well agreed with the experimental data. They also found that two ends of the cell had a relatively low temperature, and the location of highest temperature depends on the flow rate, geometry, extent of fuel reforming etc. The temperature predictions by them are helpful for our work, as we will also expect temperature gradients over the cell length and our model should be able to produce experimentally observed temperature trends.

Murthy and Fedorov [100] developed a numerical model for monolithic SOFC using conventional materials. Instead of repetition of similar conservation equations for building-up a numerical model, they put efforts on radiative heat transfer modelling. Their results show that the effect of radiative heat transfer are important and played a significant role in calculating temperature distribution, cell voltage and current density. When modelling SC-SOFCs, this article will help in implementing equations for radiative heat exchange. Besides above mentioned parameters, electrode selectivity is very much influenced by the radiative heat and we plan to have temperature dependent terms for parasitic loss which will be linked with radiation heat transfer via emissivity term.

Ackmann et al. [101] studied planar SOFC and calculated flow, temperature and current density distribution using commercial CFD package (Fluent). For implementing electrochemistry module, they used MATLAB programming to develop their own subroutines. In addition to general electrochemistry for hydrogen oxidation, they included methane/steam reforming and water-gas shift reactions. They claimed that their model predicted results can help in optimization of the mass transport inside an electrode by changing its structural parameters. The useful aspect of their calculation for our SC-SOFC model development is the reforming kinetics. For different kinetic parameters needed for methane/steam reforming and water-gas shift reaction, we can refer to their literature.

Jiang and Virkar [102] studied the effect of diluent on planar anode supported SOFC performance.

They used fuels consisting of hydrogen diluted with helium, nitrogen, water, carbon dioxide, mixtures of hydrogen and carbon dioxide and mixtures of carbon monoxide and carbon dioxide. They calculated open circuit potential and cell performance using diluted fuels and reported that the dilution has a considerable effect on concentration polarization. They also pointed out that the cell performance with carbon monoxide and carbon dioxide gas mixture is much worse than fuel gas mixtures containing hydrogen. In SC-SOFCs, various gas-species are produced in-situ, including hydrogen, carbon monoxide, carbon dioxide, steam etc. The model developed by Jiang and Virkar [102] could help in calculating the mass fraction of the produced species and their effect on cell performance as a diluent.

Khaleel et al. [103] developed one dimensional model for predicting cell performance using a feed of varying hydrogen concentration in the anode gas-channel and experimentally validated their modelling results. Their contribution was indeed very helpful because there is limited information available on hydrogen diluted fuels employed in SOFCs. In our case, diluting methane with nitrogen or helium can be effective in improving the fuel utilization. To this end, their model will help in reproducing the results for SC-SOFCs operated with diluted methane/air mixtures.

Li et al. [104] presented a coupled thermo-fluid-electrochemical model for a tubular SOFC. They computed axi-symmetrical flow field, temperature and mass fraction distribution in a single-cell. They used pre-reformed fuel containing hydrogen, carbon monoxide, carbon dioxide, steam and methane. The model used mixture properties for fuel and oxidant that were temperature dependent which was obtained numerically. They implemented radiation heat transfer between cold air inducing tube and hot fuel cell tube. They found that both the heat generation from electrochemical effect and cooling from the air flow can affect the temperature distribution inside the cell. Furthermore, the weak oxygen diffusion in nitrogen may cause concentration overpotentials. The study is relevant to our work, as we can calculate mixture properties in a similar way and radiation heat transfer between gas-chamber wall and cathode outer layer can be modelled in a similar fashion.

Fleig et al. [105] compared conventional and co-planar SOFCs. They reported that relatively thick electrolytes are favorable in SC-SOFCs, as the cell performance is limited by the electrode gap and not by the thickness in case of single-chamber design. On the other hand, thin electrodes are preferred in conventional SOFCs in order to reduce ohmic overpotential. Their modelling efforts could serve as a basis for our numerical study on co-planar type SC-SOFC. A parametric study related to electrode thickness, gap and position will be quite useful to compare our results with their study.

Zhu et al. [106] presented a new approach for modelling SOFCs using elementary heterogeneous chemical kinetics in a form of multi-step reaction mechanism. Instead of using global reaction mechanism, the detailed multi-step reactions provide realistic modelling strategy by implementing surface reactions such as adsorption, dissociation, desorption, diffusion etc. They also discussed two examples of their model capabilities; one using button cell reported by Jiang and Virkar [102] to obtain related parameters for the electrochemistry model and the other showing multi-step reaction mechanism validated for oxidative steam reforming of methane over nickel [107]. As yet, the global reaction mechanism on anode side of SC-SOFC is not known, taking help from their study will be useful for defining anode side reactions in our study.

It is well known that stresses are the important causes in the failure of SOFC materials. The residual and thermal stresses are likely to occur during manufacturing and operation. Fischer et al. [108] calculated in-plane residual stress distribution in a YSZ electrolyte for different processing steps including, green state, co-firing, co-firing and flattening and anode reduction. They compared their results with literature data and concluded that the critical fracture stress of the anode was much higher than the residual stress in the reduced anodes at room temperature. In a similar study, Selimovic et al. [109] calculated steady state and transient thermal stresses in a planar SOFC by using coupled thermo-fluid, electrochemical-structural model. They run various simulations with different interconnect materials and using different fuels and found that the anode-electrolyte interface is showing largest stress when using pre-reformed methane. In order to ensure reliability of the cell materials, they compared their maximum principal stresses with yield strengths of the SOFC materials. The load following capability under transient conditions was also one of the issue that was raised in their study. Their study is helpful for carrying out a detailed thermal stress analysis in SC-SOFCs which will be the future task in order to continue work on SC-SOFC design in our group.

3.5 Summary

This chapter discusses the safety, optimum performance and stability issues, and describes their importance and inter-connectivity. This chapter also summarizes the experimental and modelling activities on SC-SOFCs, performed so far, prior to this thesis.

The models on conventional SOFCs are based on strict separation of anode and cathode side reactions, therefore selectivity of electrodes is not necessary to take into account. On the contrary, in SC-SOFCs selectivity of electrodes is of great importance, as the performance decreases with decrease

in selectivity of the electrodes towards specific reactions. In case of SC-SOFCs, the flow properties are defined for the gas-oxidant mixture, whereas in case of conventional SOFCs, these are based on single-reactant. In SC-SOFCs, the energy/chemical equations are extended to take into account the combustion and reforming heat/chemsitry and parasitic losses. In contrast, parasitic losses associated with non-selective electrodes are normally not required to model in conventional SOFCs. The performance cycling and degradation modelling for SC-SOFCs will be much complicated as compared to conventional SOFC modelling because of additional equations required for combustion/reforming to model degradation in mixed-reactant enviornment. Not only this, the thermal stress modelling will also require huge struggle to incorporate a coupled thermo-structural interaction in case of SC-SOFCs.

CHAPTER 4

MODELLING OF SC-SOFCs[1]

4.1 Introduction

As stated in Chapter-3, the research work on SC-SOFC is mainly experimentally driven with a very few reports on modelling of SC-SOFCs. These experiments give information about the overall cell performance, a deeper understanding of the hydrodynamic and electrochemical interaction is lacking. Modelling can be a best tool to study all insights but unfortunately there is a very little work in this direction. The models developed so far are mainly limited to two-dimensional analysis [73-78], showing that the theoretical studies are at an early stage yet. The only two active groups (Hao et al., USA and Chung et al., Korea) have reported initial numerical studies mainly focused on understanding the causes of low performance in SC-SOFCs. The numerical results of both of the above groups were pointing towards poor fluid flow and electrochemical management, which is the main cause in lowering the cell performance. We tried to focus on these issues and our modelling objective was to look more closely into the hydrodynamic issues (related to the fluid flow) and electrochemical issues (related to the cell performance) of the conventional-planar and co-planar designs. We focused on three-dimensional analysis in order to capture the insights more close to the reality. The final aim was to suggest a suitable geometry that can minimize the adverse effects of both of the above issues, directing towards the realization of a better experimental setup, if possible.

---

[1] The results described in this chapter have been published in:

• N. Akhtar et al., Intl. J. Hydrogen Energy 34 (2009) 8645-8663.

4.2 The Mathematical Model

As stated in Chapter-1, the SC-SOFCs operate on a mixture of fuel and oxidant supply. Though, hydrocarbons (like methane, propane and butane) are the most practical fuels due to their relatively narrow explosive limit compared to hydrogen, their anode chemistry is much complicated and not very well understood yet [110]. On the other hand, use of hydrogen as a fuel simplifies the overall anode chemistry and does not lead to coking problems which are normally encountered in case of hydrocarbons. For the sake of simplicity, our initial efforts will focus on hydrogen/oxygen mixtures diluted with nitrogen for safety reasons.

The complete cell system is subdivided into individual layers, and modelling of each layer is presented in below. The cell considered in this study is composed of nickel supported anode gas diffusion electrode, nickel-yttria stabilized zirconia (Ni-YSZ) anode catalyst layer, yttria-stabilized zirconia (YSZ) electrolyte, yttria stabilized zirconia-lanthanum strontium manganite (YSZ-LSM) cathode catalyst layer and lanthanum strontium manganite (LSM) as cathode electrode. In a first attempt to simplify the model, it has been assumed that the cell is fed with nitrogen diluted hydrogen/oxidant mixture instead of hydrocarbon/oxidant mixtures. The addition of 96% nitrogen is necessary to ensure that the mixture is safe [111]. The simulation results shown in this study are on the basis of the remainder 4%.

The following reactions are assumed to occur in the electrodes (full direct combustion is avoided due to the dilution effect):

1) Reaction in the anode:

$$H_2 + O^{2-} \rightarrow H_2O + 2e^- \tag{4.1}$$

2) Reaction in the cathode:

$$\frac{1}{2}O_2 + 2e^- \rightarrow O^{2-} \tag{4.2}$$

4.3 Model Description

The fuel cell analyzed in the present study is of planar type configuration with a hole in the middle of the cell to allow radial flow into and through the porous electrodes. It is composed of seven subdomains, namely the gas chamber, two porous electrodes (anode and cathode), two porous catalyst layers (anode and cathode catalyst layer), the electrolyte and the hole in the cell. The geometrical

dimensions of the gas chamber are listed in Table 4.1:

Dimensions	Values (mm)
Chamber length (x-axis)	150
Chamber height (y-axis)	25
Chamber width (z-axis)	25
PEN width	20
PEN height	20
Anode thickness	70×10^{-3}
Cathode thickness	50×10^{-3}
Electrolyte thickness	20×10^{-3}
Anode catalyst layer thickness	5×10^{-3}
Cathode catalyst layer thickness	5×10^{-3}
Hole diameter	2.6

Table 4.1: Geometrical dimensions

The following modelling assumptions have been made:

4.3.1 Model Assumptions

• The flow is steady and isothermal.

• Hydrogen and oxygen are the only electrochemically active species.

• The electrodes are assumed to be ideally selective for the respective electrochemical reactions, therefore, electrochemical oxidation of fuel and reduction of oxygen is taking place in the anode and cathode catalyst layers, respectively [76].

• Ohmic heating (in the porous electrodes and catalyst layers) due to electrical current transport is neglected because of high electrical conductivity as compared to the ionic conductivity [110].

• The electrolyte is a non-porous material.

• The outer surfaces of the anode and cathode diffusion electrodes are used as current collectors, therefore the effects of interconnects are neglected.

In following sections, detailed modelling strategy is presented for each sub-domain.

4.3.2 Computational Domain

Gas Chamber

The gas chamber consists of a rectangular duct with a membrane electrode assembly also called positive electrode, electrolyte and negative electrode (PEN) located in the center of the duct (Figure 4.1). The PEN element has a hole in the center to allow gaseous mixture to pass through in the axial direction thereby relieving the pressure that could be built-up in front of the cell. In Figure 4.2, a close-up

view of the PEN element has been shown. The applicable equations are:

• Continuity equation:

$$\nabla \cdot (\rho \mathbf{u}) = 0 \tag{4.3}$$

• Momentum equation:

$$\rho(\mathbf{u} \cdot \nabla)\mathbf{u} = -\nabla p + \mu \nabla^2 \mathbf{u} + \frac{1}{3}\mu \nabla(\nabla \cdot \mathbf{u}) \tag{4.4}$$

• Species conservation equation:

$$\nabla \cdot (\rho \mathbf{u} Y_i) = -\nabla \cdot \mathbf{j}_i \tag{4.5}$$

The density of the mixture is calculated using [112]:

$$\rho = \frac{1}{\sum_{i=1}^{N} Y_i/\rho_i} \tag{4.6}$$

The density of each species, ρ_i is obtained from the perfect gas law relation [112]:

$$\rho_i = \frac{pM_i}{RT} \tag{4.7}$$

The concentration of each species is calculated by:

$$c_i = \frac{pX_i}{RT} \tag{4.8}$$

where

$$X_i = Y_i \left(\frac{M}{M_i} \right) \tag{4.9}$$

and

$$M = \sum_{i=1}^{N} X_i M_i \tag{4.10}$$

In equation (4.5), the multicomponent diffusive mass flux vector ($\mathbf{j}_i$) is described by the generalized Fick's law [113, 114]:

$$\mathbf{j}_i = -\sum_{j=1}^{N-1} \rho D_{ij} \nabla Y_j \tag{4.11}$$

where, N = total number of species in the mixture.

D_{ij} in equation (4.11) is the multicomponent diffusion coefficient, which in general is not symmetric ($D_{ij} \neq D_{ji}$). Also, the multicomponent D_{ij} does not have the physical significance of the binary

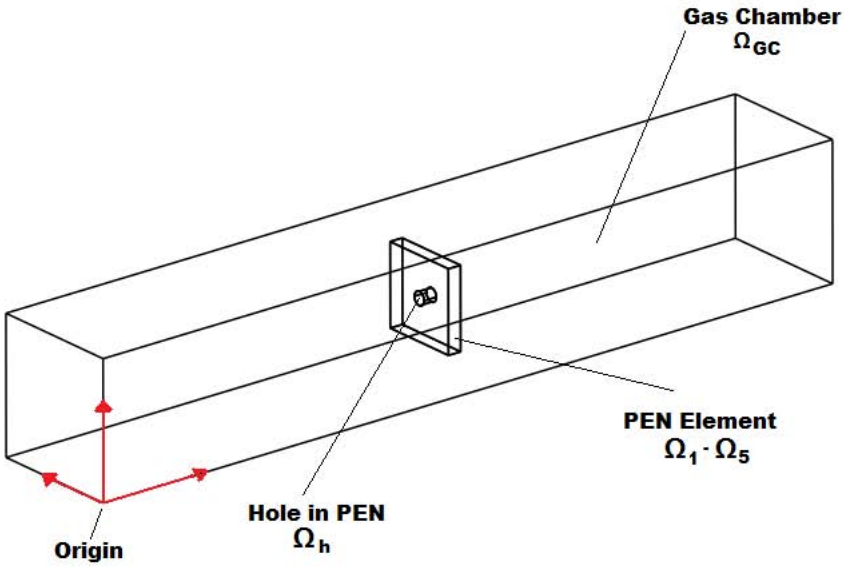

Figure 4.1: Gas chamber with PEN element inside

Fick diffusivity in that the D_{ij} does not reflect the $i-j$ interactions [115]. Multicomponent diffusion coefficients D_{ij} are interrelated with Maxwell-Stefan diffusion coefficients $\mathcal{D}_{ij}$ through the matrix B, such that [115]:

$$D = B^{-1}\Gamma \tag{4.12}$$

Here D is the matrix with components D_{ij}. For ideal gases, the thermodynamic matrix Γ reduces to the identity matrix and equation (4.12) becomes:

$$D = B^{-1} \tag{4.13}$$

where D is the multicomponent diffusion coefficient matrix and B is a square matrix of order $N-1$ with elements given by:

$$B_{ii} = \frac{Y_i M}{M_i \mathcal{D}_{iN}} + \sum_{k=1, i\neq k}^{N} \frac{Y_k M}{M_k \mathcal{D}_{ik}} \tag{4.14}$$

$$B_{ij} = -\frac{Y_i M}{M_i}\left(\frac{1}{\mathcal{D}_{ij}} - \frac{1}{\mathcal{D}_{iN}}\right), \qquad i \neq j \tag{4.15}$$

where $\mathcal{D}_{ij}$ in equation (4.14) and (4.15) are the Maxwell-Stefan diffusion coefficients for binary pairs and are dependent on both temperature and pressure [82-87]. For gas pressures up to about 10 atmo-

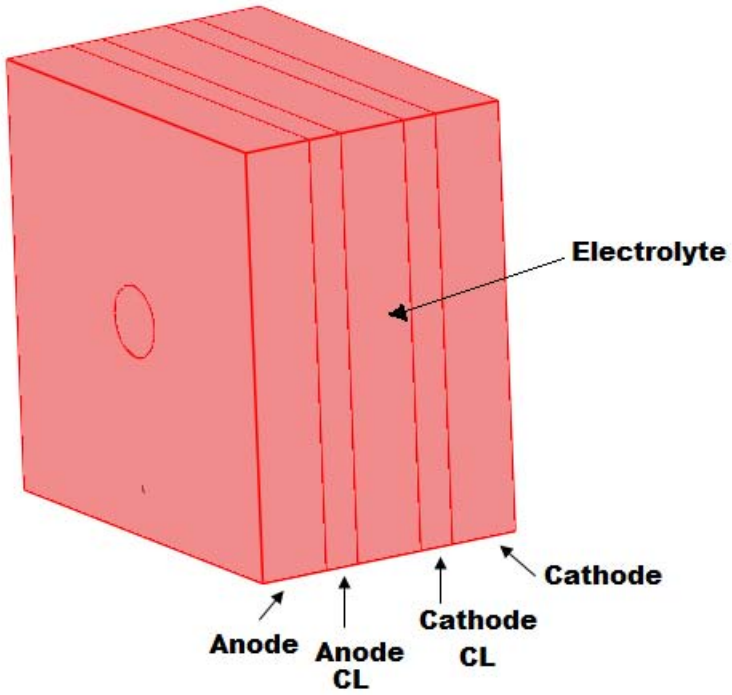

Figure 4.2: Close view of PEN element

sphere at moderate to high temperatures, the diffusion coefficient for a binary mixture of gases i and j may be estimated from the empirical relation from Fueller, Schettler and Giddings [117, 119, 120]:

$$\mathcal{D}_{ij} = \frac{T^{1.75}(1/M_i + 1/M_j)^{1/2}}{p(V_i^{1/3} + V_j^{1/3})^2} \times 10^{-7} \tag{4.16}$$

where $\mathcal{D}_{ij}$ is the Maxwell-Stefan diffusion coefficient in $m^2 s^{-1}$, T is the temperature in kelvin (K), p is the pressure in atmospheres (atm), M_i is the molecular weight of molecules in $gmol^{-1}$, and V_i is the molecular diffusion volume in $cm^3 mol^{-1}$. The values of V_i for different molecules are tabulated in [118] and for some of the molecules of interest are given in Table 4.2.

Molecule	Diffusion Volume (cm^3/mol)
H_2	7.07
O_2	16.6
H_2O	12.7
N_2	17.9

Table 4.2: Diffusion volumes in Fueller-Schettler-Giddings correlation parameters [118].

Note that equation (4.16) is a result of a regression analysis of 340 experimentally determined binary diffusion coefficients [118]. Also, this equation can be easily applied for pressure and temperature

ranges used in a typical fuel cell operation.

Typical values of $\mathcal{D}_{ij}(m^2 s^{-1})$ for the above molecules (commonly used in fuel cells) are calculated using equation (4.16) and are given in Table 4.3 at a pressure of 1 atmosphere and at an average temperature of 773 kelvin, which is assumed to be the operating condition for the single-chamber solid oxide fuel cell in this study.

Molecular Pair	$\mathcal{D}_{ij}(m^2/s)$
$H_2 - N_2$	4.0176×10^{-4}
$H_2 - O_2$	4.1178×10^{-4}
$N_2 - O_2$	1.0982×10^{-4}
$H_2 - H_2O$	4.6541×10^{-4}
$N_2 - H_2O$	1.3972×10^{-4}
$O_2 - H_2O$	1.3992×10^{-4}

Table 4.3: Maxwell-Stefan diffusion coefficients calculated using equation (4.16).

Gas Diffusion Electrodes

Gas diffusion electrodes consist of an anode and a cathode which are porous media. The following equations model gas diffusion in the electrodes:

• Continuity equation:

$$\nabla \cdot (\rho \mathbf{u}) = S_m \tag{4.17}$$

S_m is the source/sink term for the production/consumption of gas molecules and is zero for gas diffusion electrodes because the electrochemical reaction is assumed to take place only in the catalyst layers. The reason for introducing the source/sink term (given in Ref. [121]), is that sometimes the reactive layers can extend into the electrodes.

• Momentum equation:

In a porous media flow where viscous forces dominate convective ones, the momentum equation in the porous media may be modified from the Navier-Stokes equation to the Brinkman equation. In order to do so, the convective term has been neglected and an additional term for pressure drop in porous media, given by Darcy's law, has been added. This describes flow in porous media with a pressure gradient as the only driving force.

$$\nabla p = -\frac{\mu}{\kappa}\mathbf{u} \tag{4.18}$$

By inserting this term in the Navier-Stokes equation, we have the Brinkman equation as [122, 123]:

$$\frac{\mu}{\kappa}\mathbf{u} = -\nabla p + \mu\nabla^2\mathbf{u} + \frac{1}{3}\mu\nabla(\nabla\cdot\mathbf{u}) \tag{4.19}$$

• Species conservation equation:

$$\nabla\cdot(\rho\mathbf{u}Y_i) = -\nabla\cdot\mathbf{j}_i + S_i \tag{4.20}$$

where S_i is the source/sink term for the production/consumption of species, set to zero for gas diffusion electrodes, because of the above mentioned reason.

$\mathbf{j}_i$ is the multicomponent diffusive mass flux vector in porous media, given by:

$$\mathbf{j}_i = -\sum_{j=1}^{N-1}\rho D_{DG}^{eff}\nabla Y_j \tag{4.21}$$

where D_{DG}^{eff} is the effective dusty gas diffusivity.

Diffusion in porous media is usually described by a molecular (particle-particle collision) and/or a Knudsen (particle-wall collision) diffusion mechanism [124]. In order to account for a detailed diffusion mechanism, both modes have been considered by implementing the Dusty Gas Model (DGM). The DGM is derived by considering the solid matrix as large stationary spheres suspended in the gas mixture as one of the species present. The DGM diffusivity is then given by [124]:

$$\mathcal{D}_{DG_{i,j}} = \frac{\mathcal{D}_{ij}\mathcal{D}_{k,i}}{\mathcal{D}_{ij} + \mathcal{D}_{k,i}} \tag{4.22}$$

where

$$\mathcal{D}_{k,i} = \frac{1}{3}d_p\sqrt{\frac{8RT}{\pi M_i}} \tag{4.23}$$

The values of $\mathcal{D}_{ij}$ are calculated using equation (4.16) and the DGM diffusitivities are further corrected using the following expression [124]:

$$\mathcal{D}_{DG_{i,j}}^{eff} = (\frac{\epsilon}{\tau})\mathcal{D}_{DG_{i,j}} \tag{4.24}$$

Finally, the value of $\mathcal{D}^{eff}_{DG_{i,j}}$ is used to calculate $D^{eff}_{DG_{i,j}}$ as:

$$B^{eff}_{DG_{ii}} = \frac{Y_i M}{M_i \mathcal{D}^{eff}_{DG_{i,N}}} + \sum_{k=1, i\neq k}^{N} \frac{Y_k M}{M_k \mathcal{D}^{eff}_{DG_{i,k}}} \tag{4.25}$$

$$B^{eff}_{DG_{ij}} = -\frac{Y_i M}{M_i}\left(\frac{1}{\mathcal{D}^{eff}_{DG_{i,j}}} - \frac{1}{\mathcal{D}^{eff}_{DG_{i,N}}}\right), \qquad i \neq j \tag{4.26}$$

• Charge conservation equation:

Electrical current transport is described by a governing equation for conservation of charge [124, 125]:

$$\nabla \cdot (-\sigma_s \nabla \phi_s) = A_s S_{\phi_s} \tag{4.27}$$

S_{ϕ_s} = electrical current source term which is kept zero in the anode and cathode gas diffusion electrodes.

Catalyst Layers

An additional ionic charge conservation equation in the catalyst layer will represent the ionic current, and is given by [124, 125]:

$$\nabla \cdot (-\sigma^{eff}_e \nabla \phi_e) = A_s S_{\phi_e} \tag{4.28}$$

S_{ϕ_e} = ionic current source term defined below.

Other transport equations in the catalyst layers are the same as in the electrodes, except the source/sink terms are activated in the conservation equations and the electrical conductivity term (σ_s) in equation (4.27) is changed to effective electrical conductivity (σ^{eff}_s) in order to account for mixed ionic-electronic conductivity in the catalyst layers. The source/sink terms in mass and species conservation equation are given below.

At the anode side, hydrogen is consumed and water is produced, so that [125]:

$$S_m = S_i = S_{H_2} = -\frac{M_{H_2}}{2F} i_a \tag{4.29}$$

$$S_m = S_i = S_{H_2O} = +\frac{M_{H_2O}}{2F} i_a \tag{4.30}$$

At the cathode side, oxygen is consumed [125]:

$$S_m = S_i = S_{O_2} = -\frac{M_{O_2}}{4F} i_c \tag{4.31}$$

The source/sink terms in the electrical and ionic charge conservation equation are given below [125]. In the anode catalyst layer, electrical current density is a sink term:

$$S_{\phi_s} = -i_a \tag{4.32}$$

In the anode catalyst layer, ionic current density is a source term:

$$S_{\phi_e} = +i_a \tag{4.33}$$

In the cathode catalyst layer, electrical current density is a sink term:

$$S_{\phi_s} = -i_c \tag{4.34}$$

In the cathode catalyst layer, ionic current density is a source term:

$$S_{\phi_e} = +i_c \tag{4.35}$$

where i_a and i_c are calculated using equation (1.7) and (1.8). The exchange current densities, $i_{0,a}$ and $i_{0,c}$ are expressed as a function of local partial pressure of the species [125]:

$$i_{0,a} = \gamma_a (\frac{p_{H2}}{p^{ref}})(\frac{p_{H2O}}{p^{ref}})^{-0.5} exp(\frac{-E_{act,a}}{RT}) \tag{4.36}$$

$$i_{0,c} = \gamma_c (\frac{p_{O2}}{p^{ref}})^{0.25} exp(\frac{-E_{act,c}}{RT}) \tag{4.37}$$

where p^{ref} is the reference pressure in the gas-chamber, i.e. the total pressure of 1 atmosphere. γ_a and γ_c are the anodic and cathodic pre-exponential coefficients, $E_{act,a}$ and $E_{act,c}$ are the anodic and cathodic activation energies, respectively.

The anode and cathode side activation overpotentials are calculated by [126]:

η_{act_a}= $\phi_{s/a,cl} - \phi_{e/a,cl}$ = anode side activation overpotential.

η_{act_c}= $\phi_{s/c,cl} - \phi_{e/c,cl} - V_{oc}$ = cathode side activation overpotential.

where $\phi_{s/a,cl}$ and $\phi_{e/a,cl}$ are respectively the solid phase (electronic) and electrolyte phase (ionic) potential in the anode catalyst layer, $\phi_{s/c,cl}$ and $\phi_{e/c,cl}$ are the electronic and ionic potential in the cathode catalyst layer, and V_{oc} is the open circuit (Nernst) voltage, as expressed by [124]:

$$V_{oc} = V^o + \frac{RT}{2F} ln(\frac{p_{H_2}}{p_{H_2O}}) + \frac{RT}{4F} ln(p_{O_2}) \tag{4.38}$$

Since the model is solved using "Finite Element Methods (FEM)", all unknown variables are calculated at each node. For example, the operating voltage is defined at the cathode outer surface and a zero voltage is set at the anode outer surface. By implementing the charge conservation equation (i.e. the Ohm's law), the ohmic loss is embedded while calculating the current at each node (since at each node, all equations are solved in FEM). The pressure distribution is calculated via mass transport model, and, at each node, current is calculated corresponding to that concentration. Therefore, there is no need for explicit expressions for ohmic and concentration overpotentials in FEM, rather they are an integral part of the model being solved numerically.

Electrolyte

The electrolyte is impermeable to gases and allows only ionic charge transfer, so that [125]:

$$\nabla \cdot (-\sigma_e \nabla \phi_e) = 0 \tag{4.39}$$

Since there is no generation of ionic or electrical current inside the electrolyte, the right hand side of the above equation is zero.

4.3.3 Boundary Conditions

The boundary conditions for each layer are given below and the respective layers are labeled in Figures 4.3-4.4.

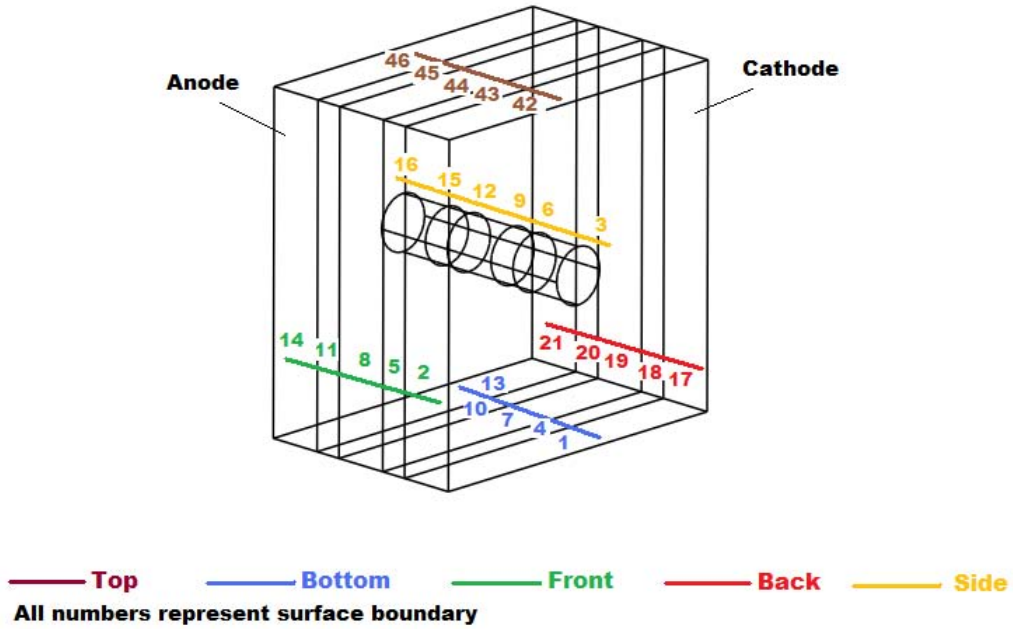

Figure 4.3: Surface boundaries in PEN element

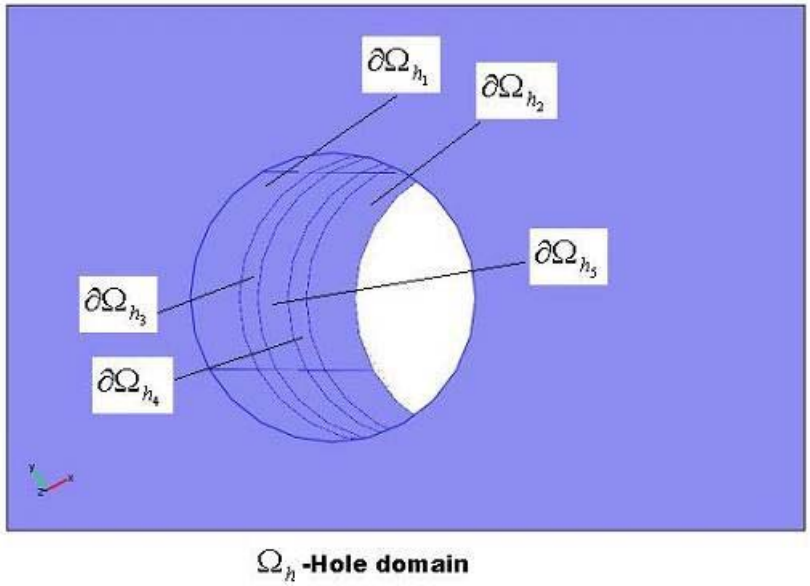

Figure 4.4: Surface boundaries in hole

Gas Chamber

- **Inlet**

At the inlet, the velocity in the x-direction is prescribed to be:

$$\mathbf{u} = \mathbf{u_{in}} \tag{4.40}$$

At the inlet, the mass fraction is defined as:

$$Y_i = Y_{i_{in}} \tag{4.41}$$

- **Walls**

At the walls no-slip boundary condition is applied. A no-slip condition means that the fluid's velocity is equal to the boundary velocity, which is zero in the case of a fixed wall.

$$\mathbf{u} = 0 \tag{4.42}$$

A mass insulation boundary condition is applied at the walls, meaning that no mass flux is allowed to cross these boundaries [126].

$$\mathbf{n} \cdot (-\rho D_{ij} \nabla Y_i + \rho \mathbf{u} Y_i) = 0 \tag{4.43}$$

- **Outlet**

The outflow boundary condition is prescribed as [126]:

$$p = p_o \tag{4.44}$$

The convective flux boundary condition is applied at the outlet, meaning that at the outlet boundary, diffusion term is negligible [126].

$$\mathbf{n} \cdot (-\rho D_{ij} \nabla Y_i) = 0 \tag{4.45}$$

Gas Diffusion Electrodes

- **Anode electrode**

At all exterior surfaces of the anode and at an interface between the anode electrode and anode catalyst

layer, continuity of flow is applied. This puts no constraints on the velocity and mass flux. The current on the anode side is collected from the outer surface which face inlet flow direction. Therefore, a zero voltage (ground) boundary condition is applied at the anode outer surface.

$$\phi_s = 0 \tag{4.46}$$

All other outer surfaces of the anode electrode are insulated to the electrical current, hence it is assumed that there is no current flow across these boundaries.

$$\mathbf{n} \cdot (-\sigma_s \nabla \phi_s) = 0 \tag{4.47}$$

At the interface between the anode electrode and anode catalyst layer, continuity of electrical current is maintained.

- **Cathode electrode**

The same boundary conditions which are described above for the anode will also hold for the cathode, except the electrical potential boundary condition for the cathode electrode surface which faces the outlet flow direction has been modified to:

$$\phi_s = V_c \tag{4.48}$$

This boundary condition defines the operating cell voltage and closes the current circuit.

Catalyst Layers

- **Anode catalyst layer**

At all exterior surfaces of the anode catalyst layer continuity of flow is applied, meaning putting no constraints on the velocity and mass flux. However, at the interface between the anode catalyst layer and the electrolyte, gases are not allowed to enter into the electrolyte because of its non-porous nature. Hence, normal to the electrolyte boundary, both the velocity and mass flux are zero.

$$\mathbf{n} \cdot \mathbf{u} = 0 \tag{4.49}$$

$$\mathbf{n} \cdot (-\rho D^{eff}_{DG_{i,j}} \nabla Y_i + \rho \mathbf{u} Y_i) = 0 \tag{4.50}$$

At all exterior surfaces of the anode catalyst layer and at interface between the anode catalyst layer and the electrolyte, electrical insulation boundary condition has been applied.

$$\mathbf{n} \cdot (-\sigma_s^{eff} \nabla \phi_s) = 0 \tag{4.51}$$

Ionic current cannot flow out of the catalyst layers. All exterior surfaces of the anode catalyst layer and at interface between the anode electrode and the anode catalyst layer, ionic current is insulated by applying ionic current insulation boundary condition.

$$\mathbf{n} \cdot (-\sigma_e^{eff} \nabla \phi_e) = 0 \tag{4.52}$$

- **Cathode catalyst layer**

The same boundary conditions as described above for the anode catalyst layer will also hold for the cathode catalyst layer.

Electrolyte

Since the electrolyte is impermeable to gases, both the mass flux and velocity normal to all surfaces of the electrolyte are zero.

$$\mathbf{n} \cdot \mathbf{u} = 0 \tag{4.53}$$

$$\mathbf{n} \cdot (-\rho D_{DG_{i,j}}^{eff} \nabla Y_i + \rho \mathbf{u} Y_i) = 0 \tag{4.54}$$

Continuity of ionic current is maintained at interfaces between the anode/cathode catalyst layers and the electrolyte. All outer surfaces of the electrolyte are insulated to ionic current by applying an ionic insulation boundary condition.

$$\mathbf{n} \cdot (-\sigma_e \nabla \phi_e) = 0 \tag{4.55}$$

The hole in the PEN allows free flow in a similar way as in the gas chamber, therefore continuity of flow is maintained in the hole. However, we consider the electrolyte surface boundaries consisting of a hole to not allow the gases to permeate into the electrolyte, therefore insulation boundary conditions have been applied at these boundaries.

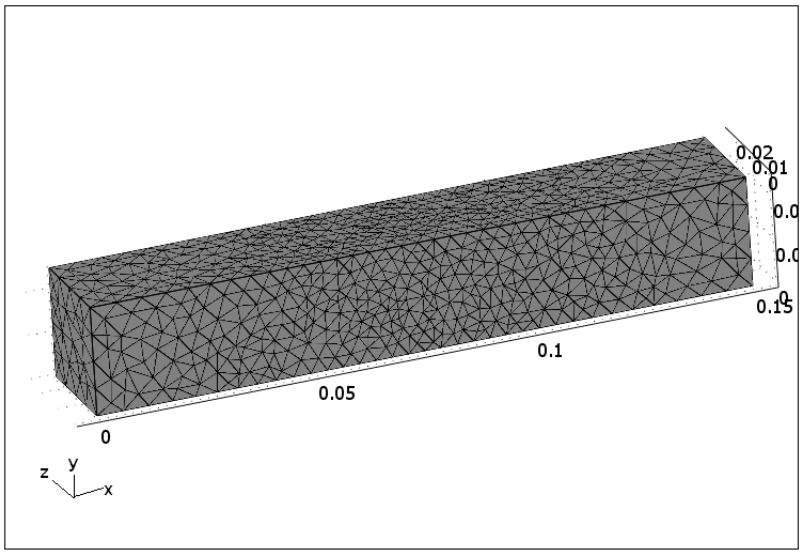

Figure 4.5: The computational mesh (9,398 elements)

4.4 Numerical implementation

The model equations are solved using COMSOL Multiphysics 3.4, a commercial Finite Element Method (FEM) based software package. The computations were performed on a 32-node Linux cluster; 32 x dual 3GHz Intel Xeon Sun Fire V60 servers each with 4GB memory. The mesh consists of 9,398 triangular elements of good quality and is shown in Figure 4.5. In order to ensure convergence and accuracy of the results in three dimensional domain, the following were employed:

- Use of lower element order to reduce the number of unknowns.
- The mesh was kept more refined in the cell element where higher resolution was needed to capture large gradients.
- A direct solver such as UMFPACK is very stable but not good for large problems, since it requires too much memory. Therefore, an iterative solver (GMRES) with a preconditioner (Incomplete LU) and tolerance of 0.005 was used.

The system of equations was solved iteratively, i.e. first the charge balance, then the Navier-Stokes equation, then the mass/species balance, while at each stage the solution was stored and used as an initial condition for the subsequent stage. The total computing time for all stages (with $65,192$ degrees of freedom) was approximately 13.5 minutes for one value of voltage scan. The grid independency test was performed using using different mesh sizes. Figure 4.6 shows that the velocity field becomes grid independent as we move above 7,154 elements. In order to keep balance between accuracy and computational time, a mesh with 9,398 elements was opted.

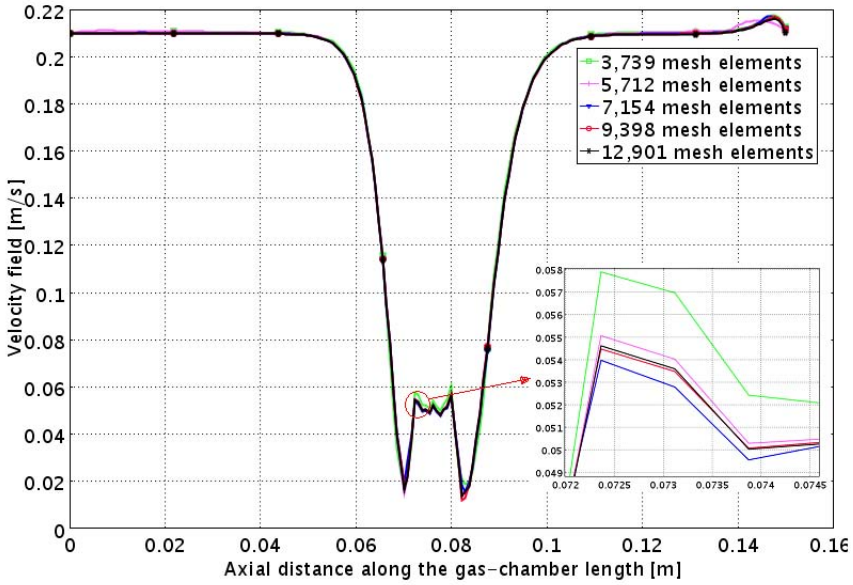

Figure 4.6: The grid independency test

4.5 Results and Discussion

The values of the electrochemical/hydrodynamic transport parameters for the base case operating conditions are listed in Table 4.4. The governing equations and the boundary conditions are summarized

Property	Symbol	Value	Units	References
Working electrical potential at anode	$\phi_{s,a}$	0	V	[5]
Working electrical potential at cathode	$\phi_{s,c}$	0.7	V	[5]
Anodic pre-exponential coefficient	γ_a	$1.6e^{-9}$	$-$	[125]
Cathodic pre-exponential coefficient	γ_c	$3.9e^{-9}$	$-$	[125]
Anodic activation energy	$E_{act,a}$	120	$Jmol^{-1}$	[125]
Cathodic activation energy	$E_{act,c}$	120	$Jmol^{-1}$	[125]
Faraday's constant	F	96487	$Cmole^{-1}$	[127]
Universal gas constant	R_g	8.314	$Jmole^{-1}K^{-1}$	[128]
Effective anode ionic conductivity	σ_{ea}^{eff}	0.29	Sm^{-1}	[5]
Effective cathode ionic conductivity	σ_{ec}^{eff}	0.24	Sm^{-1}	[5]
Effective anode electronic conductivity	σ_{sa}^{eff}	4800	Sm^{-1}	[5]
Effective cathode electronic conductivity	σ_{sc}^{eff}	1600	Sm^{-1}	[5]
Anode electronic conductivity	σ_{sa}	2.0×10^6	Sm^{-1}	[129]
Electrolyte ionic conductivity	σ_e	$3.34 \times 10^4 exp(-10350/T)$	Sm^{-1}	[129]
Cathode electronic conductivity	σ_{sc}	$(42 \times 10^6/T) exp(-1150/T)$	Sm^{-1}	[129]
Inlet temperature	T_0	773	K	[$-$]
Anodic anodic charge transfer coefficient	α_a^a	2		[5]
Anodic cathodic charge transfer coefficient	α_c^a	1		[5]
Cathodic anodic charge transfer coefficient	α_a^c	1.5		[5]
Cathodic cathodic charge transfer coefficient	α_c^c	0.5		[5]
Porosity	ϵ	0.3		[125]
Tortuosity	τ	3.80		[128]
Electrochemically active surface area	A_s	102500	m^{-1}	[128]
Permeability	κ	1.0×10^{-13}	m^2	[126]
Hydrogen inlet mass fraction (of 4%)	$Y_{H2_{in}}$	0.5		[75]
Oxygen inlet mass fraction (of 4%)	$Y_{O2_{in}}$	0.105		[75]
Nitrogen inlet mass fraction (of 4%)	$Y_{N2_{in}}$	0.38		[75]
Water inlet mass fraction (of 4%)	$Y_{H2O_{in}}$	0.015		[75]
Operating pressure	p_o	1.013×10^5	Nm^{-2}	[124]
Inlet velocity	$\mathbf{u_{in}}$	0.1	ms^{-1}	[$-$]
Average pore diameter	d_p	1.0	μm	[124]

Table 4.4: Input parameters used in the model

in Table 4.5-4.6. In Figures 4.7-4.16, the results shown are based on parameters listed in Table 4.4,

Domain	Equation solved
$\Omega_{GC,h}$	$\nabla \cdot (\rho \mathbf{u}) = 0$ $\rho(\mathbf{u} \cdot \nabla)\mathbf{u} = -\nabla p + \mu \nabla^2 \mathbf{u} + \frac{1}{3}\mu \nabla(\nabla \cdot \mathbf{u})$ $\nabla \cdot (\rho \mathbf{u} Y_i) = -\nabla \cdot \mathbf{j}_i$
Ω_a	$\nabla \cdot (\rho \mathbf{u}) = 0$ $\frac{\mu}{\kappa}\mathbf{u}$=$-\nabla p + \mu \nabla^2 \mathbf{u} + \frac{1}{3}\mu \nabla(\nabla \cdot \mathbf{u})$ $\nabla \cdot (\rho \mathbf{u} Y_i) = -\nabla \cdot \mathbf{j}_i$ $\nabla \cdot (-\sigma_s \nabla \phi_s) = 0$
Ω_c	$\nabla \cdot (\rho \mathbf{u}) = 0$ $\frac{\mu}{\kappa}\mathbf{u}$=$-\nabla p + \mu \nabla^2 \mathbf{u} + \frac{1}{3}\mu \nabla(\nabla \cdot \mathbf{u})$ $\nabla \cdot (\rho \mathbf{u} Y_i) = -\nabla \cdot \mathbf{j}_i$ $\nabla \cdot (-\sigma_s \nabla \phi_s) = 0$
$\Omega_{a,cl}$	$\nabla \cdot (\rho \mathbf{u}) = S_m, S_m = S_{H2} + S_{H2O} = -\frac{M_{H_2}}{2F} i_a + \frac{M_{H_2O}}{2F} i_a$ $\frac{\mu}{\kappa}\mathbf{u}$=$-\nabla p + \mu \nabla^2 \mathbf{u} + \frac{1}{3}\mu \nabla(\nabla \cdot \mathbf{u})$ $\nabla \cdot (\rho \mathbf{u} Y_i) = -\nabla \cdot \mathbf{j}_i + S_i, S_i = S_{H2} = -\frac{M_{H_2}}{2F} i_a, S_{H2O} = +\frac{M_{H_2O}}{2F} i_a$ $\nabla \cdot (-\sigma_s^{eff} \nabla \phi_s) = A_s S_{\phi_s}$ $\nabla \cdot (-\sigma_e^{eff} \nabla \phi_e) = A_s S_{\phi_e}$
$\Omega_{c,cl}$	$\nabla \cdot (\rho \mathbf{u}) = S_m, S_m = S_{O2} = -\frac{M_{O_2}}{4F} i_c$ $\frac{\mu}{\kappa}\mathbf{u}$=$-\nabla p + \mu \nabla^2 \mathbf{u} + \frac{1}{3}\mu \nabla(\nabla \cdot \mathbf{u})$ $\nabla \cdot (\rho \mathbf{u} Y_i) = -\nabla \cdot \mathbf{j}_i + S_i, S_i = S_{O2} = -\frac{M_{O_2}}{4F} i_c$ $\nabla \cdot (-\sigma_s^{eff} \nabla \phi_s) = A_s S_{\phi_s}$ $\nabla \cdot (-\sigma_e^{eff} \nabla \phi_e) = A_s S_{\phi_e}$
Ω_e	$\nabla \cdot (-\sigma_e \nabla \phi_e) = 0$

Table 4.5: Computational domains and governing equations

whereas for the results shown in Figures 4.17-4.20, the value of porosity has been changed to 0.4 in order to see the effect of electrochemistry and hydrodynamics, with all other parameters remain the same as in Table 4.4. Figures 4.21-4.22 show I-V and I-P characteristics based on parameters listed in Table 4.4, respectively.

In Figure 4.7, the velocity field in the gas chamber is shown. It can be seen that as soon as the flow reaches the anode electrode surface, some of the flow is diverted through the edges of the electrode surface. It shows that the cell is an obstacle to the fluid flow with fluid traveling a tortuous path in the gas diffusion electrode leading to a reduced velocity in the cell. Due to the diversion near the cell edges, an increased velocity of the flow is observed because of the free passage available for the flow as compared to the limited passage available in the cell. Just behind the cell, the velocity is reduced and the flow regains its center velocity after a distance of approximately $0.03\ m$ from the anode electrode surface. This distance is an important parameter to be considered in a case where one plans to investigate several cells downstream.

Figure 4.8 shows pressure drop in the gas chamber. It represents another parameter to observe in the flow behavior. The pressure drop along the flow direction is responsible for accelerating the flow. Moreover, near the anode electrode surface there is a large pressure drop (due to the presence of cell as an obstacle) followed by a Darcy pressure drop in the gas diffusion electrodes which is strongly

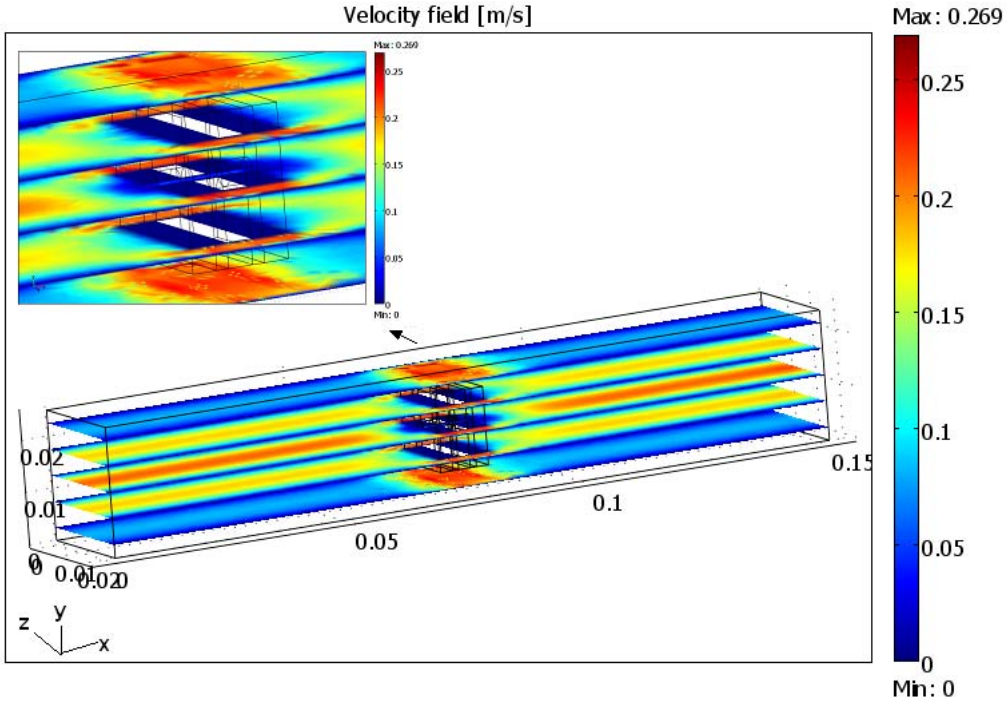

Figure 4.7: Velocity field in gas chamber

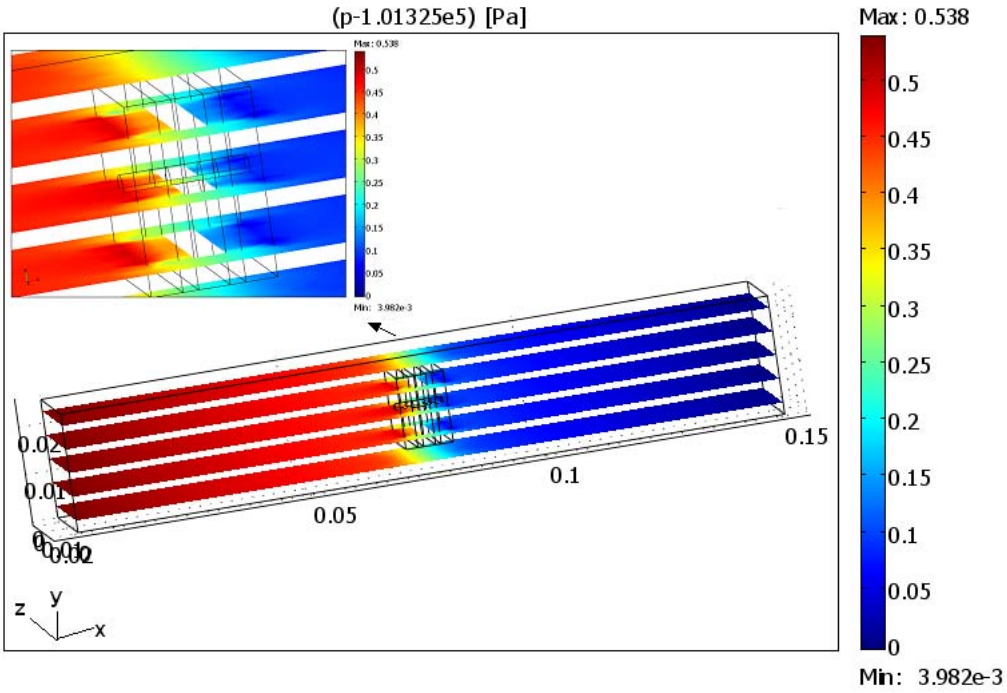

Figure 4.8: Pressure drop in gas chamber

Surface Boundary	Boundary Condition
$\partial\Omega_{GC_1}$	$\mathbf{u} = \mathbf{u_{in}}, Y_i = Y_{i_{in}}$
$\partial\Omega_{GC_2}$	$u = v = w = 0, \mathbf{n} \cdot (-\rho D_{ij} \nabla Y_i + \rho \mathbf{u} Y_i) = 0$
$\partial\Omega_{GC_3}$	$u = v = w = 0, \mathbf{n} \cdot (-\rho D_{ij} \nabla Y_i + \rho \mathbf{u} Y_i) = 0$
$\partial\Omega_{GC_4}$	$u = v = w = 0, \mathbf{n} \cdot (-\rho D_{ij} \nabla Y_i + \rho \mathbf{u} Y_i) = 0$
$\partial\Omega_{GC_5}$	$u = v = w = 0, \mathbf{n} \cdot (-\rho D_{ij} \nabla Y_i + \rho \mathbf{u} Y_i) = 0$
$\partial\Omega_{GC_6}$	$p = p_o, \mathbf{n} \cdot (-\rho D_{ij} \nabla Y_i) = 0$
$\partial\Omega_1$	$\mathbf{n}\cdot(\rho\mathbf{u})_{in} = \mathbf{n}\cdot(\rho\mathbf{u})_{out}, \mathbf{n}\cdot(-\rho D_{ij}\nabla Y_i + \rho\mathbf{u}Y_i)_{in} = \mathbf{n}\cdot(-\rho D_{ij}\nabla Y_i + \rho\mathbf{u}Y_i)_{out}, \mathbf{n}\cdot(-\sigma_s\nabla\phi_s) = 0$
$\partial\Omega_4$	$\mathbf{n}\cdot(\rho\mathbf{u})_{in} = \mathbf{n}\cdot(\rho\mathbf{u})_{out}, \mathbf{n}\cdot(-\rho D_{ij}\nabla Y_i + \rho\mathbf{u}Y_i)_{in} = \mathbf{n}\cdot(-\rho D_{ij}\nabla Y_i + \rho\mathbf{u}Y_i)_{out}, \mathbf{n}\cdot(-\sigma_s^{eff}\nabla\phi_s) = 0, \mathbf{n}\cdot(-\sigma_e^{eff}\nabla\phi_e) = 0$
$\partial\Omega_7$	$\mathbf{n}\cdot\mathbf{u} = 0, \mathbf{n}\cdot(-\rho D_{ij}\nabla Y_i + \rho\mathbf{u}Y_i) = 0, \mathbf{n}\cdot(-\sigma_e\nabla\phi_e) = 0$
$\partial\Omega_{10}$	$\mathbf{n}\cdot(\rho\mathbf{u})_{in} = \mathbf{n}\cdot(\rho\mathbf{u})_{out}, \mathbf{n}\cdot(-\rho D_{ij}\nabla Y_i + \rho\mathbf{u}Y_i)_{in} = \mathbf{n}\cdot(-\rho D_{ij}\nabla Y_i + \rho\mathbf{u}Y_i)_{out}, \mathbf{n}\cdot(-\sigma_s^{eff}\nabla\phi_s) = 0, \mathbf{n}\cdot(-\sigma_e^{eff}\nabla\phi_e) = 0$
$\partial\Omega_{13}$	$\mathbf{n}\cdot(\rho\mathbf{u})_{in} = \mathbf{n}\cdot(\rho\mathbf{u})_{out}, \mathbf{n}\cdot(-\rho D_{ij}\nabla Y_i + \rho\mathbf{u}Y_i)_{in} = \mathbf{n}\cdot(-\rho D_{ij}\nabla Y_i + \rho\mathbf{u}Y_i)_{out}, \mathbf{n}\cdot(-\sigma_s\nabla\phi_s) = 0$
$\partial\Omega_2$	$\mathbf{n}\cdot(\rho\mathbf{u})_{in} = \mathbf{n}\cdot(\rho\mathbf{u})_{out}, \mathbf{n}\cdot(-\rho D_{ij}\nabla Y_i + \rho\mathbf{u}Y_i)_{in} = \mathbf{n}\cdot(-\rho D_{ij}\nabla Y_i + \rho\mathbf{u}Y_i)_{out}, \mathbf{n}\cdot(-\sigma_s\nabla\phi_s) = 0$
$\partial\Omega_5$	$\mathbf{n}\cdot(\rho\mathbf{u})_{in} = \mathbf{n}\cdot(\rho\mathbf{u})_{out}, \mathbf{n}\cdot(-\rho D_{ij}\nabla Y_i + \rho\mathbf{u}Y_i)_{in} = \mathbf{n}\cdot(-\rho D_{ij}\nabla Y_i + \rho\mathbf{u}Y_i)_{out}, \mathbf{n}\cdot(-\sigma_s^{eff}\nabla\phi_s) = 0, \mathbf{n}\cdot(-\sigma_e^{eff}\nabla\phi_e) = 0$
$\partial\Omega_8$	$\mathbf{n}\cdot\mathbf{u} = 0, \mathbf{n}\cdot(-\rho D_{ij}\nabla Y_i + \rho\mathbf{u}Y_i) = 0, \mathbf{n}\cdot(-\sigma_e\nabla\phi_e) = 0$
$\partial\Omega_{11}$	$\mathbf{n}\cdot(\rho\mathbf{u})_{in} = \mathbf{n}\cdot(\rho\mathbf{u})_{out}, \mathbf{n}\cdot(-\rho D_{ij}\nabla Y_i + \rho\mathbf{u}Y_i)_{in} = \mathbf{n}\cdot(-\rho D_{ij}\nabla Y_i + \rho\mathbf{u}Y_i)_{out}, \mathbf{n}\cdot(-\sigma_s^{eff}\nabla\phi_s) = 0, \mathbf{n}\cdot(-\sigma_e^{eff}\nabla\phi_e) = 0$
$\partial\Omega_{14}$	$\mathbf{n}\cdot(\rho\mathbf{u})_{in} = \mathbf{n}\cdot(\rho\mathbf{u})_{out}, \mathbf{n}\cdot(-\rho D_{ij}\nabla Y_i + \rho\mathbf{u}Y_i)_{in} = \mathbf{n}\cdot(-\rho D_{ij}\nabla Y_i + \rho\mathbf{u}Y_i)_{out}, \mathbf{n}\cdot(-\sigma_s\nabla\phi_s) = 0$
$\partial\Omega_3$	$\mathbf{n}\cdot(\rho\mathbf{u})_{in} = \mathbf{n}\cdot(\rho\mathbf{u})_{out}, \mathbf{n}\cdot(-\rho D_{ij}\nabla Y_i + \rho\mathbf{u}Y_i)_{in} = \mathbf{n}\cdot(-\rho D_{ij}\nabla Y_i + \rho\mathbf{u}Y_i)_{out}, \phi_s = \phi_{sc}$
$\partial\Omega_6$	$\mathbf{n}\cdot(\rho\mathbf{u})_{in} = \mathbf{n}\cdot(\rho\mathbf{u})_{out}, \mathbf{n}\cdot(-\rho D^{eff}_{DG_{i,j}}\nabla Y_i + \rho\mathbf{u}Y_i)_{in} = \mathbf{n}\cdot(-\rho D^{eff}_{DG_{i,j}}\nabla Y_i + \rho\mathbf{u}Y_i)_{out}, \mathbf{n}\cdot(i_{c,in}) = \mathbf{n}\cdot(i_{c,out}), \mathbf{n}\cdot(-\sigma_e^{eff}\nabla\phi_e) = 0$
$\partial\Omega_9$	$\mathbf{n}\cdot\mathbf{u} = 0, \mathbf{n}\cdot(-\rho D^{eff}_{DG_{i,j}}\nabla Y_i + \rho\mathbf{u}Y_i) = 0, \mathbf{n}\cdot(-\sigma_s^{eff}\nabla\phi_s) = 0, \mathbf{n}\cdot(i_{c,in}) = \mathbf{n}\cdot(i_{c,out})$
$\partial\Omega_{12}$	$\mathbf{n}\cdot\mathbf{u} = 0, \mathbf{n}\cdot(-\rho D^{eff}_{DG_{i,j}}\nabla Y_i + \rho\mathbf{u}Y_i) = 0, \mathbf{n}\cdot(-\sigma_s^{eff}\nabla\phi_s) = 0, \mathbf{n}\cdot(i_{a,in}) = \mathbf{n}\cdot(i_{a,out})$
$\partial\Omega_{15}$	$\mathbf{n}\cdot(\rho\mathbf{u})_{in} = \mathbf{n}\cdot(\rho\mathbf{u})_{out}, \mathbf{n}\cdot(-\rho D^{eff}_{DG_{i,j}}\nabla Y_i + \rho\mathbf{u}Y_i)_{in} = \mathbf{n}\cdot(-\rho D^{eff}_{DG_{i,j}}\nabla Y_i + \rho\mathbf{u}Y_i)_{out}, \mathbf{n}\cdot(i_{a,in}) = \mathbf{n}\cdot(i_{a,out}), \mathbf{n}\cdot(-\sigma_e^{eff}\nabla\phi_e) = 0$
$\partial\Omega_{16}$	$\mathbf{n}\cdot(\rho\mathbf{u})_{in} = \mathbf{n}\cdot(\rho\mathbf{u})_{out}, \mathbf{n}\cdot(-\rho D_{ij}\nabla Y_i + \rho\mathbf{u}Y_i)_{in} = \mathbf{n}\cdot(-\rho D_{ij}\nabla Y_i + \rho\mathbf{u}Y_i)_{out}, \phi_s = \phi_{sa}$
$\partial\Omega_{17}$	$\mathbf{n}\cdot(\rho\mathbf{u})_{in} = \mathbf{n}\cdot(\rho\mathbf{u})_{out}, \mathbf{n}\cdot(-\rho D_{ij}\nabla Y_i + \rho\mathbf{u}Y_i)_{in} = \mathbf{n}\cdot(-\rho D_{ij}\nabla Y_i + \rho\mathbf{u}Y_i)_{out}, \mathbf{n}\cdot(-\sigma_s\nabla\phi_s) = 0$
$\partial\Omega_{18}$	$\mathbf{n}\cdot(\rho\mathbf{u})_{in} = \mathbf{n}\cdot(\rho\mathbf{u})_{out}, \mathbf{n}\cdot(-\rho D_{ij}\nabla Y_i + \rho\mathbf{u}Y_i)_{in} = \mathbf{n}\cdot(-\rho D_{ij}\nabla Y_i + \rho\mathbf{u}Y_i)_{out}, \mathbf{n}\cdot(-\sigma_s^{eff}\nabla\phi_s) = 0, \mathbf{n}\cdot(-\sigma_e^{eff}\nabla\phi_e) = 0$
$\partial\Omega_{19}$	$\mathbf{n}\cdot\mathbf{u} = 0, \mathbf{n}\cdot(-\rho D_{ij}\nabla Y_i + \rho\mathbf{u}Y_i) = 0, \mathbf{n}\cdot(-\sigma_e\nabla\phi_e) = 0$
$\partial\Omega_{20}$	$\mathbf{n}\cdot(\rho\mathbf{u})_{in} = \mathbf{n}\cdot(\rho\mathbf{u})_{out}, \mathbf{n}\cdot(-\rho D_{ij}\nabla Y_i + \rho\mathbf{u}Y_i)_{in} = \mathbf{n}\cdot(-\rho D_{ij}\nabla Y_i + \rho\mathbf{u}Y_i)_{out}, \mathbf{n}\cdot(-\sigma_s^{eff}\nabla\phi_s) = 0, \mathbf{n}\cdot(-\sigma_e^{eff}\nabla\phi_e) = 0$
$\partial\Omega_{21}$	$\mathbf{n}\cdot(\rho\mathbf{u})_{in} = \mathbf{n}\cdot(\rho\mathbf{u})_{out}, \mathbf{n}\cdot(-\rho D_{ij}\nabla Y_i + \rho\mathbf{u}Y_i)_{in} = \mathbf{n}\cdot(-\rho D_{ij}\nabla Y_i + \rho\mathbf{u}Y_i)_{out}, \mathbf{n}\cdot(-\sigma_s\nabla\phi_s) = 0$
$\partial\Omega_{42}$	$\mathbf{n}\cdot(\rho\mathbf{u})_{in} = \mathbf{n}\cdot(\rho\mathbf{u})_{out}, \mathbf{n}\cdot(-\rho D_{ij}\nabla Y_i + \rho\mathbf{u}Y_i)_{in} = \mathbf{n}\cdot(-\rho D_{ij}\nabla Y_i + \rho\mathbf{u}Y_i)_{out}, \mathbf{n}\cdot(-\sigma_s\nabla\phi_s) = 0$
$\partial\Omega_{43}$	$\mathbf{n}\cdot(\rho\mathbf{u})_{in} = \mathbf{n}\cdot(\rho\mathbf{u})_{out}, \mathbf{n}\cdot(-\rho D_{ij}\nabla Y_i + \rho\mathbf{u}Y_i)_{in} = \mathbf{n}\cdot(-\rho D_{ij}\nabla Y_i + \rho\mathbf{u}Y_i)_{out}, \mathbf{n}\cdot(-\sigma_s^{eff}\nabla\phi_s) = 0, \mathbf{n}\cdot(-\sigma_e^{eff}\nabla\phi_e) = 0$
$\partial\Omega_{44}$	$\mathbf{n}\cdot\mathbf{u} = 0, \mathbf{n}\cdot(-\rho D_{ij}\nabla Y_i + \rho\mathbf{u}Y_i) = 0, \mathbf{n}\cdot(-\sigma_e\nabla\phi_e) = 0$
$\partial\Omega_{45}$	$\mathbf{n}\cdot(\rho\mathbf{u})_{in} = \mathbf{n}\cdot(\rho\mathbf{u})_{out}, \mathbf{n}\cdot(-\rho D_{ij}\nabla Y_i + \rho\mathbf{u}Y_i)_{in} = \mathbf{n}\cdot(-\rho D_{ij}\nabla Y_i + \rho\mathbf{u}Y_i)_{out}, \mathbf{n}\cdot(-\sigma_s^{eff}\nabla\phi_s) = 0, \mathbf{n}\cdot(-\sigma_e^{eff}\nabla\phi_e) = 0$
$\partial\Omega_{46}$	$\mathbf{n}\cdot(\rho\mathbf{u})_{in} = \mathbf{n}\cdot(\rho\mathbf{u})_{out}, \mathbf{n}\cdot(-\rho D_{ij}\nabla Y_i + \rho\mathbf{u}Y_i)_{in} = \mathbf{n}\cdot(-\rho D_{ij}\nabla Y_i + \rho\mathbf{u}Y_i)_{out}, \mathbf{n}\cdot(-\sigma_s\nabla\phi_s) = 0$
$\partial\Omega_{h_1}$	$\mathbf{n}\cdot(\rho\mathbf{u})_{in} = \mathbf{n}\cdot(\rho\mathbf{u})_{out}, \mathbf{n}\cdot(-\rho D_{ij}\nabla Y_i + \rho\mathbf{u}Y_i)_{in} = \mathbf{n}\cdot(-\rho D_{ij}\nabla Y_i + \rho\mathbf{u}Y_i)_{out}$
$\partial\Omega_{h_2}$	$\mathbf{n}\cdot(\rho\mathbf{u})_{in} = \mathbf{n}\cdot(\rho\mathbf{u})_{out}, \mathbf{n}\cdot(-\rho D_{ij}\nabla Y_i + \rho\mathbf{u}Y_i)_{in} = \mathbf{n}\cdot(-\rho D_{ij}\nabla Y_i + \rho\mathbf{u}Y_i)_{out}$
$\partial\Omega_{h_3}$	$\mathbf{n}\cdot(\rho\mathbf{u})_{in} = \mathbf{n}\cdot(\rho\mathbf{u})_{out}, \mathbf{n}\cdot(-\rho D^{eff}_{DG_{i,j}}\nabla Y_i + \rho\mathbf{u}Y_i)_{in} = \mathbf{n}\cdot(-\rho D^{eff}_{DG_{i,j}}\nabla Y_i + \rho\mathbf{u}Y_i)_{out}$
$\partial\Omega_{h_4}$	$\mathbf{n}\cdot(\rho\mathbf{u})_{in} = \mathbf{n}\cdot(\rho\mathbf{u})_{out}, \mathbf{n}\cdot(-\rho D^{eff}_{DG_{i,j}}\nabla Y_i + \rho\mathbf{u}Y_i)_{in} = \mathbf{n}\cdot(-\rho D^{eff}_{DG_{i,j}}\nabla Y_i + \rho\mathbf{u}Y_i)_{out}$
$\partial\Omega_{h_5}$	$\mathbf{n}\cdot\mathbf{u} = 0, \mathbf{n}\cdot(-\rho D_{ij}\nabla Y_i + \rho\mathbf{u}Y_i) = 0$

Table 4.6: Boundary conditions

dependent on the permeability of porous electrodes, that in turn depends upon porosity and tortuosity of the porous media. The pressure drop behind the cell is responsible for further acceleration of the fluid downstream.

Figure 4.9 shows the hydrogen concentration distribution in the gas chamber. As can be seen, the hydrogen concentration remains constant until the gaseous mixture reaches the anode electrode surface as there is no electrochemical reaction upstream in front of the anode electrode. As soon as the flow reaches the anode catalyst layer, it starts reacting electrochemically (according to equation (4.1)).

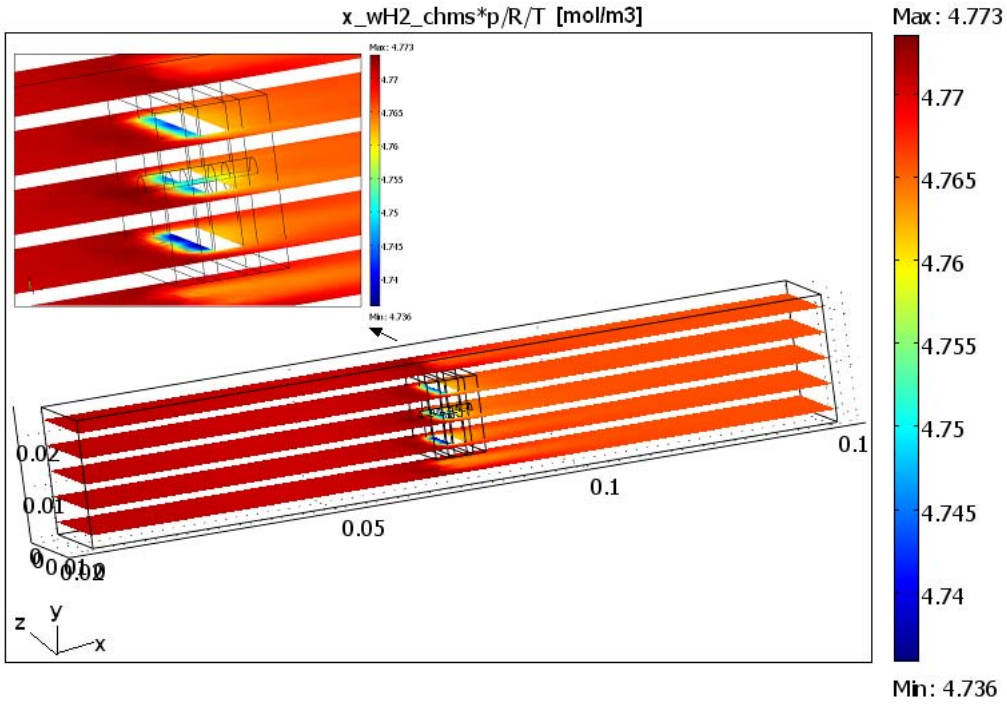

Figure 4.9: Hydrogen concentration in gas chamber

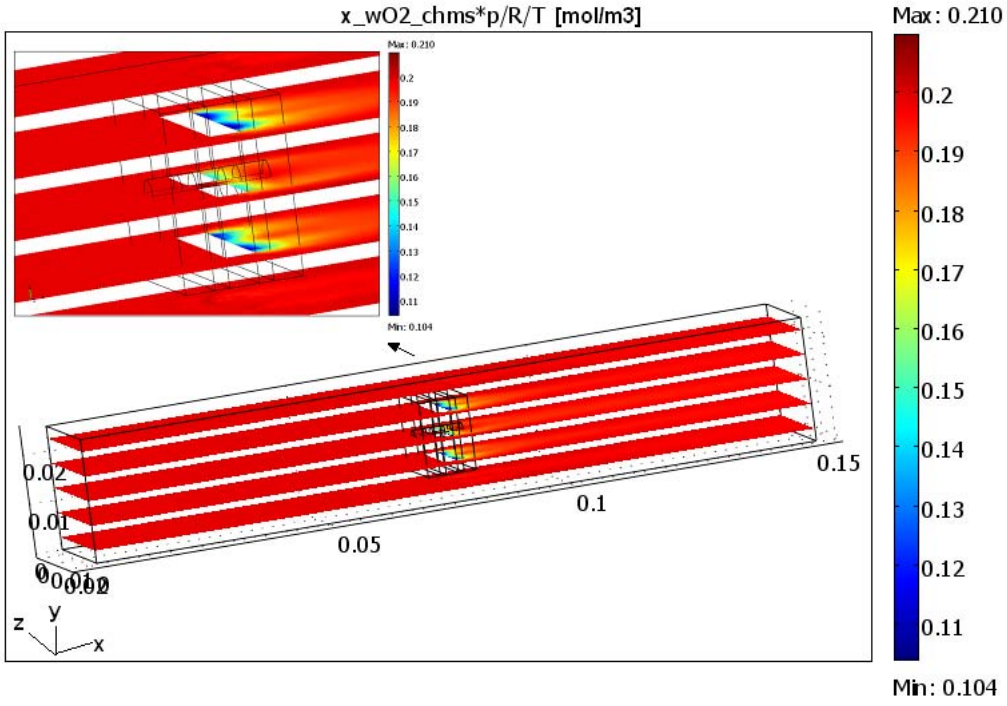

Figure 4.10: Oxygen concentration in gas chamber

Since concentration is pressure dependent, one observes a slight increase near the cell front edges due to the increase of pressure, as discussed before. Just behind the cell, hydrogen concentration is low but quickly mixes with diverted (non-reacted) hydrogen coming through the cell edges via convection and diffusion. Just after approximately, $0.02\ m$ from the cathode last edge, hydrogen concentration attains another lower constant value of $4.765\ mole \cdot m^{-3}$. Again, this parameter is of interest when one plans to put several cells downstream. Also, it is important to note that the hydrogen available for the downstream cell may be depleted partly due to consumption at the anode electrode of the upstream cell and partly due to mixing with the by-product water vapor. Therefore, additional supply of hydrogen is suggested for uniform cell performance in a stack of several cells. Alternatively, one could use a distributed feed for all cells in a stack e.g. in a parallel cell arrangement rather than serial.

Figure 4.10 shows the oxygen concentration in the gas chamber where it can be seen that the oxygen due to electrochemical reaction (according to equation (4.2)) starts consuming in the cathode catalyst layer. The large concentration gradient is along the cell due to electrochemical reduction of oxygen at the cathode catalyst layer. Just behind the cell a lower oxygen concentration is observed and attains another lower constant value ($0.195\ mole \cdot m^{-3}$) at approximately $0.038\ m$ from cathode last edge. This distance is approximately double what is needed for hydrogen mixing and the reason could be that hydrogen has a high diffusion coefficient as compared to oxygen, therefore hydrogen diffuses quicker than oxygen. Also, hydrogen is the lightest molecule and the same momentum can give a high velocity to a light molecule as compared to heavy molecule like oxygen. Therefore mixing by convection/diffusion for hydrogen is quicker than for oxygen.

Figure 4.11 represents water vapor concentration due to the electrochemical reaction (according to equation (4.1)), water is produced at the anode catalyst layer and this effect is clearly observed near the anode electrode surface. The by-product water mixes with hydrogen and oxygen, diluting the gaseous mixture downstream.

In Figure 4.12, the legend description corresponding to Figures 4.13-4.20 is shown. As can be seen the variables plotted in Figures 4.13-4.20 are along the channel length with varying values of the y coordinate. The z coordinate is kept fixed in the center of the PEN in all these figures.

Figure 4.13 shows the velocity field plot in the gas chamber. Blue and black curves are almost on top of each other showing the same trends in velocity profile, these lines are plotted at a distance of $2\ mm$ below and above the cell in y-direction. Initially the velocity is constant until it reaches the cell.

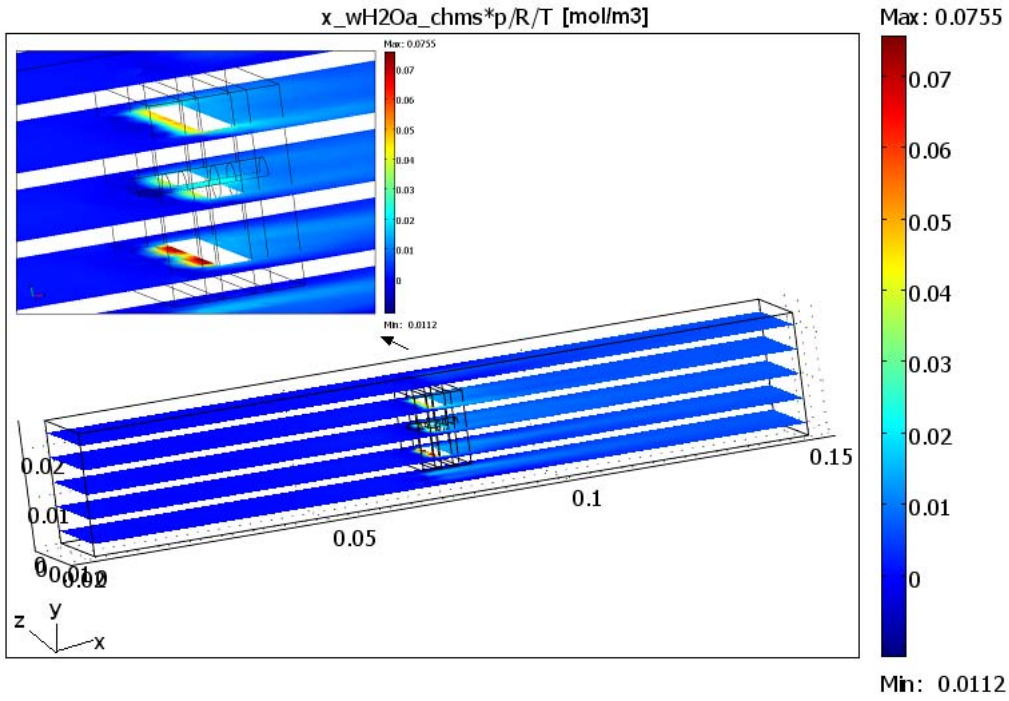

Figure 4.11: Water vapor concentration in gas chamber

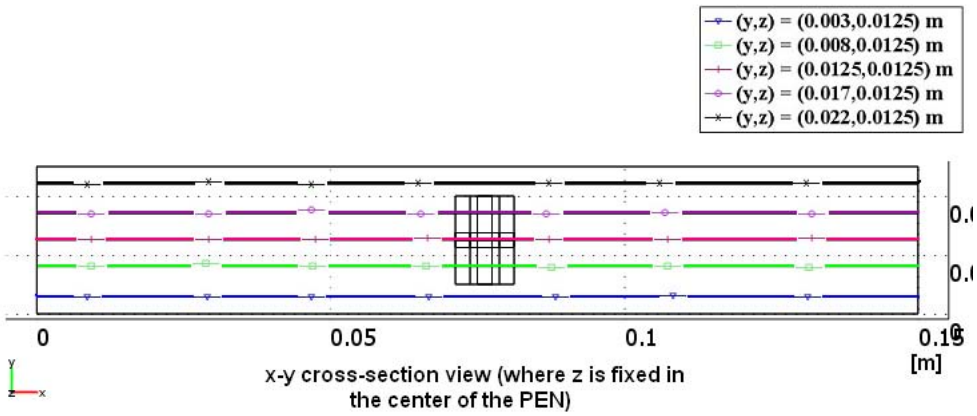

Figure 4.12: Description of the legend used in Figures 4.13-4.20

Then, due to diversion of the flow (due to the presence of the cell) the velocity starts increasing (up to approximately $0.24\ ms^{-1}$) and then settles behind the cell at a value of approximately $0.0996\ ms^{-1}$. Lavender and light green curves show the velocity plot inside the cell at a distance of $3\ mm$ from top and bottom edge of the cell. Due to be on same distances they are also on top of each other and show that the velocity remains constant until it reaches the cell. In close vicinity of the cell, the flow feels the presence of the obstacle (the cell), therefore the velocity decreases and becomes almost zero in the PEN. This suggests that the flow in the PEN is no more convective but only diffusive. Just behind the cell the flow again accelerates and attains a velocity of approximately $0.18\ ms^{-1}$. The red curve shows the center line velocity and as can be seen from the plot, the center line velocity has the maximum value just before and after the cell. The center line velocity also feels the effect of the obstacle and therefore drops to a value of $0.025\ ms^{-1}$ at the anode electrode surface and then due to the presence of hole in the center of the PEN, the flow sees a free flow (accelerates again). Due to the radial convection/diffusion in the hole domain the velocity fluctuates for a while and then the flow comes out of the hole with a greater (nozzle like) push. Finally it re-gains its maximum center line velocity at a distance of approximately $0.03\ m$ from the cathode electrode.

Figure 4.14 shows the hydrogen mass fraction plot and it can be seen that the mass fraction remains constant until the reactants reach the cell, where the electrochemical reaction is taking place. A mass fraction drop (though very little due to high degree of dilution in the mixture) is observed in the cell (light green, lavender and red curves), precisely at the anode catalyst layer due to the consumption of hydrogen. Also, the hole is not a completely non-reactive domain and there is some consumption along radial direction in the hole. Only the electrolyte is impermeable and; although it is possibly hard to see in the plot the light green and lavender curves show a discontinuity of mass fraction in the electrolyte.

Figure 4.15 shows the oxygen mass fraction in the gas chamber and as discussed before for hydrogen consumption, the same trend is seen for oxygen consumption but this time in the cathode catalyst layer. Also, a discontinuity of the curves (light green and especially of lavender) is clearly seen at the electrolyte due to its impermeable nature.

Figure 4.16 shows the water vapor mass fraction and it can be seen that due to the water generated at the anode catalyst layer, a sharp increase in the mass fraction is observed. Clearly, light green and lavender curves show a discontinuity as discussed before.

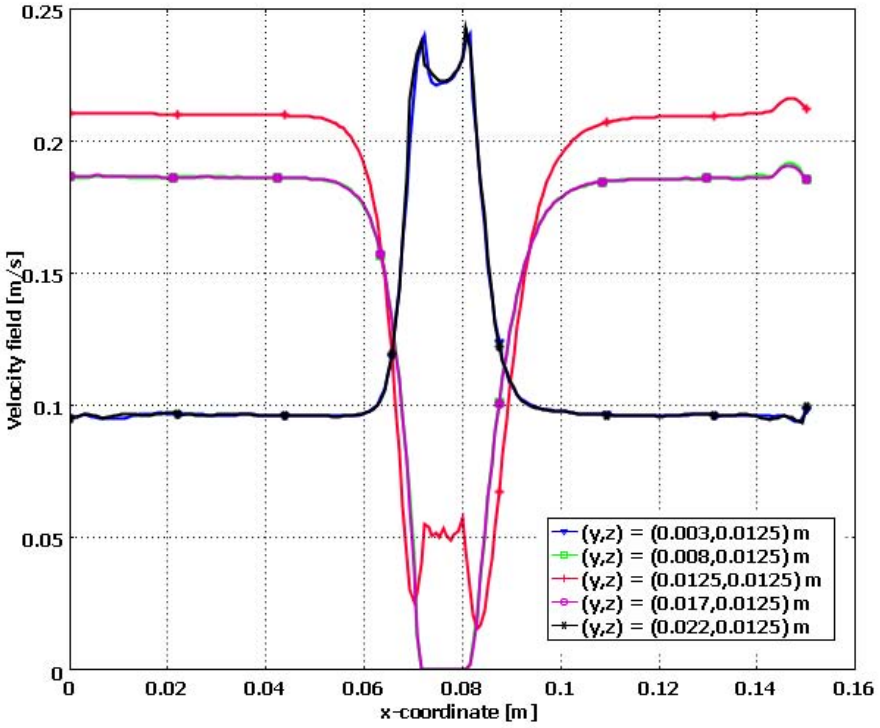

Figure 4.13: Velocity along the channel length at different y-coordinate for $\epsilon = 0.3$

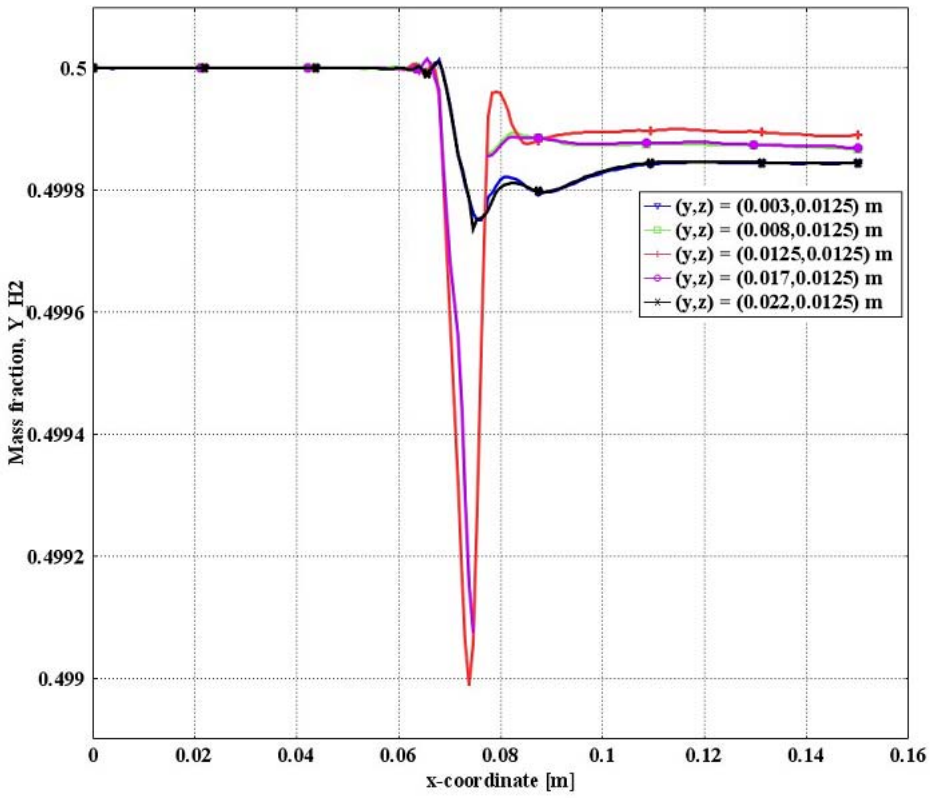

Figure 4.14: Hydrogen mass fraction along the channel length at different y-coordinate for $\epsilon = 0.3$

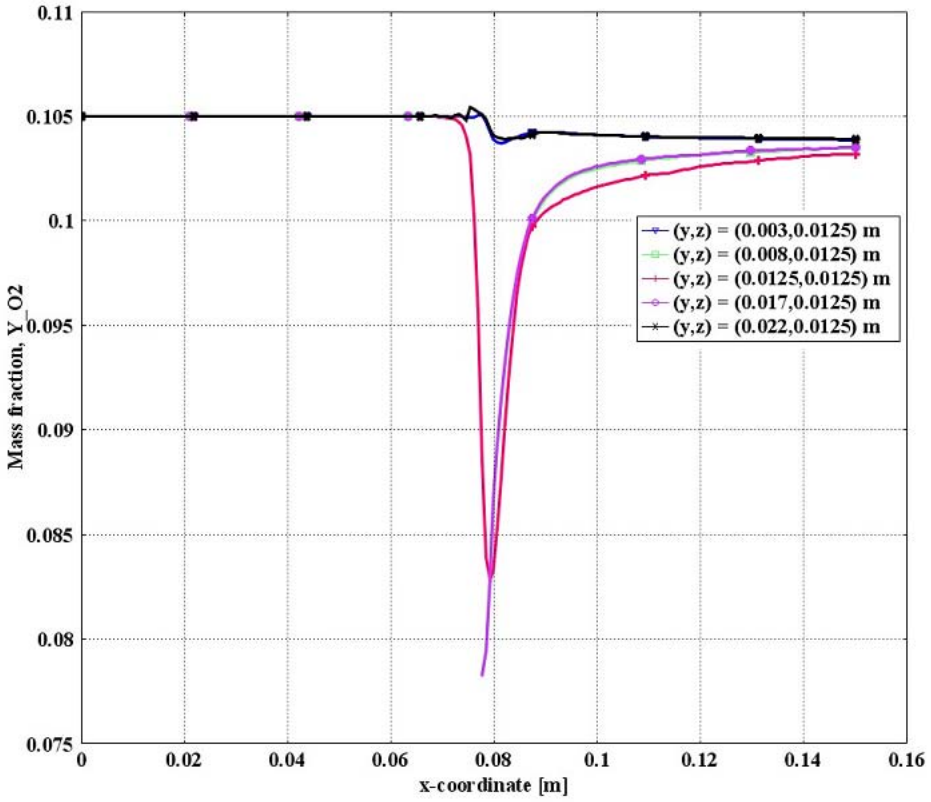

Figure 4.15: Oxygen mass fraction along the channel length at different y-coordinate for $\epsilon = 0.3$

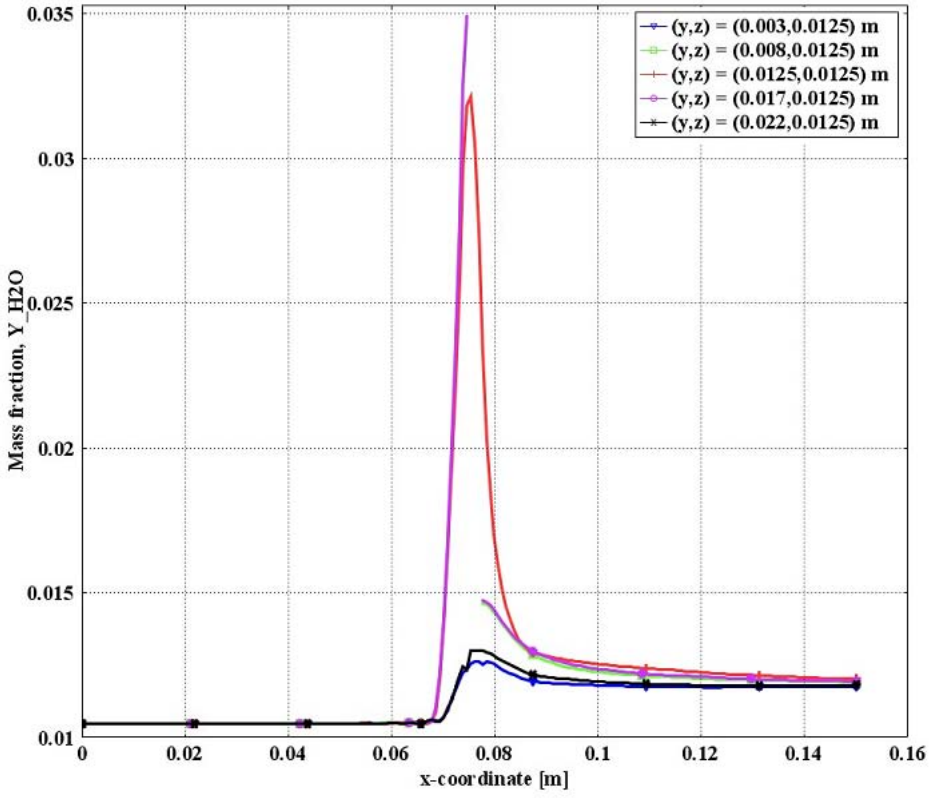

Figure 4.16: Water mass fraction along the channel length at different y-coordinate for $\epsilon = 0.3$

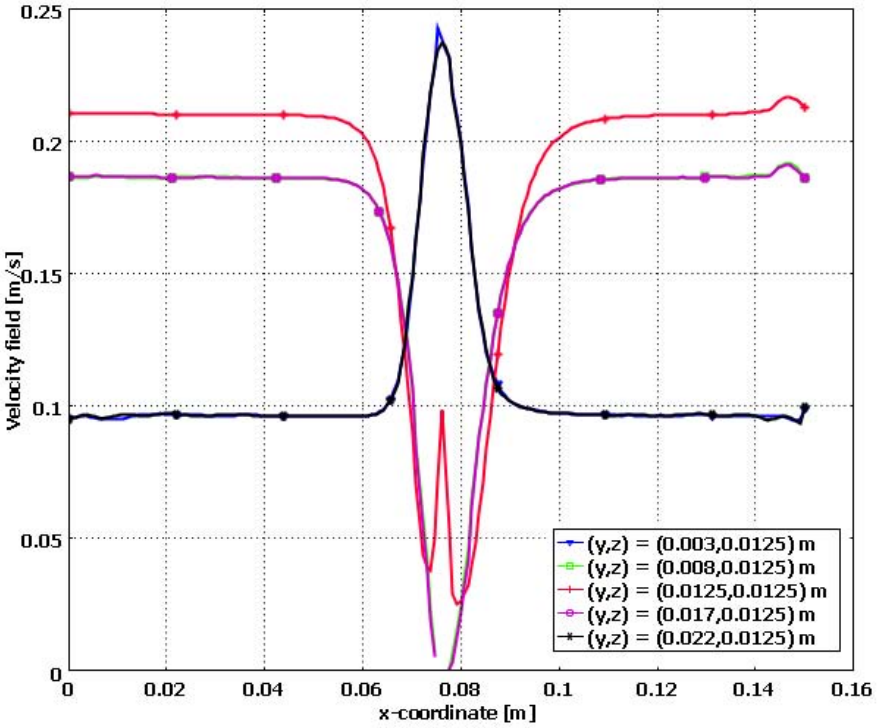

Figure 4.17: Velocity along the channel length at different y-coordinate for $\epsilon = 0.4$

Figures 4.17-4.20 are the repetition of simulations with an increased value of porosity ($\epsilon = 0.4$). In contrast to Figure 4.13, there is some convective flow (Figure 4.17) in the cell element due to ease of the Darcy flow through the porous media. Increase in porosity reduces the resistance in the fluid flow and thus both convective/diffusive fluxes exist in the porous electrodes. Although, it looks like that the increase in porosity will have a better effect on hydrodynamics of the flow but Figures 4.18-4.19 show a less utilization of reactants (compared with Figures 4.14 and 4.15). This effect suggests that increase in porosity will reduce the available active area for the electrochemical reaction, possibly due to more open pores rather than connected. Figure 4.20 is a plot of the water vapor distribution and shows a reduced value of water produced as compared with Figure 4.16. Therefore, increasing the porosity could have an effect on electrochemical performance of the cell.

Figure 4.21 and 4.22 shows the calculated I-V and I-P characteristics curves at 500°C for hydrogen/oxygen/nitrogen mixture (with input parameters given in Table 4.4), respectively. As can be seen the maximum power density obtained is 218.5 Wm^{-2}(i.e. 21.85 $mWcm^{-2}$). The observed low current is due to the low operating temperature and dilution effect. Furthermore, the power density is quite low as compared to the dual-chamber configuration, this is because of extremely low fuel utilization due to the presence of large amount of inert gas in the mixture.

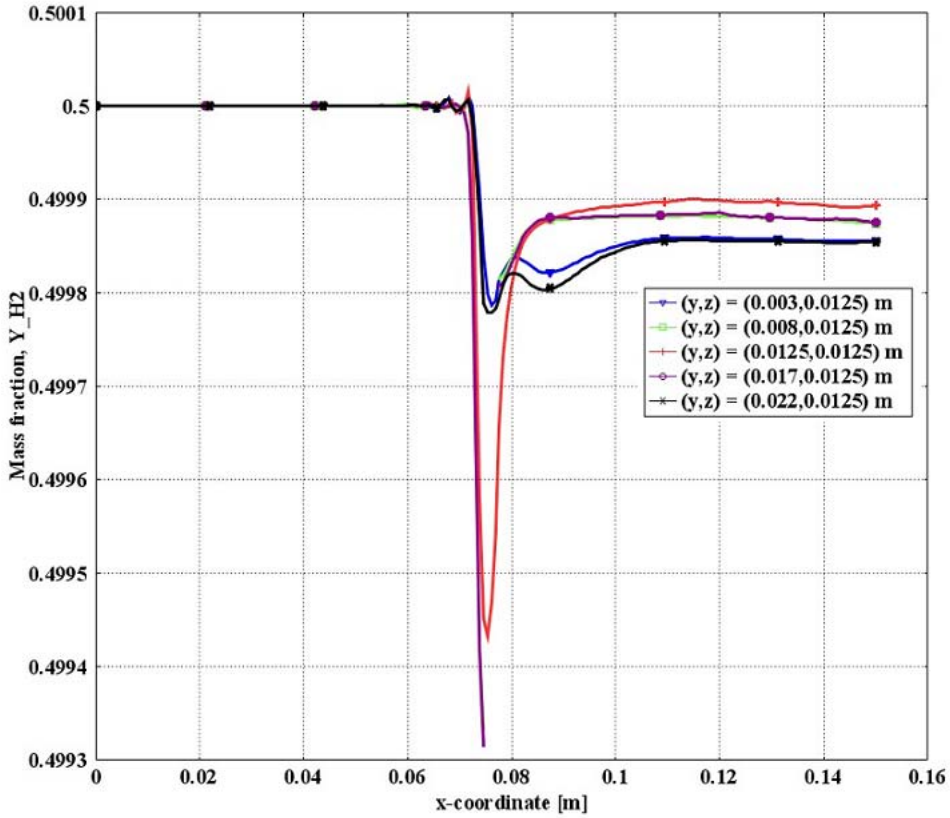

Figure 4.18: Hydrogen mass fraction along the channel length at different y-coordinate for $\epsilon = 0.4$

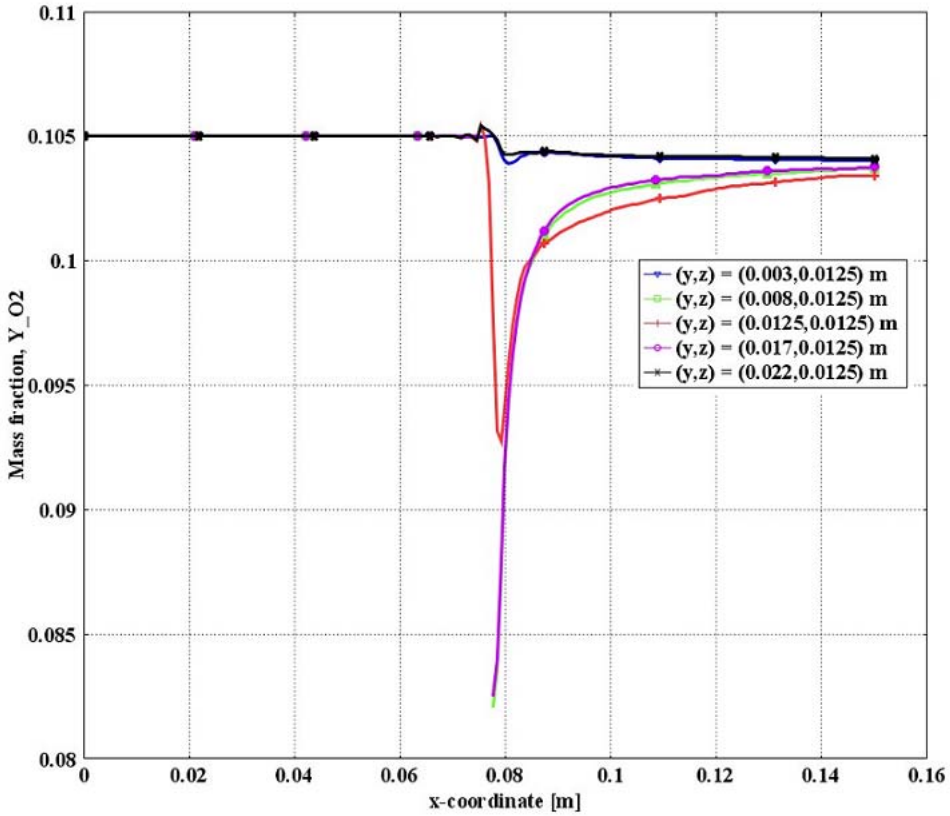

Figure 4.19: Oxygen mass fraction along the channel length at different y-coordinate for $\epsilon = 0.4$

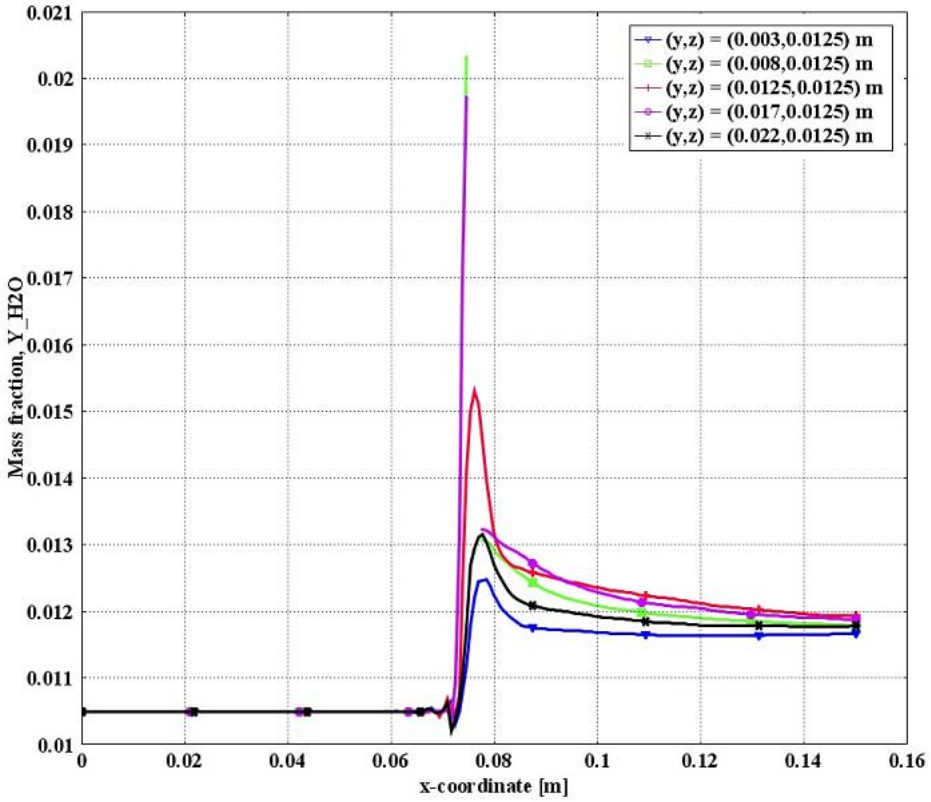

Figure 4.20: Water mass fraction along the channel length at different y-coordinate for $\epsilon = 0.4$

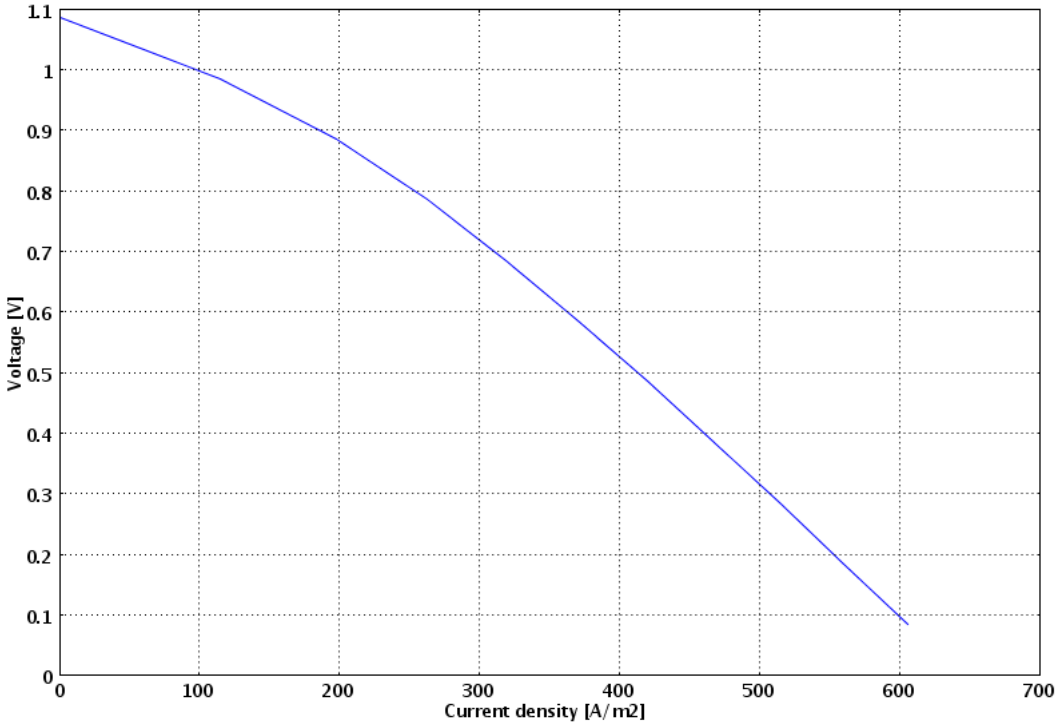

Figure 4.21: I-V characteristic curve for SC-SOFC

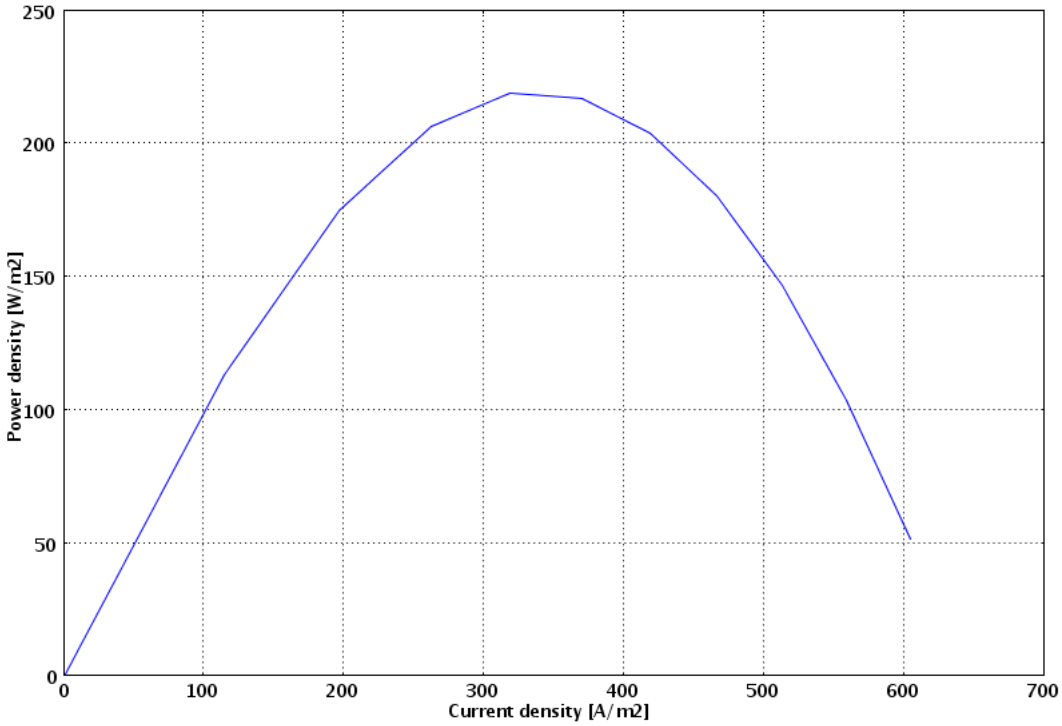

Figure 4.22: I-P characteristic curve for SC-SOFC

4.6 Conclusions

A three dimensional numerical model of a single-chamber solid oxide fuel cell was developed. The model accounts for all transport phenomena and cell potential. Results show that varying one parameter (associated with the hydrodynamics) can affect another parameter (associated with the electrochemical performance). Increase of porosity in the catalyst layers can reduce the available active area for electrochemical reaction, conversely, fine pores can cause a large pressure drop and subsequently lead to a hydrodynamic problem. The best design could be to stay with fine porosity of the electrodes and optimize the hydrodynamic problem by reducing the tortuous path of the flow inside the porous electrodes. This could be done by varying the permeability of the porous electrodes with a fixed fine porosity. Instead of using dense solid (non-porous) electrolyte, use of a fully porous cell (including the porosity of the electrolyte) can give ease in flow with reduced manufacturing cost. Another idea could be instead of having holes inside the PEN element, the holes can be provided at the circumference/edges of the interconnect (or separator layer). This would not reduce the active area but still provides better hydrodynamics. Distributed feed to a number of cells placed in a stack can give a uniform reactant utilization in each cell, therefore parallel feed with branches at each cell could give

a better performance both hydrodynamically and electrochemically.

This model did not take into account heat generation due to electrochemical reaction and this could further affect the electrochemical performance of the cell. Placing the anode first exposed to the feed will lead to partial oxidation reaction when hydrocarbons are used as a fuel. The heat generated will contribute to convection, thus the gaseous mixture can be depleted (due to water production), via natural convection, prior to reaching the cathode. The next part of the ongoing research work is to implement energy equation.

CHAPTER 5

MODELLING OF PLANAR SC-SOFCS[2]

5.1 Introduction

In this chapter modelling of conventional planar SOFC design has been investigated under single-chamber conditions. The main objective of this study is to analyze the gas flow and electrochemical effects in an SC-SOFC. The cell performance is studied with respect to its position i.e. parallel or perpendicular placement with respect to the flow. The effects of flow rate, porosity and cell position (i.e. parallel, perpendicular with anode or cathode first exposed to the gas stream) have also been examined. The main emphasis is to propose a geometrical position which can provide uniform electrochemical performance while diminishing hydrodynamic issues related to the pressure drop as discussed in Chapter-4.

5.2 Model Development

The model developed in Chapter-4 has been applied to a conventional-planar geometry (Figure 1.6) considered here. The domains/boundaries considered are shown in Figures 5.1 and 5.2. The geometrical dimensions are given in Table 5.1. The model assumptions and the input parameters remain same as given in Chapter-4.

5.3 Computational Domain and Boundary Conditions

The governing equations and the boundary conditions are summarized in Table 5.2-5.3.

---

[2] The results described in this chapter have been published in:

• N. Akhtar et al., ECS Transactions, 13 (28) 107-124 (2008).

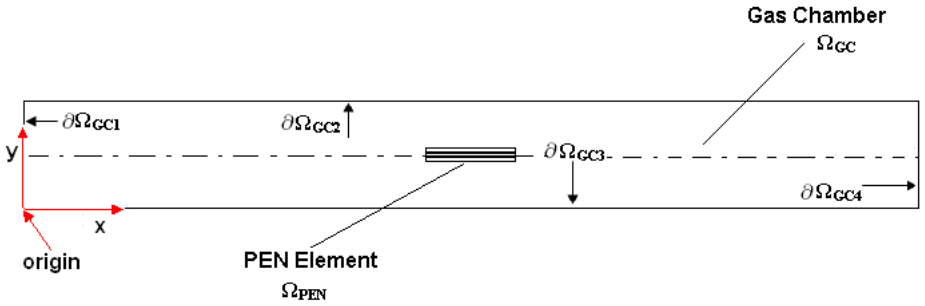

Figure 5.1: Gas chamber domain and boundaries

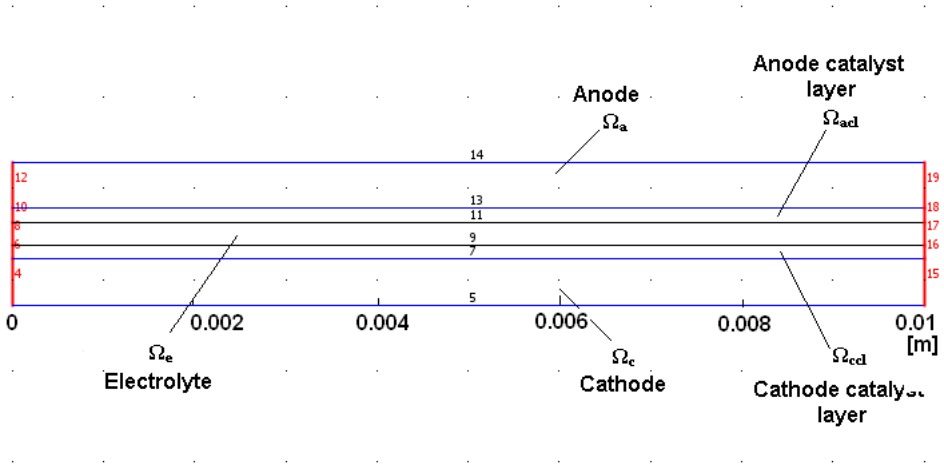

Figure 5.2: PEN element domains and boundaries

Dimensions	Values (mm)
Chamber length	100
Chamber height	12
Length of PEN element	10
Anode electrode thickness	190×10^{-3}
Cathode electrode thickness	40×10^{-3}
Electrolyte thickness	15×10^{-3}
Anode catalyst layer thickness	10×10^{-3}
Cathode catalyst layer thickness	10×10^{-3}

Table 5.1: Geometrical dimensions

5.4 Results and Discussion

The solution methodology as discussed in Chapter-4 was employed. The total computing time for all stages (with 39, 520 degrees of freedom) was approximately 1.8 minutes. The computational mesh is shown in Figure 5.3. The values of the electrochemical/hydrodynamic transport parameters for operating conditions were taken from Table 4.4. The results show simulations for three different setups as shown earlier in Figure 1.6 (a-c). Figure 1.6 (a) is the parallel configuration, Figure 1.6 (b)

Domain	Equation solved
Ω_{GC}	$\nabla \cdot (\rho \mathbf{u}) = 0$ $\rho(\mathbf{u} \cdot \nabla)\mathbf{u} = -\nabla p + \mu \nabla^2 \mathbf{u} + \frac{1}{3}\mu \nabla(\nabla \cdot \mathbf{u})$ $\nabla \cdot (\rho \mathbf{u} Y_i) = -\nabla \cdot \mathbf{j}_i$
Ω_a	$\nabla \cdot (\rho \mathbf{u}) = 0$ $\frac{\mu}{\kappa}\mathbf{u} = -\nabla p + \mu \nabla^2 \mathbf{u} + \frac{1}{3}\mu \nabla(\nabla \cdot \mathbf{u})$ $\nabla \cdot (\rho \mathbf{u} Y_i) = -\nabla \cdot \mathbf{j}_i$ $\nabla \cdot (-\sigma_s \nabla \phi_s) = 0$
Ω_c	$\nabla \cdot (\rho \mathbf{u}) = 0$ $\frac{\mu}{\kappa}\mathbf{u} = -\nabla p + \mu \nabla^2 \mathbf{u} + \frac{1}{3}\mu \nabla(\nabla \cdot \mathbf{u})$ $\nabla \cdot (\rho \mathbf{u} Y_i) = -\nabla \cdot \mathbf{j}_i$ $\nabla \cdot (-\sigma_s \nabla \phi_s) = 0$
Ω_{acl}	$\nabla \cdot (\rho \mathbf{u}) = S_m, S_m = S_{H2}, S_{H2O} = -\frac{M_{H_2}}{2F} i_a, \frac{M_{H_2O}}{2F} i_a$ $\frac{\mu}{\kappa}\mathbf{u} = -\nabla p + \mu \nabla^2 \mathbf{u} + \frac{1}{3}\mu \nabla(\nabla \cdot \mathbf{u})$ $\nabla \cdot (\rho \mathbf{u} Y_i) = -\nabla \cdot \mathbf{j}_i + S_i, S_i = S_{H2}, S_{H2O} = -\frac{M_{H_2}}{2F} i_a, \frac{M_{H_2O}}{2F} i_a$ $\nabla \cdot (-\sigma_s^{eff} \nabla \phi_s) = A_s S_{\phi_s}$ $\nabla \cdot (-\sigma_e^{eff} \nabla \phi_e) = A_s S_{\phi_e}$
Ω_{ccl}	$\nabla \cdot (\rho \mathbf{u}) = S_m, S_m = S_{O2} = -\frac{M_{O_2}}{4F} i_c$ $\frac{\mu}{\kappa}\mathbf{u} = -\nabla p + \mu \nabla^2 \mathbf{u} + \frac{1}{3}\mu \nabla(\nabla \cdot \mathbf{u})$ $\nabla \cdot (\rho \mathbf{u} Y_i) = -\nabla \cdot \mathbf{j}_i + S_i, S_i = S_{O2} = -\frac{M_{O_2}}{4F} i_c$ $\nabla \cdot (-\sigma_s^{eff} \nabla \phi_s) = A_s S_{\phi_s}$ $\nabla \cdot (-\sigma_e^{eff} \nabla \phi_e) = A_s S_{\phi_e}$
Ω_e	$\nabla \cdot (-\sigma_e \nabla \phi_e) = 0$

Table 5.2: Computational domains and governing equations

Surface Boundary	Boundary Condition
$\partial\Omega_{GC_1}$	$\mathbf{u} = \mathbf{u_{in}}, Y_i = Y_{i_{in}}$
$\partial\Omega_{GC_2}$	$u = v = w = 0, \mathbf{n} \cdot (-\rho D_{ij} \nabla Y_i + \rho \mathbf{u} Y_i) = 0$
$\partial\Omega_{GC_3}$	$u = v = w = 0, \mathbf{n} \cdot (-\rho D_{ij} \nabla Y_i + \rho \mathbf{u} Y_i) = 0$
$\partial\Omega_{GC_4}$	$p = p_o, \mathbf{n} \cdot (-\rho D_{ij} \nabla Y_i) = 0$
$\partial\Omega_4$	$\mathbf{n}\cdot(\rho\mathbf{u})_{in} = \mathbf{n}\cdot(\rho\mathbf{u})_{out}, \mathbf{n}\cdot(-\rho D_{ij}\nabla Y_i + \rho\mathbf{u}Y_i)_{in} = \mathbf{n}\cdot(-\rho D_{ij}\nabla Y_i + \rho\mathbf{u}Y_i)_{out}, \mathbf{n}\cdot(-\sigma_s\nabla\phi_s) = 0$
$\partial\Omega_6$	$\mathbf{n}\cdot(\rho\mathbf{u})_{in} = \mathbf{n}\cdot(\rho\mathbf{u})_{out}, \mathbf{n}\cdot(-\rho D_{ij}\nabla Y_i + \rho\mathbf{u}Y_i)_{in} = \mathbf{n}\cdot(-\rho D_{ij}\nabla Y_i + \rho\mathbf{u}Y_i)_{out}, \mathbf{n}\cdot(-\sigma_s^{eff}\nabla\phi_s) = 0, \mathbf{n}\cdot(-\sigma_e^{eff}\nabla\phi_e) = 0$
$\partial\Omega_8$	$\mathbf{n}\cdot\mathbf{u} = 0, \mathbf{n}\cdot(-\rho D_{ij}\nabla Y_i + \rho\mathbf{u}Y_i) = 0, \mathbf{n}\cdot(-\sigma_e\nabla\phi_e) = 0$
$\partial\Omega_{10}$	$\mathbf{n}\cdot(\rho\mathbf{u})_{in} = \mathbf{n}\cdot(\rho\mathbf{u})_{out}, \mathbf{n}\cdot(-\rho D_{ij}\nabla Y_i + \rho\mathbf{u}Y_i)_{in} = \mathbf{n}\cdot(-\rho D_{ij}\nabla Y_i + \rho\mathbf{u}Y_i)_{out}, \mathbf{n}\cdot(-\sigma_s^{eff}\nabla\phi_s) = 0, \mathbf{n}\cdot(-\sigma_e^{eff}\nabla\phi_e) = 0$
$\partial\Omega_{12}$	$\mathbf{n}\cdot(\rho\mathbf{u})_{in} = \mathbf{n}\cdot(\rho\mathbf{u})_{out}, \mathbf{n}\cdot(-\rho D_{ij}\nabla Y_i + \rho\mathbf{u}Y_i)_{in} = \mathbf{n}\cdot(-\rho D_{ij}\nabla Y_i + \rho\mathbf{u}Y_i)_{out}, \mathbf{n}\cdot(-\sigma_s\nabla\phi_s) = 0$
$\partial\Omega_{15}$	$\mathbf{n}\cdot(\rho\mathbf{u})_{in} = \mathbf{n}\cdot(\rho\mathbf{u})_{out}, \mathbf{n}\cdot(-\rho D_{ij}\nabla Y_i + \rho\mathbf{u}Y_i)_{in} = \mathbf{n}\cdot(-\rho D_{ij}\nabla Y_i + \rho\mathbf{u}Y_i)_{out}, \mathbf{n}\cdot(-\sigma_s\nabla\phi_s) = 0$
$\partial\Omega_{16}$	$\mathbf{n}\cdot(\rho\mathbf{u})_{in} = \mathbf{n}\cdot(\rho\mathbf{u})_{out}, \mathbf{n}\cdot(-\rho D_{ij}\nabla Y_i + \rho\mathbf{u}Y_i)_{in} = \mathbf{n}\cdot(-\rho D_{ij}\nabla Y_i + \rho\mathbf{u}Y_i)_{out}, \mathbf{n}\cdot(-\sigma_s^{eff}\nabla\phi_s) = 0, \mathbf{n}\cdot(-\sigma_e^{eff}\nabla\phi_e) = 0$
$\partial\Omega_{17}$	$\mathbf{n}\cdot\mathbf{u} = 0, \mathbf{n}\cdot(-\rho D_{ij}\nabla Y_i + \rho\mathbf{u}Y_i) = 0, \mathbf{n}\cdot(-\sigma_e\nabla\phi_e) = 0$
$\partial\Omega_{18}$	$\mathbf{n}\cdot(\rho\mathbf{u})_{in} = \mathbf{n}\cdot(\rho\mathbf{u})_{out}, \mathbf{n}\cdot(-\rho D_{ij}\nabla Y_i + \rho\mathbf{u}Y_i)_{in} = \mathbf{n}\cdot(-\rho D_{ij}\nabla Y_i + \rho\mathbf{u}Y_i)_{out}, \mathbf{n}\cdot(-\sigma_s^{eff}\nabla\phi_s) = 0, \mathbf{n}\cdot(-\sigma_e^{eff}\nabla\phi_e) = 0$
$\partial\Omega_{19}$	$\mathbf{n}\cdot(\rho\mathbf{u})_{in} = \mathbf{n}\cdot(\rho\mathbf{u})_{out}, \mathbf{n}\cdot(-\rho D_{ij}\nabla Y_i + \rho\mathbf{u}Y_i)_{in} = \mathbf{n}\cdot(-\rho D_{ij}\nabla Y_i + \rho\mathbf{u}Y_i)_{out}, \mathbf{n}\cdot(-\sigma_s\nabla\phi_s) = 0$
$\partial\Omega_5$	$\mathbf{n}\cdot(\rho\mathbf{u})_{in} = \mathbf{n}\cdot(\rho\mathbf{u})_{out}, \mathbf{n}\cdot(-\rho D_{ij}\nabla Y_i + \rho\mathbf{u}Y_i)_{in} = \mathbf{n}\cdot(-\rho D_{ij}\nabla Y_i + \rho\mathbf{u}Y_i)_{out}, \phi_s = \phi_{sc}$
$\partial\Omega_7$	$\mathbf{n}\cdot(\rho\mathbf{u})_{in} = \mathbf{n}\cdot(\rho\mathbf{u})_{out}, \mathbf{n}\cdot(-\rho D^{eff}_{DG_{i,j}}\nabla Y_i + \rho\mathbf{u}Y_i)_{in} = \mathbf{n}\cdot(-\rho D^{eff}_{DG_{i,j}}\nabla Y_i + \rho\mathbf{u}Y_i)_{out}, \mathbf{n}\cdot(i_{c,in}) = \mathbf{n}\cdot(i_{c,out}), \mathbf{n}\cdot(-\sigma_e^{eff}\nabla\phi_e) = 0$
$\partial\Omega_9$	$\mathbf{n}\cdot\mathbf{u} = 0, \mathbf{n}\cdot(-\rho D^{eff}_{DG_{i,j}}\nabla Y_i + \rho\mathbf{u}Y_i) = 0, \mathbf{n}\cdot(-\sigma_s^{eff}\nabla\phi_s) = 0, \mathbf{n}\cdot(i_{c,in}) = \mathbf{n}\cdot(i_{c,out})$
$\partial\Omega_{11}$	$\mathbf{n}\cdot\mathbf{u} = 0, \mathbf{n}\cdot(-\rho D^{eff}_{DG_{i,j}}\nabla Y_i + \rho\mathbf{u}Y_i) = 0, \mathbf{n}\cdot(-\sigma_s^{eff}\nabla\phi_s) = 0, \mathbf{n}\cdot(i_{a,in}) = \mathbf{n}\cdot(i_{a,out})$
$\partial\Omega_{13}$	$\mathbf{n}\cdot(\rho\mathbf{u})_{in} = \mathbf{n}\cdot(\rho\mathbf{u})_{out}, \mathbf{n}\cdot(-\rho D^{eff}_{DG_{i,j}}\nabla Y_i + \rho\mathbf{u}Y_i)_{in} = \mathbf{n}\cdot(-\rho D^{eff}_{DG_{i,j}}\nabla Y_i + \rho\mathbf{u}Y_i)_{out}, \mathbf{n}\cdot(i_{a,in}) = \mathbf{n}\cdot(i_{a,out}), \mathbf{n}\cdot(-\sigma_e^{eff}\nabla\phi_e) = 0$
$\partial\Omega_{14}$	$\mathbf{n}\cdot(\rho\mathbf{u})_{in} = \mathbf{n}\cdot(\rho\mathbf{u})_{out}, \mathbf{n}\cdot(-\rho D_{ij}\nabla Y_i + \rho\mathbf{u}Y_i)_{in} = \mathbf{n}\cdot(-\rho D_{ij}\nabla Y_i + \rho\mathbf{u}Y_i)_{out}, \phi_s = \phi_{sa}$

Table 5.3: Boundary conditions

is the anode first perpendicular and Figure 1.6 (c) is the cathode first perpendicular configuration. We name them as setup A, B and C in our simulations, respectively. The results shown in Figures 5.4-5.6 are for setup (A) and in Figures 5.7-5.9 for setup (B). Figure 5.10 compares setup (B) and (C) and Figure 5.11 shows the flow in case of parallel and perpendicular setup. In Figure 5.12, the

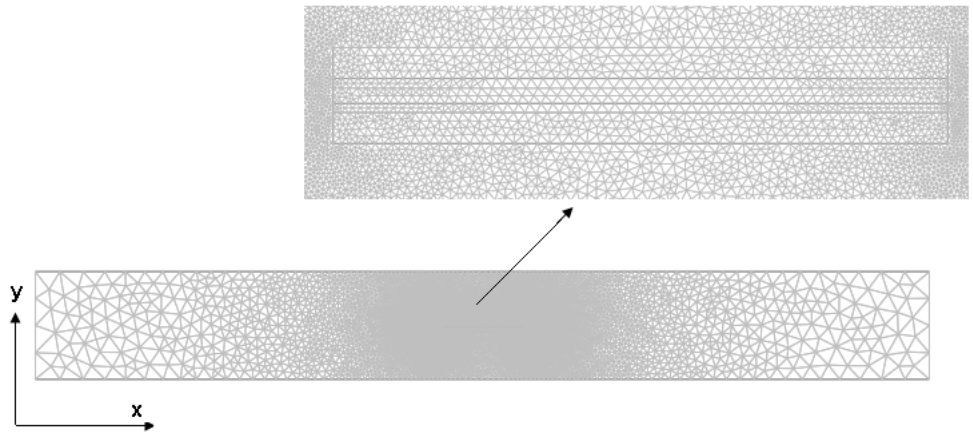

Figure 5.3: The computational mesh (7,061 elements)

performance characteristics for these three setups have been compared. The abbreviate CLL is used for catalyst layers and all variables are plotted along the cell length.

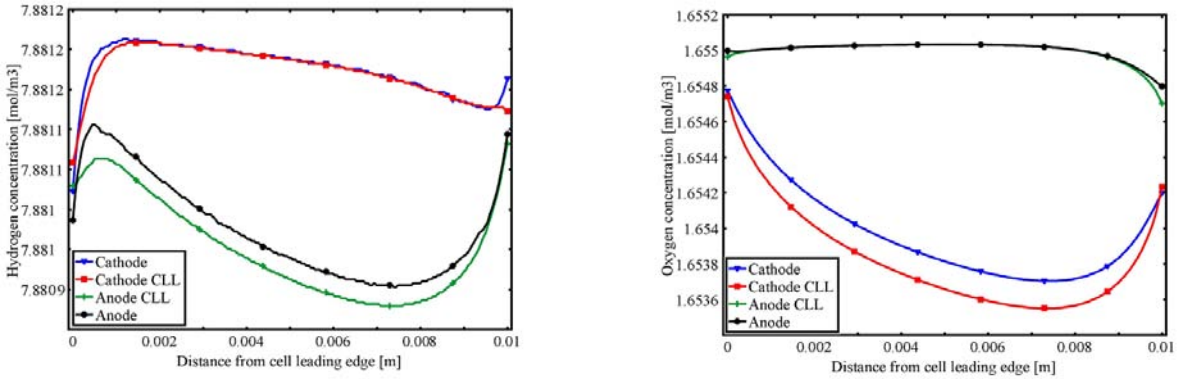

(a) (b)

Figure 5.4: Hydrogen concentration (a) and oxygen concentration (b) for setup (A).

Figure 5.4 (a) shows the hydrogen concentration in the cell. The concentration drop is observed (although fairly low) in the anode catalyst layer (green curve) where the hydrogen is consumed. Figure 5.4 (b) shows the oxygen concentration and the oxygen concentration drop (as expected) is observed in the cathode catalyst layer (red curve). It is important to note that the concentration drops shown are very low showing that the current produced will be very low due to very small area of the cell. However, if the design is scaled-up then it is clear that in parallel type setup, the concentration distribution will be non-uniform over the cell length and the location of maximum concentration drop depends upon the inlet flow rate (or inlet velocity). A high inlet velocity will give a greater push to the fluid, therefore the fluid has less time available for an electrochemical reaction to occur. This effect is

responsible for determining uniformity in concentration drop along the cell's length.

In Figure 5.5 (a) hydrogen concentration is shown with varying inlet velocity of the gas mixture. At low velocity (e.g. $0.1\ ms^{-1}$, blue curve) hydrogen concentration drops soon after entering the anode catalyst layer. However, as we increase the inlet velocity (e.g. 1.0 or $10\ ms^{-1}$, red and green curves, respectively), there is a jump in concentration near the cell inlet (which is not observed in oxygen concentration, Figure 5.5 (b)). The reason for this increase in hydrogen concentration near the cell inlet is the large acceleration of hydrogen (the lightest) molecule in backward direction after hitting the cell (particularly the electrolyte which is impermeable). The deflected hydrogen (through the front edge of the cell) finds the nearest possible open passage at the anode upper surface from where it tries to permeate into the cell. Due to this deflection at the cell edges we observe high diffusive/convective fluxes near the cell front edges. Figure 5.5 (b) shows oxygen concentration in the cathode catalyst layer. It can be seen that higher velocities (although enhance mass transport by forced convection) lead to low concentration gradient (red and green curves). This phenomena is well explained by Riess et al. [70] and according to him the short residence time (due to high inlet velocities) for an electrochemical reaction is responsible for this behaviour.

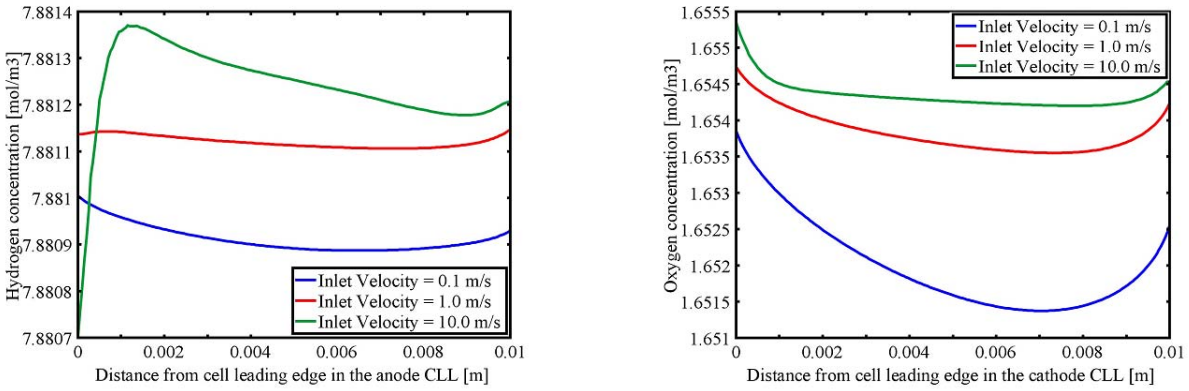

(a) (b)

Figure 5.5: Effect of inlet velocity on hydrogen concentration (a) and oxygen concentration (b) for setup (A).

Figure 5.6 (a) shows velocity profile in the cell with varying porosity of the electrodes. High velocities are observed in an electrode when this electrode has large porosity (green curve). In contrast, low velocities are visible in an electrode with low porosity (blue curve). This behavior is obviously

as expected because increasing the porosity provides more voids (free passage) which offer less resistance in fluid's travel.

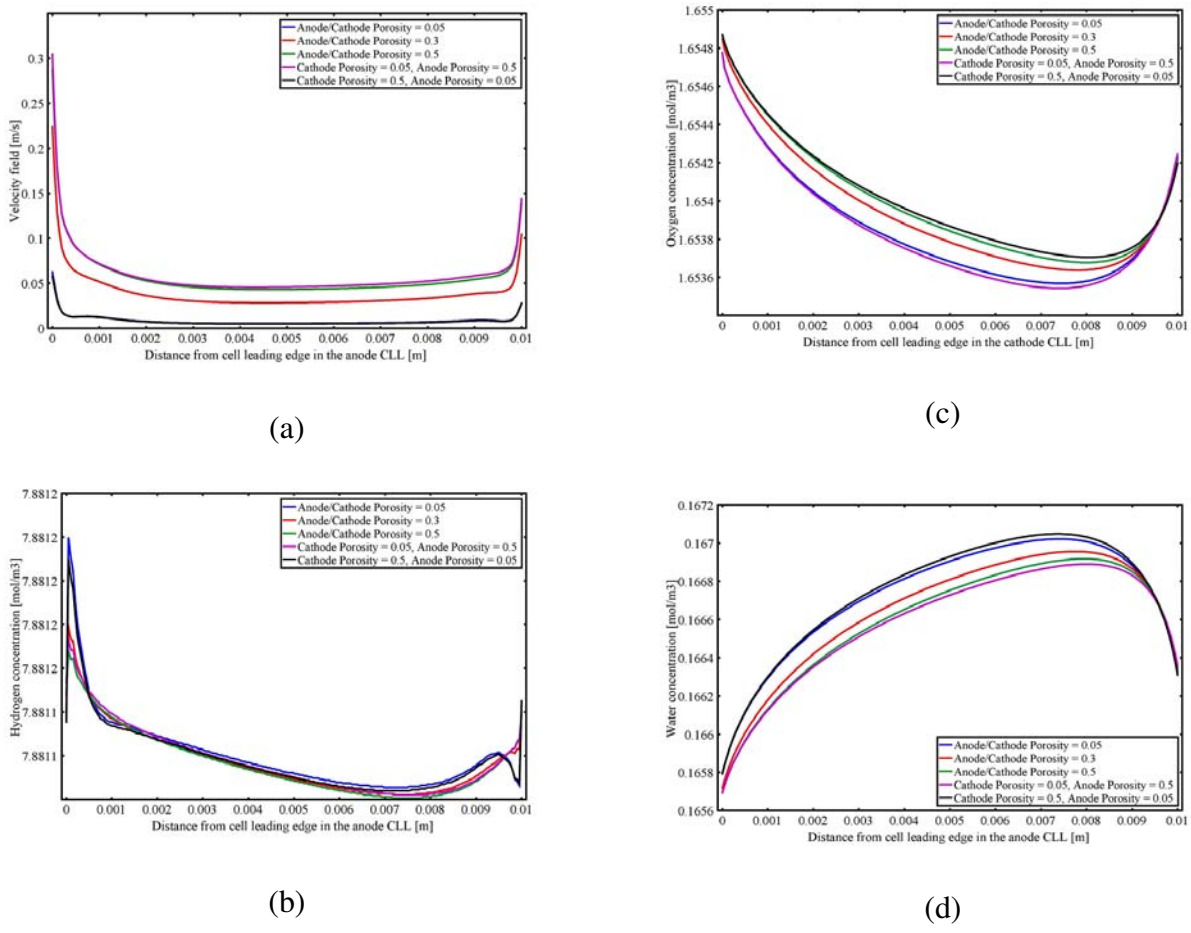

Figure 5.6: Effect of electrode porosity on velocity field (a), hydrogen concentration (b), oxygen concentration (c) and water vapor concentration (d) for setup (A).

Figures 5.6 (b), (c) and (d) show hydrogen, oxygen and water concentration, respectively. The concentration drop (for hydrogen and oxygen) is observed when both electrodes have the lowest porosity. Low porosity provides more active surface and also increases residence time, both of which contributes to improved reactant utilization. Furthermore, a relatively large amount of water production in this case supports this argument.

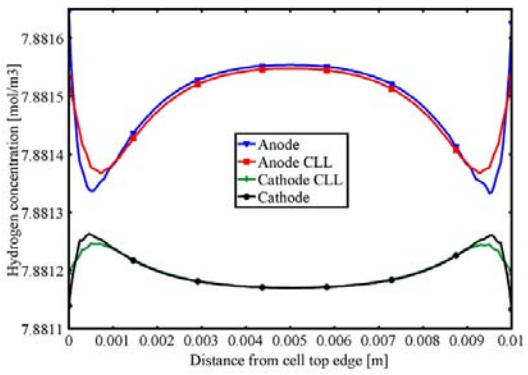

(a)

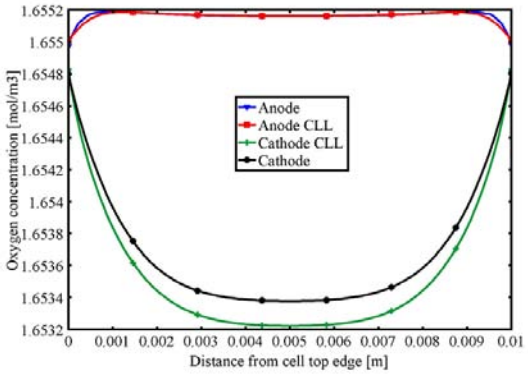

(b)

Figure 5.7: Hydrogen concentration (a) and oxygen concentration (b) for setup (B).

Figure 5.7 (a) shows hydrogen concentration for setup (B). In case of anode first perpendicular design, hydrogen concentration is building-up at the anode-electrolyte interface (Figure 5.7 (a)) which is due to non-permeable electrolyte blocking the gases. However, a lower hydrogen concentration is clearly observed at the top and bottom edges of the electrodes (because most of the hydrogen can escape through the cell edges) and also at the opposite (cathode) electrode (because the escaped hydrogen through the cell edges cannot revert back). Figure 5.7 (b) shows oxygen concentration with a concentration drop observed in the cathode catalyst layer, whereas oxygen is nearly un-consumed at the anode. The concentration gradient is much more uniform in this setup compared to parallel configuration.

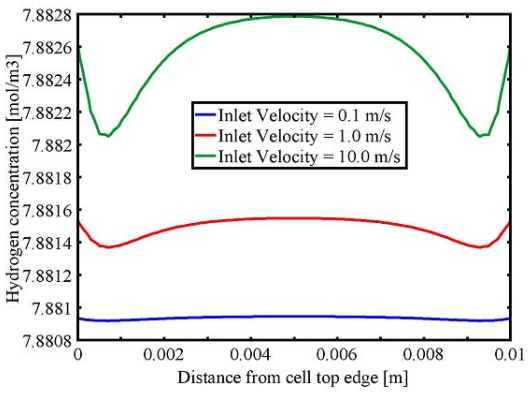

(a)

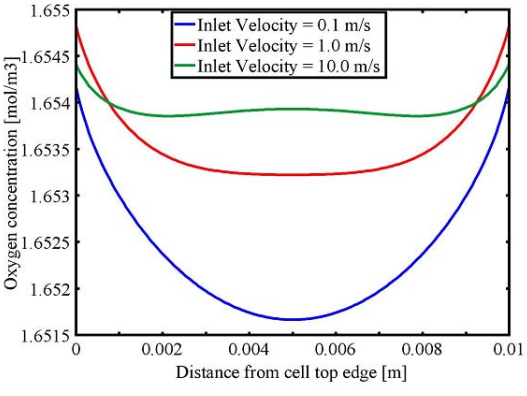

(b)

Figure 5.8: Effect of inlet velocity on hydrogen concentration (a) and oxygen concentration (b) for setup (B).

Figure 5.8 (a) shows the hydrogen concentration with varying inlet velocity of the gaseous mixture for setup (B). At low velocity (e.g. $0.1\ ms^{-1}$, blue curve), there is almost no build-up of hydrogen concentration in the anode catalyst layer (Figure 5.8 (a)). However, as we increase the inlet velocity to $1.0\ ms^{-1}$, hydrogen concentration starts to build-up at the anode. Figure 5.8 (b) shows the oxygen concentration in the cathode catalyst layer and suggests that low inlet velocities are favorable in anode first perpendicular setup.

Figures 5.9 (a-d) shows the velocity, hydrogen, oxygen and water concentration for setup (B), respectively. As observed in case of parallel setup, low porosity (of both electrodes) leads to better utilization of the reactants in the perpendicular setup, as well . Furthermore, a much uniform concentration drop is observed in perpendicular setup compared to parallel one.

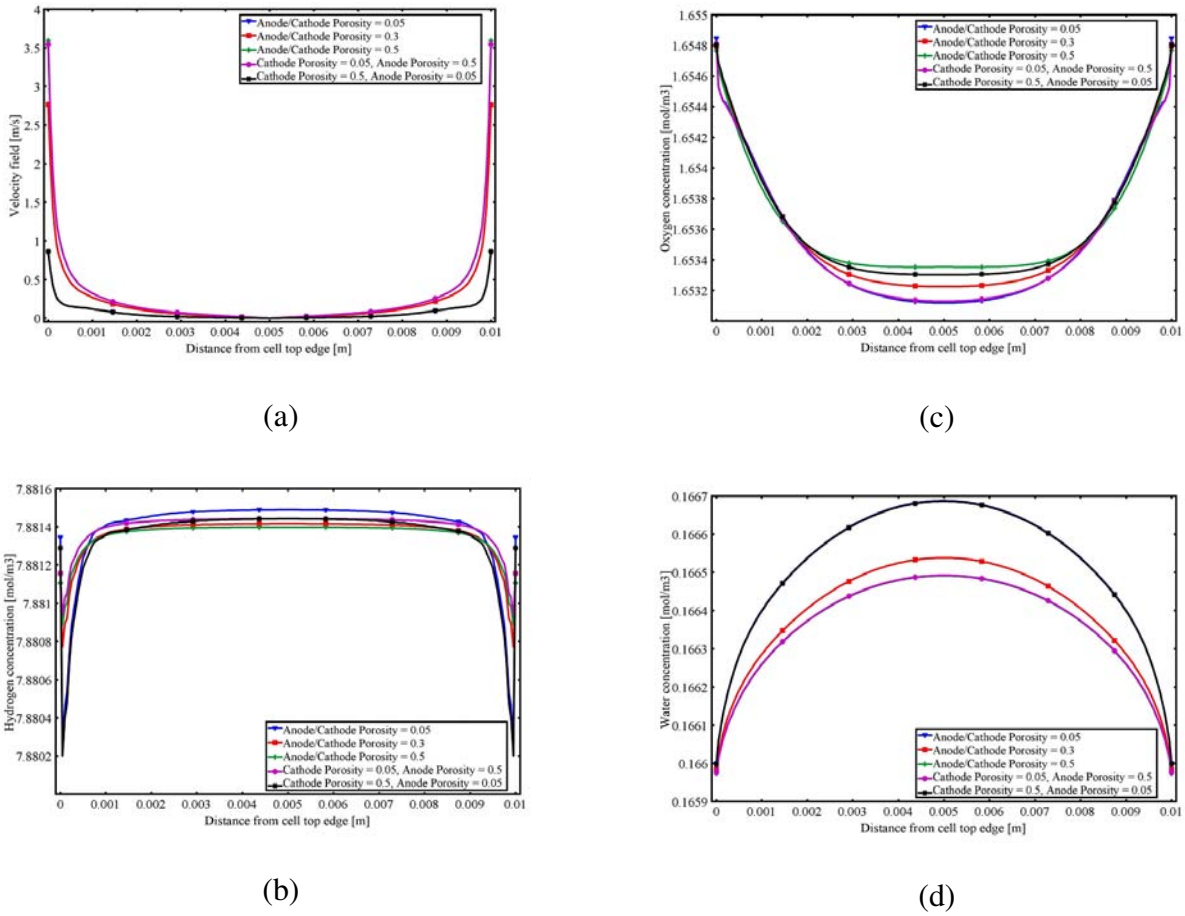

Figure 5.9: Effect of electrode porosity on velocity field (a), hydrogen concentration (b), oxygen concentration (c) and water vapor concentration (d) for setup (B).

Figures 5.10 (a) and (b) compare the anode and cathode first perpendicular setup, respectively. It concludes, the cathode first perpendicular setup is preferable over anode first because it provides

much uniform hydrogen utilization at the anode and oxygen consumption at the cathode. Moreover, no hydrogen build-up is observed in cathode first perpendicular setup.

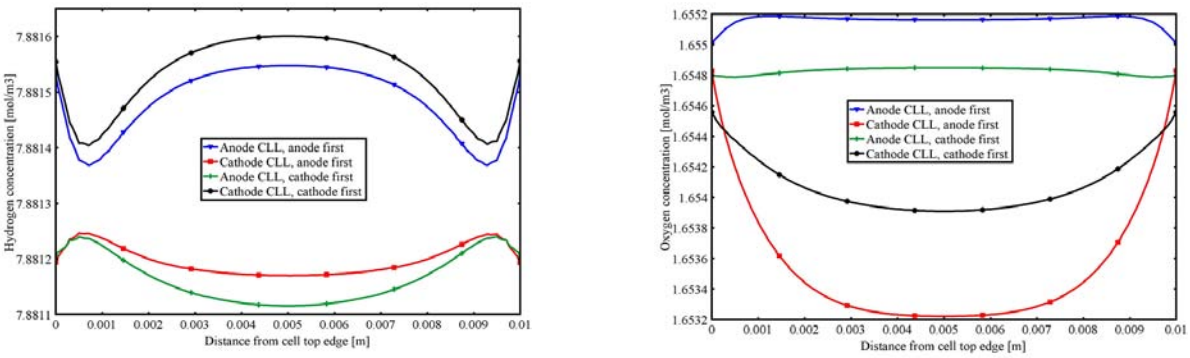

(a) (b)

Figure 5.10: Hydrogen concentration (a) and oxygen concentration (b) in perpendicular setup.

Figure 5.11 (a-b) compares parallel and perpendicular setups and shows that in case of perpendicular setup, there are large vortices formed behind the cell. The electrode which is located in this position may be affected by reactant starvation due to the lack of fresh stream in this location. On the contrary, parallel setup provides smooth flow across the cell.

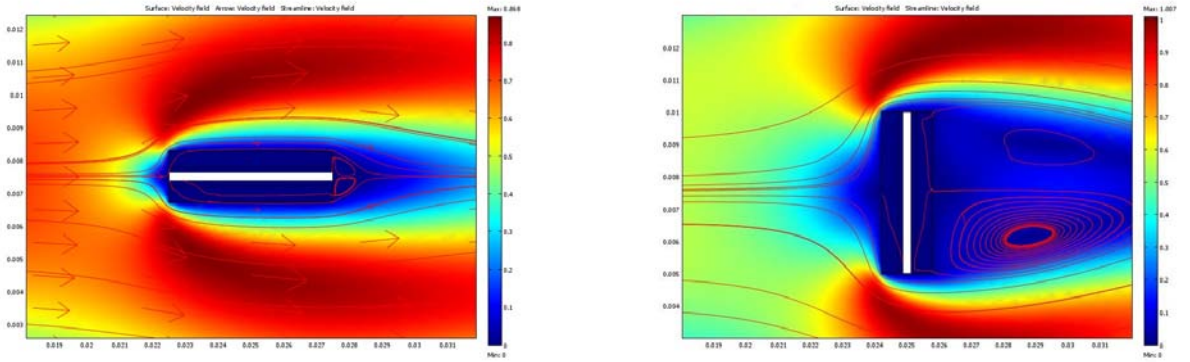

(a) (b)

Figure 5.11: Comparison of parallel (a) and perpendicular setup (b)

Figure 5.12 compares performance of setup (A), (B) and (C). It comes out that the setup (A) gives the highest power density ($26.5\ mWcm^{-2}$) as compared to the other two setups ($23.1\ mWcm^{-2}$ for setup (B) and $24.5\ mWcm^{-2}$ for setup (C)). The reason for the best performance of setup (A) lies

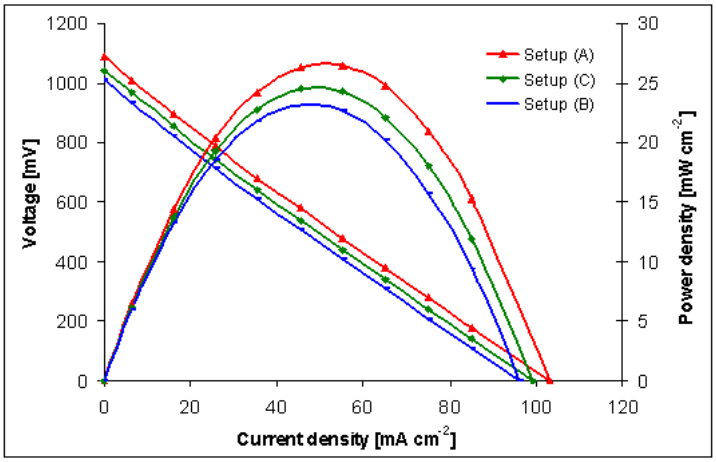

Figure 5.12: I-V and I-P curves for three different setups

in the relatively large concentration drop for both of the reactants in the respective catalyst layers (Figures 5.4 (a) and (b)). The next best performance is of setup (C) and Figures 5.10 (a) and (b) clearly support this phenomena as discussed earlier.

5.5 Conclusions

A numerical model has been developed for conventional-planar SC-SOFC. Three different setups have been studied, namely: A) parallel, B) anode first perpendicular and C) cathode first perpendicular. The results show that the perpendicular setup provides more uniform reactant utilization than the parallel setup. In order to take advantage of both the gas flow and electrochemical performance of the cell, use of a fully porous cell (including the porosity of the electrolyte) is suggested in perpendicular configuration. The cathode first perpendicular configuration provides better utilization at both electrodes than the anode first perpendicular setup. The performance curves show that setup (A) provides the highest power density because of improved reactant utilization.

The results presented are in agreement with the experimental study reported by Stefan et al. [54].

CHAPTER 6

MODELLING OF CO-PLANAR TYPE SC-SOFCs[3]

6.1 Introduction

Conventional solid oxide fuel cells (SOFCs) are based on a design in which two electrodes are located on opposite surfaces of the electrolyte [130]. In this type of configuration ionic current flow direction is perpendicular and through the thickness of the electrolyte, which essentially requires the use of a thin electrolyte to reduce the ohmic resistance. On the other hand, in a single-chamber setup where both electrodes can be located on the same side of the electrolyte, the ionic current has to flow in a lateral direction (i.e. parallel to the electrolyte). Hence the gap and width of the electrodes becomes important and, in this geometry, thickness is considered as one of the dimensions in the cross sectional area. Therefore, thick electrolytes are favorable (due to less ohmic resistance) in this type of design in opposite to conventional fuel cell designs [31].

Though the electrode, electrolyte materials for use in single-chamber solid oxide fuel cell (SC-SOFC) are based on specific requirements at each electrode (anode must be selective for electrochemical fuel oxidation reaction and cathode must be selective towards electrochemical reduction of oxygen). Both materials should be inert for complete oxidation reaction of the fuel [70]. Conventional materials used in SOFCs are not perfectly selective for either reaction, therefore researchers are

---

[3] The results described in this chapter have been published in:

• N. Akhtar et al., Paper: FuelCell2008-65150, ASME 6th International Fuel Cell Science, Engineering and Technology Conference, June 16-18, 2008, Denver, Colorado, USA.

exploring new materials for use in mixed reactant environment aiming at improved cell performance [17, 42]. However, our calculations rely on using conventional materials because of their well known material properties reported in various publications [5, 125, 112, 128].

The objective of this work is to investigate the transport and electrochemical characteristics of a co-planar type SC-SOFC. A Finite Element Method (FEM) based, multiphysics (i.e. coupled thermo-fluid-electrochemical) SC-SOFC model is developed. The model solves conservation equations for mass, momentum, energy, multicomponent species, and charge balance along with the electrochemical kinetics. The results obtained in this study can assist the designer to realize a practical design most suitable for co-planar type SC-SOFC. Also, based on this study one can plan to optimize the geometry for a stack of several cells. The cell considered in this study is composed of nickel yttria-stabilized zirconia (Ni-YSZ) anode electrode, yttria-stabilized zirconia (YSZ) electrolyte and yttria stabilized zirconia-lanthanum strontium manganite (YSZ-LSM) cathode electrode. For the simplicity, hydrogen-air mixture was considered. The respective electrochemical reactions are described in equations (4.1) and equation (4.2).

6.2 Model Description

The fuel cell analyzed in the present study is of co-planar type configuration with a single chamber setup. It is composed of four sub-domains, namely the gas chamber, two porous electrodes (anode and cathode) and the electrolyte. The electrolyte, electrodes assembly also called PEN (positive electrode-electrolyte-negative electrode) is located in the centre of the duct (Figure 6.1). The geometrical dimensions of the single chamber setup are listed in Table 6.1 [75]. A set of equations is applied to each sub-domain and solved numerically by applying appropriate boundary conditions. The corresponding domains and boundaries are defined in Figure 6.2. For nomenclature definition, the reader should refer to Chapter-4.

The following modelling assumptions have been made:

6.2.1 Model Assumptions

• The flow is steady and compressible [128].

• The electrodes are assumed to be ideally selective for the respective electrochemical reactions, therefore, electrochemical oxidation of fuel and reduction of oxygen is taking place in the anode and

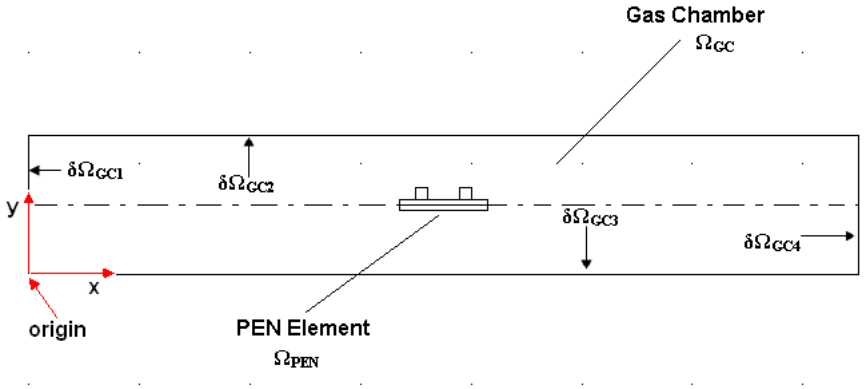

Figure 6.1: Schematic diagram of a co-planar SC-SOFC.

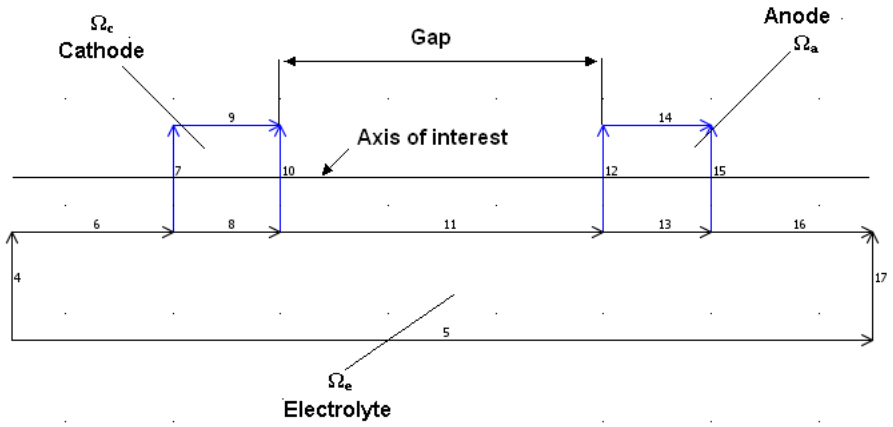

Figure 6.2: Close view of the PEN element

Dimensions	Values (mm)
Chamber length (x-axis)	150
Chamber height (y-axis)	25
Anode width (x-axis)	2
Anode thickness (y-axis)	20×10^{-3}
Cathode width (x-axis)	2
Cathode thickness (y-axis)	20×10^{-3}
Electrolyte width (x-axis)	16
Electrolyte thickness (y-axis)	20×10^{-3}

Table 6.1: Geometrical dimensions

cathode, respectively [76].

• The effect of radiative heat exchange is negligible in comparison with heat transfer by convection [125].

• The walls of the gas chamber are insulated, therefore heat transfer to the environment is restricted.

• The electrolyte is a dense, non-porous material.

• The outer surfaces of the anode and cathode diffusion electrodes are used as current collectors,

therefore the effects of interconnects are neglected.

The model equations for mass, momentum and species conservation are taken from the isothermal model described in Chapter-4. It has been realized that due to the heat transfer effects, the momentum equation may be slightly modified to incorporate the free convection (buoyancy driven flow) term. In the open literature [131, 132, 133] there are two modifications suggested for this purpose: 1) Boussinesq approximation, where the density changes are small and the density is approximated as temperature dependent, while the other physical properties such as viscosity, thermal conductivity etc. remain constant, 2) Non-Boussinesq approximation, where the density changes are very strong with temperature variations. In this case, all the physical properties are described as temperature dependent. In addition to this, the density is not simply the linear temperature dependent property, it is defined via temperature dependent polytropic index (γ) instead [131]. This type of approximation is applicable to systems in which the free convection is dominating over forced convection and the system is subjected to non-uniform heating (e.g. one side is heated, the other is cooled) [131].

In our case, we have to first determine which approximation is going to be valid and what are the background assumptions for this validation. We will take the help of dimensionless numbers in order to determine the effect of various physical quantities. The most relevant dimensionless numbers in our case are:

• Reynolds number: It gives a measure of the ratio of inertial forces to viscous forces [134]:

$$Re = \frac{\rho U d}{\mu} \tag{6.1}$$

where ρ is the density (kgm^{-3}), U is the mean fluid velocity (ms^{-1}), d is the diameter (m) and μ is the dynamic viscosity ($Pa\ s$).

• Prandtl number: It is a ratio of momentum diffusivity (kinematic viscosity) and thermal diffusivity [134].

$$Pr = \frac{\nu}{\alpha_{th}} = \frac{C_p \mu}{k} \tag{6.2}$$

where ν is the kinematic viscosity ($m^2 s^{-1}$), α_{th} is the thermal diffusivity ($m^2 s^{-1}$), C_p is the specific heat at constant pressure ($J\ kg^{-1}\ K^{-1}$) and k is the thermal conductivity ($W\ m^{-1}\ K^{-1}$). In heat transfer problems, the Prandtl number controls the relative thickness of the momentum and thermal boundary layers. In gases, both the viscosity and the thermal conductivity are lower as compared

to liquids, that is why generally the gases have very low values of Prandtl number i.e. around 0.1-0.7 [134].

• Schmidt number: It is the ratio of momentum diffusivity (viscosity) to mass diffusivity, and is used to characterize fluid flows in which there are simultaneous momentum and mass diffusion convection processes [134].

$$Sc = \frac{\nu}{\alpha_m} = \frac{\mu}{\rho \alpha_m} \tag{6.3}$$

where α_m is the mass diffusivity ($m^2 s^{-1}$).

• Grashof number: It is the ratio of the buoyancy to viscous force acting on a fluid [134].

$$Gr_d = \frac{g\beta(T_s - T_\infty)d^{\,3}}{\nu^2} \tag{6.4}$$

where g is the acceleration due to gravity (9.81 ms^{-2}), β is the volumetric thermal expansion coefficient (K^{-1}) equal to approximately T^{-1} for ideal gases (T is absolute temperature in K), T_s is the source temperature (K) and T_∞ is the bulk temperature (K).

The relative magnitudes of the Grashof and Reynolds number determine which form of convection dominates: if $\frac{Gr}{Re^2} >> 1$ forced convection may be neglected; whereas if $\frac{Gr}{Re^2} << 1$ natural (free) convection may be neglected. If the ratio is approximately one, both forced and natural convection need to be taken into account [134].

In SC-SOFC experiments [72], for example, we suggest that for a gaseous mixture with $\rho_{mix}\sim10^{-2}$ kgm^{-3}, $C_{p_{mix}}\sim10^4$ $J\ kg^{-1}\ K^{-1}$, $k_{mix}\sim10^{-1}$ $W\ m^{-1}\ K^{-1}$, $\mu_{mix}\sim10^{-5}$ $Pa\ s$, $\alpha_m\sim10^{-4}$ $m^2 s^{-1}$. Using these estimates and taking typical values associated with the experimental conditions, $g\sim9.81$ ms^{-2}, $U\sim1$ ms^{-1}, $d\sim0.025$ m, $\beta\sim1/500$ K^{-1} and $T_s - T_\infty\sim100$ K (typically in case of partial oxidation of methane). In our case we are not implementing the partial oxidation of the fuel (due to ideally selective electrodes) the $T_s - T_\infty$ term will be even lower$\sim$10-20 K. The typical magnitudes of the non-dimensional groups comes out to be: Re = 10^1, Pr = 10^0, Gr = 10^0, Sc = 10^1 and $\frac{Gr}{Re^2} = 10^{-2} << 1$. This analysis shows that the free convection may be neglected in comparison with the forced convection. Due to this reason, we have neglected the free convection term (buoyancy driven flow) in the Navier-Stokes equation. However, for the forced convection, all the physical properties are assumed to be temperature dependent. Here, we will only discuss the energy equations added into the previous developed isothermal model, all other transport equations as discussed in Chapter-4 will remain valid.

6.2.2 Computational Methodology

Gas chamber allows gaseous mixture (composed of hydrogen, oxygen, nitrogen and a small amount of water vapor) entering at a temperature of 773 K to pass through/over the PEN. The mixture considered is safe due to the following two reasons: (1) its composition (80% hydrogen, 20% air by volume) is outside the flammability range (4-75% hydrogen in air is considered as flammable), (2) operating temperature (773 K) is well below the autoignition temperature (858 K) of a combustible hydrogen/air mixture [13]. All physical properties such as density, heat capacity, viscosity, thermal conductivity and diffusivity are considered as temperature dependent. These properties do not depend on composition proportionality because of the very different behavior of the species considered in the mixture, therefore these individual properties are further corrected for gaseous mixture. Detailed formulation of mixture properties is presented by Todd et al. [135].

Following equations describe energy transport in a gas chamber:

Gas Chamber

The heat transport in the gas chamber is driven by conduction and convection [125].

$$\nabla \cdot (\rho C_p \mathbf{u} T) = \nabla \cdot (k \nabla T) \tag{6.5}$$

where C_p is the gas specific heat at constant pressure and k is the gas thermal conductivity.

Gas Diffusion Electrodes

Heat transport in gas diffusion electrodes is modelled by considering porous nature of the electrodes. Instead of using the thermal conductivity (k_s), density (ρ_s) and specific heat ($C_{p,s}$) of the solid matrix, effective thermal conductivity (k_{eff}), effective density ((ρ_{eff}) and effective specific heat ($C_{p,eff}$) have been used in the model [128].

$$\nabla \cdot ((\rho C_p)_{eff} \mathbf{u} T) = \nabla \cdot (k_{eff} \nabla T) + E \tag{6.6}$$

Effective properties of the porous media are given by [128]:

$$(\rho C_p)_{eff} = (1 - \epsilon)\rho_s C_{p,s} + \epsilon \rho C_p \tag{6.7}$$

$$k_{eff} = -2k_s + (\frac{\epsilon}{2k_s + k} + \frac{1-\epsilon}{3k_s})^{-1} \tag{6.8}$$

In equation (6.6), E is the heat source term and for anode it is given by [125]:

$$E_a = E_{rev_a} + E_{irr_a} + E_{ohm_e a} \tag{6.9}$$

where reversible heat generation in the anode [123, 125]:

$$E_{rev_a} = Tds(i_a/nF) \tag{6.10}$$

$$\frac{ds}{n} = -(23.28 + 0.0042T) \tag{6.11}$$

irreversible heat generation in the anode [125]:

$$E_{irr_a} = \eta_a i_a \tag{6.12}$$

ohmic heat due to ionic resistance [125]:

$$E_{ohm_e a} = \sigma_{ea}^{eff} \nabla\phi_e \cdot \nabla\phi_e \tag{6.13}$$

Heat source term for the cathode is given by [125]:

$$E_c = E_{irr_c} + E_{ohm_e c} \tag{6.14}$$

irreversible heat generation in the cathode [125]:

$$E_{irr_c} = \eta_c i_c \tag{6.15}$$

ohmic heat due to ionic resistance [125]:

$$E_{ohm_e c} = \sigma_{ec}^{eff} \nabla\phi_e \cdot \nabla\phi_e \tag{6.16}$$

Electrolyte

Electrolyte is a dense, non-porous material and thus only conduction is possible. The only source term in electrolyte is the ohmic resistance due to ionic current transfer [125, 126].

$$\nabla \cdot (k\nabla T) + E = 0 \tag{6.17}$$

$$E_e = \sigma_e \nabla \phi_e \cdot \nabla \phi_e \tag{6.18}$$

6.2.3 Boundary Conditions

The boundary conditions for mass, momentum and species conservation will remain same as described in Chapter-4. In below boundary conditions for energy conservation are described.

Gas Chamber

The boundary conditions at each boundary of the gas chamber are given below.

- Inlet

At the inlet, air-fuel mixture's temperature is defined [125]:

$$T = T_0 \tag{6.19}$$

- Walls

The walls of the gas chamber are assumed to be insulated, meaning that the heat transfer across these boundaries is zero [125].

$$-\mathbf{n} \cdot (-k\nabla T + \rho C_p \mathbf{u} T) = 0 \tag{6.20}$$

- Outlet

At the outlet, the heat transport is convection dominated. Convective heat flux boundary condition ensures that at the outlet boundary, the only heat transport is by convection and thus conduction heat transfer is negligible at this boundary [125].

$$\mathbf{n} \cdot (-k\nabla T) = 0 \tag{6.21}$$

Gas Diffusion Electrodes

At all exterior and interior boundaries of the gas diffusion electrodes, continuity of heat flux is maintained. This boundary condition specifies that the normal heat flux inside of the boundary is equal to the normal heat flux outside of the boundary [125].

$$(-\mathbf{n}\cdot(-k_{eff}\nabla T+(\rho C_p)_{eff}\mathbf{u}T))_{in}=(-\mathbf{n}\cdot(-k_{eff}\nabla T+(\rho C_p)_{eff}\mathbf{u}T))_{out} \tag{6.22}$$

Electrolyte

Continuity of heat flux is maintained at all exterior surfaces of the electrolyte, i.e.

$$(-\mathbf{n}\cdot(-k\nabla T))_{in}=(-\mathbf{n}\cdot(-k\nabla T))_{out} \tag{6.23}$$

The governing equations and boundary conditions applied are summarized in Tables 6.2 and 6.3.

Domain	Equation solved
Ω_{GC}	$\nabla\cdot(\rho\mathbf{u})=0$
	$\rho(\mathbf{u}\cdot\nabla)\mathbf{u}=-\nabla p+\mu^*\nabla^2\mathbf{u}+\frac{1}{3}\mu\nabla(\nabla\cdot\mathbf{u})$
	$\nabla\cdot(\rho\mathbf{u}Y_i)=-\nabla\cdot\mathbf{j}_i$
	$\nabla\cdot(\rho C_p\mathbf{u}T)=\nabla\cdot(k\nabla T)$
Ω_a	$\nabla\cdot(\rho\mathbf{u})=S_m, S_m=S_{H2}, S_{H2O}=-\frac{M_{H_2}}{2F}i_a, \frac{M_{H_2O}}{2F}i_a$
	$\frac{\mu}{\kappa}\mathbf{u}=-\nabla p+\mu\nabla^2\mathbf{u}+\frac{1}{3}\mu\nabla(\nabla\cdot\mathbf{u})$
	$\nabla\cdot(\rho\mathbf{u}Y_i)=-\nabla\cdot\mathbf{j}_i+S_i, S_i=S_{H2}, S_{H2O}=-\frac{M_{H_2}}{2F}i_a, \frac{M_{H_2O}}{2F}i_a$
	$\nabla\cdot(-\sigma_s^{eff}\nabla\phi_s)=A_sS_{\phi_s}$
	$\nabla\cdot(-\sigma_e^{eff}\nabla\phi_e)=A_sS_{\phi_e}$
	$\nabla\cdot((\rho C_p)_{eff}\mathbf{u}T)=\nabla\cdot(k_{eff}\nabla T)+E, E=E_{rev_a}+E_{irr_a}+E_{ohm_ea}$
Ω_c	$\nabla\cdot(\rho\mathbf{u})=S_m, S_m=S_{O2}=-\frac{M_{O_2}}{4F}i_c$
	$\frac{\mu}{\kappa}\mathbf{u}=-\nabla p+\mu\nabla^2\mathbf{u}+\frac{1}{3}\mu\nabla(\nabla\cdot\mathbf{u})$
	$\nabla\cdot(\rho\mathbf{u}Y_i)=-\nabla\cdot\mathbf{j}_i+S_i, S_i=S_{O2}=-\frac{M_{O_2}}{4F}i_c$
	$\nabla\cdot(-\sigma_s^{eff}\nabla\phi_s)=A_sS_{\phi_s}$
	$\nabla\cdot(-\sigma_e^{eff}\nabla\phi_e)=A_sS_{\phi_e}$
	$\nabla\cdot((\rho C_p)_{eff}\mathbf{u}T)=\nabla\cdot(k_{eff}\nabla T)+E, E=E_{irr_c}+E_{ohm_ec}$
Ω_e	$\nabla\cdot(k\nabla T)+E=0, E=\sigma_e\nabla\phi_e\cdot\nabla\phi_e$
	$\nabla\cdot(-\sigma_e\nabla\phi_e)=0$

$^*\ \mu=\sum_{i=1}^{N}Y_i\mu_i$

Table 6.2: Computational domains and governing equations

6.3 Results and Discussion

The model equations are solved using methodology given in Chapter-4. The total computing time for all stages (with $47,019$ degrees of freedom) was approximately 2.5 minutes. The values of the transport parameters for operating conditions are listed in Table 6.4. Due to same inlet cross-sectional area and density of the mixture entering into the gas chamber, change in mass flow rate is proportional to the change in velocity. Therefore, simulations are based on varying the velocity of the inlet

Surface Boundary	Boundary Condition
$\partial\Omega_{GC_1}$	$\mathbf{u} = \mathbf{u_{in}}, Y_i = Y_{i_{in}}, T = T_0$
$\partial\Omega_{GC_2}$	$u = v = w = 0, \mathbf{n} \cdot (-\rho D_{ij} \nabla Y_i + \rho \mathbf{u} Y_i) = 0, -\mathbf{n} \cdot (-k \nabla T + \rho C_p \mathbf{u} T) = 0$
$\partial\Omega_{GC_3}$	$u = v = w = 0, \mathbf{n} \cdot (-\rho D_{ij} \nabla Y_i + \rho \mathbf{u} Y_i) = 0, -\mathbf{n} \cdot (-k \nabla T + \rho C_p \mathbf{u} T) = 0$
$\partial\Omega_{GC_4}$	$p = p_o, \mathbf{n} \cdot (-\rho D_{ij} \nabla Y_i) = 0, \mathbf{n} \cdot (-k \nabla T) = 0$
$\partial\Omega_4$	$\mathbf{n} \cdot \mathbf{u} = 0, \mathbf{n} \cdot (-\rho D_{ij} \nabla Y_i + \rho \mathbf{u} Y_i) = 0, \mathbf{n} \cdot (-\sigma_e \nabla \phi_e) = 0, (-\mathbf{n} \cdot (-k \nabla T))_{in} = (-\mathbf{n} \cdot (-k \nabla T))_{out}$
$\partial\Omega_5$	$\mathbf{n} \cdot \mathbf{u} = 0, \mathbf{n} \cdot (-\rho D_{ij} \nabla Y_i + \rho \mathbf{u} Y_i) = 0, \mathbf{n} \cdot (-\sigma_e \nabla \phi_e) = 0, (-\mathbf{n} \cdot (-k \nabla T))_{in} = (-\mathbf{n} \cdot (-k \nabla T))_{out}$
$\partial\Omega_6$	$\mathbf{n} \cdot \mathbf{u} = 0, \mathbf{n} \cdot (-\rho D_{ij} \nabla Y_i + \rho \mathbf{u} Y_i) = 0, \mathbf{n} \cdot (-\sigma_e \nabla \phi_e) = 0, (-\mathbf{n} \cdot (-k \nabla T))_{in} = (-\mathbf{n} \cdot (-k \nabla T))_{out}$
$\partial\Omega_{16}$	$\mathbf{n} \cdot \mathbf{u} = 0, \mathbf{n} \cdot (-\rho D_{ij} \nabla Y_i + \rho \mathbf{u} Y_i) = 0, \mathbf{n} \cdot (-\sigma_e \nabla \phi_e) = 0, (-\mathbf{n} \cdot (-k \nabla T))_{in} = (-\mathbf{n} \cdot (-k \nabla T))_{out}$
$\partial\Omega_{17}$	$\mathbf{n} \cdot \mathbf{u} = 0, \mathbf{n} \cdot (-\rho D_{ij} \nabla Y_i + \rho \mathbf{u} Y_i) = 0, \mathbf{n} \cdot (-\sigma_e \nabla \phi_e) = 0, (-\mathbf{n} \cdot (-k \nabla T))_{in} = (-\mathbf{n} \cdot (-k \nabla T))_{out}$
$\partial\Omega_{11}$	$\mathbf{n} \cdot \mathbf{u} = 0, \mathbf{n} \cdot (-\rho D_{ij} \nabla Y_i + \rho \mathbf{u} Y_i) = 0, \mathbf{n} \cdot (-\sigma_e \nabla \phi_e) = 0, (-\mathbf{n} \cdot (-k \nabla T))_{in} = (-\mathbf{n} \cdot (-k \nabla T))_{out}$
$\partial\Omega_7$	$\mathbf{n} \cdot (\rho \mathbf{u})_{in} = \mathbf{n} \cdot (\rho \mathbf{u})_{out}, \mathbf{n} \cdot (-\rho D^{eff}_{DG_{i,j}} \nabla Y_i + \rho \mathbf{u} Y_i)_{in} = \mathbf{n} \cdot (-\rho D^{eff}_{DG_{i,j}} \nabla Y_i + \rho \mathbf{u} Y_i)_{out}$, $\mathbf{n} \cdot (-\sigma_s^{eff} \nabla \phi_s) = 0, \mathbf{n} \cdot (-\sigma_e^{eff} \nabla \phi_e) = 0, (-\mathbf{n} \cdot (-k_{eff} \nabla T + (\rho C_p)_{eff} \mathbf{u} T))_{in} = (-\mathbf{n} \cdot (-k_{eff} \nabla T + (\rho C_p)_{eff} \mathbf{u} T))_{out}$
$\partial\Omega_{10}$	$\mathbf{n} \cdot (\rho \mathbf{u})_{in} = \mathbf{n} \cdot (\rho \mathbf{u})_{out}, \mathbf{n} \cdot (-\rho D^{eff}_{DG_{i,j}} \nabla Y_i + \rho \mathbf{u} Y_i)_{in} = \mathbf{n} \cdot (-\rho D^{eff}_{DG_{i,j}} \nabla Y_i + \rho \mathbf{u} Y_i)_{out}$, $\mathbf{n} \cdot (-\sigma_s^{eff} \nabla \phi_s) = 0, \mathbf{n} \cdot (-\sigma_e^{eff} \nabla \phi_e) = 0, (-\mathbf{n} \cdot (-k_{eff} \nabla T + (\rho C_p)_{eff} \mathbf{u} T))_{in} = (-\mathbf{n} \cdot (-k_{eff} \nabla T + (\rho C_p)_{eff} \mathbf{u} T))_{out}$
$\partial\Omega_{12}$	$\mathbf{n} \cdot (\rho \mathbf{u})_{in} = \mathbf{n} \cdot (\rho \mathbf{u})_{out}, \mathbf{n} \cdot (-\rho D^{eff}_{DG_{i,j}} \nabla Y_i + \rho \mathbf{u} Y_i)_{in} = \mathbf{n} \cdot (-\rho D^{eff}_{DG_{i,j}} \nabla Y_i + \rho \mathbf{u} Y_i)_{out}$, $\mathbf{n} \cdot (-\sigma_s^{eff} \nabla \phi_s) = 0, \mathbf{n} \cdot (-\sigma_e^{eff} \nabla \phi_e) = 0, (-\mathbf{n} \cdot (-k_{eff} \nabla T + (\rho C_p)_{eff} \mathbf{u} T))_{in} = (-\mathbf{n} \cdot (-k_{eff} \nabla T + (\rho C_p)_{eff} \mathbf{u} T))_{out}$
$\partial\Omega_{15}$	$\mathbf{n} \cdot (\rho \mathbf{u})_{in} = \mathbf{n} \cdot (\rho \mathbf{u})_{out}, \mathbf{n} \cdot (-\rho D^{eff}_{DG_{i,j}} \nabla Y_i + \rho \mathbf{u} Y_i)_{in} = \mathbf{n} \cdot (-\rho D^{eff}_{DG_{i,j}} \nabla Y_i + \rho \mathbf{u} Y_i)_{out}$, $\mathbf{n} \cdot (-\sigma_s^{eff} \nabla \phi_s) = 0, \mathbf{n} \cdot (-\sigma_e^{eff} \nabla \phi_e) = 0, (-\mathbf{n} \cdot (-k_{eff} \nabla T + (\rho C_p)_{eff} \mathbf{u} T))_{in} = (-\mathbf{n} \cdot (-k_{eff} \nabla T + (\rho C_p)_{eff} \mathbf{u} T))_{out}$
$\partial\Omega_9$	$\mathbf{n} \cdot (\rho \mathbf{u})_{in} = \mathbf{n} \cdot (\rho \mathbf{u})_{out}, \mathbf{n} \cdot (-\rho D^{eff}_{DG_{i,j}} \nabla Y_i + \rho \mathbf{u} Y_i)_{in} = \mathbf{n} \cdot (-\rho D^{eff}_{DG_{i,j}} \nabla Y_i + \rho \mathbf{u} Y_i)_{out}$, $\phi_s = \phi_{sc}, (-\mathbf{n} \cdot (-k_{eff} \nabla T + (\rho C_p)_{eff} \mathbf{u} T))_{in} = (-\mathbf{n} \cdot (-k_{eff} \nabla T + (\rho C_p)_{eff} \mathbf{u} T))_{out}$
$\partial\Omega_8$	$\mathbf{n} \cdot \mathbf{u} = 0, \mathbf{n} \cdot (-\rho D^{eff}_{DG_{i,j}} \nabla Y_i + \rho \mathbf{u} Y_i) = 0, \mathbf{n} \cdot (-\sigma_s^{eff} \nabla \phi_s) = 0, \mathbf{n} \cdot (i_{c,in}) = \mathbf{n} \cdot (i_{c,out})$, $(-\mathbf{n} \cdot (-k \nabla T))_{in} = (-\mathbf{n} \cdot (-k \nabla T))_{out}$
$\partial\Omega_{13}$	$\mathbf{n} \cdot \mathbf{u} = 0, \mathbf{n} \cdot (-\rho D^{eff}_{DG_{i,j}} \nabla Y_i + \rho \mathbf{u} Y_i) = 0, \mathbf{n} \cdot (-\sigma_s^{eff} \nabla \phi_s) = 0, \mathbf{n} \cdot (i_{a,in}) = \mathbf{n} \cdot (i_{a,out})$, $(-\mathbf{n} \cdot (-k \nabla T))_{in} = (-\mathbf{n} \cdot (-k \nabla T))_{out}$
$\partial\Omega_{14}$	$\mathbf{n} \cdot (\rho \mathbf{u})_{in} = \mathbf{n} \cdot (\rho \mathbf{u})_{out}, \mathbf{n} \cdot (-\rho D^{eff}_{DG_{i,j}} \nabla Y_i + \rho \mathbf{u} Y_i)_{in} = \mathbf{n} \cdot (-\rho D^{eff}_{DG_{i,j}} \nabla Y_i + \rho \mathbf{u} Y_i)_{out}$, $\phi_s = \phi_{sa}, (-\mathbf{n} \cdot (-k_{eff} \nabla T + (\rho C_p)_{eff} \mathbf{u} T))_{in} = (-\mathbf{n} \cdot (-k_{eff} \nabla T + (\rho C_p)_{eff} \mathbf{u} T))_{out}$

Table 6.3: Boundary conditions

gas mixture. Three different distances between the anode and cathode electrode are chosen as 8, 2 and 12 mm and they are named as case-1, 2 and 3 respectively. We refer case-1 as the base-case in our simulations. The axis of interest is shown in Figure 6.2 along the length of the electrolyte. This is the axis where various variables are plotted as shown in all subsequent figures. In Figure 6.3 the computational mesh is shown. The location of electrodes for three different cases is represented in Figure 6.4. Figure 6.5 shows simulation results based on parameters listed in Table 6.4 for the base-case. Figure 6.6 shows simulations results for case-2 and Figure 6.7 shows simulation results for case-3. Figures 6.8-6.10 show calculations for the base-case such that Figure 6.8 shows the variation in ohmic loss due to change in electrolyte thickness. Figure 6.9 shows hydrogen and oxygen concentration with varying porosity of the electrodes. Figure 6.10 shows temperature profile for different values of operating voltages. Figure 6.11 shows the effect of inlet velocity on cell performance.

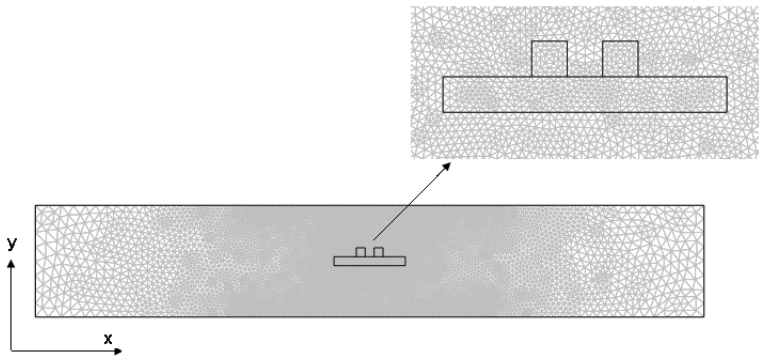

Figure 6.3: The computational mesh (6,938 elements)

Property	Symbol	Value	Units	References
Working electrical potential at anode	ϕ_{sa}	0	V	[5]
Working electrical potential at cathode	ϕ_{sc}	0.7	V	[5]
Reversible electrical potential at anode	ϕ_{ra}	0	V	[5]
Reversible electrical potential at cathode side	ϕ_{rc}	1.0	V	[5]
Ionic potential in electrolyte	ϕ_e	0	V	[5]
Volumetric anode exchange current density	$A_s i_{0,a}$	2.2×10^7	Am^{-3}	[5]
Volumetric cathode exchange current density	$A_s i_{0,c}$	2.2×10^7	Am^{-3}	[5]
Electrolyte ionic conductivity	σ_e	4.1	Sm^{-1}	[5]
Effective anode ionic conductivity	σ_{ea}^{eff}	0.29	Sm^{-1}	[5]
Effective cathode ionic conductivity	σ_{ec}^{eff}	0.24	Sm^{-1}	[5]
Effective anode electronic conductivity	σ_{sa}^{eff}	4800	Sm^{-1}	[5]
Effective cathode electronic conductivity	σ_{sc}^{eff}	1600	Sm^{-1}	[5]
Temperature	T	773	K	[76]
Anodic anodic charge transfer coefficient	α_a^a	2		[5]
Anodic cathodic charge transfer coefficient	α_c^a	1		[5]
Cathodic anodic charge transfer coefficient	α_a^c	1.5		[5]
Cathodic cathodic charge transfer coefficient	α_c^c	0.5		[5]
Faraday's constant	F	96487	$Cmole^{-1}$	[128]
Universal gas constant	R_g	8.314	$Jmole^{-1}K^{-1}$	[128]
Porosity	ϵ	0.3		[128]
Tortuosity	τ	3.80		[128]
Permeability	κ	1.0×10^{-13}	m^2	[126]
Hydrogen inlet mass fraction	$Y_{H2_{in}}$	0.80		[−]
Oxygen inlet mass fraction	$Y_{O2_{in}}$	0.10		[−]
Nitrogen inlet mass fraction	$Y_{N2_{in}}$	0.099		[−]
Operating pressure	p_o	1.013×10^5	Nm^{-2}	[124]
Inlet velocity	$\mathbf{u_{in}}$	0.5	ms^{-1}	[124]
Constant	k	3.16×10^{-8}		[−]
Average pore diameter	d_p	1.0	μm	[124]
Hydrogen viscosity	μ_{H2}	$6.162e^{-6} + 1.145e^{-8} \times T$	$Pa.s$	[125]
Oxygen viscosity	μ_{O2}	$1.668e^{-5} + 3.108e^{-8} \times T$	$Pa.s$	[125]
Water viscosity	μ_{H2O}	$4.567e^{-6} + 2.209e^{-8} \times T$	$Pa.s$	[125]
Nitrogen viscosity	μ_{N2}	$1.435e^{-5} + 2.642e^{-8} \times T$	$Pa.s$	[125]
Hydrogen specific heat	$C_{p,H2}$	$13960 + 0.950 \times T$	$Jkg^{-1}K^{-1}$	[125]
Oxygen specific heat	$C_{p,O2}$	$876.80 + 0.217 \times T$	$Jkg^{-1}K^{-1}$	[125]
Water specific heat	$C_{p,H2O}$	$1639.2 + 0.641 \times T$	$Jkg^{-1}K^{-1}$	[125]
Nitrogen specific heat	$C_{p,N2}$	$935.6 + 0.232 \times T$	$Jkg^{-1}K^{-1}$	[125]
Hydrogen thermal conductivity	k_{H2}	$0.08525 + 2.964e^{-4} \times T$	$Wm^{-1}K^{-1}$	[125]
Oxygen thermal conductivity	k_{O2}	$0.01569 + 5.690e^{-5} \times T$	$Wm^{-1}K^{-1}$	[125]
Water thermal conductivity	k_{H2O}	$-0.01430 + 9.782e^{-5} \times T$	$Wm^{-1}K^{-1}$	[125]
Nitrogen thermal conductivity	k_{N2}	$0.01258 + 5.444e^{-5} \times T$	$Wm^{-1}K^{-1}$	[130]
Anode thermal conductivity	k_a	2	$Wm^{-1}K^{-1}$	[130]
Cathode thermal conductivity	k_c	4	$Wm^{-1}K^{-1}$	[130]
Electrolyte thermal conductivity	k_e	2	$Wm^{-1}K^{-1}$	[130]
Anode specific heat	C_a	595	$Jkg^{-1}K^{-1}$	[130]
Cathode specific heat	C_c	573	$Jkg^{-1}K^{-1}$	[130]
Electrolyte specific heat	C_e	606	$Jkg^{-1}K^{-1}$	[130]
Anode density	ρ_a	6870	kgm^{-3}	[130]
Cathode density	ρ_c	6570	kgm^{-3}	[130]
Electrolyte density	ρ_e	5900	kgm^{-3}	[130]

Table 6.4: Input parameters

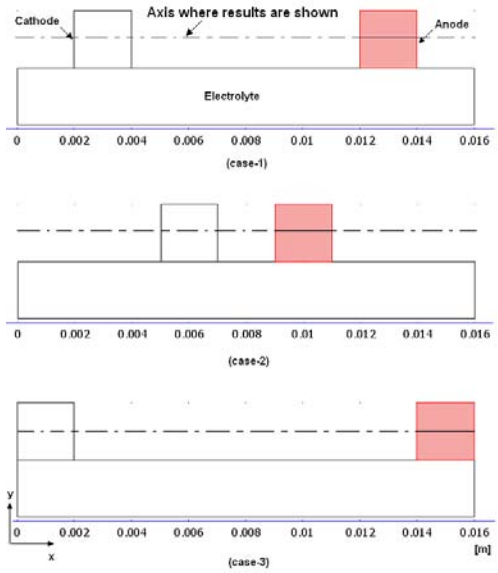

Figure 6.4: Electrode placement for three different cases

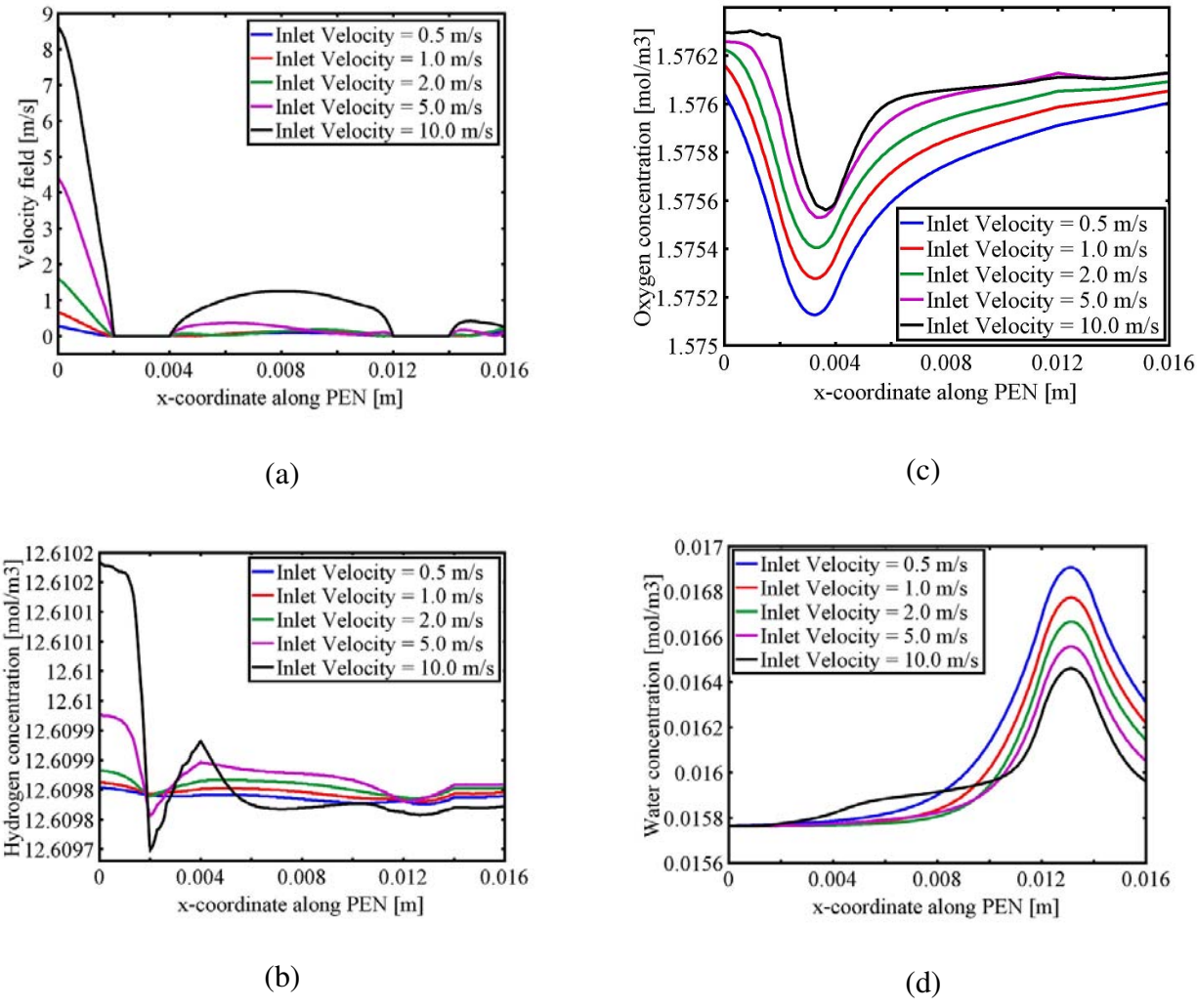

Figure 6.5: Velocity field (a), hydrogen concentration (b), oxygen concentration (c) and water concentration (d) for case-1.

In Figure 6.5 (a), velocity field in the vicinity of the electrodes (across the length of the electrolyte) has been shown. It can be seen as the flow approaches electrodes, the velocity becomes lower and lower and attains a value very close to zero in the electrodes. This reduction in velocity is due to the porous nature of the electrodes having a very low permeability. The flow in the electrodes is mainly diffusive and as soon the gaseous mixture comes out of the cathode electrode, it accelerates before it reaches to the anode electrode. Higher velocities allow greater mass flux entering into the electrodes and thus enhance mass transport by forced convection. This behavior can been seen in black curve ($10\ ms^{-1}$) compared to blue curve ($0.5\ ms^{-1}$) at a distance of 4-12 mm.

Figures 6.5 (b), (c) and (d) show hydrogen, oxygen and water concentration, respectively for the base-case. The cathode is located at a distance of 2-4 mm and anode at 12-14 mm distance from the leading edge of the electrolyte facing inlet flow. The reduction in oxygen concentration at the cathode and increase in water concentration at the anode (although fairly low) is clearly seen at these distances in Figure 6.5 (c) and (d) respectively. Although increase in velocity enhances the mass transport (as explained above) in the electrodes but on the other hand it also reduces the electrochemical reaction rate (black curve show less concentration gradient). The reduction in electrochemical performance is due to the short residence time as explained in Chapter-5. The effect will be more visible if we scale-up the design.

Simulation results shown in Figure 6.5 (b) are surprising, although no hydrogen consumption is taking place at the cathode electrode, still hydrogen concentration gradient is present at the cathode. The reason for this behavior could be eddy formation which causes swirl motion in between the two electrodes. Low concentration of hydrogen at the anode (due to consumption) and higher concentration of hydrogen at the cathode (due to no-consumption) causes a circular motion, thus some reduction in hydrogen concentration is expected at the cathode even though it is not consumed there.

Figure 6.6 (a) shows velocity profile for case-2, where the two electrodes are 2 mm apart. Though, this trend looks similar to the base-case, the velocity entering the anode electrode is much lower compared to the base-case. The narrow distance between the two electrodes does not allow the flow to accelerate enough before it enters to the anode. This can cause low mass transport in the anode due to less forced convection.

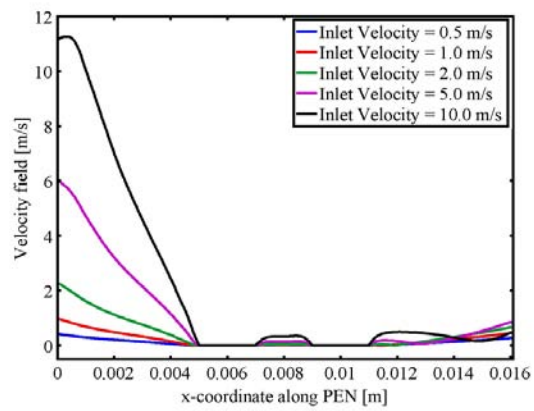

(a)

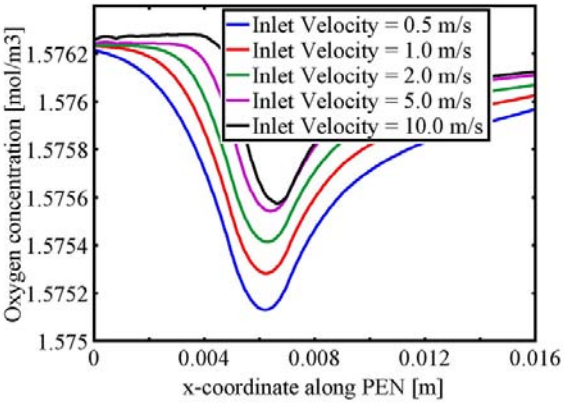

(c)

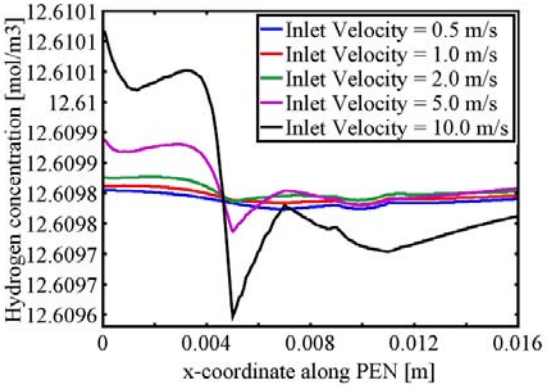

(b)

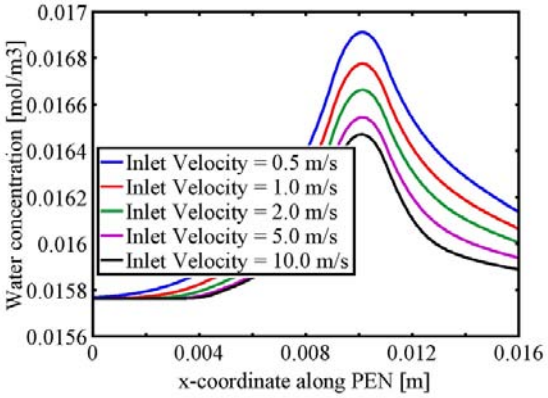

(d)

Figure 6.6: Velocity field (a), hydrogen concentration (b), oxygen concentration (c) and water concentration (d) for case-2.

Figure 6.6 (b), (c) and (d) show hydrogen, oxygen and water concentration, respectively for the case-2. Although the trends in concentration gradients look similar to the base-case, the turbulence (swirl) is enhanced due to less distance between the two electrodes. Black curve in Figure 6.6 (b) shows larger instability as compared to the base-case. It can be concluded that reducing the distance between the electrodes might generate turbulence and thus depletes the gas mixture in the near electrode. However, less distance between the electrodes improves cell performance by decreasing the ohmic resistance for ionic current flow [42].

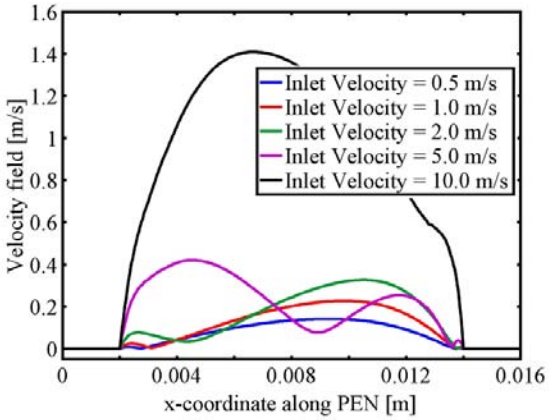

(a)

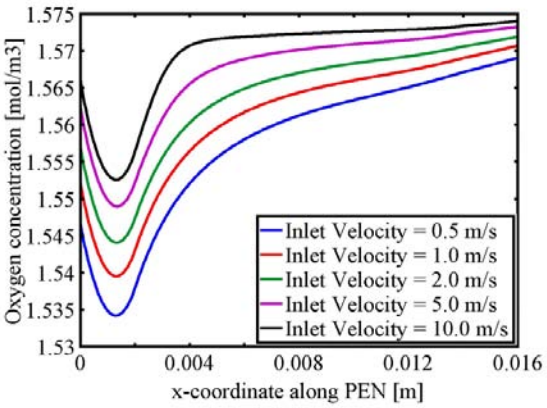

(c)

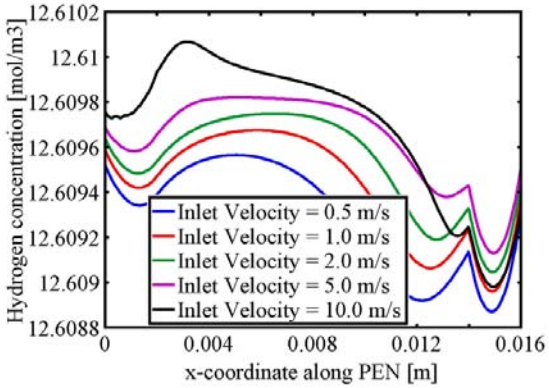

(b)

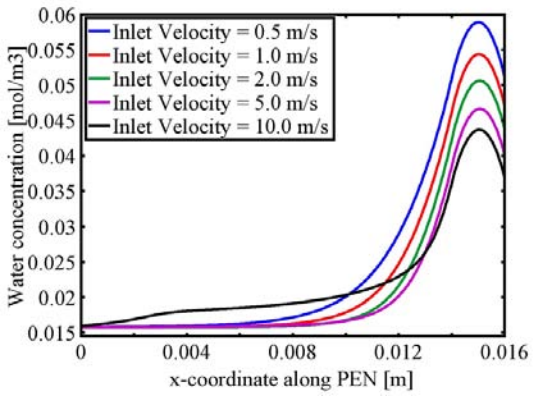

(d)

Figure 6.7: Velocity field (a), hydrogen concentration (b), oxygen concentration (c) and water concentration (d) for case-3.

Figure 6.7 (a) shows velocity field for case-3 when the electrodes are $12mm$ apart. At low velocities (e.g. blue, red and green curves) when the flow comes out of the cathode electrode, it accelerates before it enters into the anode. However, at high velocities (e.g. purple and black curves) there is a sudden jump in the velocity as soon the flow comes out of the cathode. This behavior is similar to passing a gas stream through a nozzle, where the reduction in passage increases the velocity. The electrodes (in a similar way) have reduced passage for the flow thus kinetic-pressure-kinetic energy conversion process takes place.

Figure 6.7 (b), (c) and (d) show the hydrogen, oxygen and water vapor concentration, respectively. In this case, large amount of reactants are consumed and water is produced as compared to case-1 and case-2. The reason for this behavior is enhanced forced convection at the electrodes due to sudden increase in the velocity (because electrodes are located at the edges of the electrolyte, flow sees a

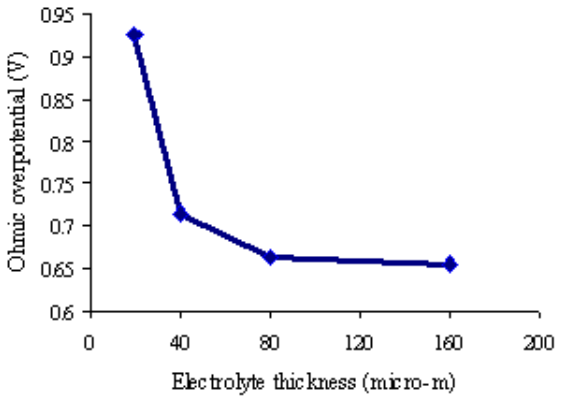

Figure 6.8: Ohmic loss variation with electrolyte thickness for case-1.

large obstacle area).

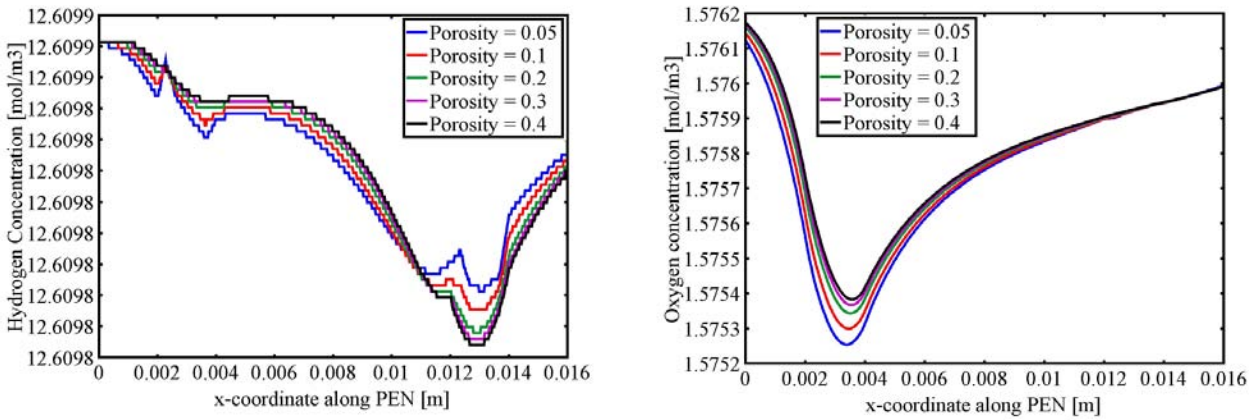

(a) (b)

Figure 6.9: Effect of electrodes porosity on hydrogen concentration (a), oxygen concentration (b) for case-1.

Figure 6.8 shows ohmic loss as a function of electrolyte thickness for the base-case. Ohmic loss decreases with increase in electrolyte thickness due to large cross-sectional area available for ionic current flow in the lateral direction. It can be concluded that this setup can permit the use of thick electrolyte, thus electrolyte supported cells are favored in this configuration.

Figure 6.9 (a) and (b) shows the hydrogen and oxygen concentration for the base-case with varying porosity of both electrodes. As can be seen from the black curve (when both electrode have porosity = 0.4) compared with the blue curve (both electrode's porosity = 0.05), increase in porosity reduces the reactant utilization. This is due to less active surface area available as porosity increases. There is

a trade-off between porosity and active area and both need optimization.

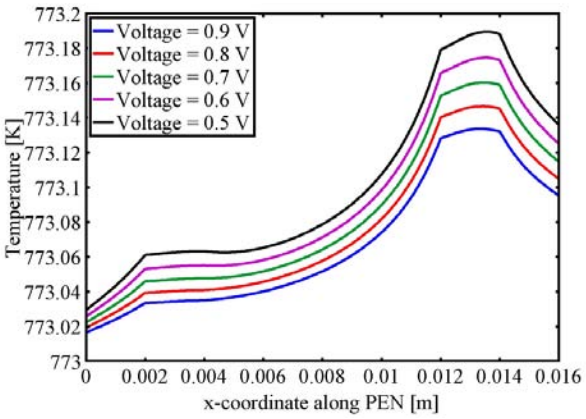

Figure 6.10: Effect of operating voltage on temperature for case-1.

Figure 6.10 show temperature profile for the base-case at different operating voltages. As can be seen, decrease in voltage increases temperature at the electrodes. Also, anode has a higher temperature than cathode and the reason is reversible heat generation at anode due to electrochemical production of water. Although the increase in temperature is insignificant, this is due to the fact that the radiation equation is not implemented and the only heat source is due to inherent reversible and irreversible effects. Furthermore, the partial oxidation of fuel is also neglected by assuming ideally selective electrodes.

The effect of inlet velocity on the cell performance is shown in Figure 6.11. It is clear that co-planar design gives very low power densities (the highest is 14.6 $mWcm^{-2}$ at an inlet velocity of 1.0 ms^{-1}) as compared to our earlier studied designs (i.e. novel-planar and conventional-planar). The main factor responsible for this lower performance is the high ohmic resistance for ionic current transfer between the electrodes. The cross-diffusion as discussed earlier is another major contributor in lowering the cell performance. It is also noticeable that increasing the inlet velocity improves the cell performance due to enhanced mass transport through the electrodes. However, very high inlet velocities (greater than $0.8ms^{-1}$ in this study) can cause fuel utilization problem (due to short residence time) and high amount of water generated can deplete the gaseous stream.

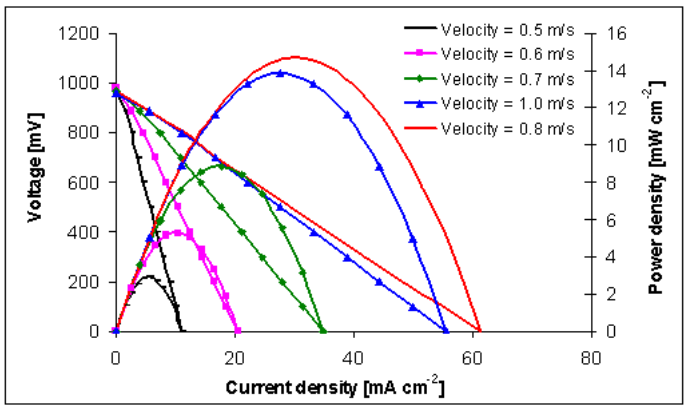

Figure 6.11: Effect of inlet velocity on cell performance.

6.4 Conclusions

A two dimensional numerical model of a co-planar type single-chamber solid oxide fuel cell is developed. The model shows the importance of structural parameters (such as distance between the electrodes, electrolyte thickness, porosity of the electrodes), effect of flow rate and temperature in case of co-planar type single-chamber solid oxide fuel cell. It has been seen that high velocities (high flow rate) can enhance the mass transport at the electrodes but the residence time for an electrochemical reaction decreases. It concludes, highly selective electrodes are necessary for operation at high flow rates because they can make use of the short residence time by efficient selection of their feed (fuel or oxygen). Less distance between the electrodes reduces the ohmic loss associated with ionic charge transfer but on the other hand narrow electrodes can give swirl motion and generate turbulence. This can deplete the mixture concentration in the nearby electrode. In order to handle this problem, barrier layers are suggested in between the electrodes. These layers can reduce the inter-mixing due to concentration gradient generated by turbulence. Low porosity electrodes are favorable because they can provide large active surface area, however too low porosity causes large pressure drop in the electrodes. This problem can be solved by varying the permeability of the electrodes while keeping the porosity as fixed. Thick electrolytes offer less ohmic resistance for ionic current flow and also serve as a mechanical support for the electrodes. Heat generation due to electrochemical reaction can be taken away by increased convection stream. However, this does not seem practical in case of using hydrocarbons as the fuel, because of large heat generation due to partial oxidation reaction. In such case, addition of some water vapor can induce endothermic reaction and the heat balance can be achieved.

The results presented are consistent with the numerical studies reported by Chung et al. [75, 76]. Nevertheless, most of the publications consider hydrocarbon/air mixtures due to being much safer than hydrogen/air mixtures and there is hardly any experimental study reported on hydrogen/air mixtures.

CHAPTER 7

SC-SOFCS: AN EXPERIMENTAL STUDY[4]

7.1 Introduction

Our modelling study (Chapter 4-6) reveals that in a single-chamber setup, the cross diffusion, convection and intermixing is the main player in lowering the cell performance. In case of planar single-chamber configuration, both of the electrodes are exposed (in an open environment) to the air-fuel mixture. Since there is no barrier or compartment in between the anode and cathode that could separate them physically, disturbance of local chemistry at the respective electrodes cannot be completely avoided. This point led us to look an alternative design in which the cross-diffusion and convection could be minimized. The alternate should provide some sort of physical separation between the electrodes, and micro-tubular geometry can certainly meet this criteria by having two separate compartments for each electrode. In a micro-tubular geometry one electrode lies in the inner side of the tube, while the other is located on the outer side, both separated by a solid (non-permeable) electrolyte. The idea of using micro-tubular design motivated us for a practical implementation of this concept for the first time. As a result, it was proposed to conduct an experimental study on micro-tubular geometry and compare the results with the work published in earlier studies.

Kendall et al. [130] reported further benefits of micro-tubular design, such as improved shock resistance, rapid start-up/shut down, high surface to volume ratio and improved thermal cycling performance [136]. Not only this, the micro-tubular cells can also be operated on mixed reactants (air/fuel mixtures).

---

[4] The results described in this chapter have been published in:

• N. Akhtar et al., J. Power Sources 193 (2009) 39-48.

This new research can open pathways to solve many of the major problems, for which the solid oxide fuel cell (SOFC) community is currently struggling, such as thermal stresses, carbon deposition on anode, robust sealing materials that can withstand in oxidizing/reducing environment and ensure leak proof cells [137, 138, 139].

The concept of operating SOFC with mixed reactants has been discussed earlier in Chapter-3 and a review work has also been summarized in Table 3.3. It can be seen that most of the research considered conventional-planar (sandwiched type) design, a few of them focused on co-planar configuration (or surface migration cell) [17, 26, 27, 28, 30, 32, 35, 39, 40, 42, 45, 58, 66, 67, 69]. Each of these two configurations has its merits and disadvantages, e.g., conventional design is limited by the use of maximum electrolyte thickness, but on the other hand offers two geometrical setup i.e. perpendicular giving better reactant utilization or parallel offering better hydrodynamics [140]. Co-planar design can offer electrolyte supported cells but the open circuit voltage (OCV) is lower than the sandwiched type design because of parasitic losses associated with intermixing of reactants/products. The short distance between the electrodes necessary for minimizing the ionic current transfer path is the main culprit for such intermixing in the vicinity of electrodes [58]. Also, in both the sandwiched and the co-planar design, electrodes are open in the air/fuel mixture environment, intermixing via flushing and convection cannot be completely avoided. However, tubular design can offer some advantages:

• Since one of the electrodes is enclosed in the electrolyte thus the parasitic losses can be reduced to a great extent because of negligible convection of the electrochemically-produced hydrogen, carbon monoxide from anode to the cathode.

• The electrode, which is located in the inner side of the tube, will accelerate the flow due to small inner diameter of the tube enclosure, as compared to the outer electrode, which is enclosed in a larger tube (i.e. the gas chamber tube). Thus, improved mass transfer is expected via forced convection in the inner electrode.

• If the anode is the inner one, the local depletion of fuel will be more by electrochemically-produced water, because the small volume of inner space cannot efficiently replenish the local stream. Cathode as the inner electrode may offer advantage in this case.

• Air/fuel mixture directly supplied to the inner cathode first and then passed to the outer anode (Hibino A-type [16]) can offer better performance.

• Short cells can offer uniform reactant utilization over the cell length.

• Reducing the diameter of the gas chamber tube downstream will accelerate the flow for the outer electrode, thus improving the mass transport via forced convection.

• The partial oxidation reaction (on which the single-chamber SOFC operates) is an exothermic reaction; cells with anode inside will have higher local temperatures than the outer cathode. This will further dilute the reactants/products at the anode via thermal convection. In this case, anode as outer layer will have lower local temperature due to heat transfer to the surrounding gas mixture and walls of the gas chamber.

• In case of stack (where the bunch of cells are located in radial direction across a centered cell) with cathode as an outer layer may cause oxygen depletion. In this case the mixture can become rich in fuel, thereby reducing the stack performance. Mixture of anode/cathode outside cells may level this effect.

In order to take benefit from the above discussion, micro-tubular geometry was opted in this study. The other motivation comes from our earlier numerical studies on single-chamber solid oxide fuel cells [140, 141, 142]. In this chapter, the concept of mixed reactant, micro-tubular solid oxide fuel cells has been presented. This chapter discusses the experimental work carried out by keeping the following objectives in mind:

7.2 Objectives

• Simple experimental set-up (using single-chamber), thus eliminating the need for separate channel for air and fuel.

• Focusing on micro-tubular design, which has several advantages over other available designs (e.g. planar, monolithic etc.) such as rapid start-up, mechanically shock resistant etc.

• Focusing on intermediate temperature (550-800°C) for operation.

• Comparing the reduction methods using hydrogen, methane and methane/air mixtures.

• Comparing the performance using hydrogen, methane and methane/air mixture as fuels.

• Investigating the stability of the cell performance on laboratory scale.

7.3 Experimental

Nickel oxide, yttria-stabilized zirconia (NiO-YSZ) anode supported micro-tubes with yttria-stabilized zirconia (YSZ) as an electrolyte already coated on top of the existing anode, were supplied by Adaptive Materials Inc. (AMI), USA. These tubes were received as anode supported electrolyte micro-

tubes. Two cathode layers were prepared by using the recipe given in [143]. Cathode layer-1 was

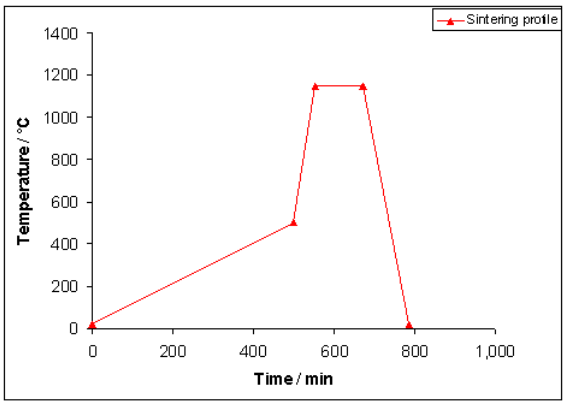

Figure 7.1: Sintering profile for cathode

painted onto the electrolyte later to a length of 30 mm and left to dry overnight. Cathode layer-2 (of same length as of layer-1) was then applied and sintered by using the scheme as shown in Figure 7.1. After sintering, approximately 10 mm length of thin electrolyte was carefully removed for current collection from the exposed anode. Afterwards, silver ink was applied to the exposed anode and also in three small segments (3 mm each) at the cathode. The purpose of applying the silver ink was to enhance electrical conductivity of anode/cathode and catalytic activity of the cathode. Finally, one silver wire was wound around the exposed anode to collect current from the anode side and the other was wound around the cathode to complete the electrical circuit. In order to fix the silver-wire on anode, high temperature cement was used as a sealant, which ensures that anode and cathode silver wires are not short-circuited. This completes the cell preparation and corresponding stages are shown in Figure 7.2.

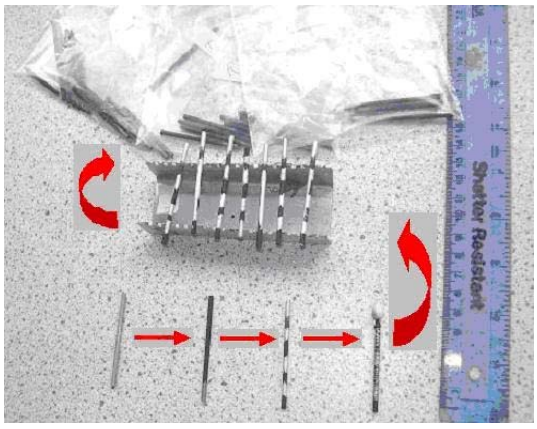

Figure 7.2: Stages in cell fabrication

Table 7.1 summarizes the dimensions of each layer of the cell and the gas chamber tube. Figure 7.3 shows the cross section view of the anode-electrolyte-cathode layer.

Dimensions	Value	Units
Gas-chamber length	285	mm
Gas-chamber outer diameter	13	mm
Gas-chamber inner diameter	11	mm
Cell outer diameter	2	mm
Cell length	55	mm
Anode thickness	200	μm
Cathode-1 thickness	10	μm
Cathode-2thickness	40	μm
Electrolyte thickness	15	μm
Cathode active length	30	mm
Active area	1.885	cm^2

Table 7.1: Geometry dimensions

The cell was kept in the center of the gas-chamber tube with a holder (Figure 7.4). A brick furnace was controlled by a Eurotherm 2402 controller with a K-type thermocouple to measure the furnace temperature. Two Unit Instruments 7300 mass flow controllers were used to control the flow of gases (fuel and air) to the system. The voltage and current data was displayed on a potentiostat which was further manipulated by Microsoft Office Excel programme. The gases used were hydrogen (purity 99.95%), methane (CP-grade) and air (21% oxygen, 79% nitrogen) supplied by British Oxygen Company (BOC).

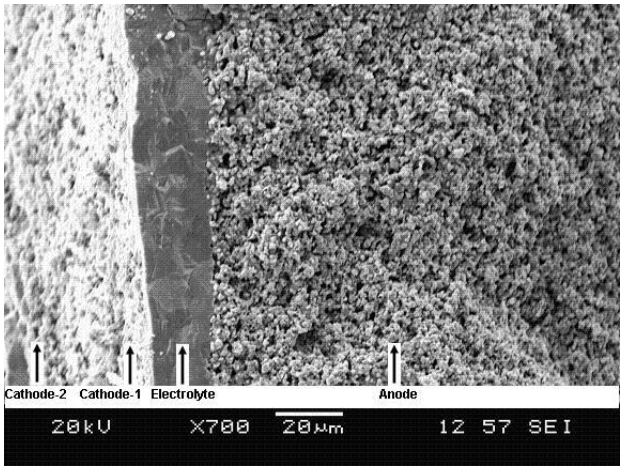

Figure 7.3: SEM photograph of anode-electrolyte-cathode cross section

Figure 7.4: Experimental setup

7.4 Results and Discussion

7.4.1 Reduction Methods

We employed three different reduction mechanisms i.e. hydrogen (20 $mLmin^{-1}$, 800°C [144]), methane (10 $mLmin^{-1}$, 650°C [145]) and methane/air mixture (25/60 $mLmin^{-1}$, 750°C), the cell's OCV was recorded in-situ. Figure 7.5 compares these different reduction schemes and it can be seen that the cell reduction with hydrogen took 50 minutes and the highest OCV of 1.025 V (with 1050 $mA/0.5V$) was recorded in this case. Reduction with methane was not successful, even after 5 hours of operation the OCV was only 102 mV. The cell was then taken out of the gas chamber and it was found cracked. As reported by Shao et al. [68] the cell did reduce but was badly damaged by carbon formation over a long period of reduction. We assume the same reason for low OCV and nearly zero current in this condition. The reduction with methane/air mixture did also work but it was extremely slow, probably due to strong competition between oxygen and fuel reaching the NiO catalyst. It took approximately 9 hours to reduce the cell using air/fuel mixture and the OCV recorded thereafter was 960 mV (with 80 $mA/0.5$ V). We would like to mention here that Shao et al. [68] reported a failed reduction using methane-oxygen ratio (R_{mix} = 1.0), which is probably due to relatively high amount of oxygen present in their mixture, in contrast to our methane/oxygen mixture (R_{mix} = 2.0), which was chosen from a stability study of SC-SOFC [69].

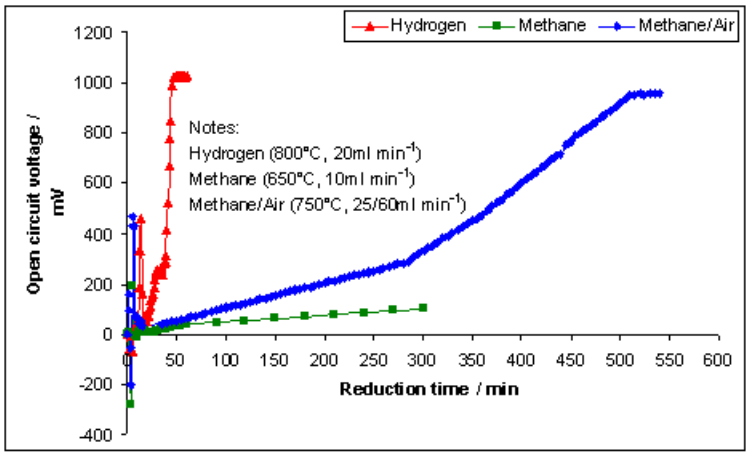

Figure 7.5: Comparison of reduction schemes for hydrogen, methane and methane/air mixture as a reducing fuel for anode

7.4.2 Effect of Mixing Ratio

In order to study the effect of mixing ratio on the cell performance, five different methane/air ratios were opted, i.e. 1:4.76, 1:4, 1:3, 1:2 and 1:1. This range was carefully selected by keeping in mind, the window of possible operation (using methane-air mixtures) under single-chamber SOFC conditions.

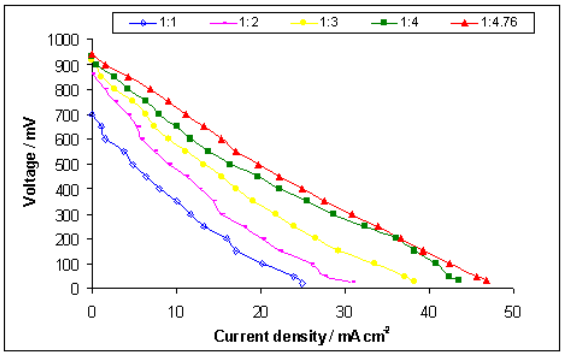

(a)

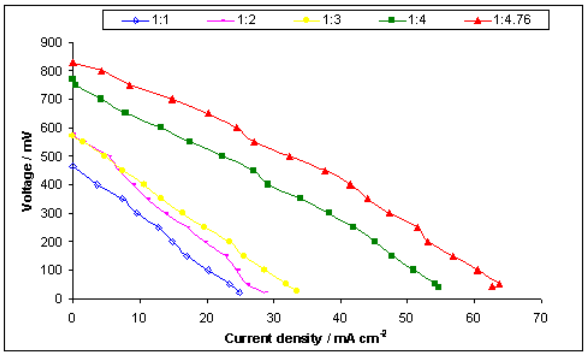

(c)

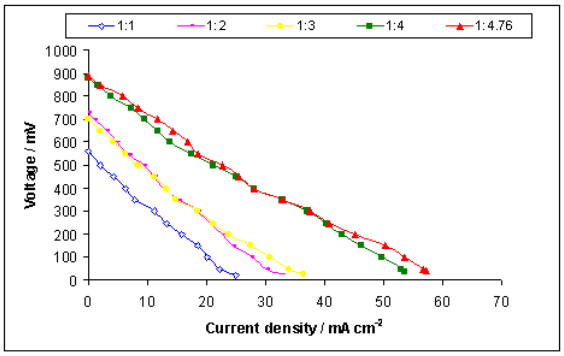

(b)

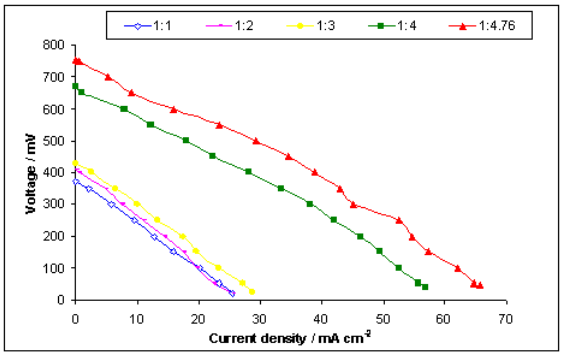

(d)

For example, decreasing the ratio below to that of 1:4.76 can cause severe oxidation of nickel

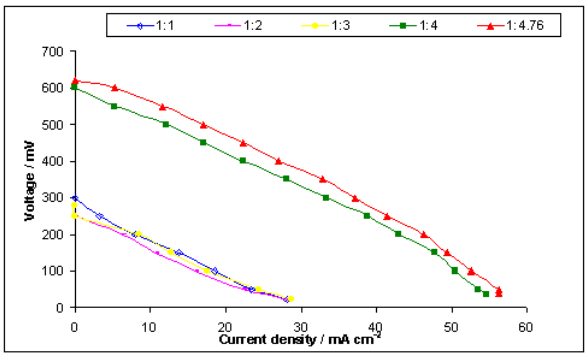

(e)

Figure 7.6: I-V curves at (a) 550, (b) 600, (c) 650, (d) 700, (e) 750°C temperatures for various methane/air mixtures (total flow rate = 12 $mLmin^{-1}$)

anode (depending upon area ratio of the electrodes) and also the mixture may become explosive (5-15% by volume methane in air is explosive at standard conditions). On the other hand, operations at high methane/air ratios beyond 1:1 can cause severe coking (depending upon area ratio of the electrodes) on nickel anodes [65].

The effect of mixing ratio on the cell performance was observed at different operating temperatures from 550-750°C. Figures 7.6 (a-e) show their effect on I-V characteristic of the cell. In all these figures a common trend has been observed showing methane/air = 1:4.76 as the best and 1:1 giving the worst performance. An interesting behavior noted is the marginal increase in performance at methane/air ratio of 1:4.76 with increasing temperature as compared to all other mixing ratios. Though this trend shows that higher air/fuel ratios are better, but nothing can be drawn about stability of the performance from these curves. A detailed stability analysis is therefore necessary to declare them as the best mixing ratios. We would like to mention here that there are several reports [20, 21, 23, 29, 32, 39, 43, 48, 56, 66] stating the best performance was achieved at methane/air ratio of 1:4.76 (R_{mix} = 1.0) and also some reports [8, 25, 27, 33, 35, 36, 41, 47, 66, 67, 69] focusing at methane/air ratio of 1: 2.4 (R_{mix} = 2.0).

This contradiction depends on many parameters such as electrode microstructure and material, geometrical configuration, reduction technique and the operational temperature. The best performance achieved in our case at methane/air ratio of 1:4.76 could possibly be due to improved oxygen reduction rate at the LSM cathode because of abundant supply of oxygen at these mixing ratios [20].

7.4.3 Effect of Operating Temperature

Figure 7.7 shows the effect of operating temperature on OCV and the current density at 0.5 V with cell operating at 10/47.6 $mLmin^{-1}$ methane/air flow rate. The maximum current density (at 0.5 V) has a peak at a temperature of 750°C, therefore, this point will be considered as the operating point temperature. The drop in performance beyond 750°C is probably due to cathode becoming active towards parasitic reactions (methane oxidation) [16]. The OCV has a peak at 600°C and it drops thereafter, and this trend is partly due to less Gibbs free energy available with increasing temperature and partly because of enhanced partial oxidation reaction at anode consuming more oxygen.

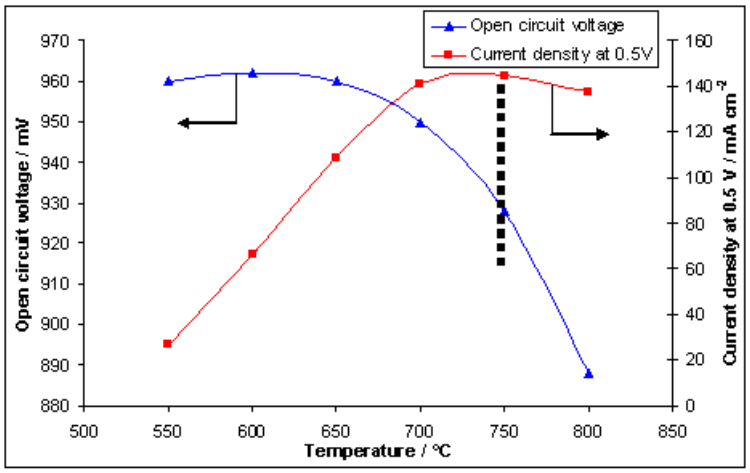

Figure 7.7: Temperature vs. OCV and current density at 0.5 V for methane/air mixture of 10/47.6 $mLmin^{-1}$

7.4.4 Effect of Flow Rate

After deducing the results from Figures 7.8 (a-e), it was found that methane/air ratios of 1:4.76 giving the better performance as compared to other mixing ratios; therefore, the effect of flow rate was analyzed at different temperatures by keeping the mixing ratio as fixed at methane/air of 1:4.76. In Figure 7.8, 0.5 V was assumed as the operating cell voltage and the cell current was recorded at different temperatures with increasing mixture flow rates. The maximum current density was found at higher flow rates with a peak at a temperature of 750°C. It is worth noting here that although the current density through the cell increases with increasing flow rate, but this could reduce the cell efficiency due to low utilization at higher flow rates. In order to maintain high electrical efficiencies, either stack of cells can be designed to increase utilization, or, off gas recirculation must be made in stages (cascading) to improve the overall efficiency of the system.

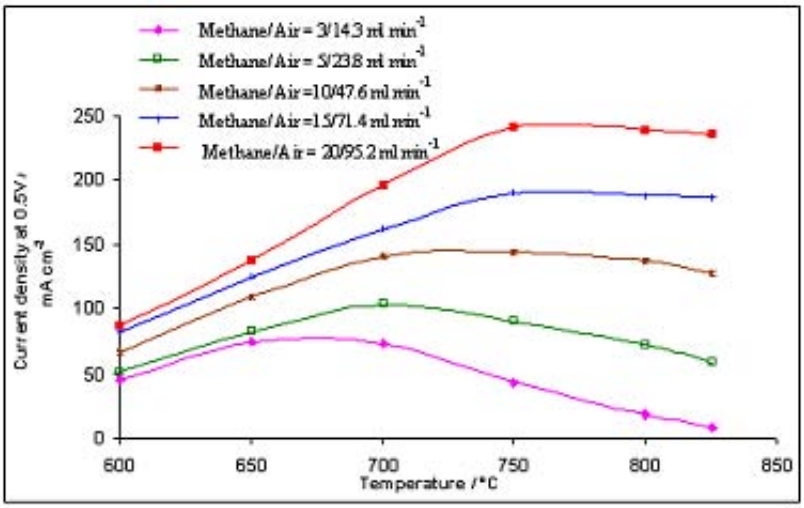

Figure 7.8: Temperature vs. current density at $0.5V$ for methane/air ratio of 1:4.76 at different flow rates

7.4.5 Effective Fuel Utilization and Effective Efficiency

The effective fuel utilization and effective efficiencies corresponding to Figures 7.6-7.8 are listed in Tables 7.2-7.4, respectively. As can be seen, these values are strongly dependent upon operating temperature, methane-air ratio and fuel flow rate. The highest effective fuel utilization (11.41%) and effective efficiency (5.48%) was obtained at 650°C, methane-air ratio of 1:4.76 with a fuel flow rate of 3 $mLmin^{-1}$. These extremely low values of fuel utilization and electrical efficiencies (of SC-SOFCs) are one of the major barriers against their practical implementation. During our experiments, it has been observed that this type of design offers more thermal heat as compared to electrical power, suggesting their potential use in combined heat and power (CHP) applications.

Shao et al. [19] in their experiments effectively used this thermal heat to sustain the fuel cell

	Fuel utilization/effective efficiency (%) at different temperatures				
CH_4:air	550°C	600°C	650°C	700°C	750°C
1:4.76	5.13/2.22	7.58/2.55	8.68/3.75	7.94/3.43	7.58/2.55
1:4	4.27/1.64	6.31/2.12	5.19/2.24	6.41/2.16	6.41/1.85
1:3	2.36/1.02	2.85/0.82	2.52/0.72	2.68/0.51	1.95/0.28
1:2	1.46/0.56	2.13/0.61	1.95/0.47	1.65/0.31	1.22/0.17
1:1	0.77/0.26	0.85/0.24	0.97/0.23	0.97/0.18	1.05/0.15

Table 7.2: Fuel utilization and effective efficiency calculated for Figures 7.6 (a-e)(total flow rate = 12 $mLmin^{-1}$)

temperature in the absence of external heat source. Liu et al. [20] have suggested some ways to improve the fuel utilization, we add some more. For example, increasing the gas velocity with a

	Fuel utilization/effective efficiency (%) at different temperatures					
CH_4:air	550°C	600°C	650°C	700°C	750°C	800°C
1:4.76	1.24/0.59	3.05/1.46	5.01/2.40	6.5/3.12	6.65/3.19	6.33/3.04

Table 7.3: Fuel utilization and effective efficiency calculated for Figure 7.7 (CH_4:air= 10/47.6 $mLmin^{-1}$)

	Fuel utilization/effective efficiency (%) at different temperatures					
CH_4/air ($mLmin^{-1}$)	600°C	650°C	700°C	750°C	800°C	825°C
3/14.3	6.92/3.33	11.41/5.48	11.24/5.40	6.52/3.13	2.85/1.37	1.22/0.58
5/23.8	4.64/2.23	7.58/3.64	9.53/4.58	8.31/3.99	6.60/3.17	5.37/2.58
10/47.6	3.05/1.46	5.01/2.40	6.50/3.12	6.65/3.19	6.33/3.04	5.86/2.82
15/71.4	2.54/1.22	3.83/1.84	4.97/2.39	5.83/2.80	5.77/2.77	5.75/2.76
20/95.2	2.00/0.96	3.17/1.52	4.52/2.17	5.55/2.66	5.50/2.64	5.42/2.60

Table 7.4: Fuel utilization and effective efficiency calculated for Figure 7.8 (CH_4:air= 1:4.76)

nozzle for injecting air/fuel mixture in to the gas-chamber or by reducing the diameter of the gas-chamber tube, exhaust gas re-circulation in cascading, combustion of exhaust air/fuel mixture in an after-burner and utilize the produced heat either for CHP purpose or to pre-heat the inlet air/fuel mixture to the gas-chamber.

7.4.6 Output Performance

The cell performance was compared (as shown in Figure 7.9) with dual-chamber hydrogen operated (750°C, 20 $mLmin^{-1}$), dual-chamber methane operated (750°C, 5 $mLmin^{-1}$) and single-chamber methane/air operated (750°C, 20/95.2 $mLmin^{-1}$) micro-tubular cell. In dual-chamber configuration

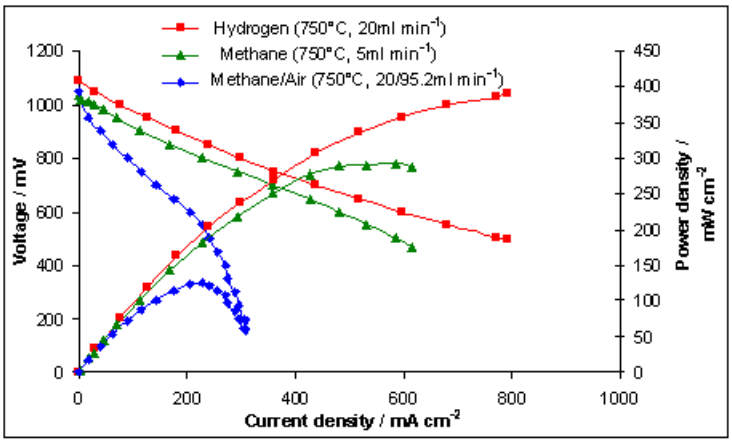

Figure 7.9: Performance curve for hydrogen (dual-chamber), methane (dual-chamber) and methane/air (single-chamber) as a fuel

the fuel was supplied to the anode and the cathode was exposed to ambient air, whereas for single-chamber condition, both the anode and the cathode were supplied with same air-fuel mixture. Since

it is not wise to compare different fuels with same flow rates (because each fuel has its own heating value, different number of electrons participating in the reaction and different mechanism to produce electrical power), therefore for hydrogen and methane, the flow rates were chosen from [144, 145] for an optimum performance of a micro-tubular cell of same dimensions used in this study. The maximum power density (p_{max}) of hydrogen (dual-chamber), methane (dual-chamber) and methane-air (single-chamber) at an operating voltage of 0.5 V was 385, 293 and 122 $mWcm^{-2}$, respectively. It shows that the cell performance under methane/air operated single-chamber conditions is approximately 3 times lower than that of hydrogen operated dual-chamber cell. This shows that even without optimization of microstructure, flow management, fuel utilization and selectiveness of the electrodes, the single-chamber conditions can provide an acceptable level of performance. Further studies are required to optimize these parameters in order to boost the performance closer to that of dual-chamber configuration.

In Table 3.3 (Chapter-3), a summary of earlier work on SC-SOFCs done by many researchers has been reported. Although, it will not be appropriate to compare this study with the work done by other groups due to different manufacturing techniques (electrode/electrolyte microstructure, thickness, sintering temperature), operating temperature, flow rates, mixing ratio etc., still it will be worth to have a quick look on those using the same conventional materials. Studies based upon using the same conventional materials (i.e. Ni-YSZ/YSZ/LSM), same SC-SOFC type (Hibino B-type [16]) and same fuel (methane) highlight the following [23, 33, 34, 46, 47, 66]:

• In this present study, the lowest fuel flow rate (20 $mLmin^{-1}$ with methane-air ratio of 1:4.76) is used.

• The total flow rate is also the lowest in this study (115.2 $mLmin^{-1}$ with methane-air ratio of 1:4.76).

• The OCV obtained in this study is the highest (1.05 V) at 750°C with methane-air ratio of 1:4.76. The same OCV was also obtained by Napporn et al. [47] at 800°C using methane-air mixture (methane-oxygen ratio of 2.0), however the total flow rate used in their study was relatively high i.e. 350 $mLmin^{-1}$.

• The highest power density reported was 360 $mWcm^{-2}$ at 800°C using methane-air mixture (methane-oxygen ratio of 0.88) with a total flow rate of 350 $mLmin^{-1}$ [46]. Since the flow rate used for obtaining this power density was rather high, we made an attempt to compare our results with a relatively comparable flow rates used in our study. In Figure 9 of Ref. [46], authors used a total flow rate of 150 $mLmin^{-1}$ (methane-oxygen ratio of 0.63) at 800°C. This corresponds to approx-

imately 17.5 $mLmin^{-1}$ of methane and 132.5 $mLmin^{-1}$ air, giving ca.140 $mWcm^{-2}$. However, the methane-oxygen ratio of 0.63 comes in the explosive range of 5-15% methane by volume in air, which is not practical for working at higher flow rates. In comparison to this, our study employs 20 $mLmin^{-1}$ of methane and 95.2 $mLmin^{-1}$ air, giving approximately 122 $mWcm^{-2}$ at a slightly lower temperature (750°C) to that of used in Ref. [46]. The total flow rate used in our study was also slightly lower (115.2 $mLmin^{-1}$) and the methane-air mixture (methane to oxygen ratio of 1.0) employed was relatively safe. Therefore, this study confirms that the micro-tubular design can offer some advantages in terms of higher OCV and comparable performance.

7.4.7 Stability

The cell stability was monitored at a methane/air ratio of 1:4.76 (at 0.5 V) for 32 hours. Initially, up to 24 hours the degradation in the cell performance was 0.05%, thereafter, oscillations (of increasing magnitude with respect to time) in current density were observed (Figure 7.10).

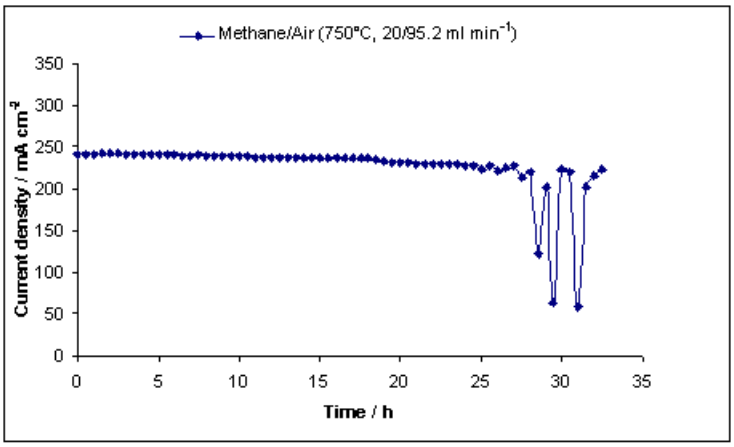

Figure 7.10: Stability test for current density at 0.5 V vs. time in hours

This shows that although, 1:4.76 was giving the best I-V curves (as shown above) but its performance was not stable and therefore this mixing ratio must be avoided, probably re-oxidizing the anode with high amount of air present in the mixture. The cell was taken out of the chamber and the anode surface was analyzed by scanning electron microscopy (SEM). Figure 7.11 shows pitting of the anode surface possibly due to oxidation-reduction cycles on anode surface resulting in loss of nickel as reported by Kuhn et al. [69]. The silver current collecting wire was also damaged (as shown in Figure 7.12), the real cause of silver rupture was not clear, but it has been speculated that either the excess local heat generation or silver dissolution due to oxidation could be the reason. We will investigate more into this in the next chapter.

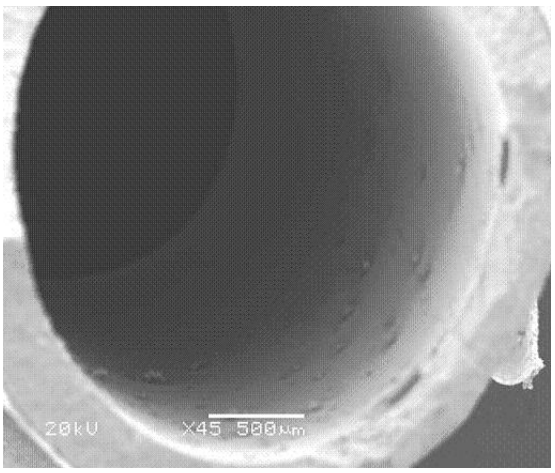

Figure 7.11: SEM photograph of anode surface after operation of 32 hours at methane/air ratio of 1:4.76

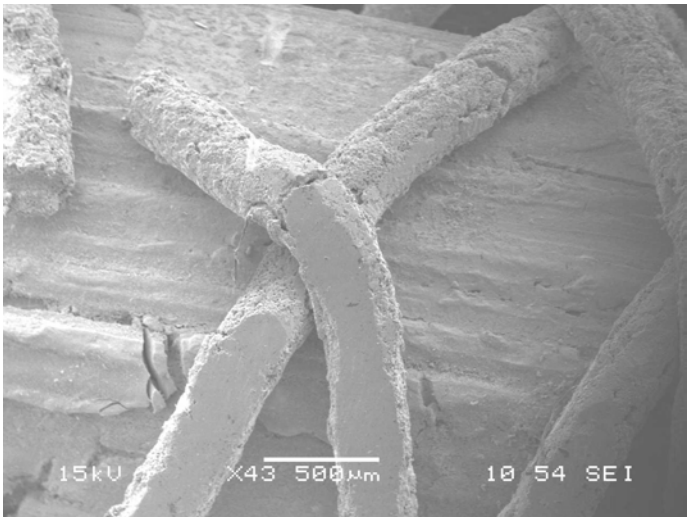

Figure 7.12: SEM photograph showing silver rupture

7.5 Conclusions

The anode was successfully reduced by using methane/air mixture ratio (1:2.4) at a temperature of 750°C but it took approximately 9 hours to reduce the anode and also the current drawn through the cell was lower. It became clear that although the methane/air mixture ratio of 1:4.76 gives best performance at all operating temperature ranges studied, however, the degradation test shows that operating at such a mixing ratio cannot run longer than 24 hour. Thereafter, oxidation/reduction of nickel is expected and fluctuations in current density are observed. It has also been observed that the output performance increases with increase in flow rate but this could reduce the fuel utilization and thus current efficiency of the cell. In order to improve utilization and efficiency, the cells must be operated in stack. The comparison of hydrogen, methane and methane-air mixture operated cell

shows that the cell can give one-third power output in single-chamber conditions without any optimization and selectiveness of the cell materials. Furthermore, the anode surface was damaged after oxidation/reduction cycles due to operation at a methane/air ratio of 1:4.76, and, pitting of the anode material is clearly observed. The silver current collecting wire was also damaged either due to silver oxidation or because of local excess heat generation.

CHAPTER 8

SC-SOFC TEMPERATURE MEASUREMENTS[5]

8.1 Introduction

Single-chamber solid oxide fuel cell's operation depends upon catalytic activity of the anode and electro-catalytic activity of the cathode. Moreover, the high selectivity of both electrodes towards electrochemical reaction (i.e. fuel oxidation at anode and oxygen reduction at cathode) is essential for better performance. The catalytic activity of the electrode materials (particularly of anode) also generates large amount of heat, which leads to the establishment of actual cell temperature that differs significantly from the furnace temperature [14, 17, 46]. The amount of heat release depends upon many parameters such as, the type of fuel, fuel-to-oxygen ratio, electrode materials, active area, cathode-to-anode area ratio and electrode placement. While previously it was thought that the core reaction within the anode (in case of SC-SOFC) is a partial oxidation reaction, recently Hao et al. [78] suggested three different reaction zones within the anode electrode, namely, the combustion zone, the reforming zone and the water-gas shift reaction zone. The existence of complete combustion zone is more severe than the partial oxidation zone and can generate large amounts of exothermic heat depending upon the type of fuel employed. Such overheating on one side could be advantageous, as one can make use of this heat to thermally self-sustain the system [19]. On the other hand, this overheating could result in structural damage and thermally driven degradation problems.

In the previous chapter it has been reported that the nickel oxidation/reduction and silver rupture

---

[5] The results described in this chapter have been published in:

- N. Akhtar et al., J. Power Sources, doi:10.1016/j.jpowsour.2009.04.078.
- N. Akhtar et al., Intl. J. Hydrogen Energy 34 (2009) 7807-7810.

are the two major causes affecting the cell's long term stability. We made an attempt to investigate the cause of silver rupture, as the nickel oxidation/reduction behavior is already under investigation by the SOFC community. In our previous stability experiment, the silver current collecting wire seems to be damaged either due to the lack of structural stability under mixed-reactant environment or due to local excess heat generation. The structural stability of silver can be tested by running short-term durability experiments under appropriate operating conditions. The local heat generation can be investigated by varying the cell's active area and to measure the cell's temperature across the length. In this chapter, we made an attempt to investigate both of these issues. We first investigated the local temperature distribution across the cell length with varying active area. For this purpose four different cells with varying cathode location/size i.e. inlet, center, outlet and full size have been prepared and tested. In the following discussion, all the results are normalized against the corresponding geometric cathode areas. Finally, scanning electron microscopy (SEM) analysis has been performed in order to observe changes in the cell structure.

8.2 Experimental

8.2.1 Cell Preparation

Four different cell configurations have been prepared as shown in Figure 8.1. The cells consist of Ni-YSZ/YSZ/LSM, anode/electrolyte/cathode assembly. The geometry dimensions and cell preparation methodology is described in the previous chapter. The cell was kept in the center of the gas-chamber tube with a holder. A brick furnace was controlled by a Eurotherm 2402 controller with a K-type thermocouple to measure the furnace temperature. An additional thermocouple was inserted into the

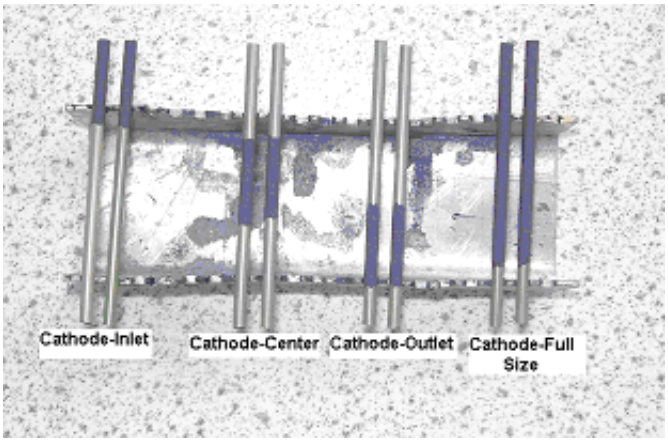

Figure 8.1: Four different cells with varying cathode location/size

micro-tube to measure the anode surface temperature as shown in Figure 8.2. Since the chemical reaction is taking place at the anode (via partial or full oxidation of the methane), it was necessary to measure the temperature directly at the anode surface because of large amount of heat generated at this location. The rest of the geometrical setup was the same as reported earlier in Chapter-7.

The anode surface temperature was measured at three different locations along the length, i.e. near the inlet (3 mm from inlet), at the center (18 mm from inlet) and near the cell outlet (36 mm from inlet). The active cell length was 18 mm for the cathode-inlet, center and outlet configurations whereas for the cathode full-size configuration, it was 39 mm with a total length of 55 mm for all cells. All cells were supplied with methane/air mixture of 25/60 $mLmin^{-1}$. The furnace temperature (T_F) was varied from 550-800°C and the cell temperature was measured for all four configurations (as described above).

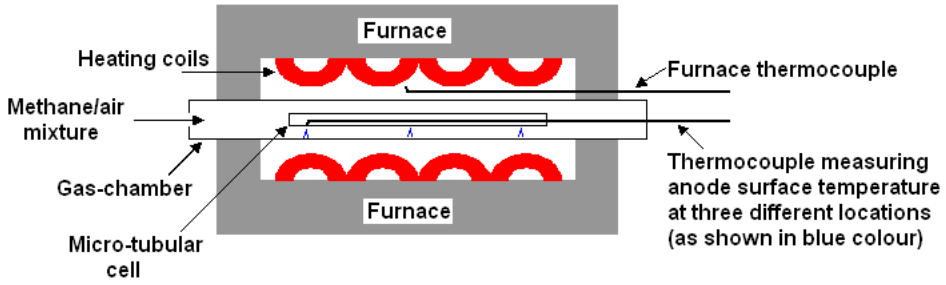

Figure 8.2: Temperature measurement setup

8.3 Results and Discussion

8.3.1 Cell Temperature

In Figures 8.3(a-f), cell temperature (at various furnace temperatures of 550-800°C) is shown for inlet, center, outlet and full-size configurations. At low temperature such as 550 and 600°C, the highest temperature rise (at the middle of the cell) is observed in cathode-center configuration (Figure 8.3(a) and (b)). However, contrary to this as we move along increasing furnace temperatures, the highest cell temperature is observed near the cell inlet in case of cathode-full size and cathode-inlet configurations (Figures 8.3(c-f)). Clearly the highest temperature rise in case of cathode-full size is misleading, since

it has larger active area (A=2.45 cm^2) as compared to the other three configurations (A=1.13 cm^2). The area-normalized values of temperature show that with increasing furnace temperature, cathode-inlet configuration has the highest temperature. Furthermore, the local cell temperature is pronounced near the cell inlet for this configuration. This observation is further supported by the following arguments:

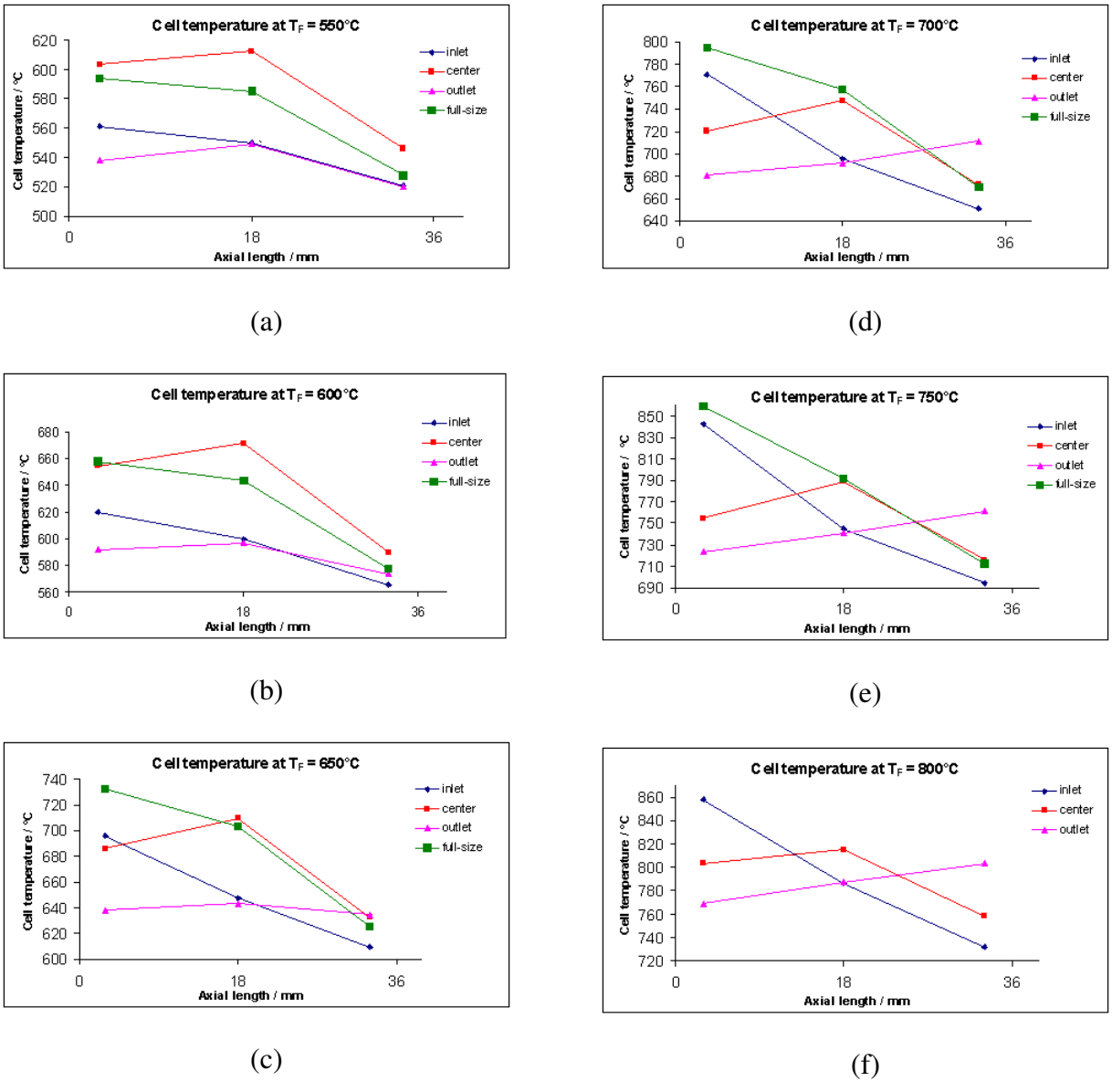

Figure 8.3: Cell temperature measurement at (a) 550, (b) 600, (c) 650, (d) 700, (e) 750, (f) 800°C furnace temperatures

• The nickel anode seems to be active towards fresh air/fuel mixture. As we move along the cell length, the mixing ratio may vary due to catalytic and electrochemical reactions. It appears that the reaction behavior of nickel is very similar to that observed in case of steam reforming (i.e. the cooling

effect near the cell inlet due to endothermic reaction). In this case, it is heating effect near the cell inlet due to exothermic reaction.

• The cathode loses its selectivity towards electrochemical oxidation (or becomes catalytically active towards methane oxidation) as the temperature increases. The presence of cathode at the inlet is an addition of parasitic loss (or in other words heat addition) at that location.

• The commonly used nickel anode is not perfectly selective for partial oxidation reaction and loses its selectivity as the temperature increases. As pointed out by Hao et al. [78], the oxygen could be nearly fully consumed in the outermost anode region (near the anode-gas interface) via complete combustion mechanism. It is obvious from this argument that the increase in temperature will promote full combustion instead of partial oxidation, thereby further addition of heat.

It is important to note that we did not measure the cell temperature for full-size configuration at T_F = 800°C, because of similar expected temperature rise may reach close to the melting point of silver and could damage the current collecting wires. Further to this, important information coming out from cathode-center and outlet configurations (pink and red curves in Figures 8.3(d-f)) is that it is not only the nickel anode, which is solely responsible for highest temperature rise in case of cathode inlet, the presence of cathode has a greater influence. For example, the cathode-center and cathode-outlet configurations show a clear maximum temperature rise near the center and outlet of the cell, respectively. This effect was not that marginal at low furnace temperatures (550-600°C) suggesting that the cathode activity towards methane oxidation at higher temperature could be the reason. Moreover, the highest cell temperature in cathode-center configuration suggests that the center location is acting as a heat confinement and this effect is dominant at low temperatures (550-600°C). At furnace temperatures greater than 600°C, the heat contribution due to catalytic/electrochemical oxidation of fresh air/fuel mixture is becoming dominant.

8.3.2 Open Circuit Voltage (OCV)

The effect of furnace heating on the open circuit voltage for four different configurations is shown in Figure 8.4. As can be seen, the highest OCV is observed in the case of cathode-outlet configuration. This observation is in good agreement with the study done by Morel et al. [146]. They used closed gas distribution plates (GDP) to prevent any gas leakage due to combustion resulting in volume expansion. Their idea was to maintain high oxygen partial pressures on the cathode side by confining the surrounding fresh gas mixture in cathode-outlet configuration. Our study further confirms their

hypothesis of local gas confinement resulting in higher OCV in cathode-outlet configuration. The micro-tubular geometry is itself acting as a closed GDP and preventing any cross diffusion across the electrodes. The cathode-outlet configuration further confirms the availability of fresh air/fuel mixture with nearly unaltered oxygen partial pressure at the cathode located near the cell outlet. Contrary to

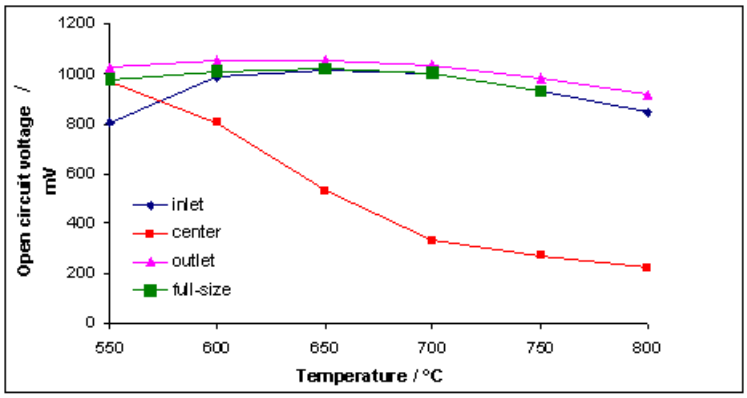

Figure 8.4: Temperature vs. open circuit voltage

this, the air/fuel mixture in the anode (located inside of the micro-tube) is continuously depleted and becomes oxygen deficient when it reaches to the cell outlet. The higher oxygen partial pressure differential across the electrodes gives a clear indication of highest OCV in cathode-outlet configuration.

The cathode-center configuration was giving very low OCV as we increase furnace temperature. This can be explained by two mechanisms: 1) as previously mentioned the cathode parasitic losses (due to fuel oxidation) increase with increasing temperature, 2) the gas velocity (and the amount of gas available) in the vicinity of the center of the tube could be limited which can increase the residence time for parasitic reactions at the cathode located at the center.

8.3.3 Output Performance

For measuring the output performance, the cells were supplied with a methane/air mixture of 25/60 $mLmin^{-1}$ for all four configurations. The flow rate was kept very low in order to improve the effective fuel utilization and electrical efficiency. The highest effective fuel utilization and electrical efficiency was 2.35% and 1.13% (at a furnace temperature of 750°C) for cathode-full size, respectively (for details about this calculation the reader should refer to Ref.[72]). The other three configurations (i.e. cathode-inlet, center and outlet) showed even lower fuel utilization because of less amount of total current generated due to less active area.

Figure 8.5 shows the performance curves for four configurations. As can be seen at low temperature (less than 600°C), cathode-center configuration is giving the best performance (Figure 8.5(a)).

However, as the temperature increases beyond 600°C, its performance is becoming worse than the other three configurations (see Figures 8.5(b-e)). This trend is due to steep decrease in OCV of the cathode-center position as discussed above. It should be noted that the OCV provides the driving force for current flow once the circuit is opened.

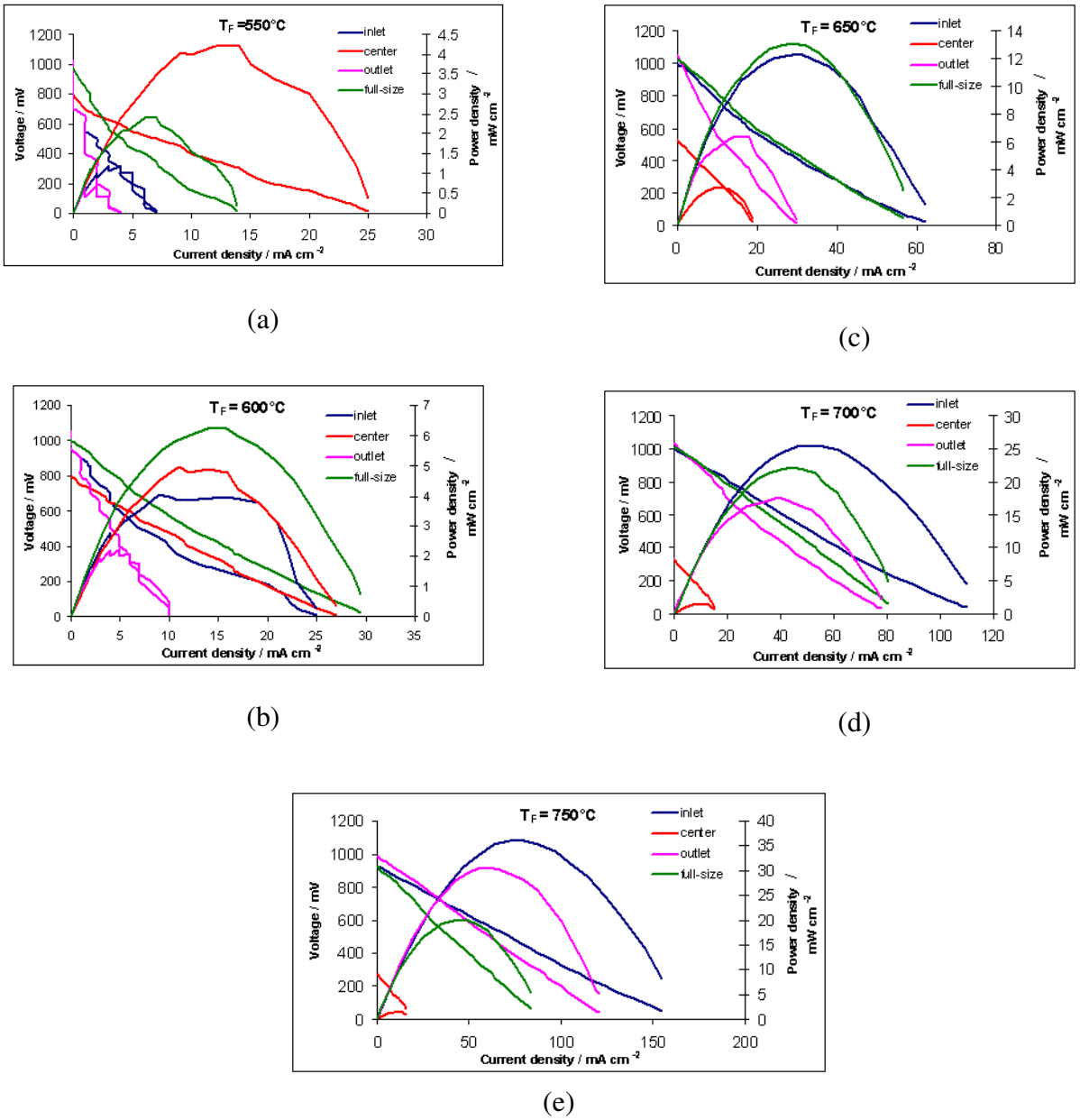

Figure 8.5: Performance curves at (a) 550, (b) 600, (c) 650, (d) 700, (e) 750°C furnace temperatures

All other configurations (i.e. inlet, outlet and full-size) follow nearly same trend with increase in temperature, i.e. the electrolyte conductivity improves with increasing temperature, and therefore more current is expected. The best performance was observed in case of cathode-inlet configuration in the temperature range of 700-750°C, which is the most practical operating regime for high

temperature ionic conductor (YSZ) employed in SC-SOFCs. The highest cell temperature in the cathode-inlet configuration enhances local ionic conductivity of the electrolyte, thereby resulting in improved performance. Furthermore, it is also observed that with increasing temperature cathode-outlet configuration is showing improved performance. The next highest performance at 750°C is of cathode-outlet configuration (Figure 8.5(e)). It is suggested that in this case the inner anode is acting as a catalytic reactor up to two-third of the cell length, thus supplying pre-reformed reactants (such as hydrogen and carbon monoxide) to the last part of cell where the cathode is located and to be ready for electrochemical reactions.

8.3.4 Structural Analysis using Scanning Electron Microscopy

The above results show that the cathode inlet configuration has the highest temperature rise and the cathode-outlet configuration is undergoing less temperature gradient across the length. We therefore analyzed these cells by taking a sample of anode and cathode surfaces near the inlet for both configurations. The SEM photograph (Figure 8.6(a, b)) shows that both the anode and cathode surfaces (near the inlet) are badly damaged and cracked in case of cathode-inlet configuration. This effect confirms the severity of local temperature rise near the inlet.

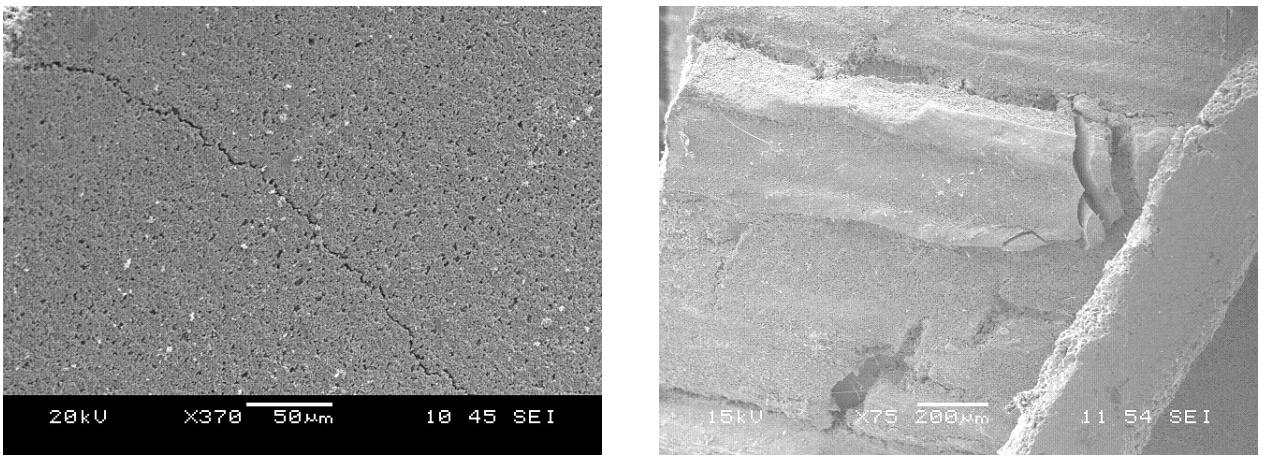

(a) (b)

Figure 8.6: Cracked anode (a) and damaged cathode (b) near the cell inlet for cathode-inlet configuration

On the contrary, Figure 8.7 (a, b) shows that both the anode and cathode surfaces (near the inlet) were relatively undamaged and no visible crack was observed in case of cathode-outlet configuration.

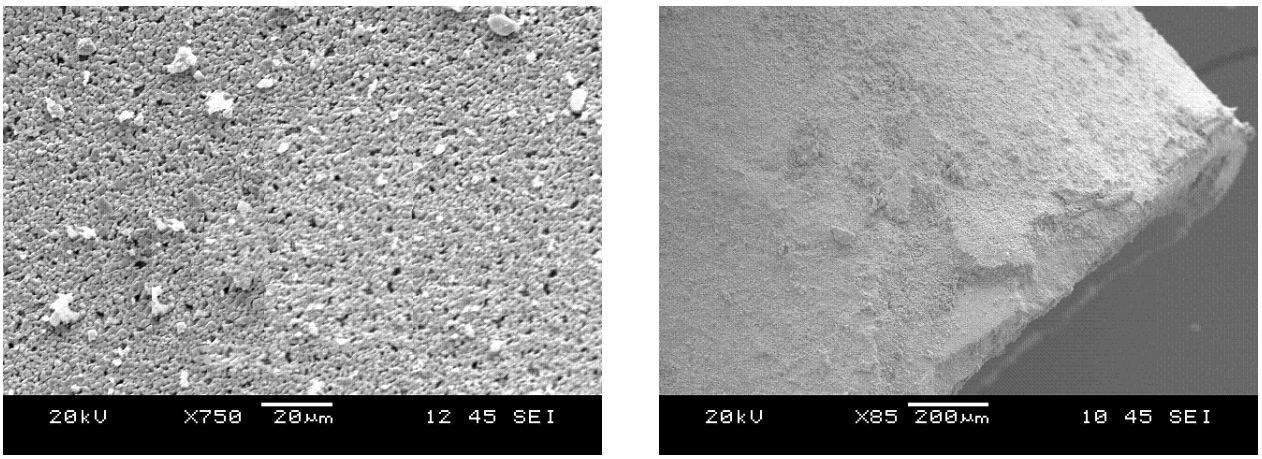

(a) (b)

Figure 8.7: Undamaged anode (a) and cathode (b) near the cell inlet for cathode-outlet configuration

It is therefore concluded that the local temperature may have a serious effect in structural damage that could lead into thermal shock problems.

8.4 Structural Stability of Silver

The current collectors are one of the cell components, which have to be resistant and structurally stable under single-chamber conditions. The past work on SC-SOFC shows that silver (Ag), gold (Au), platinum (Pt), nickel (Ni) and stainless steel (SUS) are the most commonly employed current collectors [17, 18, 19, 71]. Among these various current collectors, silver is widely employed in solid oxide fuel cells due to its high electrical conductivity and lower cost as compared to other current collecting materials such as Pt and Au. Although, the behavior of silver in a dual-atmospheric environment has been reported earlier [147, 148, 149], its exposure under real SC-SOFC conditions has never been addressed. This section is devoted to demonstrate the structural stability of silver under SC-SOFC conditions.

For structural stability test, silver current collecting wire (99.99% silver, 0.5 mm diameter, 25 SWG, Scientific Wire, UK) was examined which was used for current collection from both electrodes. The micro-tubular cells were operated using a methane/air mixture of 25/60 $mLmin^{-1}$ at an operating temperature of 750°C with a current loading corresponding to 0.5 V. Different cells were exposed under these conditions for different time spans (i.e. one, two, three and four days of continuous operation, after which the wire was broken) in order to investigate the extent of structural degradation in the silver current collectors located at the cathode side.

8.5 Results and Discussion

Figure 8.8 shows the scanning electron microscope (SEM) photograph of silver current collecting wire after first day of operation. As can be seen, no visible degradation is observed in the current collecting wire, except some surface changes possibly due to the formation of silver oxide in the presence of oxygen (this will be discussed, shortly). When the SEM photograph was taken again after

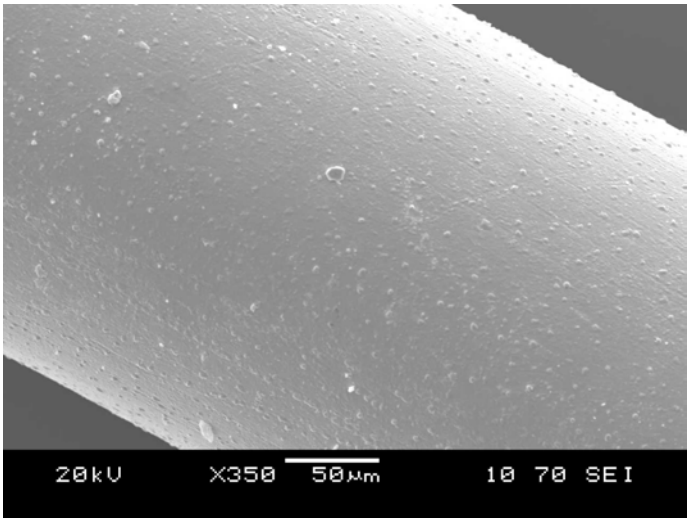

Figure 8.8: SEM photograph showing silver current-collecting wire after the first day of exposure under SC-SOFC conditions

second day of continuous operation, some porosity has been observed in the current collecting wire (Figure 8.9(a)). A magnified view of the SEM photograph shows a clear presence of cavities and some melting of the silver wire (Figure 8.9(b)).

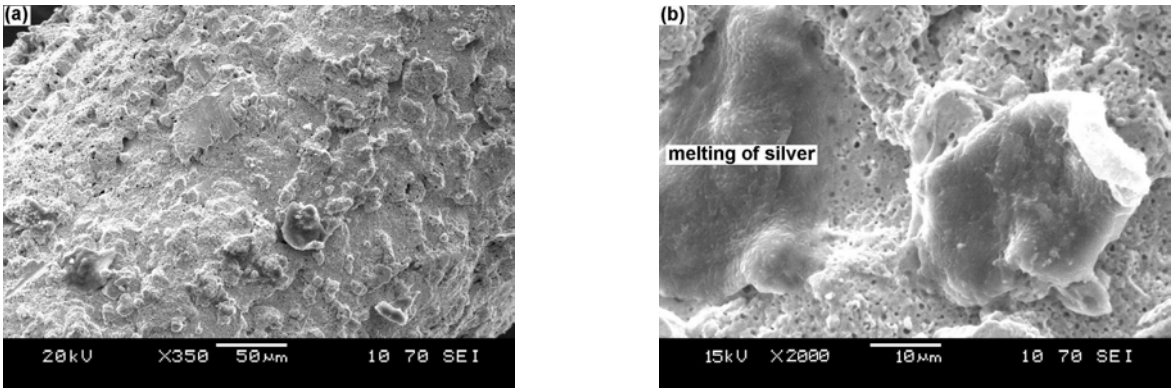

(a) (b)

Figure 8.9: (a) SEM photograph showing cavity nucleation in silver wire after the second day of exposure under SC-SOFC conditions, (b) Magnified view of (a)

This observation is not surprising, as it is well documented that when silver is exposed to the dual-atmospheric environment (i.e. oxygen on one side and hydrogen on the other); it undergoes rapid structural degradation [147]. The main cause of reported degradation was the simultaneous dissolution of various species, particularly hydrogen and oxygen that react together to form water vapors. The water vapor pressure tends to increase with increase in gaseous solubility until a critical pressure is attained corresponding to the critical solubility of the species. Once this threshold is reached, any additional oxygen and hydrogen diffusion led to the formation of water bubbles followed by cavity nucleation and growth [147]. Furthermore, It is believed that silver in the presence of oxygen (in the temperature range below 230°C) forms oxide scales. On the other hand, at temperatures above 230°C, silver loses its affinity for oxygen and the formed silver oxide becomes thermodynamically unstable. The silver releases oxygen at this point and results in the formation of a foam like structure [149, 150].

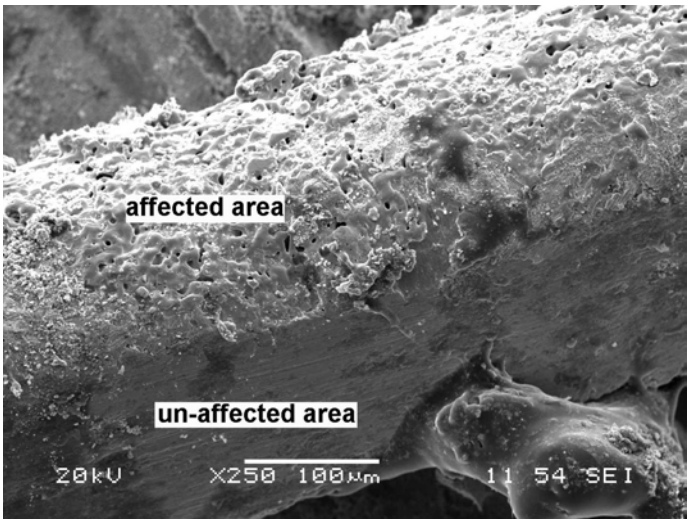

Figure 8.10: SEM photograph showing affected and unaffected area in silver wire after the second day of exposure under SC-SOFC conditions

In our experiments, although, no hydrogen (or carbon monoxide) is present at the cathode side (due to the tubular cell configuration), water formation due to the above mechanism seems to be highly unlikely. However, it should be noted that silver has been studied as a cathode material because of its high catalytic activity for oxygen reduction [151]. It provides active sites for oxygen reduction reaction; oxygen can adsorb, dissociate and diffuse through silver [151]. The likeness of oxygen by silver provides a catalyst support for methane oxidation. This results in full combustion of methane over silver, causing similar effects as reported in case of hydrogen combustion by other researchers [147, 148, 149]. Furthermore, as reported by other researchers, silver oxide formation

followed by its vaporization and silver melting could also have had contributed to its degradation in our experiments.

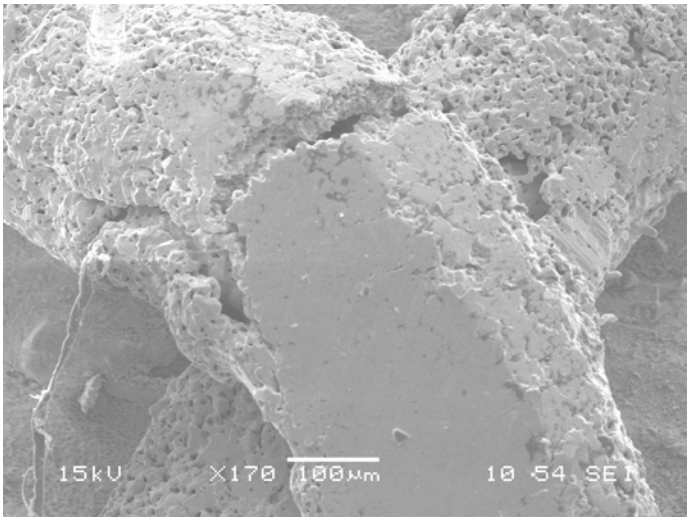

Figure 8.11: SEM photograph showing extended porosity and mechanical failure of silver wire after the third day of exposure under SC-SOFC conditions

Figure 8.10 shows that the area of current collecting wires that was not fully exposed to the gaseous environment has little degradation and porosity as compared to the upper part that was under direct exposure. Meulenberg et al. [149] have reported that the mass loss of silver (due to silver vaporization) is related to the silver surface area being directly exposed to the gas atmosphere. They used silver rivets as contact material in order to reduce the directly exposed area and found that the absolute mass loss of silver is significantly reduced because of less area exposed to the gas environment. A similar argument will support our investigation.

Figure 8.11 was taken after third day of continuous operation. It shows that the current collecting wire has undergone extended degradation and porosity with respect to time and it was ruptured at locations of greater stress (such as bends).

After fourth day of continuous operation under single-chamber conditions, a fully porous structure (looking like nano-wires) has been seen (Figure 8.12). As described earlier, water bubble formation will promote cavity growth and this is directly related to the exposure time. Clearly, after fourth day of continuous operation under single-chamber conditions, more cavities nucleated and a greater mass loss of silver is expected due to vaporization.

It should also be noted that the local cell temperature (at some locations) could be higher than the furnace temperature during SC-SOFC operation. In our earlier study (Ref: [152]), we have observed a temperature increase of 93°C under the same operating conditions used in this study. Due to this

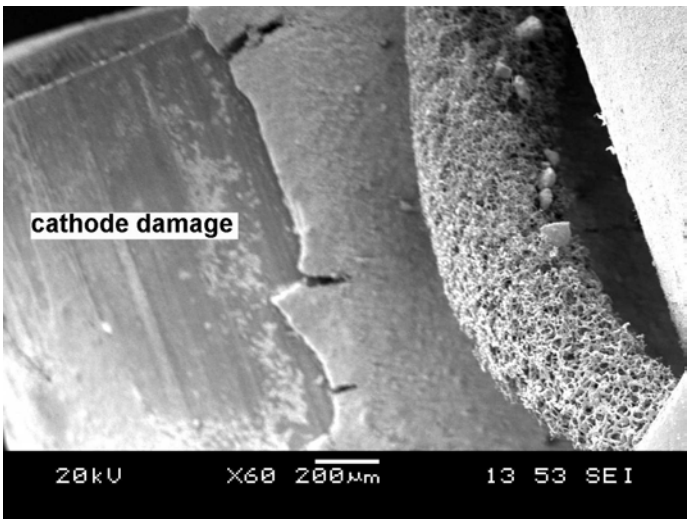

Figure 8.12: SEM photograph showing a highly porous silver wire after the fourth day of exposure under SC-SOFC conditions

effect, the heat may accumulate at some locations causing silver vaporization. The silver vaporization rate depends on many parameters such as flow rate, surrounding atmosphere, specimen geometry and its surface [149].

8.6 Conclusions

The study shows that the highest temperature rise of 93°C (at a furnace temperature of 750°C with methane/air = 25/60 $mLmin^{-1}$) is observed in case of cathode-inlet configuration. It is also observed that the cell inlet is more sensitive to damage because of large exothermic heat due to fuel oxidation directly at the anode inlet. The cathode-outlet configuration shows little temperature gradients as compared to all other configurations. This design may be preferred because of less thermal stresses. Since the silver current collecting wire used in this study has a fairly low melting point (960°C), it is quite possible that the generated heat may accumulate, raise the local temperature and finally break the silver wire. In this case, either the replacement of current collecting wire must be sought or the operating temperature must be kept well below the silver melting point. The operation at low temperature does not seem feasible because the ionic conductivity of YSZ electrolyte sharply drops with decrease in temperature.

The present study demonstrates that the continuous heat generation can result in local hot spots and structural damage at the cell inlet. Not only this, the inhomogeneous temperature distributions and steep temperature gradients along the length of the fuel cell can give rise to state of compression and tension. The power density is also highly non-uniform over the cell length because of large variations

in the ionic conductivity of the electrolyte. While it is generally believed that this exothermic heat is useful in order to lower the external heat demand, its negative effects have been simply neglected. However, it should be noted that its possible contribution to the early degradation and structural damage of SC-SOFCs cannot be compromised, especially with the use of higher hydrocarbon fuels that produce even larger quantities of reaction heat.

The current study also shows that silver current collector is not a good choice to be employed under single-chamber SOFC conditions. If employed, void nucleation and growth in the silver wire, as well as vaporization of silver is expected due to simultaneous dissolution of different species, particularly methane and oxygen, which react and form water vapors. The pressure of water vapor determines the size of the cavity and its growth rate. Furthermore, silver oxide formation and expected overheating in case of SC-SOFC may result in silver vaporization. Both of these effects, i.e. methane combustion and silver oxide formation, followed by its vaporization and melting at high temperatures can degrade the structural stability of silver.

CHAPTER 9

MODELLING OF MICRO-TUBULAR SC-SOFC[6]

9.1 Introduction

As reported earlier, the research work on SC-SOFC is mainly experimentally driven. While, most of the researchers focused on improving the power density-a few of them reported the effective fuel utilization [72]. It should be noted that improving the power density by means of increasing the inlet fuel flow rate would result in lower fuel utilization, because only a certain part of the fuel will contribute in power production depending upon the operating conditions. Also, during experiments, the distribution of species, current density distribution and temperature distribution in a cell is not so easy to determine. Furthermore, the gas velocity in the cell may differ from that supplied at the gas-chamber inlet. Therefore, the measurement of the gas velocity in the cell-channels (especially inside the micro-tube, in case of a micro-tubular cell) will be very useful in order to determine, whether the flow inside the cell is convection dominated or mainly diffusive. This will also ensure that enough reactants are transported from the gas-chamber inlet into the cell-channels via mass transport mechanism. However, still it is not so easy to measure the gas velocity in-situ. The species distribution inside the cell would help in determining the concentration of the reactants available downstream. During experimentation, it is not known whether the reactants are poorly depleted (by the reaction products) or fully consumed (by complete combustion) in a certain portion of the cell.

---

[6] The results described in this chapter have been submitted to:

• N. Akhtar et al., J. Power Sources, submitted.

If this is the case, then the remaining portion of the cell cannot generate enough power, therefore, the power density distribution could be non-uniform over the cell length.

Furthermore, the operation of SC-SOFC with hydrocarbon/air mixtures is so complicated that the exact reaction mechanism on the anode side is still unknown. For example, most of the researchers assumed partial oxidation of fuel in the anode, the generated hydrogen and carbon monoxide undergo electrochemical oxidation to produce electrical current [6,7,16,36,38-42,46-48,51,54,55,57,60,61,71]. On the other hand, it has been reported that the rate of carbon monoxide conversion via electrochemical oxidation is very slow, it prefers to undergo water-gas shift reaction, thereby producing carbon dioxide and additional hydrogen [153]. Some of the authors suggested that the partial oxidation of methane takes place via methane full combustion followed by steam and dry reforming over nickel anode [56,59,65]. Very recently, Hao et al. [78] suggested three different reaction zones in the anode, i.e. a full combustion zone (where hydrogen and carbon monoxide are oxidized which are produced deeper within the anode) at the gas-anode interface, followed by methane wet-reforming zone, and a water-gas shift reaction zone deeper within the anode. If these reaction zones are existing within the anode thickness, then one would expect a temperature gradient deeper within the anode (because of different nature of these reactions; some exothermic and the other endothermic). Furthermore, the temperature at the outermost layer (the anode-gas interface) should nearly be the dominant effect of full combustion reaction mechanism (although the temperature distribution within the anode is highly coupled with the other two reaction mechanisms deeper within the anode, the outside layer, because of combustion of hydrogen and carbon monoxide will govern the anode surface temperature). In our recent experimental study we have reported a temperature gradient of as high as 150°C over the cell length [152]. This steep temperature gradient is an indication of different reaction chemistry over the cell length which further supports the modelling results reported by Hao et al. [78]. With the help of their modelling study and our experimental work, we were able to develop a numerical model in order to optimize our experimental setup. The model formulation is discussed in detail as below.

9.2 The Mathematical Model

In order to develop a mathematical model which can capture the experimental trends reported in our earlier study [152], we carried out some survey of the open literature. It was found that the proper implementation of the anode side reactions in an SC-SOFC should be the main driving thrust towards the achievement of our goal. We, therefore, focused on proper selection of anode side reactions with

the help of available literature on partial oxidation of methane over nickel anode. At this stage, we also took help from the temperature profiles (over the cell length) as reported in our earlier experimental study [152]. The temperature trends could be very helpful in order to determine the extent of reforming/combustion activity over the cell length. With this information, one could obtain some useful information about the proper selection of a set of possible reactions. It should be noted that all these efforts are not necessarily true unless validated against the experimental work, nevertheless, at the beginning stage, these assumptions will allow us to narrow down the large window of possible reactions as reported by Hao et al. (Table-II in Ref.[78]). With a further study of literature, we found that the partial oxidation of methane over nickel anode is itself a combination of three different reactions occurring within the anode [123-129]. The explanation for this behavior is reported as follows: The nickel catalyst quickly loses its reforming activity in the presence of oxygen as it gets oxidized. Furthermore, over the oxidized catalyst, only methane combustion proceeds, therefore a substantial temperature increase is expected due to full combustion of methane near the cell inlet. Once oxygen is nearly consumed at the inlet, the reforming (dry and wet) reactions take place over the rest of the cell length. Since reforming is an endothermic reaction, a decrease in temperature occurs downstream [107]. This observation was further supported by our experimental study, as we observed a nearly linear temperature drop over the cell length [152]. The presence of high temperature at the inlet fully supports the existence of full combustion of methane directly at the inlet, and a steep temperature drop downstream is expected to occur due to strong endothermic reactions (possibly steam reforming and dry reforming). Other reactions, like hydrogen and carbon monoxide combustion were excluded being taken into account because of their exothermic nature does not coincide with the existence of steep temperature gradients downstream. In conclusion, the short-listed reactions are: 1) methane full oxidation, 2) methane steam reforming, 3) methane dry reforming and 4) water-gas shift reaction followed by the electrochemical oxidation of produced hydrogen. The electrochemical oxidation of carbon monoxide is less preferred because of its slow reaction rate compared to hydrogen electrochemical oxidation [153]. Therefore, we assumed carbon monoxide will took part via water-gas shift reaction, producing additional hydrogen in order to generate electrical current. On the cathode side, parasitic combustion of methane is considered because the selectivity of cathode degrades with increase in temperature [37, 74]. The possible reactions in the anode and cathode are summarized in Table 9.1 and 9.2, respectively.

Reaction	Equation	Δ H $kJmol^{-1}$
Methane full combustion	$CH_4 + 2O_2 \rightarrow 2H_2O + CO_2$	-803
Methane steam reforming	$CH_4 + H_2O \rightarrow 3H_2 + CO$	+206
Methane dry reforming	$CH_4 + CO_2 \rightarrow 2H_2 + 2CO$	+247
Shift reaction	$CO + H_2O \rightarrow H_2 + CO_2$	-33
Hydrogen electrochemical oxidation	$H_2 + O^{-2} \rightarrow H_2O + 2e^-$	-

Table 9.1: Reactions in the anode [72, 78, 152]

Reaction	Equation	Δ H $kJmol^{-1}$
Methane full combustion	$CH_4 + 2O_2 \rightarrow 2H_2O + CO_2$	-803
Oxygen electrochemical reduction	$\frac{1}{2}O_2 + 2e^- \rightarrow O^{2-}$	-

Table 9.2: Reactions in the cathode [74]

9.2.1 Model Description

A micro-tubular geometry was opted for the sake of optimizing our experimental setup. The cell's material and experimental setup have been described in Chapter-8. In order to take benefit from the symmetrical structure of micro-tubular cell, a two-dimensional axisymmetrical setup has been considered. The geometrical dimensions of the gas chamber and cell are taken from our experimental study (Chapter-8) and are listed in Table 9.3.

The diffusion parameters are given in Table 9.4-9.5. All physical properties such as density, heat

Dimensions	Values (mm)
Gas-chamber length (L_c)	285
Gas-chamber diameter (D_c)	12
Micro-tube diameter (D_t)	1.6
Micro-tube length	55
Cathode active length	39
Anode thickness	200×10^{-3}
Cathode thickness	50×10^{-3}
Electrolyte thickness	15×10^{-3}

Table 9.3: Geometry dimensions [72, 152]

capacity, viscosity and thermal conductivity are considered as temperature dependent and their values are taken from Todd et al. [135]. Detailed formulation of mixture properties is presented in Ref. [135].

Molecule	Diffusion Volume (cm^3/mol)
CH_4	24.42
CO_2	26.9
CO	18.9
H_2	7.07
O_2	16.6
H_2O	12.7
N_2	17.9

Table 9.4: Diffusion volumes in Fueller-Schettler-Giddings correlation parameters [119]

Molecular Pair	$\mathcal{D}_{ij}(m^2/s)$
$CH_4 - H_2O$	2.3185×10^{-4}
$CH_4 - CO$	1.8708×10^{-4}
$CH_4 - H_2$	5.9505×10^{-4}
$CH_4 - CO_2$	1.5516×10^{-4}
$CH_4 - O_2$	1.9043×10^{-4}
$CH_4 - N_2$	1.9034×10^{-4}
$H_2O - CO$	2.2382×10^{-4}
$H_2O - H_2$	7.5998×10^{-4}
$H_2O - CO_2$	1.8222×10^{-4}
$H_2O - O_2$	2.2849×10^{-4}
$H_2O - N_2$	2.2817×10^{-4}
$CO - H_2$	6.4243×10^{-4}
$CO - CO_2$	4.0176×10^{-4}
$CO - O_2$	4.0176×10^{-4}
$CO - N_2$	1.7738×10^{-4}
$H_2 - CO_2$	5.5158×10^{-4}
$H_2 - O_2$	6.7242×10^{-4}
$H_2 - N_2$	6.5605×10^{-4}
$CO_2 - O_2$	1.3970×10^{-4}
$CO_2 - N_2$	1.4200×10^{-4}
$O_2 - N_2$	1.7935×10^{-4}

Table 9.5: Maxwell-Stefan diffusion coefficients calculated using values given in Table 9.4

9.2.2 Model Assumptions

• The flow is steady and fully developed.

• The carbon formation (coking) in the anode is neglected due to the presence of sufficient oxygen in the mixture [70].

• The ohmic heating (in the porous electrodes) due to electrical current transport is neglected because of high electrical conductivity as compared to the ionic conductivity [125].

• The electrolyte is a non-porous (dense, solid) material.

• The parasitic loss within the cathode (due to its non-ideal selectivity) is assumed to be due to methane combustion, which is temperature and pressure dependent [74].

In following sections, detailed modelling strategy is presented for each sub-domain. The corresponding domains and boundaries are shown in Figures 9.1-9.2.

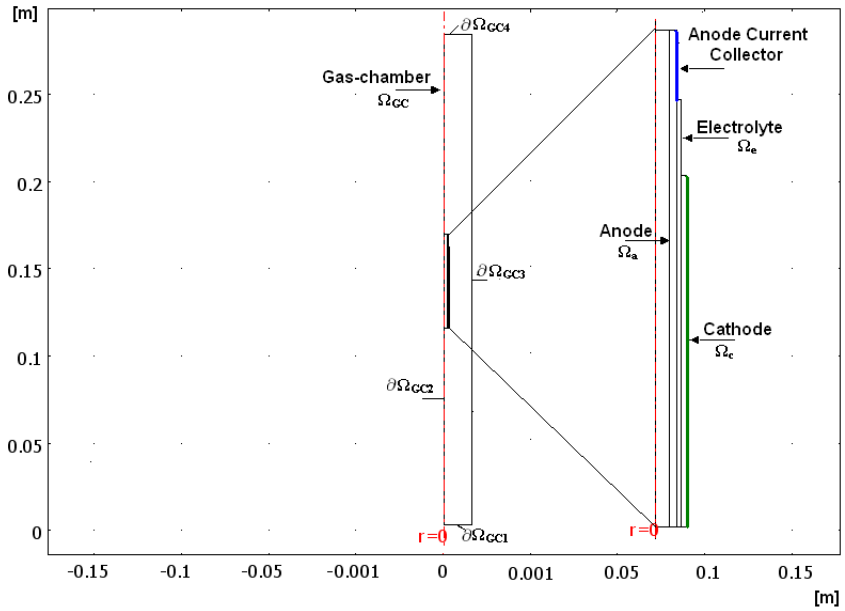

Figure 9.1: The geometrical setup

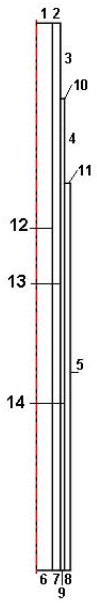

Figure 9.2: Boundary layers in the PEN element

9.2.3 Computational Domain

Gas Chamber

The gas chamber consists of a cylindrical glass tube with a micro-tubular cell placed in its center [Figure 9.1]. The applicable equations are, the continuity, momentum, species and the energy conservation. These equations (in generalized form) are described in Chapter-4 in detail and are customized for the special case as discussed in this Chapter. The extended formulation is described in below.

Gas Diffusion Electrodes

The gas diffusion electrodes consist of an anode and a cathode which are porous media. The equations required to model gas-diffusion electrodes are already discussed in Chapter-4, however, the source terms in the continuity, momentum and species equation are modified to take into account the net effect of species production/consumption in case of methane-air mixtures. The Brinkman equation has an additional term $\mathbf{F}$ added on the right hand side, as:

$$\frac{\mu}{\kappa}\mathbf{u} = -\nabla p + \mu\nabla^2\mathbf{u} + \frac{1}{3}\mu\nabla(\nabla\cdot\mathbf{u}) + \mathbf{F} \tag{9.1}$$

where $\mathbf{F}$ is the source term that accounts for external force applied to the fluid due to production/consumption of species during fuel cell reaction. This term is defined as [86]:

$$\mathbf{F} = \begin{bmatrix} S_i\mathbf{u} \\ S_i\mathbf{v} \end{bmatrix}$$

where S_i is the net reaction rate source term, which will be defined shortly.

• Species conservation equation:

$$\nabla\cdot(\rho\mathbf{u}Y_i + \mathbf{j}_i) = S_i \tag{9.2}$$

The right hand side term, S_i, in equation (9.2) is the net reaction rate source term as a result of production/consumption of species. Since several reactions are taking place in the electrodes, simultaneously, the S_i term is calculated on the basis of net reaction rate on each electrode for each species. The corresponding reaction rates for each reaction and a net reaction rate for each species are given in Table 9.6-9.7 [65-68].

Reaction rate ($mol\ m^{-3}\ s^{-1}$)	Reaction rate constant
R_{FOX}=$k_1[CH_4][O_2]^{2.0}$	$k_1 = 3.0 \times 10^8 exp(-\frac{90000}{RT})$
R_{SR}=$k_2[CH_4][H_2O] - k_3[CO][H_2]^{3.0}$	$k_2 = 2.3 \times 10^{-8}$, $k_3 = 1.4 \times 10^{-20}$
	$K_1k_4 = 2.61 \times 10^{-3} exp(-\frac{4300}{T})$
R_{DR}=$\frac{K_1k_4*K_3*k_5*[CH_4][CO]}{K_1k_4*K_3*[CH_4][CO_2]+K_1k_4*[CH_4]+K_3k_5*[CO_2]}$	$K_3 = 5.17 \times 10^{-5} exp(\frac{8700}{T})$
	$k_5 = 5.35 \times 10^{-1} exp(-\frac{7500}{T})$
R_{SH}=$k_6[CO][H_2O] - k_7[CO_2][H_2]$	$k_6 = 1.5 \times 10^{-7}$, $k_7 = 1.4 \times 10^{-7}$
R_{PAR}=$k_8[CH_4]^d[O_2]^f$	$k_8 = 3.0 \times 10^5 exp(-\frac{90000}{RT})$
R_{H_2}=$-A_a i_a (M_{H_2}/2F)$	–
R_{H_2O}=$+A_a i_a (M_{H_2O}/2F)$	–
R_{O_2}=$-A_c i_c (M_{O_2}/4F)$	–

Table 9.6: Reaction rates and equilibrium constants [65-68]

Species	$S_{m,a} = S_{i,a}$	$S_{m,c} = S_{i,c}$
CH_4	$(-R_{FOX} - R_{SR} - R_{DR})M_{CH_4}$	$(-R_{PAR})M_{CH_4}$
H_2O	$(2R_{FOX} - R_{SR} - R_{SH})M_{H_2O} + A_a i_a (M_{H_2O}/2F)$	$(2R_{PAR})M_{H_2O}$
H_2	$(3R_{SR} + 2R_{DR} + R_{SH})M_{H_2} - A_a i_a (M_{H_2}/2F)$	0
CO	$(R_{SR} + 2R_{DR} - R_{SH})M_{CO}$	0
CO_2	$(R_{FOX} - R_{DR} + R_{SH})M_{CO_2}$	$(R_{PAR})M_{CO_2}$
O_2	$(-2R_{FOX})M_{O_2}$	$(-2R_{PAR})M_{O_2} - A_c i_c (M_{O_2}/4F)$

Table 9.7: Reaction source terms in the electrodes

• Charge conservation equation:

The electronic charge transfer in the electrodes is described by a governing equation for the conservation of charge [124, 125]:

$$\nabla \cdot (-\sigma_s^{eff} \nabla \phi_s) = A_s S_{\phi_s} \tag{9.3}$$

where S_{ϕ_s} is the electronic current source term. In the anode, this term is defined as:

$$S_{\phi_s} = -i_a \tag{9.4}$$

and in the cathode, this term is described as:

$$S_{\phi_s} = +i_c \tag{9.5}$$

The ionic charge transfer in the electrodes is given by [124, 125]:

$$\nabla \cdot (-\sigma_e^{eff} \nabla \phi_e) = A_s S_{\phi_e} \tag{9.6}$$

where S_{ϕ_e} is the ionic current source term. In the anode, this term is defined as:

$$S_{\phi_e} = -i_a \tag{9.7}$$

and in the cathode, this term is described as:

$$S_{\phi_e} = +i_c \tag{9.8}$$

The anode and cathode side current densities (i_a and i_c, respectively) are calculated using equations (1.7) and (1.8). The exchange current densities, $i_{0,a}$ and $i_{0,c}$ are expressed as a function of local partial pressure of the species and are calculated using equations (4.36) and (4.37). The overpotentials are calculated by following the procedure mentioned in section (4.3.2).

• Energy conservation equation:

The energy conservation equation has been modified to take into account the effect of energy transport due to species diffusion and the source term on the right hand side includes various terms for heat production/consumption.

$$\nabla \cdot (-k_{eff}\nabla T + (\rho C_p)_{eff}\mathbf{u}T + \sum_{i=1}^{N} h_i \mathbf{j}_i) = E \tag{9.9}$$

The first term on the left hand side refers to conduction, the second term stands for convection and the third term accounts for heat transfer due to species diffusion. The enthalpy of specie i is calculated as [160]:

$$h_i = \int_{T^{ref}}^{T} C_{p,i}\, dT \tag{9.10}$$

where T^{ref} is the known (reference) temperature and T is the target temperature.

Effective properties of the porous media are calculated using equation (6.7)-(6.8). In equation (9.9), E is the energy source term. For the anode, this term is given by [106, 125]:

$$E_a = E_{rev_a} + E_{irr_a} + E_{ohm_e a} + E_{FOX} + E_{SR} + E_{DR} + E_{SH} \tag{9.11}$$

where E_{rev_a}, E_{irr_a} and $E_{ohm_e a}$ are the reversible, irreversible and ohmic heat generation due to ionic resistance within the anode, respectively. These terms are defined earlier in equations (6.10)-(6.13).

The other last four terms in equation (9.11) are defined as:

heat produced due to full combustion of methane [106]:

$$E_{FOX} = R_{FOX}\Delta H_{FOX} \tag{9.12}$$

heat consumed due to steam reforming of methane [106]:

$$E_{SR} = R_{SR}\Delta H_{SR} \tag{9.13}$$

heat consumed due to dry reforming of methane [106]:

$$E_{DR} = R_{DR}\Delta H_{DR} \tag{9.14}$$

heat produced due to water-gas shift reaction [106]:

$$E_{SH} = R_{SH}\Delta H_{SH} \tag{9.15}$$

The energy source term for the cathode is given by:

$$E_c = E_{irr_c} + E_{ohm_{ec}} + E_{PAR} \tag{9.16}$$

where E_{irr_c} and $E_{ohm_{ec}}$ are the irreversible and ohmic heat generation due to ionic resistance within the cathode, respectively. These terms are defined in equations (6.15)-(6.16). The last term on the right-hand side in equation (9.16) is defined as:

heat produced due to parasitic combustion of methane [106]:

$$E_{PAR} = R_{PAR}\Delta H_{FOX} \tag{9.17}$$

Electrolyte

The electrolyte is impermeable to gases and allows only ionic charge transfer, so that:

$$\nabla \cdot (-\sigma_e \nabla \phi_e) = 0 \tag{9.18}$$

Since there is no generation of ionic or electrical current inside the electrolyte, the right hand side of the above equation is zero. Furthermore, the electrolyte is a dense, non-porous material and thus only conduction is possible. The only heat source term in electrolyte is the ohmic resistance due to ionic current transfer [125, 126].

$$\nabla \cdot (k_s \nabla T) = E \tag{9.19}$$

$$E_e = \sigma_e \nabla \phi_e \cdot \nabla \phi_e \tag{9.20}$$

The above discussed governing equations and source terms are summarized in Table 9.8-9.9.

Domain	Equations solved
Ω_{GC}	$\nabla \cdot (\rho \mathbf{u}) = 0$
	$\rho(\mathbf{u} \cdot \nabla)\mathbf{u} = -\nabla p + \mu \nabla^2 \mathbf{u} + \frac{1}{3}\mu \nabla(\nabla \cdot \mathbf{u})$
	$\nabla \cdot (\rho \mathbf{u} Y_i + \mathbf{j}_i) = 0$
	$\nabla \cdot (-k\nabla T + \rho C_p \mathbf{u} T + \sum_{i=1}^{N} h_i \mathbf{j}_i) = 0$
$\Omega_{a,c}$	$\nabla \cdot (\rho \mathbf{u}) = S_m$
	$\frac{\mu}{\kappa}\mathbf{u}$=$-\nabla p + \mu \nabla^2 \mathbf{u} + \frac{1}{3}\mu \nabla(\nabla \cdot \mathbf{u}) + \mathbf{F}$
	$\nabla \cdot (\rho \mathbf{u} Y_i + \mathbf{j}_i) = S_i$
	$\nabla \cdot (-\sigma_s^{eff} \nabla \phi_s) = A_s S_{\phi_s}$
	$\nabla \cdot (-\sigma_e^{eff} \nabla \phi_e) = A_s S_{\phi_e}$
	$\nabla \cdot (-k_{eff} \nabla T + (\rho C_p)_{eff} \mathbf{u} T + \sum_{i=1}^{N} h_i \mathbf{j}_i) = E$
Ω_e	$\nabla \cdot (-\sigma_e \nabla \phi_e) = 0$
	$\nabla \cdot (-k_s \nabla T) = E$

Table 9.8: Computational domain and governing equations

Source term	Anode	Electrolyte	Cathode
$\mathbf{F}$	$S_{i,a}\mathbf{u}$	-	$S_{i,c}\mathbf{u}$
$A_s S_{\phi_s}$	$-A_a i_a$	-	$+A_c i_c$
$A_s S_{\phi_e}$	$-A_a i_a$	0	$+A_c i_c$
E	$E_{rev,a} + E_{irr,a} + E_{ohm,a} + E_{FOX} + E_{SR} + E_{DR} + E_{SH}$	$E_{ohm,e}$	$E_{irr,c} + E_{ohm,c} + E_{PAR}$

Table 9.9: Source terms defined in Table 9.8

9.2.4 Boundary Conditions

The boundary conditions for each layer are given below:

Gas Chamber

- **Inlet**

At the inlet, an average velocity normal to the inlet boundary is prescribed:

$$\mathbf{u} = \mathbf{u_{in}} \tag{9.21}$$

At the inlet, the mass fraction is defined as:

$$Y_i = Y_{i_{in}} \tag{9.22}$$

At the inlet, air-fuel mixture's temperature is defined. Although, the mixture enters the gas-chamber at room temperature, the furnace heating (in our experiments) was so quick that the steady state temperature was arrived within few seconds. It is therefore assumed that the inlet temperature is equal to the operating furnace temperature.

$$T = T_0 \tag{9.23}$$

- **Axis of symmetry**

At the axis of symmetry, an axial symmetry boundary condition is applied for mass, species and energy transport. This boundary is treated as the center of the gas-chamber, i.e:

$$r = 0 \tag{9.24}$$

- **Wall**

At the wall no-slip boundary condition is applied. A no-slip condition means that the fluid's velocity is equal to the boundary velocity, which is zero in the case of a fixed wall.

$$\mathbf{u} = 0 \tag{9.25}$$

A mass insulation boundary condition is applied at the wall, meaning that no mass flux is allowed to cross this boundary.

$$\mathbf{n} \cdot (-\rho D_{ij} \nabla Y_i + \rho \mathbf{u} Y_i) = 0 \tag{9.26}$$

The wall is assumed to be at furnace temperature, therefore operating furnace temperature is defined at the wall.

$$T = T_0 \tag{9.27}$$

- **Outlet**

The outflow boundary condition is prescribed as:

$$p = p_o \tag{9.28}$$

The convective flux boundary condition is applied at the outlet, meaning that at the outlet boundary, diffusion term is negligible.

$$\mathbf{n} \cdot (-\rho D_{ij} \nabla Y_i) = 0 \tag{9.29}$$

At the outlet, the heat transport is convection dominated. Convective heat flux boundary condition ensures that at the outlet boundary the only heat transport is by convection and thus conduction heat transfer is negligible at this boundary [125].

$$\mathbf{n} \cdot (-k \nabla T) = 0 \tag{9.30}$$

Gas diffusion electrodes

- **Anode electrode**

The current from the anode side was collected from the outlet side of the cell (i.e $8\ mm$ length at the end of the cell). Therefore, a zero voltage (ground) boundary condition is applied at this location.

$$\phi_s = 0 \tag{9.31}$$

All other outer surfaces of the anode electrode are insulated to the electrical current, hence it is assumed that there is no current flow across these boundaries.

$$\mathbf{n} \cdot (-\sigma_s^{eff} \nabla \phi_s) = 0 \tag{9.32}$$

- **Cathode electrode**

An operating cell voltage was applied at the cathode current collector, which is the outer layer of the cathode.

$$\phi_s = V_c \tag{9.33}$$

All other surfaces of the cathode electrode are insulated to the electrical current. Furthermore, ionic current cannot flow out of the electrodes. All outer surfaces of the electrodes are insulated to ionic current by applying an ionic insulation boundary condition.

$$\mathbf{n} \cdot (-\sigma_e^{eff} \nabla \phi_e) = 0 \tag{9.34}$$

At outer surface of the cathode, radiative heat exchange boundary condition is applied between the cathode outer surface and the furnace wall.

$$\mathbf{n} \cdot (\mathbf{q_1} - \mathbf{q_2}) = \epsilon_{rad} \sigma_o (T^4 - T_0^4); \mathbf{q_i} = -k_i \nabla T_i + \rho_i C_{p,i} \mathbf{u_i} T_i \tag{9.35}$$

where ϵ_{rad} and σ_o are the radiative emissivity and Stefan-Boltzmann constant, respectively. At all interior boundaries of the cell, continuity of heat flux is maintained. This boundary condition specifies that the normal heat flux inside of the boundary is equal to the normal heat flux outside of the boundary [125].

$$(-\mathbf{n} \cdot (-k_s \nabla T))_{in} = (-\mathbf{n} \cdot (-k_s \nabla T))_{out} \tag{9.36}$$

Electrolyte

Since the electrolyte is impermeable to gases, both the mass flux and velocity normal to all surfaces of the electrolyte are zero.

$$\mathbf{n} \cdot \mathbf{u} = 0 \tag{9.37}$$

$$\mathbf{n} \cdot (-\rho D_{DG_{i,j}}^{eff} \nabla Y_i + \rho \mathbf{u} Y_i) = 0 \tag{9.38}$$

Continuity of ionic current is maintained at interfaces between the electrodes and electrolyte. All outer surfaces of the electrolyte are insulated to ionic current by applying an ionic insulation boundary condition.

$$\mathbf{n} \cdot (-\sigma_e \nabla \phi_e) = 0 \tag{9.39}$$

Continuity of heat flux is maintained at all surfaces of the electrolyte, i.e.

$$(-\mathbf{n} \cdot (-k_s \nabla T))_{in} = (-\mathbf{n} \cdot (-k_s \nabla T))_{out} \tag{9.40}$$

The above discussed boundary conditions are summarized in Table 9.10.

Surface Boundary	Boundary Condition
$\partial\Omega_{GC_1}$	$\mathbf{u} = \mathbf{u_{in}}, Y_i = Y_{i_{in}}, T = T_0$
$\partial\Omega_{GC_2}$	$r = 0$
$\partial\Omega_{GC_3}$	$u = v = w = 0, \mathbf{n} \cdot (-\rho D_{ij} \nabla Y_i + \rho \mathbf{u} Y_i) = 0, T = T_0$
$\partial\Omega_{GC_4}$	$p = p_o, \mathbf{n} \cdot (-\rho D_{ij} \nabla Y_i) = 0, \mathbf{n} \cdot (-k \nabla T) = 0$
$\partial\Omega_{10}$	$\mathbf{n} \cdot \mathbf{u} = 0, \mathbf{n} \cdot (-\rho D_{ij} \nabla Y_i + \rho \mathbf{u} Y_i) = 0, \mathbf{n} \cdot (-\sigma_e \nabla \phi_e) = 0, (-\mathbf{n} \cdot (-k \nabla T))_{in} = (-\mathbf{n} \cdot (-k \nabla T))_{out}$
$\partial\Omega_4$	$\mathbf{n} \cdot \mathbf{u} = 0, \mathbf{n} \cdot (-\rho D_{ij} \nabla Y_i + \rho \mathbf{u} Y_i) = 0, \mathbf{n} \cdot (-\sigma_e \nabla \phi_e) = 0, (-\mathbf{n} \cdot (-k \nabla T))_{in} = (-\mathbf{n} \cdot (-k \nabla T))_{out}$
$\partial\Omega_{13}$	$\mathbf{n} \cdot \mathbf{u} = 0, \mathbf{n} \cdot (-\rho D_{ij} \nabla Y_i + \rho \mathbf{u} Y_i) = 0, \mathbf{n} \cdot (-\sigma_e \nabla \phi_e) = 0, (-\mathbf{n} \cdot (-k \nabla T))_{in} = (-\mathbf{n} \cdot (-k \nabla T))_{out}$
$\partial\Omega_{14}$	$\mathbf{n} \cdot \mathbf{u} = 0, \mathbf{n} \cdot (-\rho D_{ij} \nabla Y_i + \rho \mathbf{u} Y_i) = 0, \mathbf{n} \cdot (-\sigma_e \nabla \phi_e) = 0, (-\mathbf{n} \cdot (-k \nabla T))_{in} = (-\mathbf{n} \cdot (-k \nabla T))_{out}$
$\partial\Omega_9$	$\mathbf{n} \cdot \mathbf{u} = 0, \mathbf{n} \cdot (-\rho D_{ij} \nabla Y_i + \rho \mathbf{u} Y_i) = 0, \mathbf{n} \cdot (-\sigma_e \nabla \phi_e) = 0, (-\mathbf{n} \cdot (-k \nabla T))_{in} = (-\mathbf{n} \cdot (-k \nabla T))_{out}$
$\partial\Omega_1$	$\mathbf{n} \cdot (\rho \mathbf{u})_{in} = \mathbf{n} \cdot (\rho \mathbf{u})_{out}, \mathbf{n} \cdot (-\rho D^{eff}_{DG_{i,j}} \nabla Y_i + \rho \mathbf{u} Y_i)_{in} = \mathbf{n} \cdot (-\rho D^{eff}_{DG_{i,j}} \nabla Y_i + \rho \mathbf{u} Y_i)_{out}$, $\mathbf{n} \cdot (-\sigma_s^{eff} \nabla \phi_s) = 0, \mathbf{n} \cdot (-\sigma_e^{eff} \nabla \phi_e) = 0, (-\mathbf{n} \cdot (-k_{eff} \nabla T + (\rho C_p)_{eff} \mathbf{u} T))_{in} = (-\mathbf{n} \cdot (-k_{eff} \nabla T + (\rho C_p)_{eff} \mathbf{u} T))_{out}$
$\partial\Omega_2$	$\mathbf{n} \cdot (\rho \mathbf{u})_{in} = \mathbf{n} \cdot (\rho \mathbf{u})_{out}, \mathbf{n} \cdot (-\rho D^{eff}_{DG_{i,j}} \nabla Y_i + \rho \mathbf{u} Y_i)_{in} = \mathbf{n} \cdot (-\rho D^{eff}_{DG_{i,j}} \nabla Y_i + \rho \mathbf{u} Y_i)_{out}$, $\mathbf{n} \cdot (-\sigma_s^{eff} \nabla \phi_s) = 0, \mathbf{n} \cdot (-\sigma_e^{eff} \nabla \phi_e) = 0, (-\mathbf{n} \cdot (-k_{eff} \nabla T + (\rho C_p)_{eff} \mathbf{u} T))_{in} = (-\mathbf{n} \cdot (-k_{eff} \nabla T + (\rho C_p)_{eff} \mathbf{u} T))_{out}$
$\partial\Omega_6$	$\mathbf{n} \cdot (\rho \mathbf{u})_{in} = \mathbf{n} \cdot (\rho \mathbf{u})_{out}, \mathbf{n} \cdot (-\rho D^{eff}_{DG_{i,j}} \nabla Y_i + \rho \mathbf{u} Y_i)_{in} = \mathbf{n} \cdot (-\rho D^{eff}_{DG_{i,j}} \nabla Y_i + \rho \mathbf{u} Y_i)_{out}$, $\mathbf{n} \cdot (-\sigma_s^{eff} \nabla \phi_s) = 0, \mathbf{n} \cdot (-\sigma_e^{eff} \nabla \phi_e) = 0, (-\mathbf{n} \cdot (-k_{eff} \nabla T + (\rho C_p)_{eff} \mathbf{u} T))_{in} = (-\mathbf{n} \cdot (-k_{eff} \nabla T + (\rho C_p)_{eff} \mathbf{u} T))_{out}$
$\partial\Omega_7$	$\mathbf{n} \cdot (\rho \mathbf{u})_{in} = \mathbf{n} \cdot (\rho \mathbf{u})_{out}, \mathbf{n} \cdot (-\rho D^{eff}_{DG_{i,j}} \nabla Y_i + \rho \mathbf{u} Y_i)_{in} = \mathbf{n} \cdot (-\rho D^{eff}_{DG_{i,j}} \nabla Y_i + \rho \mathbf{u} Y_i)_{out}$, $\mathbf{n} \cdot (-\sigma_s^{eff} \nabla \phi_s) = 0, \mathbf{n} \cdot (-\sigma_e^{eff} \nabla \phi_e) = 0, (-\mathbf{n} \cdot (-k_{eff} \nabla T + (\rho C_p)_{eff} \mathbf{u} T))_{in} = (-\mathbf{n} \cdot (-k_{eff} \nabla T + (\rho C_p)_{eff} \mathbf{u} T))_{out}$
$\partial\Omega_5$	$\mathbf{n} \cdot (\rho \mathbf{u})_{in} = \mathbf{n} \cdot (\rho \mathbf{u})_{out}, \mathbf{n} \cdot (-\rho D^{eff}_{DG_{i,j}} \nabla Y_i + \rho \mathbf{u} Y_i)_{in} = \mathbf{n} \cdot (-\rho D^{eff}_{DG_{i,j}} \nabla Y_i + \rho \mathbf{u} Y_i)_{out}$, $\phi_s = \phi_{sc}, \mathbf{n} \cdot (\mathbf{q_1} - \mathbf{q_2}) = \epsilon_{rad} \sigma_o (T^4 - T_0^4); \mathbf{q_i} = -k_i \nabla T_i + \rho_i C_{p,i} \mathbf{u_i} T_i$
$\partial\Omega_8$	$\mathbf{n} \cdot (\rho \mathbf{u})_{in} = \mathbf{n} \cdot (\rho \mathbf{u})_{out}, \mathbf{n} \cdot (-\rho D^{eff}_{DG_{i,j}} \nabla Y_i + \rho \mathbf{u} Y_i)_{in} = \mathbf{n} \cdot (-\rho D^{eff}_{DG_{i,j}} \nabla Y_i + \rho \mathbf{u} Y_i)_{out}$, $\mathbf{n} \cdot (-\sigma_s^{eff} \nabla \phi_s) = 0, \mathbf{n} \cdot (-\sigma_e^{eff} \nabla \phi_e) = 0, (-\mathbf{n} \cdot (-k_{eff} \nabla T + (\rho C_p)_{eff} \mathbf{u} T))_{in} = (-\mathbf{n} \cdot (-k_{eff} \nabla T + (\rho C_p)_{eff} \mathbf{u} T))_{out}$
$\partial\Omega_{11}$	$\mathbf{n} \cdot (\rho \mathbf{u})_{in} = \mathbf{n} \cdot (\rho \mathbf{u})_{out}, \mathbf{n} \cdot (-\rho D^{eff}_{DG_{i,j}} \nabla Y_i + \rho \mathbf{u} Y_i)_{in} = \mathbf{n} \cdot (-\rho D^{eff}_{DG_{i,j}} \nabla Y_i + \rho \mathbf{u} Y_i)_{out}$, $\mathbf{n} \cdot (-\sigma_s^{eff} \nabla \phi_s) = 0, \mathbf{n} \cdot (-\sigma_e^{eff} \nabla \phi_e) = 0, (-\mathbf{n} \cdot (-k_{eff} \nabla T + (\rho C_p)_{eff} \mathbf{u} T))_{in} = (-\mathbf{n} \cdot (-k_{eff} \nabla T + (\rho C_p)_{eff} \mathbf{u} T))_{out}$
$\partial\Omega_{12}$	$\mathbf{n} \cdot (\rho \mathbf{u})_{in} = \mathbf{n} \cdot (\rho \mathbf{u})_{out}, \mathbf{n} \cdot (-\rho D^{eff}_{DG_{i,j}} \nabla Y_i + \rho \mathbf{u} Y_i)_{in} = \mathbf{n} \cdot (-\rho D^{eff}_{DG_{i,j}} \nabla Y_i + \rho \mathbf{u} Y_i)_{out}$, $\mathbf{n} \cdot (-\sigma_s^{eff} \nabla \phi_s) = 0, \mathbf{n} \cdot (-\sigma_e^{eff} \nabla \phi_e) = 0, (-\mathbf{n} \cdot (-k_{eff} \nabla T + (\rho C_p)_{eff} \mathbf{u} T))_{in} = (-\mathbf{n} \cdot (-k_{eff} \nabla T + (\rho C_p)_{eff} \mathbf{u} T))_{out}$
$\partial\Omega_3$	$\mathbf{n} \cdot (\rho \mathbf{u})_{in} = \mathbf{n} \cdot (\rho \mathbf{u})_{out}, \mathbf{n} \cdot (-\rho D^{eff}_{DG_{i,j}} \nabla Y_i + \rho \mathbf{u} Y_i)_{in} = \mathbf{n} \cdot (-\rho D^{eff}_{DG_{i,j}} \nabla Y_i + \rho \mathbf{u} Y_i)_{out}$, $\phi_s = \phi_{sa}, (-\mathbf{n} \cdot (-k_{eff} \nabla T + (\rho C_p)_{eff} \mathbf{u} T))_{in} = (-\mathbf{n} \cdot (-k_{eff} \nabla T + (\rho C_p)_{eff} \mathbf{u} T))_{out}$

Table 9.10: Boundary conditions

9.3 Numerical Implementation

The model equations are solved using COMSOL Multiphysics 3.4, a commercial Finite Element Method (FEM) based software package. The computations were performed on a 32-node Linux cluster; 32 x dual 3GHz Intel Xeon Sun Fire V60 servers each with 4GB memory. The mesh consists of 5,746 triangular elements and is shown in Figure 9.3. The system of equations was solved simultaneously using a parametric solver (PARDISO). The cell voltage was defined as the parameter whose value was stepped decreased from the open circuit voltage to the short circuit current. The total computing time for a single I-V curve scan was approximately 35.8 minutes.

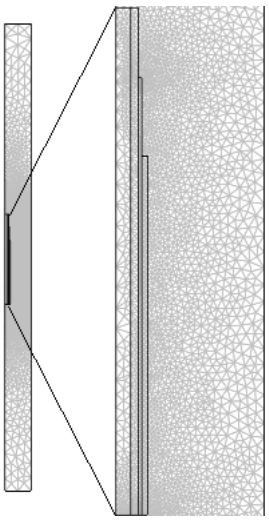

Figure 9.3: The computational mesh (5,746 elements)

Property	Symbol	Value	Units	References
Working electrical potential at anode	ϕ_{sa}	0	V	[5]
Working electrical potential at cathode	ϕ_{sc}	0.5	V	[5]
Effective anode ionic conductivity	σ_{ea}^{eff}	0.29	Sm^{-1}	[5]
Effective cathode ionic conductivity	σ_{ec}^{eff}	0.24	Sm^{-1}	[5]
Effective anode electronic conductivity	σ_{sa}^{eff}	4800	Sm^{-1}	[5]
Effective cathode electronic conductivity	σ_{sc}^{eff}	1600	Sm^{-1}	[5]
Electrolyte ionic conductivity	σ_e	$3.34 \times 10^4 exp(-10300/T)$	Sm^{-1}	[124]
Inlet temperature	T_0	1023	K	[–]
Anodic anodic charge transfer coefficient	α_a^a	2		[5]
Anodic cathodic charge transfer coefficient	α_c^a	1		[5]
Cathodic anodic charge transfer coefficient	α_a^c	1.5		[5]
Cathodic cathodic charge transfer coefficient	α_c^c	0.5		[5]
Anode active surface area	A_a	$1.05e^7$	m^{-1}	[–]
Cathode active surface area	A_c	$4.25e^6$	m^{-1}	[–]
Faraday's constant	F	96487	$Cmole^{-1}$	[128]
Universal gas constant	R_g	8.314	$Jmole^{-1}K^{-1}$	[128]
Porosity	ϵ	0.4		[–]
Tortuosity	τ	3.80		[128]
Permeability	κ	1.0×10^{-13}	m^2	[126]
Methane inlet mass fraction	$Y_{CH4_{in}}$	0.28		[–]
Oxygen inlet mass fraction	$Y_{O2_{in}}$	0.14		[–]
Operating pressure	p_o	1.013×10^5	Nm^{-2}	[124]
Inlet velocity	$\mathbf{u_{in}}$	0.04	ms^{-1}	[–]
Average pore diameter	d_p	1.0	μm	[124]
Anode thermal conductivity	k_a	1.86	$Wm^{-1}K^{-1}$	[124]
Cathode thermal conductivity	k_c	5.84	$Wm^{-1}K^{-1}$	[124]
Electrolyte thermal conductivity	k_e	2.16	$Wm^{-1}K^{-1}$	[124]
Anode specific heat	$C_{p,a}$	450	$Jkg^{-1}K^{-1}$	[124]
Cathode specific heat	$C_{p,c}$	470	$Jkg^{-1}K^{-1}$	[124]
Electrolyte specific heat	$C_{p,e}$	430	$Jkg^{-1}K^{-1}$	[124]
Anode density	ρ_a	3310	kgm^{-3}	[124]
Cathode density	ρ_c	3030	kgm^{-3}	[124]
Electrolyte density	ρ_e	5160	kgm^{-3}	[124]
Stefan-Boltzmann Constant	σ_o	5.6704×10^{-8}	$Wm^{-2}K^{-4}$	[124]

Table 9.11: Input parameters

9.4 Model Calibration

A single set of experimental data obtained in our earlier study (full size cathode, operating temperature of 750°C in Ref. [152]) was used to calibrate the model. There are some variables such as temperature, pressure, mixing ratio, flow velocity that are chosen from our experimental study. Other variables that

are difficult to measure during our experimentation, such as permeability, tortuosity, electrode charge transfer coefficient were taken from the available literature. For fitting the measured performance curves, some variables (as given in Table 9.12) are chosen from the study of Hao et al. [74] in order to calibrate the model. These variables are the anodic and cathodic pre-exponential coefficient, γ_a and γ_c, the anodic and cathodic activation energy, $E_{act,a}$ and $E_{act,c}$, Arrhenius rate constant for cathode parasitic reaction, k_8, methane and oxygen parasitic index, d, f and the radiative emissivity of cathode, ϵ_{rad}.

It is evident that the first four variables in Table 9.12 have greater influence on current density, whereas the last four variables are effective in changing the local temperature distribution. Though, there is a coupling between the current density and temperature distribution (i.e. increase in current density generates additional heat, whereas, increase in temperature improves ionic conductivity of the electrolyte), we first analyzed the effect of change in the first four variables. The ultimate goal was to vary different parameter per simulation in order to achieve the best match between the calculated and measured performance curves. The starting values of these first four parameters were taken from the open literature and a number of simulations were run until the final goal has been achieved. In order to see further improvement in matching, the last four parameters were varied (by following the same procedure) to match the measured and calculated temperature profiles. In this way, a coupling between these parameters was introduced so that both the calculated performance and temperature curves matched in a fair agreement with the experimental ones. It should be noted that the last four parameters related to temperature have direct influence on the cathode surface temperature which is related to cathode selectivity that in turn reflects the cell performance.

In Table 9.12, sensitivity analysis of the fitting parameters for some of the simulation runs is shown. The total number of simulations exceeded over 100 before a good match was obtained between the model and experiment. A graphical view of the sensitivity study is shown in Figure 9.4, in which the calculated and measured current densities are plotted. The dotted black line is the best fit line (simulation run no. 1) on which both the model and experimental current density coincides. In order to show more influential simulations and to make the graphical presentation more legible, only 20 simulations results were plotted in Figure 9.4. To emphasize more influence of exchange current density over temperature dependent parameters, simulations no. 17, 19 and 16, 20 are helpful and explained here. As can be seen in all these four selected simulations, the last four parameters related

Simulation run no.	γ_a	γ_c	$E_{act,a}$	$E_{act,c}$	k_8	d	f	ϵ_{rad}
1	–	–	–	–	–	–	–	–
2	$1.0e^{-7}$	$2.0e^{-7}$	200	200	3×10^6	0.1	0.1	0.5
3	$1.0e^{-9}$	$2.0e^{-9}$	300	300	3×10^6	0.1	0.1	0.5
4	$1.5e^{-5}$	$2.5e^{-9}$	120	180	3×10^6	0.1	0.1	0.5
5	$1.5e^{-7}$	$2.5e^{-9}$	140	200	3×10^6	0.1	0.1	0.5
6	$1.5e^{-9}$	$2.5e^{-9}$	160	220	3×10^6	0.1	0.1	0.5
7	$1.3e^{-7}$	$2.2e^{-7}$	130	190	3×10^6	0.1	0.1	0.5
8	$1.4e^{-7}$	$2.5e^{-7}$	130	190	3×10^6	0.1	0.1	0.5
9	$1.5e^{-7}$	$2.7e^{-7}$	130	190	3×10^6	0.1	0.1	0.5
10	$1.4e^{-7}$	$2.7e^{-7}$	130	190	1×10^6	0.01	0.01	0.8
11	$1.4e^{-7}$	$2.7e^{-7}$	130	190	2×10^5	0.2	0.2	0.8
12	$1.4e^{-7}$	$2.7e^{-7}$	130	190	3×10^5	0.1	0.5	0.8
13	$1.4e^{-7}$	$2.7e^{-7}$	130	190	3×10^5	0.1	0.01	0.6
14	$1.4e^{-7}$	$2.7e^{-7}$	130	190	3×10^5	0.01	0.1	0.6
15	$1.4e^{-7}$	$2.7e^{-7}$	130	190	3×10^5	0.1	0.1	0.6
16	$1.4e^{-9}$	$2.7e^{-9}$	130	190	3×10^5	0.1	0.2	0.3
17	$1.4e^{-5}$	$2.7e^{-5}$	130	190	3×10^5	0.1	0.2	0.3
18	$1.4e^{-7}$	$2.7e^{-7}$	130	190	3×10^5	0.1	0.2	0.3
19	$1.4e^{-7}$	$2.7e^{-5}$	130	190	3×10^5	0.1	0.2	0.3
20	$1.4e^{-7}$	$2.7e^{-9}$	130	190	3×10^5	0.1	0.2	0.3

Table 9.12: Search for fitting parameters through various simulation runs

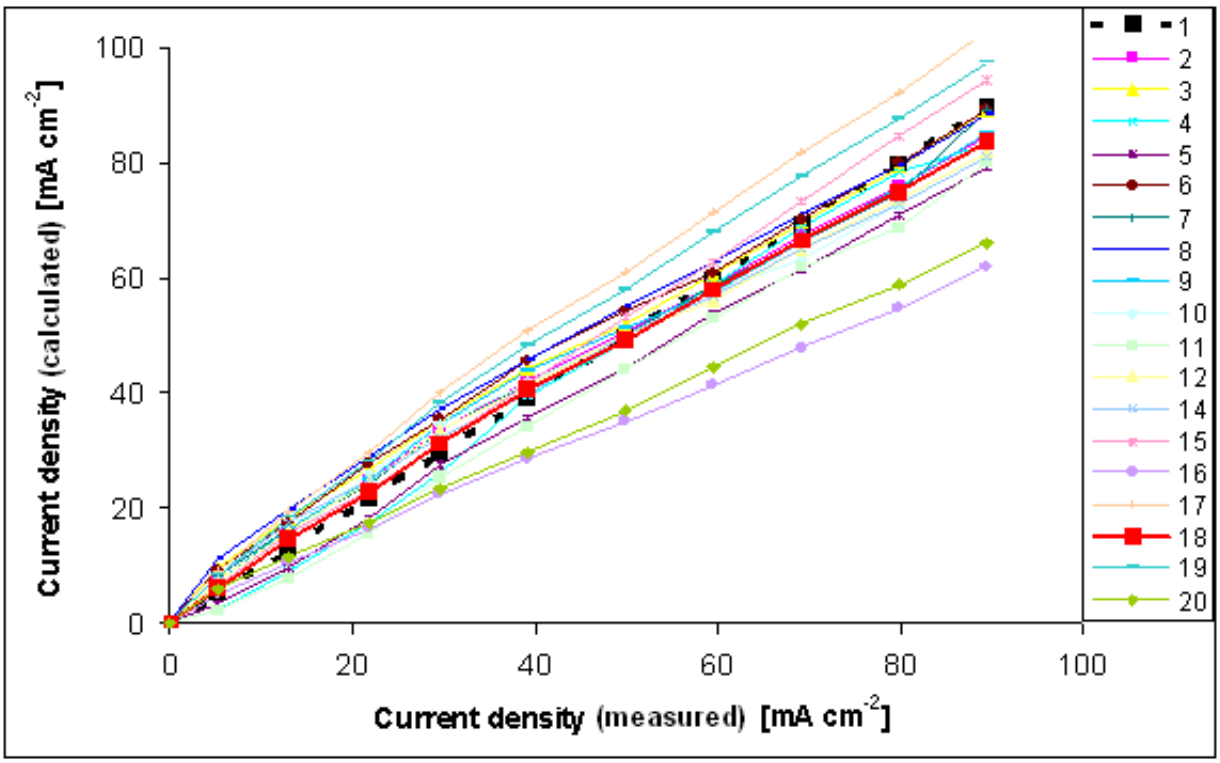

Figure 9.4: Calculated vs. measured current density for R_{mix} = 2.0 at an operating temperature of 750°C for calibration experiments

to temperature are remained unchanged. Among paramaters related to current density, the first two parameters, namely, the anodic and cathodic pre-exponential coefficients (γ_a and γ_c) were seen more

effective in changing the calculated current density. By increasing the value of γ_a and γ_c to $1.4e^{-5}$ and $2.7e^{-5}$, respectively, the calculated current density was the highest (simulation run no. 17) and far away from the best fit line. With decrease in the value of γ_a down to $1.4e^{-7}$, the calculated current density (simulation run no. 19) reduces but it is still far from the best fit line. On the other hand, when the values of γ_a and γ_c were decreased, the calculated current density (simulation run no. 16 and 20) became lower than the measured values. A careful control of these parameters narrowed down the difference between the calculated and measured current densities. As can be seen from Figure 9.4, simulation run no. 18 (red curve), is very close to the best fit line (dotted black). Therefore, the parameter values listed in simulation run no. 18 were used in Table 9.13 for fitting parameters.

Property	Symbol	Value	Units
Anodic pre-exponential coefficient	γ_a	$1.4e^{-7}$	–
Cathodic pre-exponential coefficient	γ_c	$2.7e^{-7}$	–
Anodic activation energy	$E_{act,a}$	130	$Jmol^{-1}$
Cathodic activation energy	$E_{act,c}$	190	$Jmol^{-1}$
Arrhenius rate constant for cathode parasitic reaction	k_8	3×10^5	–
Methane parasitic index	d	0.1	–
Oxygen parasitic index	f	0.2	–
Radiative emissivity of cathode	ϵ_{rad}	0.3	–

Table 9.13: Fitting parameters

With the help of calibrated model (parameters shown in Table 9.11 and 9.13), the calculated performance curve was plotted against the measured performance curve in Figure 9.5. The cell was operated with methane/air mixture of 25/60 $mL\ min^{-1}$ (with inflow velocity of 0.04 ms^{-1}) at an operating temperature of 750°C. As can be seen from Figure 9.5, a good match was obtained between the experimental and model predicted performance curve. A slight discrepancy between the experiment and the model is observed at higher current densities perhaps due to carbon (electrochemical) gasification that generates additional current. Since this model does not consider carbon formation (coking), this mismatch at higher current densities is attributed to this effect.

In Figure 9.6, the temperature profile (on the anode surface) along the cell length is shown. As can be seen, there is a steep decrease in temperature downstream, interesting to note that the calculated temperature decreases up to the complete cathode length (39 mm), and then increases until the remaining cell length. In our experimental study (Ref. [152]), we measured the temperature profiles (on the anode surface) up to the cathode active length and this calculated temperature profile is in good agreement with the experimental curve up to this length. The increase in calculated temperature for the remaining cell length is due to the presence of anode current collection which generates additional resistive heat.

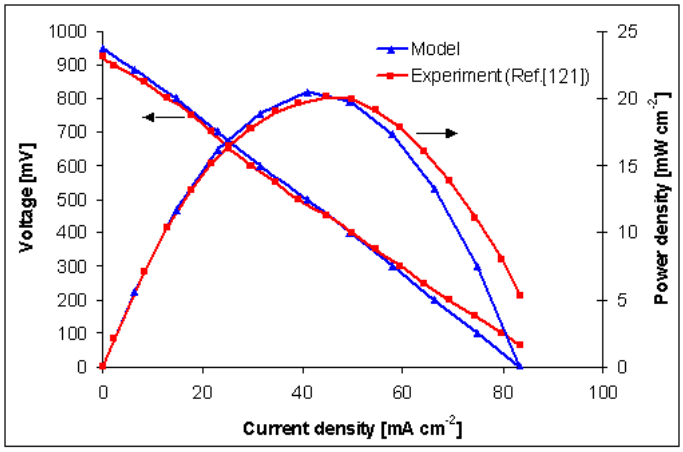

Figure 9.5: Simulated vs. experimental performance curve for R_{mix} = 2.0 at an operating temperature of 750°C

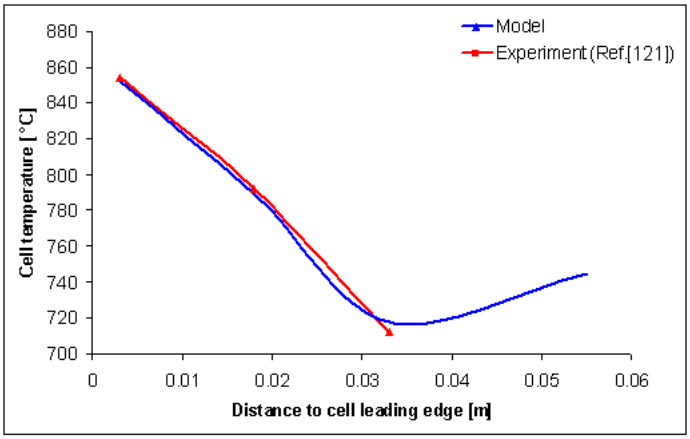

Figure 9.6: Calculated vs. measured temperature profile at cell temperature of 750°C

9.5 Model Validation

After calibrating the model with a single set of operating conditions, it was necessary to check its reliability under other set of operating conditions. In this respect, the performance curves and temperature profiles were calculated at different operating temperatures as shown in Figures 9.7-9.8. As can be seen from Figure 9.7, with increase in operating temperature, there is a marginal increase in the cell performance up to 973 K. The highest power density (of 21.69 $mW\ cm^{-2}$) is calculated at an operating temperature of 973 K. With further increase in temperature, the power density drops, and at an operating temperature of 1023 K, the maximum power density reduces to 20.44 $mW\ cm^{-2}$. The reason for this opposite trend beyond 973 K is the parasitic losses associated with the cathode that consume the fuel due to its non-ideal selectivity. Our experimental study shows that the cell surface temperature is more than 100°C higher than the operating temperature at these conditions. This over-temperature could result in current collecting silver wire damage and also possibly the cath-

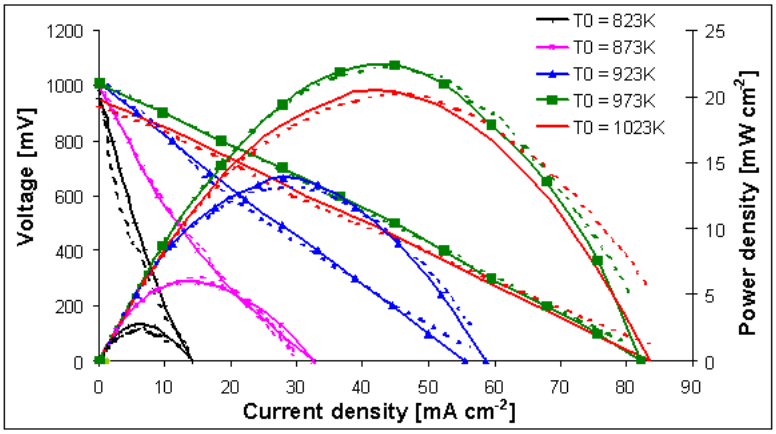

Figure 9.7: Calculated and measured performance curves at different furnace temperatures (dotted lines show experimental results of Ref. [152])

ode parasitic losses will contribute more heat at this operating temperature. Therefore, in order to make balance between the power density and the cell life, it is recommended to operate in between 973-1023 K.

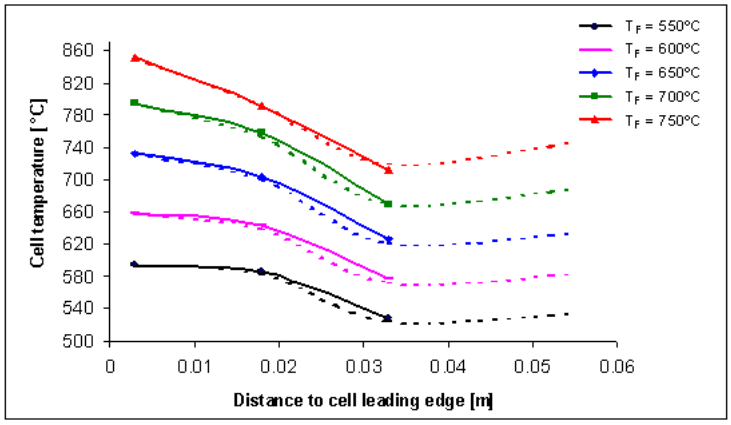

Figure 9.8: Calculated and measured cell temperature distribution at different furnace temperatures (dotted lines show experimental results of Ref. [152])

The calculated cell temperature distribution is validated against the measured temperature profiles at different furnace temperatures. As can be seen from Figure 9.8, there is a fair agreement between the measured and calculated results. This shows that the reaction chemistry chosen on the anode side is appropriate and the model results are reliable. As discussed earlier in the calibration section, the measured temperature profiles are only up to the active cathode length, and a slight over-temperature (in the calculated profiles) at the cell exit is due to the presence of anode current collector.

9.6 Results and Discussion

The values of various electrochemical/hydrodynamic transport parameters along with the fitting parameters are given in Table 9.11 and 9.13. The results presented in all figures are based on parameters listed therein, unless stated otherwise.

In Figure 9.9, the velocity field in the gas chamber is shown. It can be seen that the velocity around the cell and inside the micro-tube significantly differs than that at the gas-chamber inlet. In Figure 9.10, the velocity profile inside the micro-tube and both electrodes (anode and cathode) has been shown along the axial direction. From this plot, it is evident that the gas velocity inside the micro-tube is significantly reduced and approaching to nearly zero value. The gas velocity in both electrodes is almost zero, showing that the mass transport inside the electrodes is mainly diffusive. The reduced velocity in the electrodes is due to the porous nature of the electrodes providing limited passage for the gas flow. This low gas velocity would result in mass transport limitation on the anode side due to insufficient gas supply to the anode electrode. Furthermore, anode chemistry is much more complicated than the cathode, severe fuel depletion is likely to happen in such a small volume.

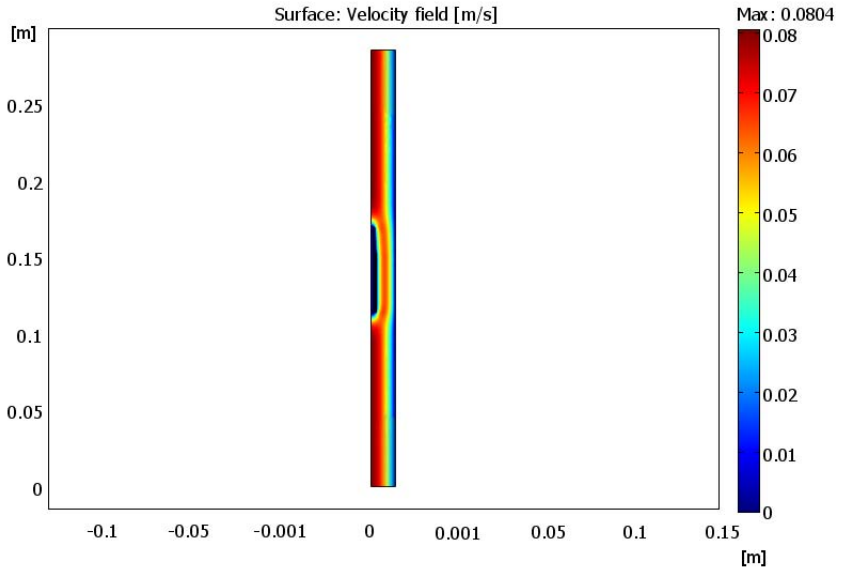

Figure 9.9: Velocity profile in the gas-chamber

Our experimental results (Ref. [72]) show that micro-tubular geometry can compete other designs such as planar, co-planar in terms of effective fuel utilization. The current modelling study clearly shows that the design opted in our experimental study was not optimized and there is a possibility of further improvement in the fuel utilization. The mass transport limitation due to very low gas

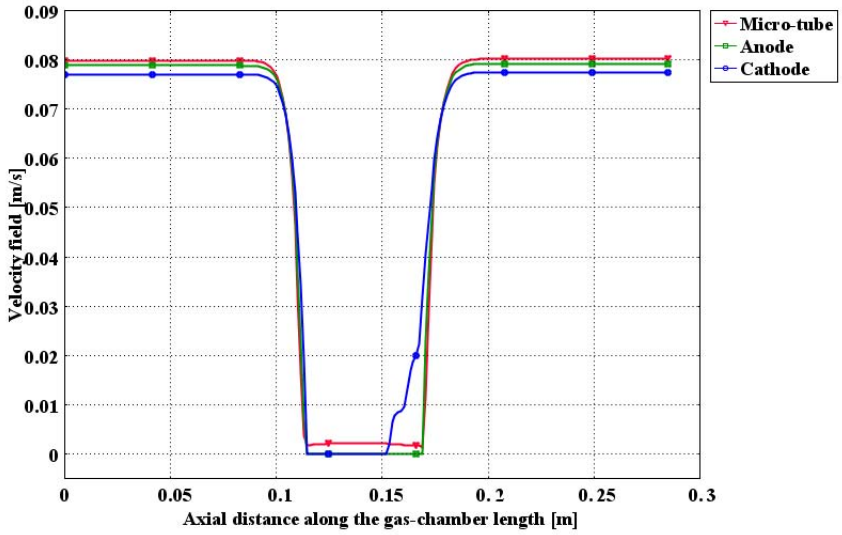

Figure 9.10: Velocity field inside the micro-tube and electrodes along the gas-chamber length

velocity inside the micro-tube is the main culprit in lowering the performance. Due to this limitation, it is not appropriate to compare the performance of micro-tube under single-chamber conditions with that under dual-chamber (conventional) operation. In order to improve the performance under single-chamber conditions, parametric study related to the geometry and cell positioning is important, which will be discussed later in this study.

In Figure 9.11, the mass fraction of different species is plotted (at methane-to-oxygen ratio, R_{mix}= 2.0 and operating voltage of 0.5 V) in the anode along the axial direction. As can be seen, the mass fraction of each species remains unchanged until it reaches the cell. The methane is nearly consumed in the anode via full combustion reaction producing water vapor and carbon dioxide. The increase in carbon dioxide mass fraction near the cell inlet clearly shows that the methane combustion precedes at that location. The decrease in carbon dioxide mass fraction downstream indicates that the methane dry reforming is dominating. The water produced via methane full combustion and electrochemistry is balanced by its consumption via steam reforming and water-gas shift reaction. The production of hydrogen via reforming and water-gas shift reactions is balanced by its electrochemical consumption, whereas the net carbon monoxide production is a result of its production via reforming reactions and consumption via water-gas shift reaction. The decrease in oxygen mass fraction on the anode side is due to methane combustion consuming oxygen.

Figure 9.12 shows the mass fraction of oxygen in the cathode at different R_{mix} values along the gas-chamber length. As can be seen, slight dips and peaks are observed at the cell edges, where the

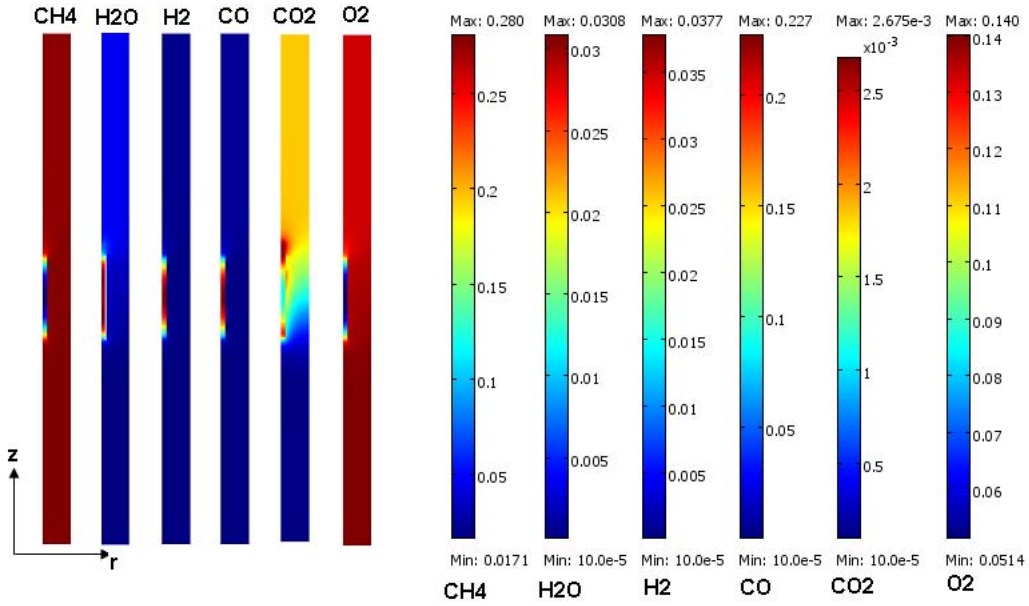

Figure 9.11: Mass fraction of different species in the gas-chamber at R_{mix} = 2.0 and 0.5V

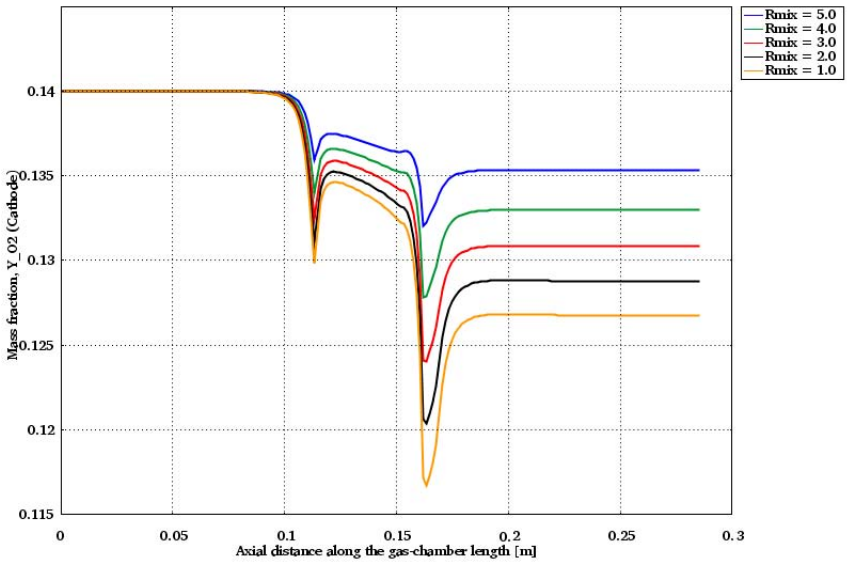

Figure 9.12: Mass fraction plot of oxygen in the cathode at different mixing ratios at 0.5V

gaseous mixtures splits-up, some is directed towards the anode, the remaining passes over the cathode and then recombines. Due to parasitic combustion and electrochemical oxygen consumption, there is a reduction in oxygen mass fraction along the cell length. Furthermore, the oxygen consumption increases with decrease in R_{mix} value. This behavior is often observed in experiments, as the decrease in mixing ratio supplies additional oxygen which promotes full combustion. Ideally, there should be

no oxygen on the anode side and maximum oxygen on the cathode side in order to generate maximum oxygen partial pressure differential across the electrodes. However, in practice the electrodes are non-selective and parasitic combustion occurs which lowers the cell performance. From the above argument, it is clear that the cathode's selectivity and anode's catalytic activity are important factors in improving the cell performance.

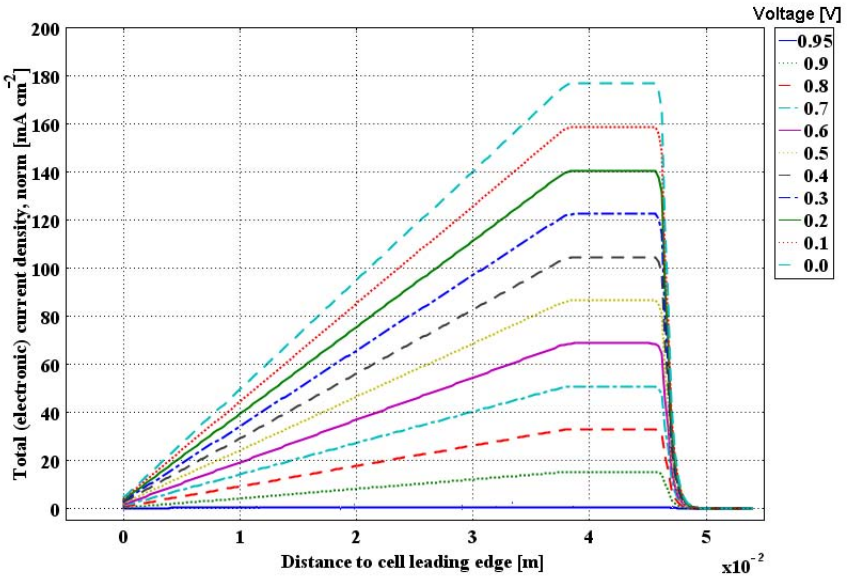

Figure 9.13: Distribution of electronic current density at the anode-electrolyte interface at different operating voltages

Figure 9.13 shows the electronic current density along the anode-electrolyte interface at various operating voltages. As can be seen, the current density is highly non-uniform over the cell length. This highly non-uniform local current density distribution affects the average value of the current density as evident in the performance curves. In order to reduce this non-uniformity, the current collection from the anode side must be made throughout the anode length. As shown in Figure 9.13, the current density is at minimum at the cell edges, increases from the cell inlet, reaches to its maximum near the cathode outlet position and remains constant for up to 8 mm before dropping to zero at the electrolyte outer edge. Furthermore, there is a steep increase in the current density at lower operating voltages due to less resistance at these voltages. It is also clear that the current prefers a shortest conduction path, therefore current density is higher in the vicinity of the current collection point (electrolyte outer edge).

In Figure 9.14, the ionic current density distribution in the electrolyte is shown at various operating voltages. As can be seen, in opposite to the electronic current density distribution, the ionic

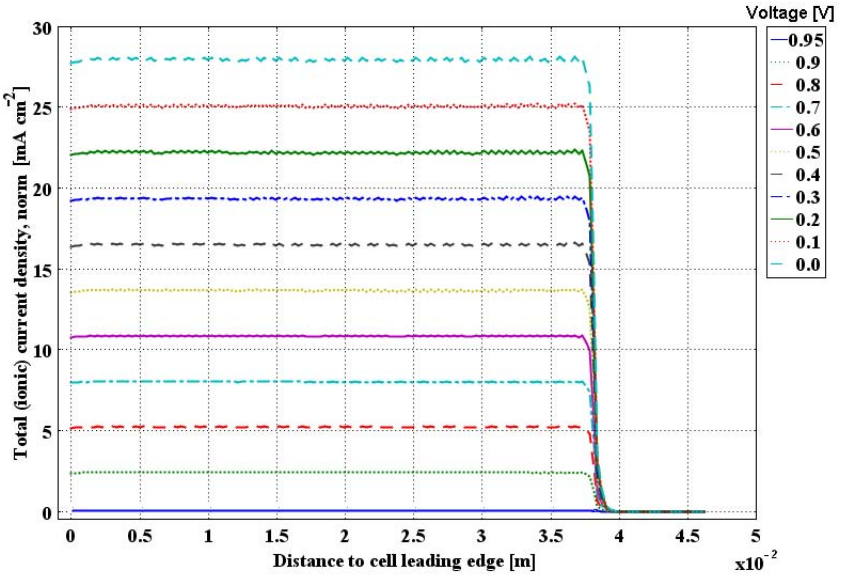

Figure 9.14: Distribution of ionic current density within the electrolyte at different operating voltages

current density is uniform over the cell length. The ionic current density increases with decrease in operating voltage, dropping to zero near the cathode outer edge. The very low values of ionic current densities as compared to the electronic current densities are due to low ionic conductivity of the electrolyte in comparison with the electronic conductivity of the electrodes. Similar to the short electronic conduction path, ionic current within the electrolyte only exists for the active cathode length.

9.7 Parametric Study

9.7.1 Effect of Geometrical Parameters

Figure 9.15 shows the performance curves as a result of geometrical parametric study. The results shown in this figure discuss the effect of change in micro-tube diameter (D_t), gas-chamber length (L_c) and the gas-chamber diameter (D_c). The obtained performance curves are compared with the standard (base-case) geometry i.e. having dimensions D_t, L_c and D_c as given in Table 9.3. The results show that reducing the diameter of the micro-tube is effective in improving the maximum power density (MPD). By reducing the micro-tube diameter to one-half, increases the MPD by 4.60$\%$ (red curve) and increasing it to double, decreases the MPD by 3.95$\%$(pink curve). The decrease in diameter increases the velocity inside the micro-tube (by keeping the gas-chamber inlet velocity unchanged), therefore it enhances the mass transport and lowers the diffusion losses on the anode side which results in improved MPD. Contrary to this, the decrease in gas-chamber diameter by one-half,

decreases the MPD by 1.90% (yellow curve). In this case (in opposite to decreasing the micro-tube diameter), the decrease in gas-chamber diameter (by keeping the inlet velocity fixed) reduces the inlet mass flow rate (according to the continuity equation). The decrease in inlet flow rate would result in lowering the MPD. It has also been observed that the change in the length of the gas-chamber has minimal effect on the MPD value.

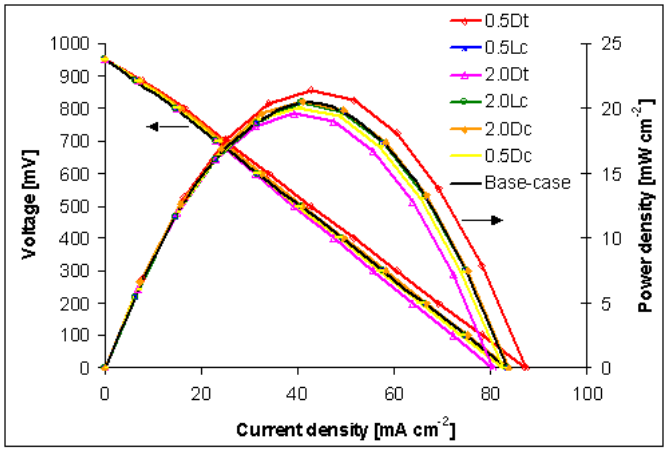

Figure 9.15: Effect of geometrical parameters on the performance curves

9.7.2 Effect of Cell Positioning

In Figure 9.16, the performance curves are shown by varying the cell position. Five positions, namely A, B, C, D and E were simulated. The positions A and E refer to cell location at the inlet and outlet of the gas-chamber, respectively, the position C is the standard (base-case) position with cell located in the middle of the gas-chamber. The positions B and D are in the middle of A-C and C-E positions, respectively. As can be seen, when the cell is placed in the inlet of the gas-chamber (position-A), the

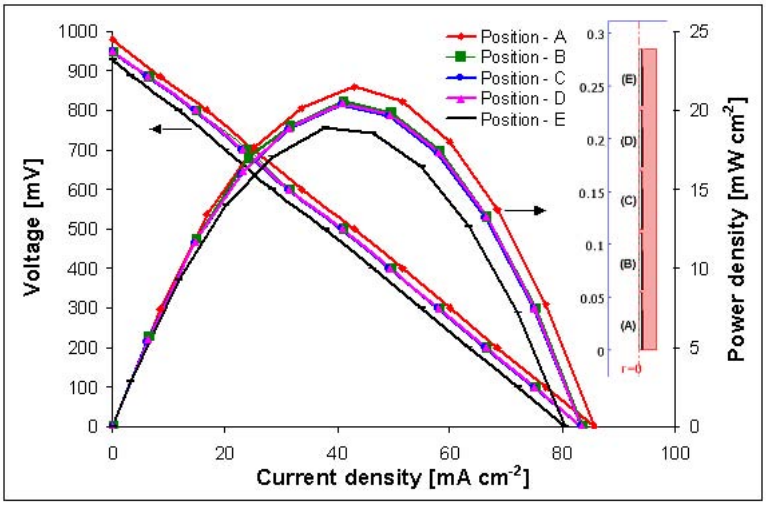

Figure 9.16: Effect of cell positioning on the performance curves

MPD improves by 5.17% (red curve). Whereas, when the cell is located at the outlet (position-E), the MPD drops by 7.33% (black curve). On the other hand, positions B, C and D have minimal effect in changing the MPD value. The improvement in cell performance at position-A is due to increase in velocity at the cell inlet as compared to the other positions. The cell located at the inlet of the gas-chamber minimizes the flow bypass which would happen otherwise. The comparatively poor performance in position-E is due to low gas velocity and greater bypass at that location. Furthermore, in real experiments, the back pressure may affect the cell performance significantly due to ambient air back diffusion. The gas-chamber wall friction may also reduce the gas velocity during experiments. Therefore, this position is not preferred in SC-SOFC experimental setup.

9.7.3 Effect of Exchange Current Density

The exchange current density (i_o) is one of the parameter that controls the performance of the fuel cell. It depends on the mechanism of the electrochemical processes, the material properties, the microstructure of the cell components and the operating conditions, including the gas composition and the temperature, its value therefore is not easy to determine. If this parameter is high, then the surface of the electrode is more active and it results in lowering the activation overpotential. On the other hand, a low value of exchange current density would result in lowering the cell performance due to high activation overpotential. It is therefore recommended to improve this parameter as much as possible. In real practice, the semi-electrode reactions are responsible for a possible enhancement in this parameter. For example, the oxygen reduction reaction on cathode is considered to be a set of

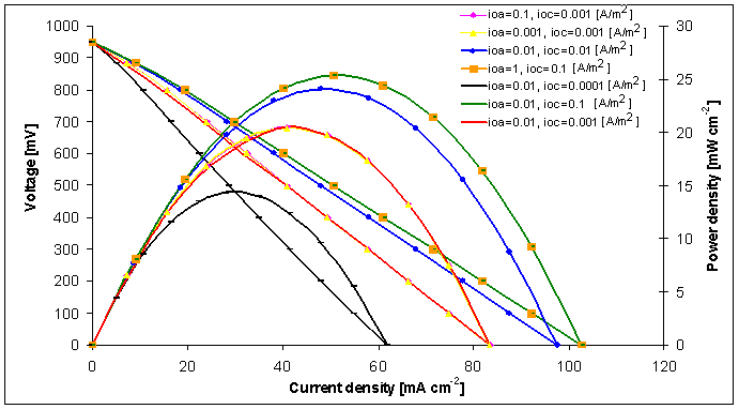

Figure 9.17: Effect of exchange current density on the performance curves

elementary reactions, such as diffusion, adsorption, dissociation, ionization, and finally, incorporation of oxygen into the crystal lattice of the electrolyte [161]. The oxygen reduction reaction can be limited by any of the above steps, therefore, it is vital to determine the rate limiting step in order to improve

the value of i_o.

In Figure 9.17, the effect of this parameter is shown on the fuel cell performance. As can be seen, the poor performance is observed when the cathodic exchange current density, $i_{o,c}$, has a value of 0.0001 $A\ m^{-2}$ (black curve). On the other hand, when its value is changed to 0.1 $A\ m^{-2}$, the best performance is observed under the specified operating conditions (golden and green curves). It is also interesting to note that the cell performance is mainly limited by the cathodic exchange current density, as by increasing the value of $i_{o,a}$ from 0.001 to 0.1 $A\ m^{-2}$ shows a negligible effect on the cell performance (yellow and pink curves). In contrast to this, a similar change in $i_{o,c}$ value results in approx. 23.8$\%$ improvement in cell performance (red and green curves). In summary, the cathodic exchange current density plays an important role in improving the cell performance, therefore oxygen reduction kinetics and cathode electrode material should be given more attention during manufacturing.

9.7.4 Effect of Inlet Velocity

The increase in flow velocity has a similar effect on the fuel cell performance as the flow rate does. Increasing the flow rate could reduce the diffusion and mass transport related losses, but too much increase in the flow rate would result in fuel utilization problems. As described in Chapter-7, increasing the flow rate although improves the performance, but the cell efficiency decreases due to lower fuel utilization. In this respect, we changed the value of inlet flow velocity from 0.005 ms^{-1} to 0.05 ms^{-1}. As can be seen in Figure 9.18, increase in the flow velocity beyond the base-case (0.04 ms^{-1}) improves the performance (approx. 40.21$\%$ for 0.05 ms^{-1}). Similarly, decreasing the flow velocity below the base-case (0.04 ms^{-1}) decreases the performance (approx. 32.25$\%$ for 0.03 ms^{-1}, 56.72$\%$ for 0.02 ms^{-1}, 74.19$\%$ for 0.01 ms^{-1} and 85.82$\%$ for 0.005 ms^{-1}).

The strong effect of flow rate on the cell performance has also been observed during our experimental investigation as described earlier in section (7.4.4).

9.7.5 Effect of Operating Pressure

The effect of operating pressure on the cell performance is shown in Figure 9.19. As can be seen increase in pressure from 1 bar (base-case) to 10 bar improves the maximum power density by 3.3$\%$ only. Furthermore, there is also a little increase in the maximum power density at other operating pressure higher than 1 bar. To this end, it shows that the increase in operating pressure could enhance

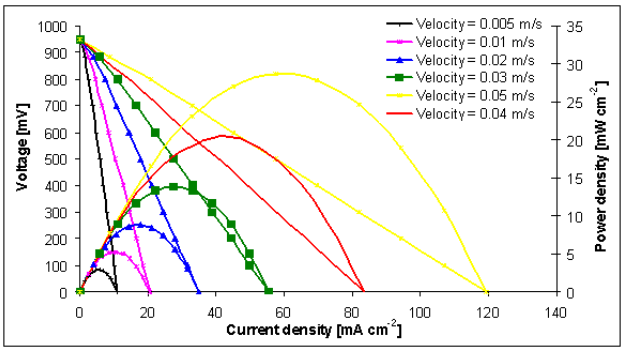

Figure 9.18: Effect of inlet velocity on the performance curves

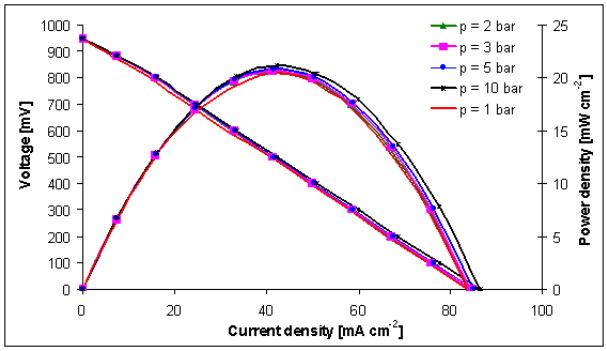

Figure 9.19: Effect of operating pressure on the performance curves

the diffusion coefficients and concentration of the species, as both are pressure dependent. The improvement in these parameters results in power density enhancement. However, in practice for small scale applications, this improvement in performance is not affordable because of additional cost involved in pressurizing the gases. Nevertheless, if SC-SOFCs are employed for combined heat and power (CHP) applications, then some additional power can be obtained via recycling the exhaust gas through a micro-turbine which runs the compressor to pressurize the inlet gaseous mixture. It is therefore concluded that this option is only successful when an overall energy analysis is properly carried out and gives an acceptable net efficiency.

9.7.6 Effect of Electrode Porosity

As can been seen in Figure 9.20, the electrode porosity has minimal effect on the cell performance. By increasing the porosity to 0.5 only slightly improves the power density and this effect is more visible at higher current densities. This is mainly due to the fact that the electrode overpotential reduces due to improved mass and diffusional transport. On the other hand, decreasing the porosity to 0.2 shows a slight decrease in power density due to diffusional loss within the electrodes. It should be noted that increase in porosity although improves the mass transport within the electrodes, a too high porosity

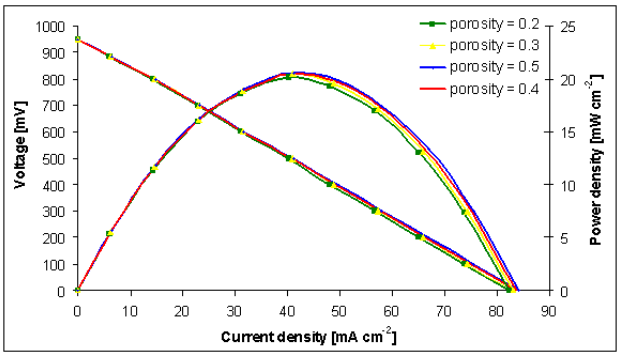

Figure 9.20: Effect of electrode porosity on the performance curves

would result in lowering the fuel utilization due to increased water production on the cathode side. Therefore, there is a trade-off in between the performance and the required porosity.

9.7.7 Effect of Electrode Permeability

In Figure 9.21, the effect of electrode permeability on the cell performance is shown. As can be seen,

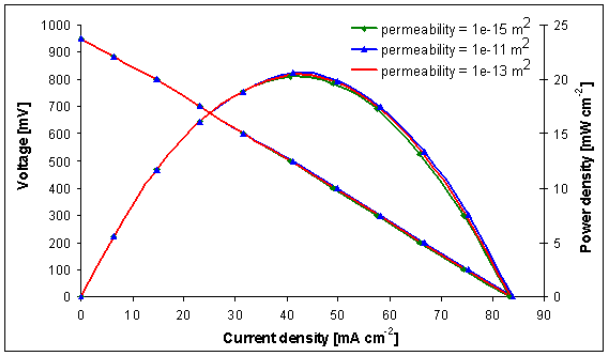

Figure 9.21: Effect of electrode permeability on the performance curves

there is a very slight improvement in power density (visible at higher current densities) at higher value of permeability corresponding to $10^{-11}\ m^2$. On the other hand, with permeability value of $10^{-15}\ m^2$, the power density is slightly lower than the base-case ($10^{-13}\ m^2$) value. This trend is probably due to the fact that increase in permeability reduces the flow resistance, therefore, more species are transported to the active sites in order to produce power.

9.7.8 Effect of Radiative Emissivity of the Cathode

The radiative emissivity of the cathode (ϵ_{rad}) is opted to be 0.3 in this study for the base-case. In Figure 9.22, the effect of this parameter has been studied on the cell performance. As can be seen, the maximum power density slightly decreases with decrease in the emissivity. This trend can be correlated with the cathode surface temperature, a low value of emissivity means a higher cathode surface

temperature which could result in higher parasitic loss at the cathode and subsequent decrease in the power density. On the other hand, a higher emissivity means a lower cathode surface temperature which will result in higher cell performance because the cathode selectivity improves with decrease in temperature. Nevertheless, the effect of this parameter is insignificant on the cell performance.

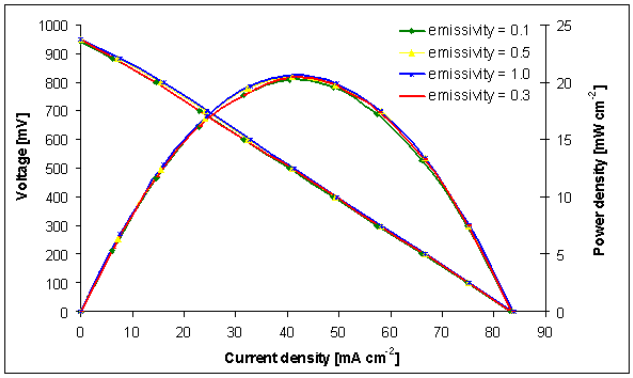

Figure 9.22: Effect of radiative emissivity of the cathode on the performance curves

9.7.9 Effect of Mixing Ratio

The effect of mixing ratio on cell performance is shown in Figure 9.23. Five different mixing ratios have been chosen, namely R_{mix} = 1.0, 2.0, 3.0, 4.0 and 5.0. It can be seen that with increase in mixing ratio, the cell performance decreases. The best performance is observed at a mixing ratio of

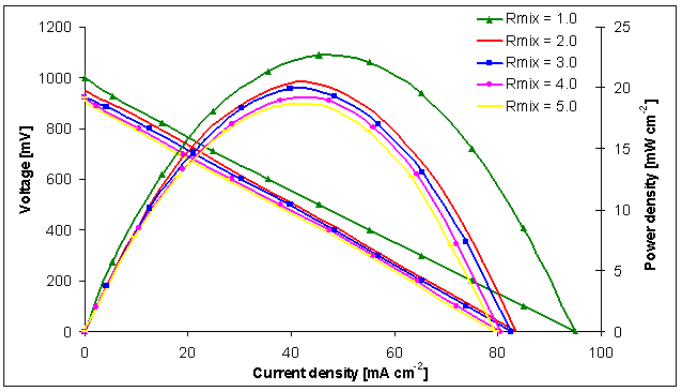

Figure 9.23: Effect of mixing ratio on the performance curves

1.0. Clearly, at this lower mixing ratio, the oxygen concentration in the gaseous mixture is higher as compared to other mixing ratios. Due to higher oxygen content in the mixture, the equilibrium tends to shift towards full combustion of methane. Since methane combustion is an exothermic reaction, large amount of heat is released which results in higher cell surface temperature. The ionic conductivity of the electrolyte is a function of temperature and with increase in temperature, more ions are passed through the electrolyte towards anode and generate power.

On the other hand, there is a slight reduction in performance with increasing methane content in the mixture. This trend is explained by the shift away from the full combustion regime and operation on these higher mixing ratios must be avoided due to the coking problems which could reduce performance and life time of the cell.

9.8 Conclusions

A two-dimensional, axisymmetric, numerical model of a micro-tubular, single-chamber solid oxide fuel cell (MT-SC-SOFC) has been developed. The model considers, methane full combustion followed by steam and dry reforming of methane with water-gas shift reaction producing additional hydrogen for electrochemistry within the anode. The cathode side considers methane parasitic combustion along with the electrochemical reduction of oxygen. The results show that the poor performance of MT-SC-SOFC as compared to the conventional (dual-chamber) MT-SOFC is due to the mass transport limitation on the anode side. The gas velocity inside the micro-tube is far too low than that at the gas-chamber inlet. Furthermore, the current density along the cell length is highly non-uniform, suggesting that the anode current collection should be made throughout the anode length or the cell length must be shortened in order to make the current density as uniform as possible.

The calculated and measured temperature profiles are in good agreement, indicating the appropriate selection of anode side chemistry. With the help of calculated performance curves, the model was validated against our experimental work. A detailed parametric study has also been made. The results show that cell positioning, micro-tube diameter and cathode electrode morphology (i.e. structure, and material selection) are important parameters to be considered for experimental setup optimization.

The other parameters such as inlet velocity (flow rate), operating temperature and mixing ratio are although effective in improving the cell performance but their counter-effects should be considered. For example, too high operating temperature can cause problems for cathode and current collecting materials and also results in thermally driven degradation. The higher inlet flow velocity could reduce the fuel utilization and electrical efficiency. The higher mixing ratios could cause coking problems, on the other hand, operating at lower mixing ratio may cause oxidation of nickel in the anode. Therefore, for these parameters, experimental results (as described in Chapters 7-8) would be helpful to set the boundary limits for operation.

There are other parameters like, electrode porosity, permeability, operating pressure and emissivity of the cathode material. These parameters have very little effect on the cell performance. There-

fore, care must be taken before investing time and cost on their study and a detailed cost and energy analysis must be made beforehand.

CHAPTER 10

CONCLUSIONS AND OUTLOOK

10.1 Conclusions

In this work a numerical model has been developed for a novel-planar (with a hole in the center of the PEN), conventional-planar and a co-planar design. All three designs were computer analyzed under mixed-reactant conditions i.e. using hydrogen/air mixtures. The novel-planar cell (with perpendicular placement) design uses a hole in the center of the PEN to allow the flow to pass through, thus offering a kind of pressure relaxation. The model was run for two different values of electrode porosity ($\epsilon = 0.3$ and 0.4). The results show that highly porous electrodes offer less pressure drop associated with Darcy's flow. The rearrangement of the electrode pores/solid structure (permeability) may affect the porosity, thereby reducing the active area. It appears that increasing the permeability of the electrodes may handle the hydrodynamic problem (pressure drop across the cell), but the electrochemical performance could be at risk. One strategy to handle this issue is the use of a fully porous cell, allowing the porosity in the electrolyte. The fully porous cells allow pressure relaxation while maintaining electrochemical performance.

The results coming out from the novel-planar design show that the perpendicular placement of the cell can cause severe pressure drop across the cell. This study led us to investigate more into different placements of the planar cell. As a result, we rerun our numerical code for conventional-planar design with three different setups: 1) parallel, 2) anode first perpendicular and 3) cathode first perpendicular placement. The conventional-planar design suggests that the parallel placement of cell in the gas-chamber can provide high electrochemical performance, however, the uniform cell output (over the cell length) is strongly related to the flow rate. A high flow rate gives greater push to the flow while passing over the electrodes, thus offering less residence time for an electrochemical

reaction. On the other hand, low flow rates give better cell performance due to increased reaction time. The perpendicular setup was offering uniform cell performance but the pressure drop was a major problem in this placement. Most of the flow area was exposed to high resistance in the flow because of the porous electrodes (high tortuous path) and the flow was completely blocked near the electrode-electrolyte interfaces due to non-permeable nature of the electrolyte. The cathode first perpendicular placement gave the next highest performance as compared to the anode first placement. Since up to this stage we did not implement the energy equation, the heat generation could affect the performance of anode first placement very seriously. The heat generated contributes to convection, thus the gaseous mixture can be depleted (due to water production) via natural convection prior reaching the cathode. This will lower the oxygen partial pressure at the cathode resulting in lower OCV and finally lower output.

As it appears from the open literature that the heat generation has a potential effect on the cell performance, an energy equation was implemented. The idea was to consider another design in which the effect of energy contribution is more visible than the conventional-planar design. As a result, a non-isothermal model was developed and applied to a co-planar design. For this design, the short inter-distance (gap) between the electrodes is essential in order to minimize the ohmic loss. The short inter-distance will give a clear contribution of heat (via convention and diffusion) in affecting the cell performance. Less distance between the electrodes reduces the ohmic loss associated with ionic charge transfer but on the other hand narrow electrodes can give swirl motion and generate turbulence, depleting the mixture concentration in the nearby electrode. In order to handle this problem, barrier layers are suggested in between the electrodes. These layers can reduce the inter-mixing due to concentration gradient generated by turbulence. The heat generation due to electrochemical reaction can be taken away by increased convection stream. However, this does not seem to be practical in case of hydrocarbon as the fuel, because of large heat generation due to partial oxidation reaction. In such case, addition of some water vapor can induce endothermic reaction and the heat balance can be achieved.

The modelling study reveals that in a single-chamber setup, the cross diffusion, convection and intermixing is the main player in lowering the cell performance. As a result, it was proposed to realize and prove a practical design which can provide high OCV and an acceptable performance. The experimental study on micro-tubular cells under single-chamber conditions proved this hypothesis

(Chapter-7). It was also observed that the heat generation in case of SC-SOFCs can affect the cell's long term stability (Chapter-8) and silver current collecting wire is not a good choice for SC-SOFC operation.

In Chapter-9, we extended our earlier developed numerical model to be applicable for methane/air mixtures and micro-tubular geometry. The developed model incorporates methane full combustion, steam reforming, dry reforming and water-gas shift reaction followed by electrochemical oxidation of produced hydrogen within the anode. On the cathode side, parasitic combustion of methane along with the electrochemical oxygen reduction is implemented. The results show that the poor performance of single-chamber SOFC as compared to the conventional (dual-chamber) SOFC (in case of micro-tubes) is due to the mass transport limitation on the anode side. The gas velocity inside the micro-tube is far too low than the gas-chamber inlet velocity. The electronic current density is also non-uniform over the cell length, mainly due to the short length of the anode current collector located at the cell outlet. Furthermore, the higher temperature near the cell edges is due to the methane combustion (very close to the cell inlet) and current collection point (at the cell outlet). Both of these locations could be sensitive to the silver current collecting wire, as silver may rupture due to cell overheating.

The calculated results are in good agreement with our experimental study, suggesting that the model is reliable for optimization of experimental setup. To this end, we made a detailed parametric study for different parameters such as, the gas-chamber geometry, cell position, flow rate, temperature, pressure and the mixing ratio. These are the variables that can easily be controlled during experiments, therefore a feedback between the model and experiment is possible. Our modelling results show that reducing the micro-tube diameter and its placement near the cell inlet is effective in improving the cell performance. The flow rate, temperature and mixing ratio are also very effective in improving the cell performance but these parameters should be controlled very carefully in order to avoid their counter-effects as described in our experimental work.

There are some other parameters such as, exchange current density, electrode porosity, permeability, cathode radiative emissivity, that are rather difficult to measure experimentally. Among these parameters, the cathode exchange current density was very effective in improving the cell performance. It shows that the cathode morphology (micro-structure and material) is very important to consider. The other remaining parameters were seen less effective in terms of performance improve-

ment. Therefore, it is suggested before investing time on these parameters, a net energy and cost analysis would be very helpful.

10.2 Outlook

Much progress has been made during this work, though it is clear that there are still some issues with choosing appropriate materials for building an SC-SOFC with both an acceptable life time and production of electrical energy. While it has been observed that most of the problems related to material degradation are thermally driven, it would be very helpful to lower the operating temperature by using intermediate-temperature SOFC materials. Further to this, long term studies will benefit in order to determine their suitability under mixed-reactant environment.

A detailed modelling capability has been developed for SC-SOFCs, though its use to date has been limited to reproducing a single set of experimental results mainly due to lack of experimental data under other operating conditions. Further experiments and modelling simulations will be very helpful in order to take full benefit from the model-experiment-interactive mode and to optimize the design. For example, with the help of various parameters as discussed above, an optimized design can be suggested that can provide an acceptable efficiency with optimum performance. In a way forward, the suggested (through modelling) optimized design can be built in the lab in order to validate modelling results and to demonstrate the proof of concept. Also, the model calibration described in section (9.4) should be examined in further detail, which requires more extensive experimental data.

The extension of model to include redox behavior in the anode will further enhance its capability to predict coking and nickel oxidation under long term operating conditions. Furthermore, implementation of unsteady effects into the code will further enhance its capability to predict performance under thermal cycling which is very important in order to establish cyclic degradation during on and off.

BIBLIOGRAPHY

[1] L. BLUM, Elective course on fuel cells, FH-Aachen, 2004.

[2] Y. HAO, D.G. GOODWIN, J. Electrochem. Soc. 155 (2008) B666-B674.

[3] S.H. CLARKE, A.L. DICKS, K. POINTON, T.A. SMITH, A. SWAN, Catal. Today 38 (1997) 411-423.

[4] EG&G TECHNICAL SERVICES INC., Fuel Cell Handbook, 7th ed., U. S. Department of Energy, Office of Fossil Energy, National Energy Technology Laboratory, 2004, pp. 2-9.

[5] J.I. GAZZARRI, O. KESLER, J. Power Sources 167 (2007) 430-441.

[6] M. LIU, Z. LEU, B. WEI, R. ZHU, X. HUANG, K. CHEN, G. AI, W. SU, J. Electrochem. Soc. 154 (2007) B588-B592.

[7] T. SUZUKI, P. JASINSKI, V. PETROVSKY, H.U. ANDERSON, F. DOGAN, J. Electrochem. Soc. 151 (2004) A1473-A1476.

[8] T.W. NAPPORN, X.J. BEDARD, F. MORIN, M. MEUNIER, J. Electrochem. Soc. 151 (2004) A2088-A2094.

[9] T. SUZUKI, P. JASINSKI, V. PETROVSKY, H.U. ANDERSON, F. DOGAN, J. Electrochem. Soc. 152 (2005) A527-A531.

[10] Y. HAO, D.G. GOODWIN, J. Power Sources 183 (2008) 157-163.

[11] A. FAES, A. NAKAJO, A.H. WYSER, D. DUBOIS, A. BRISSE, S. MODENA, J.V. HERLE, J. Power Sources, doi:10.1016/j.jpowsour.2008.12.118.

[12] Y. LI, J. WU, C. JOHNSON, R. GEMMEN, X.M. SCOTT, X. LIU, Int. J. Hydrogen Energy, doi:10.1016/j.ijhydene.2008.11.050.

[13] http://www.banksengineering.com

[14] T. HIBINO, A. HASHIMOTO, T. INOUE, J. TOKUNO, S. YOSHIDA, M. SANO, J. Electrochem. Soc. 148 (2001) A544-A549.

[15] B.E. BUERGLER, Diss. ETH No. 16634.

[16] M. YANO, A. TOMITA, M. SANO, T. HIBINO, Solid State Ionics 177 (2007) 3351-3359.

[17] Z. SHAO, S.M. HAILE, Nature 431 (2004) 170-173.

[18] T. HIBINO, K. USHIKI, T. SATO, Y. KUWAHARA, Solid State Ionics 81 (1995) 1-3.

[19] Z. SHAO, S.M. HAILE, J. AHN, P.D. RONNEY, Z. ZHAN, S.A. BARNETT, Nature 435 (2005) 795-798.

[20] M. LIU, Z. L, B.WEI., R. ZHU, X. HUANG, K. CHEN, G. AI, W. SU, J. Electrochem. Soc. 154 (2007) B588-B592.

[21] T. SUZUKI, P. JASINSKI, V. PETROVSKY, H.U. ANDERSON, F. DOGAN, J. Electrochem. Soc. 151 (2004) A1473-A1476.

[22] Z. SHAO, C. KWAK, S.M. HAILE, Solid State Ionics 175 (2004) 39-46.

[23] B. MOREL, R. ROBERGE, S. SAVOIE, T.W. NAPPORN, M. MEUNIER, Appl. Catal. A 323 (2007) 181-187.

[24] T.HIBINO, A. HASHIMOTO, T. INOUE, J. TOKUNO, S. YOSHIDA, M. SANO, Science 288 (2000) 2031-2033.

[25] A. TOMITA, S. TERANISHI, M. NAGAO, T. HIBINO, M. SANO, J. Electrochem. Soc. 153 (2006) A956-A960.

[26] J. -P. VIRICELLE, C. PIJOLAT, B. RIVIERE, D. ROTUREAU, D. BRIAND, N.F. DE ROOIJ, Sens. Actuators B 118 (2006) 263-268.

[27] X.J.-BEDARD, T.W. NAPPORN, R. ROBERGE, M. MEUNIER, J. Electrochem. Soc. 154 (2007) B305-B309.

[28] D. ROTUREAU, J. -P. VIRICELLE, C. PIJOLAT, N. CAILLOL, M. PIJOLAT, J. Electrochem. Soc. 25 (2005) 2633-2636.

[29] B. MOREL, R. ROBERGE, S. SAVOIE, T.W. NAPPORN, M. MEUNIER, Electrochem. Solid-State Lett. 10 (2007) B31-B33.

[30] S. -J. AHN, Y. -B. KIM, J. MOON, J. -H. LEE, J. KIM, J. Electroceram. 17 (2006) 689-693.

[31] J. FLEIG, H.L. TULLER, J. MAIER, Solid State Ionics 174 (2004) 261-270.

[32] T. HIBINO, S. WANG, S. KAKIMOTO, M. SANO, Solid State Ionics 127 (2000) 89-98.

[33] B. WEI, Z. L, X. HUANG, M. LIU, K. CHEN, W. SU, J. Power Sources 167 (2007) 58-63.

[34] T.W. NAPPORN, F. MORIN, M. MEUNIER, Electrochem. Solid-State Lett. 7 (2004) A60-A62.

[35] B.E. BUERGLER, M. OCHSNER, S. VUILLEMIN, L.J. GAUCKLER, J. Power Sources 171 (2007) 310-320.

[36] T. HIBINO, A. HASHIMOTO, M. YANO, M. SUZUKI, S. YOSHIDA, M. SANO, Electrochem. Soc. 149 (2002) A133-A136.

[37] Z. SHAO, J. MEDEROS, W.C. CHUEH, S.M. HAILE, J. Power Sources 162 (2006) 589-596.

[38] P. JASINSKI, T. SUZUKI, F. DOGAN, H.U. ANDERSON, Solid State Ionics 175 (2004) 35-38.

[39] T. HIBINO, H. TSUNEKAWA, S. TANIMOTO, M. SANO, J. Electrochem. Soc. 147 (2000) 1338-1343.

[40] S. -J. AHN, Y. -B. KIM, J. MOON, J. -H. LEE, J. KIM, J. Power Sources 171 (2007) 511-516.

[41] K. ASANO, T. HIBINO, H. IWAHARA, J. Electrochem. Soc. 142 (1995) 3241-3245.

[42] T. HIBINO, A. HASHIMOTO, M. SUZUKI, M. YANO, S. YOSHIDA, M. SANO, J. Electrochem. Soc. 149 (2002) A195-A200.

[43] T. HIBINO, Y. KUWAHARA, S. WANG, J. Electrochem. Soc. 146 (1999) 2821-2826.

[44] B. ZHU, G. MENG, B. -E. MELLANDER, J. Power Sources 79 (1999) 30-36.

[45] T. HIBINO, K. USHIKI, Y. KUWAHARA, Solid State Ionics 91 (1996) 69-74.

[46] T.W. NAPPORN, X.J. BEDARD, F. MORIN, M. MEUNIER, J. Electrochem. Soc. 151 (2004) A2088-A2094.

[47] X.J. BEDARD, T.W. NAPPORN, R. ROBERGE, M. MEUNIER, J. Power Sources 153 (2006) 108-113.

[48] T. SUZUKI, P. JASINSKI, V. PETROVSKY, H.U. ANDERSON, F. DOGAN, J. Electrochem. Soc. 152 (2005) A527-A531.

[49] L. BAY, T. HORITA, N. SAKAI, M. ISHIKAWA, K. YAMAJI, H. YOKOKAWA, Solid State Ionics 113-115 (1998) 363-367.

[50] K. ASANO, H. IWAHARA, J. Electrochem. Soc. 144 (1997) 3125-3130.

[51] T. SUZUKI, P. JASINSKI, H.U. ANDERSON, F. DOGAN, J. Electrochem. Soc. 151 (2004) A1678-A1682.

[52] I. RIESS, Solid State Ionics 177 (2006) 1591-1596.

[53] T. SUZUKI, P. JASINSKI, H.U. ANDERSON, F. DOGAN, Electrochem. Solid-State Lett. 7 (2004) A391-A393.

[54] I.C. STEFAN, C.P. JACOBSON, S.J. VISCO, L.C. DE JONGHE, Electrochem. Solid-State Lett. 7 (2004) A198-A200.

[55] A. TOMITA, D. HIRABAYASHI, T. HIBINO, M. NAGAO, M. SANO, Electrochem. Solid-State Lett. 8 (2005) A63-A65.

[56] T. HIBINO, S. WANG, S. KAKIMOTO, M. SANO, Electrochem. Solid-State Lett. 2 (1999) 317-319.

[57] S. ASAHARA, D. MICHIBA, M. HIBINO, T. YAO, Electrochem. Solid-State Lett. 8 (2005) A449-A451.

[58] S. -J. AHN, J. -H. LEE, J. KIM, J. MOON, Electrochem. Solid-State Lett. 9 (2006) A228-A231.

[59] T. HIBINO, A. HASHIMOTO, T. INOUE, J. TOKUNO, S. YOSHIDA, M. SANO, J. Electrochem. Soc. 147 (2000) 2888-2892.

[60] B.E. BUERGLER, M.E. SIEGRIST, L.J. GAUCKLER, Solid State Ionics 176 (2005) 1717-1722.

[61] M. YANO, T. KAWAI, K. OKAMOTO, M. NAGAO, M. SANO, A. TOMITA, T. HIBINO, J. Electrochem. Soc. 154 (2007) B865-B870.

[62] I. RIESS, P.J. VAN DER PUT, J. SCHOONMAN, Solid State Ionics 82 (1995) l-4.

[63] S. RAZ, M.J.G. JAK, J. SCHOONMAN, I. Riess, Solid State Ionics 149 (2002) 335-341.

[64] I.RIESS, Solid State Ionics 176 (2005) 1667-1674.

[65] B.E. BUERGLER, A.N. GRUNDY, L.J. GAUCKLER, J. Electrochem. Soc. 153 (2006) A1378-A1385.

[66] M. KUHN, T. NAPPORN, M. MEUNIER, D. THERRIAULT, S. VENGALLATORE, J. Power Sources 177 (2008) 148-153.

[67] M. KUHN, T. NAPPORN, M. MEUNIER, S. VENGALLATORE, D. THERRIAULT, J. Micromech. Microeng. 18 (2008) 015005.

[68] C. ZHANG, Y. ZHENG, R. RAN, Z. SHAO, W. JIN, N. XU, J. AHN, J. Power Sources 179 (2008) 640-648.

[69] M. KUHN, T.W. NAPPORN, M. MEUNIER, D. THERRIAULT, J. Electrochem. Soc. 155 (2008) B994-B1000.

[70] I. RIESS, J. Power Sources 175 (2008) 325-337.

[71] M. YANO, M. NAGAO, K. OKAMOTO, A. TOMITA, Y. UCHIYAMA, N. UCHIYAMA, T. HIBINO, Electrochem. Solid-State Lett. 11 (2008) B29-B33.

[72] N. AKHTAR, S.P. DECENT, D. LOGHIN, K. KENDALL, J. Power Sources 193 (2009) 39-48.

[73] Y. HAO, D.G. GOODWIN, J. Electrochem. Soc. 154 (2007) B207-B217.

[74] Y. HAO, Z. SHAO, J. MEDEROS, W. LAI, D.G. GOODWIN, S.M. HAILE, Solid State Ionics 177 (2006) 2013-2021.

[75] C. -Y. CHUNG, Y. -C. CHUNG, J. Power Sources 154 (2006) 35-41.

[76] C. -Y. CHUNG, Y. -C. CHUNG, J. KIM, J. LEE, H.W. LEE, J. Electroceram. 17 (2006) 959-964.

[77] Y. HAO, D.G. GOODWIN, J. Power Sources 183 (2008) 157-163.

[78] Y. HAO, D.G. GOODWIN, J. Electrochem. Soc. 155 (2008) B666-B674.

[79] S. H. CHAN, Z. T. XIA, J. Electrochem Soc. 148 (2001) A388-A394.

[80] S. H. CHAN, X. J. CHEN, K. A. KHOR , J. Electrochem Soc. 151 (2004) A164-A172.

[81] S. AHMED, C. MCPHEETERS, R. KUMAR, J. Electrochem Soc. 138 (1991) 2712-2718.

[82] A. HIRANO, M. SUZUKI, M. IPPOMMATSU, J. Electrochem. Soc. 139 (1992) 2744-2751.

[83] H. KAROLIUSSEN, K. NISANCIOGLU, Proc. 3rd international symposium on SOFC, Honolulu, Hawaii, May 1993.

[84] E. ACHENBACH, J. Power Sources 49 (1994) 333-348.

[85] R. BOVE, S. UBERTINI, J. Power Sources 159 (2006) 543-559.

[86] M.F. SERINCAN, U. PASAOGULLARI, N.M. SAMMES, J. Electrochem. Soc. 155 (2008) B1117-B1127.

[87] T. SUZUKI, T. YAMAGUCHI, Y. FUJISHIRO, M. AWANO, J. Electrochem. Soc. 153 (2006) A925-A928.

[88] R. SUWANWARANGKUL, E. CROISET, M. W. FOWLER, P.L. DOUGLAS, E. ENTCHEV, M. A. DOUGLAS, J. Power Sources 122 (2003) 9-18.

[89] H. YAKABE, M. HISINUMA, M. URATANI, Y. MATSUZAKI, I. YASUDA, J. Power Sources 86 (2000) 423-431.

[90] C. HAYNES, W. WEPFER, Int J Hydrogen Energy 26 (2001) 369-379.

[91] N.F. BESSETTE, W.J. WEPFER, J. WINNICK, J. Electrochem. Soc. 142 (1995) 3792-3800.

[92] J. BILLINGHAM, A.C. KING, R.C. COPCUTT, K. KENDALL, J. Appl. Math. 60 (1999) 574-601.

[93] P. AGUIAR, D. CHADWICK, L. KERSHENBAUM, Chem. Eng. Sci. 57 (2002) 1665-1677.

[94] S.H. CHAN, F.C. LOW, O.L. DING, J. Power Sources 103 (2002) 188-200.

[95] K.P RECKNAGLE, R.E. WILLIFORD, L.A. CHICK, D.R. RECTOR, M.A. KHALEEL, J. Power Sources 113 (2003) 109-114.

[96] J.V. HERLE, F. MARECHAL, S. LEUENBERGER, D. FAVRAT, J. Power Sources 118 (2003) 375-383.

[97] K.M. WALTERS, A.M. DEAN, H.Y. ZHU, R.J. KEE, J. Power Sources 123 (2003) 182-189.

[98] U. PASAOGULLARI, C.Y. WANG, Proc. ECS 07 (2003) 1403-1412.

[99] P. LI, M.K. CHYU, J. Power Sources 124 (2003) 487-498.

[100] S. MURTHY, A.G. FEDOROV, J. Power Sources 124 (2003) 453-458.

[101] T. ACKMANN, L.G.J. DE HAART, W. LEHNERT, D. STOLTEN, J. Electrochem. Soc. 150 (2003) A783-A798.

[102] Y. JIANG, A.V. VIRKAR, J. Electrochem. Soc. 150 (2003) A942-A951.

[103] M.A. KHALEEL, J.R. SELMAN In: S.C. Singhal, K. Kendall, editors. High-temperature solid oxide fuel cells-fundamentals, design and applications. Oxford: Elsevier Science; 2003. p. 293331.

[104] P.W. LI, L. SCHAEFER, M.K. CHYU, ASME J. Heat Transfer 126 (2004) 219-229.

[105] J. FLEIG, Annu. Rev. Mater. Res. 33 (2003) 361-382.

[106] H. ZHU, R.J. KEE, J. Electrochem. Soc. 152 (2005) A2427-A2440.

[107] B. LI, K. MARUYAMA, M. NURUNNABI, K. KUNIMORI, K. TOMISHIGE, Ind. Eng. Chem. Res. 44 (2005) 485-494.

[108] W. FISCHER, J. MALZBENDER, G. BLASS, R.W. STEINBRECH, J. Power Sources 150 (2005) 73-77.

[109] A. SELIMOVIC, M. KEMM, T. TORISSON, M. ASSADI, J. Power Sources 145 (2005) 436-469.

[110] E.S. HECHT, G.K. GUPTA, H. ZHU, A.M. DEAN, R.J. KEE, L. MAIER, O. DEUTSCHMANN, Appl. Catal. A 295 (2005) 40-51.

[111] R.K. KUMAR, J. Fire Sciences 3 (1985) 245-262.

[112] W.G. BESSLER, S. GEWIES, J. Electrochem. Soc. 154 (2007) B548-B559.

[113] T. BERNING, D.M. LU, N. DJILALI, J. Power Sources 106 (2002) 284-294.

[114] B.R. SIVERTSEN, N. DJILALI, J. Power Sources 141 (2005) 65-78.

[115] R. TAYLOR, R. KRISHNA, Multi-component Mass Transfer, John Wiley and Sons, 1993.

[116] R. PERRY, D. GREEN, Perrys Chemical Engineering Handbook, sixth ed., McGraw-Hill, 1983.

[117] L.E. SISSOM, D.R. PITTS, Elements of Transport Phenomena, international student edition., McGraw-Hill, 1972.

[118] J.M. COULSON, J.F. RICHARDSON, Fluid flow, heat transfer and mass transfer, fifth ed.,Vol-1, Oxford: Butterworth-Heinemann, 1996.

[119] J.M. COULSON, J.F. RICHARDSON, Introduction to chemical engineering design, second ed., Vol-6,Oxford: Butterworth-Heinemann, 1996.

[120] E.R. GILLILAND, Ind.Eng.Chem. 26 (1934) 681.

[121] J.C.R. MORALES, J.C. VAZQUEZ, D.M. LOPEZ, J.T.S. IRVINE, P. NUNEZ, J. Electrochim. Acta 52 (2007) 7217-7225.

[122] D.F. CHEDDIE, NORMAN.D.H. MUNROE, J. Power Sources 160 (2006) 215- 223.

[123] D.F. CHEDDIE, NORMAN.D.H. MUNROE, J. Power Sources 171 (2007) 634- 643.

[124] D. CUI, Y.C. CHUNG, L. LIU,Y. DONG, M. CHENG, J. Power Sources 174 (2007) 246-254.

[125] L. ANDREASSI, G. RUBEO, S. UBERTINI, P. LUNGHI, R. BOVE, Int. J. Hydrogen Energy 32 (2007) 4559-4574.

[126] G.H. GUVELIOGLU, H.G. STENGER, J. Power Sources 147 (2005) 95-106.

[127] C. SIEGEL, Energy 33 (2008) 1331-1352.

[128] V.M. JANARDHANAN, O. DEUTSCHMANN, Chemical Eng. Sc. 62 (2007) 5473-5486.

[129] X. ZHANG, J. LI, G. LI, Z. FENG, Int. J. Thermal Sciences 48 (2009) 805-814.

[130] S.C. SINGHAL, K. KENDALL, High Temperature Solid Oxide Fuel Cells: Fundamentals, Design and Applications, Elsevier, Kidlington Oxford, 2003, p.224.

[131] F. ROBINSON, Phys. Fluids 16 (2004) 1321-1333.

[132] M. G. BRAUNSFURTH, A. C. SKELDON, A. JUEL, T. MULLIN, D. S. RILEY, J. Fluid Mech. 342 (1997) 295-314.

[133] A. SAMEEN, R. VERZICCO, K. R. SREENIVASAN, Phys. Scr. T132 (2008) 014053.

[134] F.P. INCROPERA, D.P. DEWITT, Fundamentals of Heat and Mass Transfer, Fifth Ed., R.R. Donnelley & Sons, Company, 2002.

[135] B. TODD, J.B. YOUNG, J. Power Sources 110 (2002) 186-200.

[136] W. BUJALSKI, J. PARAGREEN, G. READE, S. PYKE, K. KENDALL, J. Power Sources 157 (2006) 745-749.

[137] W. BUJALSKI, C. M. DIKWAL, K. KENDALL, J. Power Sources 171 (2007) 96-100.

[138] V.A. RESTREPO, J.M. HILL, Appl. Catal. A 342 (2008) 49-55.

[139] S. GHOSH, A.D. SHARMA, P. KUNDU, S. MAHANTY, R.N. BASU, J. Non-Cryst. Solids 354 (2008) 4081-4088.

[140] N. AKHTAR, S.P. DECENT, D. LOGHIN, K. KENDALL, ECS Transactions 13 (28) 107-124.

[141] N. AKHTAR, S.P. DECENT, D. LOGHIN, K. KENDALL, Proc. ASME 6th International Fuel Cell Science, Engineering and Technology Conference, June 16-18, 2008, Denver, Colorado, USA.

[142] N. AKHTAR, S.P. DECENT, D. LOGHIN, K. KENDALL, Proc. International Conference and Trade Fair on Hydrogen and Fuel Cell Technologies, 22-23 Oct., 2008, Hamburg, Germany.

[143] C. MALLON, K. KENDALL, J. Power Sources 145 (2005) 154-160.

[144] A. DHIR, K. KENDALL, J. Power Sources 181 (2008) 297-303.

[145] T.J. LEE, K. KENDALL, J. Power Sources 181 (2008) 195-198.

[146] B. MOREL, R. ROBERGE, S. SAVOIE, T.W. NAPPORN, M. MEUNIER, J. Power Sources 186 (2009) 89-95.

[147] R.W. JACKSON, F.S. PETTIT, G.H. MEIER, J. Power Sources 185 (2009) 1030-1039.

[148] P. SINGH, Z. YANG, V. VISWANATHAN, J.W. STEVENSON, J. Mater. Eng. Perform. 13 (2004) 287-294.

[149] W.A. MEULENBERG, O. TELLER, U. FLESCH, H.P. BUCHKREMER, D. STOEVER, J. Mater. Sci. 36 (2001) 3189-3195.

[150] S.W. SOFIE SW, P. GANNON, V. GOROKHOVSKY, J. Power Sources 191 (2009) 465-472.

[151] J.H. WANG, M.L. LIU, M.C. LIN, Solid State Ionics 177 (2006) 939-947.

[152] N. AKHTAR, S.P. DECENT, K. KENDALL, J. Power Sources, doi:10.1016/j.jpowsour.2009.04.078.

[153] M. NI, D.Y.C. LEUNG, M.K.H. LEUNG, J. Power Sources 183 (2008) 133-142.

[154] B. LI, R. WATANABE, K. MARUYAMA, M. NURUNNABI, K. KUNIMORI, K. TOMISHIGE, Appl. Catal. A 290 (2005) 36-45.

[155] K. TOMISHIGE, S. KANAZAWA, K. SUZUKI, M. ASADULLAH, M. SATO, K. IKUSHIMA, K. KUNIMORI, Appl. Catal. A 233 (2002) 35-44.

[156] B. LI, R. WATANABE, K. MARUYAMA, K. KUNIMORI, K. TOMISHIGE, Catal. Today 104 (2005) 7-17.

[157] K. TOMISHIGE, M. NURUNNABI, K. MARUYAMA, K. KUNIMORI, Fuel Process. Technol. 85 (2004) 1103-1120.

[158] K. TOMISHIGE, S. KANAZAWA, K. SUZUKI, M. ASADULLAH, M. SATO, K. IKUSHIMA, K. KUNIMORI, Appl. Catal. A 351 (2008) 54-58.

[159] K. YOSHIDA, K. OKUMURA, T. MIYAO, S. NAITO, S. ITO, K. KUNIMORI, K. TOMISHIGE, Appl. Catal. A 351 (2008) 217-225.

[160] I. ZINOVIK, D. POULIKAKOS, Electrochim. Acta 54 (2009) 6234-6243.

[161] W. ZHOU, R. RAN, Z. SHAO, J. Power Sources 192 (2009) 231-246.